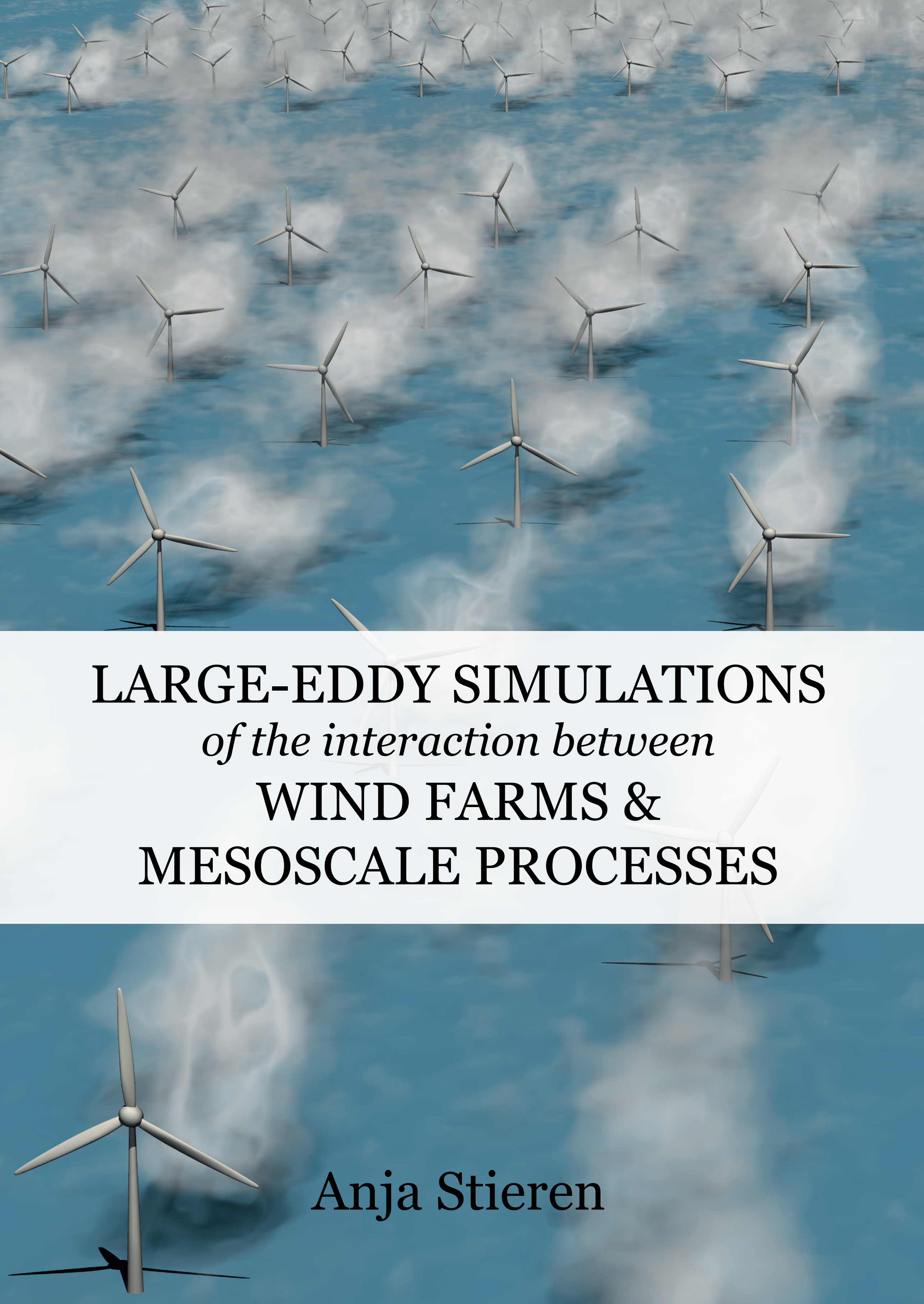

LARGE-EDDY SIMULATIONS
of the interaction between
WIND FARMS & MESOSCALE PROCESSES

Anja Stieren

LARGE-EDDY SIMULATIONS OF THE INTERACTION BETWEEN WIND FARMS AND MESOSCALE EFFECTS

Anja Stieren

Graduation committee:

prof. dr. J. L. Herek (chair / secretary)	University of Twente
prof. dr. rer. nat. D. Lohse (supervisor)	University of Twente
assoc. prof. dr. ir. R. J. A. M. Stevens (supervisor)	University of Twente
prof. dr. R. Verzicco	University of Twente
prof. dr. S. Luding	University of Twente
prof. dr. ir. J. W. van Wingerden	Delft University of Technology
prof. dr. J. Peinke	Carl-von-Ossietzky University Oldenburg & ForWind

The work in this thesis was carried out at the Physics of Fluids group of the Faculty of Science and Technology of the University of Twente. This thesis was financially supported by the Shell-NWO/FOM-initiative Computational sciences for energy research of Shell and Chemical Sciences, Earth and Live Sciences, Physical Sciences, FOM, and STW.

Dutch title: *Large eddy simulaties van de interactie tussen windmolenparken en mesoschaal effecten*

Publisher: *Anja Stieren*, Physics of Fluids, University of Twente,
P.O. Box 217, 7500 AE Enschede, The Netherlands

Cover design: Anja Stieren & Srinidhi N. Gadde. Volume flow visualization of wind turbine wakes in and between two wind farms. White contours visualize the reduced velocity behind the wind turbines.

ISBN: 978-90-365-5445-9
DOI: 10.3990/1.9789036554459

LARGE-EDDY SIMULATIONS OF THE INTERACTION BETWEEN WIND FARMS AND MESOSCALE EFFECTS

DISSERTATION

to obtain
the degree of doctor at the Universiteit Twente,
on the authority of the rector magnificus,
prof. dr. ir. A. Veldkamp,
on account of the decision of the Doctorate Board
to be publicly defended
on Friday 30th of September 2022 at 16.45 hours

by
Anja Stieren

born on the 3rd of March, 1991
in Warstein, Germany

This dissertation has been approved by the supervisors:

prof. dr. rer. nat. Detlef Lohse

and

assoc. prof. dr. ir. Richard J. A. M. Stevens

Contents

1 Introduction 1

1.1 Wind turbine and wind farm wakes . . . 1
1.2 The atmospheric boundary layer . . . 7
1.3 Numerical simulations of the ABL . . . 11
1.4 A guide through the thesis . . . 15

I Modeling sub-grid scales and mesoscale effects in large-eddy simulations 17

2 Large-eddy simulations of stratified atmospheric boundary layers: Comparison of different sub-grid scale models 19

2.1 Introduction . . . 21
2.2 Large-eddy simulations . . . 23
2.3 Results and Discussion . . . 29
2.4 Conclusions . . . 42

3 Modeling dynamic wind direction changes in large-eddy simulations of wind farms 45

3.1 Introduction . . . 46
3.2 Rotation of the mean wind direction in LES . . . 48
3.3 Dynamic wind direction changes in LES of neutral ABL . . . 50
3.4 Effect of dynamic wind direction changes on wind farm performance 56
3.5 Conclusions . . . 62

4 The impact of negative geostrophic wind shear on wind farm performance 65

4.1 Introduction . . . 67
4.2 Large-eddy simulations . . . 70
4.3 Boundary layer characteristics . . . 76

4.4 Effect of baroclinicity on the flow in and around wind farms . . 80
4.5 Energy budget analysis 83
4.6 Wind farm power production 88
4.7 Conclusion 90
4.8 Appendix 91

II Wind farm wakes 93

5 Evaluating wind farm wakes in large-eddy simulations and engineering models 95
5.1 Introduction 96
5.2 Engineering models 97
5.3 Large-eddy simulations 101
5.4 Computational setup 102
5.5 Results 103
5.6 Conclusions 106

6 Impact of wind farm wakes on flow structures in and around downstream wind farms 107
6.1 Introduction 108
6.2 Large-eddy simulations 110
6.3 Results 115
6.4 Conclusion 133
6.5 Appendix 136

7 Conlusions and Perspectives 143
7.1 Sub-grid scales and mesoscale effects in micro-scale large-eddy simulations 143
7.2 Wind farm wakes 146

Scientific output 149

References 153

Summary 177

Samenvatting 181

Zusammenfassung 185

Acknowledgements 189

1

Introduction

The research summarized in this thesis explores wakes inside, behind and between wind farms and their interactions with the atmospheric boundary layer (ABL) using large-eddy simulations (LES). This introduction begins with an elaboration on wind turbine wakes, followed by a discussion on the interaction of these wakes in wind farms, where multiple turbines are placed close to each other. Then, the importance of detailed studies of wakes behind wind farms is described, followed by a brief description of the Earth's ABL in which the turbines are situated. Finally, the motivation and justification of using LES to study ABL and wind turbine interactions is described.

1.1 Wind turbine and wind farm wakes

Humankind learned to harvest energy from the wind more than 3000 years ago [1]. However, the idea of using wind energy to generate electricity using wind turbines was first proposed by James Blyth in 1887 [2], who used a wind turbine as a battery charging machine to light his holiday home in Scotland [2]. The basic working principle of a wind turbine is as follows: The incoming wind energy lifts and rotates the wind turbine blades. The spinning of the rotor is transferred to the gear box. In the gear box, the low-speed shaft, which is connected to the rotor, is connected to a high-speed shaft, increasing the

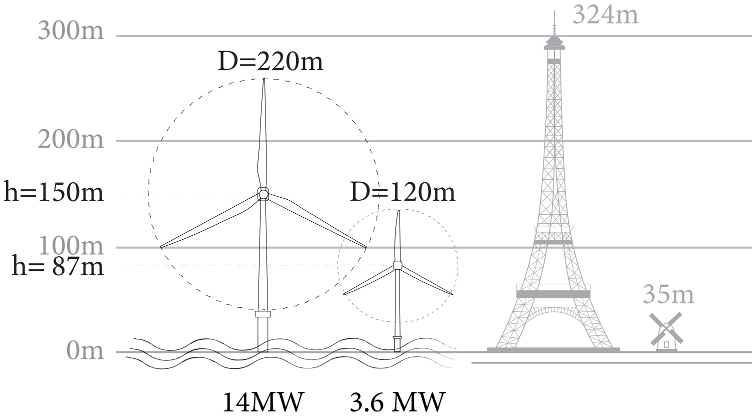

Figure 1.1 – Illustration of the relative sizes of modern wind turbines: size of the GE Haliade-X turbine (14 MW), which is currently one of largest wind turbines in the world [3], and a Siemens 3.6MW wind turbine, which is used in the London array, is shown to give a reference of typical offshore wind turbines constructed before 2013 [4]. The heights of a typical Dutch wind mill and the Eiffel tower are also shown for reference.

rotational speed. Finally, the high-speed shaft is connected to the generator to produce electricity.

While the first electricity-generating wind turbines in the late nineteenth century produced 12kW [5], modern wind turbines currently reach diameters over 220 m and are capable of producing more than 14 MW [3]. Figure 1.1 shows one of the world's largest wind turbine to date alongside the size of a typical offshore wind turbine. The size of turbines increases continuously due to the relation of power production (P) to the turbine's diameters (D) and the incoming wind velocity (v):

$$P \sim D^2 v^3. \tag{1.1}$$

Consequently, a doubling of the rotor diameter increases the power production by a factor of four. Increasing the hub-height (h) is also advantageous because the wind velocity increases with height in the lower part of the atmosphere. Turbines are generally larger in offshore regions, where higher and steadier wind velocities prevail compared to onshore regions. Furthermore, the construction of large wind turbines is difficult on land.

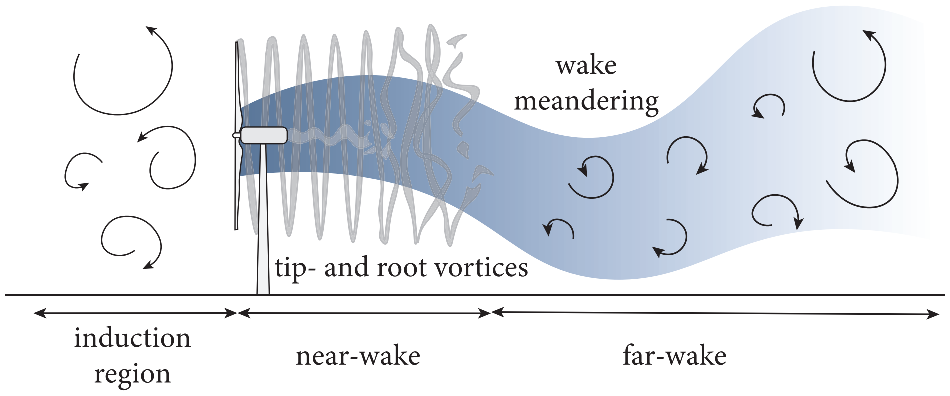

Figure 1.2 – Schematic side view of the instantaneous wake structure behind a wind-turbine, adapted from Porté-Agel et al. [6]. Shown are the helical structure of the vortices in the near wake and the recovery of the low velocity zone with downstream distance. Additionally, the induction region in front of the turbine is indicated, where the incoming flow decelerates due to the presence of the turbine.

Wakes

Wind turbines extract momentum from the flow, slowing down the wind that passes them. If a wind turbine was capable of extracting 100% of the incoming kinetic energy, the wind behind the turbine would no longer move, since the air would deflect the flow around the turbine, preventing the turbine from spinning. Consequently, there is an upper limit of energy that a wind turbine can harvest from the wind. Theoretically, the limit is shown to be 59.3% of the incoming kinetic energy, known as the Betz limit, and in practice this value has not been reached [7, 8].

Figure 1.2 illustrates the flow regimes around a wind turbine. In front of the turbine, in the induction zone, there is a small reduction in velocity since part of the flow is deflected around the turbine. However, a much larger velocity reduction occurs behind the wind turbine in the turbine *wake*. Additionally, tip and root vortices are generated behind the turbine rotor due to the sweeping of the air by the blades. The helical structure of these vortices persists only in the near-wake region, directly behind the turbine, as shown in figure 1.2. This region is influenced by the rotor geometry, its aerodynamics and the inflow conditions. Further downstream, in the far-wake region, the ABL dynamics

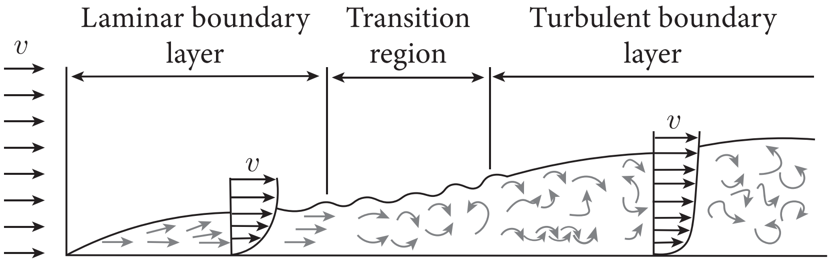

Figure 1.3 – Development of a turbulent boundary layer over a flat plate, adapted from Incropera et al. [9].

dominate the wake properties. Here, the helical structures break down due to different instability mechanisms. Figure 1.2 further highlights the meandering of the wake, including small whirls and eddies. These structures illustrates that wakes are not only regions of reduced velocity but also increased turbulence intensity. Therefore, a brief elaboration on turbulence and its importance for wake recovery is given below.

Turbulence

Even without the presence of the wind turbines, the flow development over the Earth's surface is complex due to turbulence. To describe this complexity, figure 1.3 shows the fluid flow over a flat plate. When being in contact with the leading edge of the plate, the uniform inflow will decelerate due to friction. Initially, the flow is ordered and smooth, called *laminar*. After some distance, the shear at the surface gives rise to small chaotic oscillations and the flow transitions to *turbulence*, before it eventually becomes fully turbulent. If and when the transition occurs can be estimated based on the Reynolds number $Re = \frac{v\rho L}{\mu}$, which depends on the velocity v, the dynamic viscosity μ and the density ρ of the fluid [10]. L is a characteristic length scale of the system. When viscous forces are dominant, Re is low and the flow is laminar. When inertial forces are dominant, Re is high and the flow is turbulent.

Turbulent flows are chaotic, non-deterministic and random. In turbulent flows the velocity varies significantly and irregularly in space and time, making its study extremely complex. The motions occur on a large range of scales, from the main large-scale mean flow to small whirls and eddies. When observing a river, waterfall or steam rising out of a chimney, the irregular, chaotic flow motions are visible. However, when observing a wind turbine during non-foggy days, only the rotation of the blades is visible, such that the flow development around the turbine is not intuitive.

Turbulence efficiently mixes and transports the momentum of a fluid [11], such that the low velocity zones behind turbines are replenished with the surrounding undisturbed flow. Consequently, the turbulence intensity of the flow greatly influences the extent of the wake behind a wind turbine. For example, air mixes relatively slowly when the turbulence intensity is low, i.e. above flat terrain with a low roughness, such as water or grass land. In this case, the wakes recover slowly. In contrast, when the turbulence intensity is high, i.e. over rough terrains like cropped land, forests or hilly terrain, the mixing with the surrounding air increases, allowing a faster wake recovery.

Wind farms

Wind turbines are often placed relatively close together in wind farms in order to optimize the use of available land, maintenance procedures and connection to the electricity grid. Dependent on the distance in between the wind turbines and the atmospheric conditions, the power production of wind turbines, that are arranged in wind farms, will differ from the power production of free-standing turbines.

Wind turbines, that are placed downstream, in the wake, of other wind turbines experience much lower momentum and higher turbulence than free-standing turbines. Further downstream, the turbine wakes interact with other wakes. The increased turbulence intensity and lowered kinetic energy in the wakes causes an energy entrainment from above and from the sides [6, 12–15]. In very large wind farms, the recovery of mean kinetic energy around the wind turbines that are positioned deep inside the array is found to be dominated by this vertical flux from above [12–14, 16–18]. In this case, the power production per row becomes constant.

Furthermore, as discussed above, the flow in front of wind turbines is deflected upwards and sideways due to mass conservation and consequently decelerated. While this deceleration is of negligible magnitude for single turbines, the cumulated blockage effect induced by the wind farm might be relevant [19–32]. However, much higher power losses can occur due to wind turbine wake effects.

Behind the wind farm, the flow starts to recover and accelerates in a wind farm wake. In the following, the importance of studying these wake regions is elaborated.

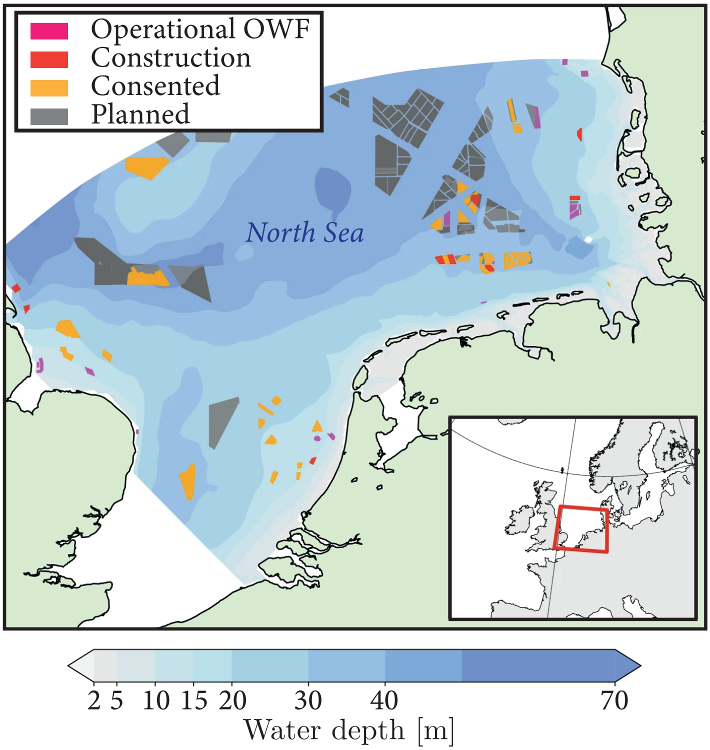

Figure 1.4 – Map of wind farms that are contructed or planned in the North Sea, adapted from Slavik et al. [33] with permission. The planning status of each offshore wind farm (OWF) as of September 2015 is indicated by different colors.

Wind farm wakes

Wakes of individual wind turbine wakes interact and form a wind farm wake behind the last turbine row of a wind farm [34]. Velocity deficits of 21% have been measured up to 55 km downstream of wind farms [34], reducing the power production of downstream wind farms. This highlights the importance of detailed studies on wind farm wakes. Figure 1.4 shows wind farms that are operational, under construction or planned to be built in the North Sea [33]. The number of wind farms in shallow offshore regions, such as the North Sea, has been increasing especially rapidly, since offshore winds are relatively steady with higher velocities compared to onshore regions [5]. Another reason for the rapid grow of offshore energy is the limited space in onshore regions, due to the low acceptance of wind turbines in the vicinity of residential areas. However, the construction and maintenance costs are lower in onshore regions.

The dense distribution of wind farms raises important questions such as: How do wind farms impact the flow development in areas like the North Sea? How is wild life affected? And how do wind farms influence each other? This thesis focuses on the latter question. However, the study of wind turbine and wind farm wakes is complex, because the extent of wind farm wakes depends on several factors, such as the wind farm layout, the surrounding terrain and the atmospheric conditions. Section 1.2 briefly describes different atmospheric conditions and how they can influence the wake recovery.

1.2 The atmospheric boundary layer

The ABL is the atmospheric layer which is in contact with and directly influenced by the Earth's surface, spanning a few hundred meters vertically. Directly above the surface, the air velocity increases in dependence on the friction forces and surface temperature. Above the ABL, the free atmosphere is assumed to be almost frictionless. In the atmosphere, high and low pressure areas are formed due to temperature differences driving the air flow from high to low pressure areas. Additionally, air flow is influenced by the Coriolis force of the Earth's rotation. Air that is driven by pressure gradient forces is deflected to the right in the Northern hemisphere and to the left in the southern hemisphere. When pressure gradient and Coriolis force are in balance, the flow is directed parallel to the isobars, which is defined as *geostrophic wind*. For simplification, air flow above the ABL is assumed to be geostrophic [35].

Due to the complex, non-linear nature of the ABL, its structure changes continuously. Based on the description of Stull [35], a diurnal cycle of a day with a clear sky is described to give an idealistic example of the ABL's structure. On a sunny day, the Earth's surface is heated up by solar radiation making the air close to the surface relatively warmer than the air above it. Warm air is lighter than cold air, and therefore, the air close to the surface rises and is replaced by relatively cooler air. This process stimulates mixing and the well-mixed boundary layer is called *convective boundary layer (CBL)*. Above the CBL a stable entrainment zone is formed, which is capped by the free atmosphere where the velocity recovers to the geostrophic value, as shown in

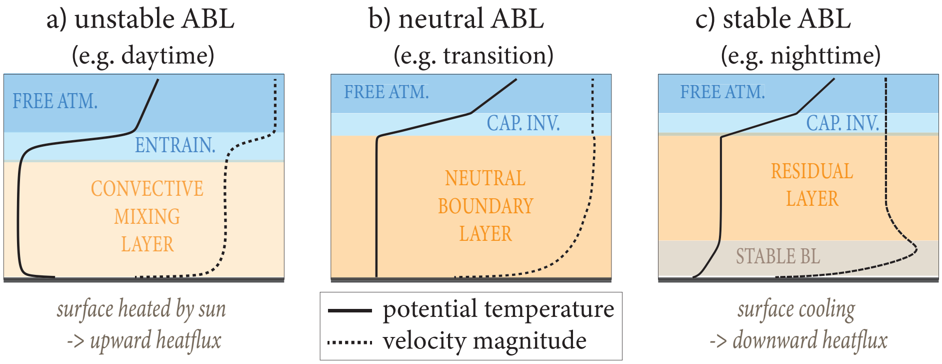

Figure 1.5 – Idealized vertical potential temperature and velocity profiles in an (a) unstable, (b) neutral, and (c) stable ABL.

figure 1.5a.

Later, when the sun sets, the surface cools and the air above it is relatively warmer. As a result, the air close to the surface no longer rises, hindering the mixing of the ABL, which creates a very *stable boundary layer (SBL)*. A residual layer of air that was mixed during the day resides above the SBL without any surface contact. Consequently, this layer does not experience surface friction forces. As a result, the air in this residual layer accelerates in the presence of horizontal pressure gradients and an inertial oscillation is triggered when the friction forces disappear [36, 37]. The wind velocity in this region can accelerate to values higher than the geostrophic wind velocity. This velocity maximum, which is mostly found between 50 and 1000 m is known as *low-level jet (LLJ)* [38], shown in figure 1.5c. Due to this phenomenon and the lower turbulence during night, wind speeds are typically higher at night than during the day.

Above the residual layer, the capping inversion that was formed during the day in form of the entrainment zone is still present and the potential temperature increases rapidly to the free-atmosphere temperature.

It is important to point out that the described daily cycle is quite idealized, as only few parameters are taken into consideration. The ABL flow is highly influenced by daily, monthly, and yearly weather patterns. Furthermore, mountain ranges, hills, sea to land transitions, ice to sea transitions, weather fronts and cities are just a few factors which make the structure of the ABL even more complex. For example, clouds obstruct the radiative surface heating,

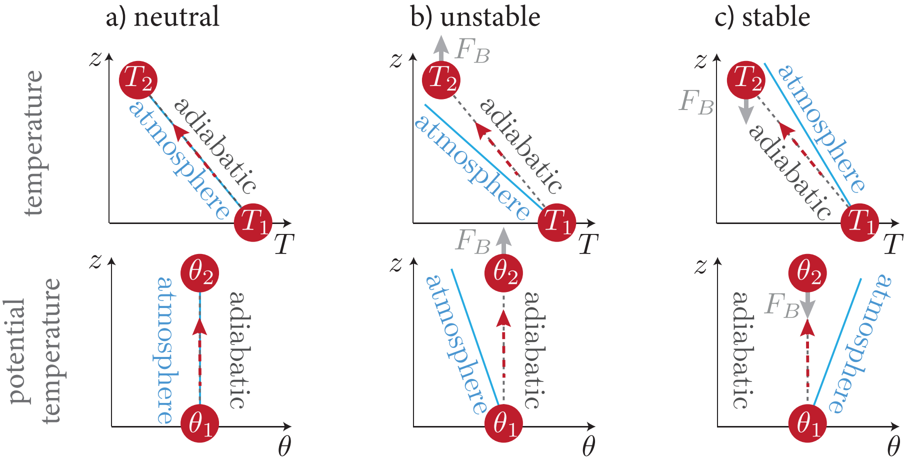

$$T_2 = T_{\mathrm{atm}}, \quad \frac{\partial T}{\partial z} < 0 \qquad T_2 > T_{\mathrm{atm}}, \quad \frac{\partial T}{\partial z} < 0 \qquad T_2 < T_{\mathrm{atm}}, \quad \frac{\partial T}{\partial z} < 0$$

$$\theta_2 = \theta_{\mathrm{atm}}, \quad \frac{\partial \theta}{\partial z} = 0 \qquad \theta_2 > \theta_{\mathrm{atm}}, \quad \frac{\partial \theta}{\partial z} < 0 \qquad \theta_2 < \theta_{\mathrm{atm}}, \quad \frac{\partial \theta}{\partial z} > 0$$

Figure 1.6 – Illustration of the vertical profiles of the temperature T and potential temperature θ for different stability regimes. Assume that an air parcel (red circle) is vertically displaced upwards adiabatically, i.e. without exchanging heat with the surroundings. (a) In a neutral atmosphere, where the temperature decreases adiabatically without an impact of buoyancy forces. (b) In an unstable atmosphere, where the temperature decreases more than adiabatically. In this case the particle accelerates due to buoyancy forces (F_B). (c) In a stable atmosphere, where the temperature decreases less than adiabatically and buoyancy restores the particle movement. Stability regimes can be distinguished based on $\partial\theta/\partial z$.

which can lead to the formation of well-mixed *neutral boundary layers (NBLs)*. NBLs are often observed in offshore regions, where surface heatflux is found to be smaller than over land [39] or around sunrise and sunset, during the transition between stable and convective conditions, as illustrated in figure 1.5b.

The schematic in figure 1.5 illustrates the three described boundary layers. Instead of the temperature T, a variable named potential temperature θ is displayed. The potential temperature is a simple means to distinguish between unstable, neutral, and stable conditions based on its change with height $\partial\theta/\partial z$,

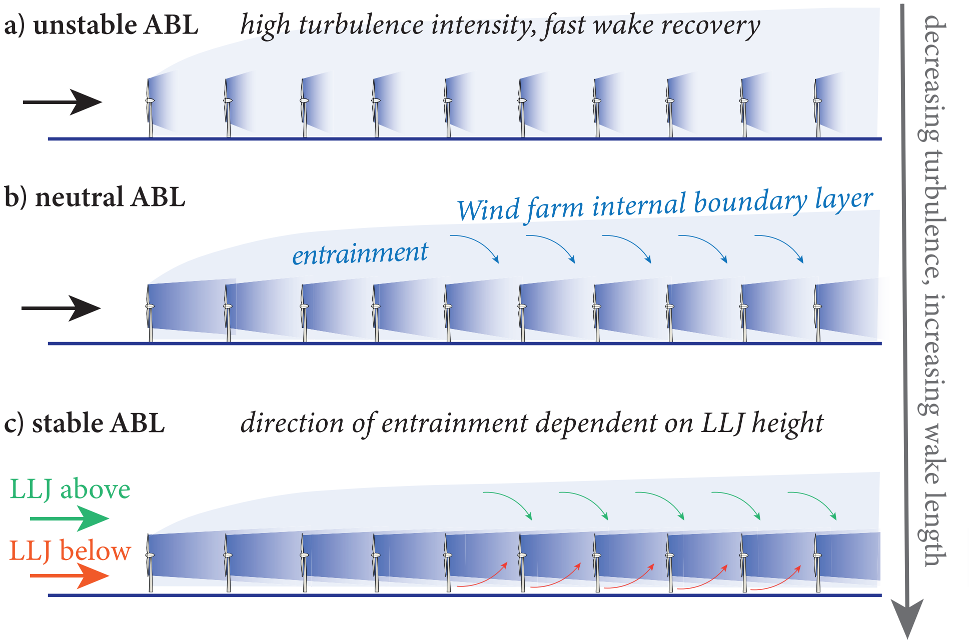

Figure 1.7 – Idealized illustration of the relative length of wind turbine wakes for (a) unstable, (b) neutral, and (c) stable conditions.

where z denotes the height, as explained in figure 1.6. The relation to the temperature and pressure p in air is given by

$$\theta = T \left[\frac{p}{p_0}\right]^{R/c_p} . \tag{1.2}$$

The potential temperature is defined as the temperature that a parcel would attain if it was brought to a standard reference pressure $p_0 = 1000$ hPa adiabatically, i.e. without transferring heat or mass [40]. R is the gas constant of air, and c_p is the specific heat capacity at a constant pressure, for air $R/c_p = 0.286$.

Figure 1.7 illustrates how different stability regimes can influence the wind turbine wake recovery. The recovery is fastest in unstable conditions, where the turbulence intensity is highest. In CBLs wake effects on downstream wind turbines are less likely to be an issue due to the high turbulent mixing driven by positive buoyancy, which results in a fast wake recovery. Therefore, CBLs will not be considered in depth in this work. Instead, the research focus is on shallow boundary layers, mostly associated with NBLs and SBLs.

In a NBL wakes are longer than in the CBL and the entrainment from above becomes an important factor for the power production. Both, energy entrainment and power production strongly depend on the stratification of the free-atmosphere. Increasing free-atmosphere stratification is expected to lead to a lower entrainment [18]. Furthermore the height and strength of the capping inversion play an important role in the wind farm wake recovery process [41].

In a SBL the turbulence mixing is restricted due to the restoring forces, such that wind turbine wakes are generally most persistent in stable conditions. Additional to the factors mentioned for the NBL, the height and strength of the LLJ influences the interaction of the wind farm and the ABL [23, 24, 41]. It is worth mentioning that, dependent on the atmospheric state, complex phenomena such as gravity waves might become relevant for the power production in wind farms, which are not studied in this thesis. The topic is shortly discussed in chapter 7.

1.3 Numerical simulations of the ABL

The governing equations to describe any Newtonian fluid flow, including the ABL, are the equations for continuity, momentum (known as Navier-Stokes equations) and energy conservation [10, 11, 35]. These equations are suitable to describe the velocity field in turbulent flows accurately for all involved length and time scales [11].

The Navier-Stokes equations are generally too complex to be solved directly, such that they are usually tailored and simplified for specific applications. ABL flows are often assumed to be incompressible and the impact of density variations on the flow is only included in terms of buoyancy forces in the form of the Boussinesq approximation [10]. If the initial and boundary conditions are defined, the simplified Navier-Stokes equations can be solved explicitly with direct numerical simulations (DNS), meaning that the equations are integrated over a discrete mesh in time and space. However, DNS are mostly used for fundamental turbulence research to develop simplified, less expensive turbulence models. Reason for the limited applicability of DNS are the associated high computational costs needed to resolve highly turbulent flows that include a large range of scales.

The prevailing flow conditions around wind farms are results of weather

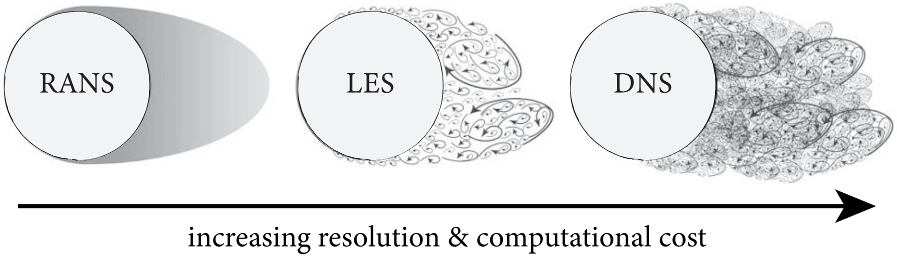

Figure 1.8 – The wake behind a circle is used to illustrate the resolution differences between different numerical methods. The resolution and computational costs increase from RANS over LES to DNS. Figure adapted with permission from Hart [46].

patterns, forming on scales much larger than the wind farm itself, which resides on scales in the order of multiple kilometers. On the other end, the smallest energy dissipating eddies span scales in the range of millimeters [11]. Consequently, accurately resolving the flow through wind farms requires numerical domains and meshes that include scales over at least six orders of magnitude. Simulations of that size are not currently feasible with DNS, even when using the worlds largest supercomputers.

Instead of solving the Navier-Stokes equations in detail, many researchers make use of statistical approaches. For instance, the Reynolds-averaged Navier–Stokes (RANS) equations model the time-averaged mean flow field [42, 43]. In this way, non-linear characteristics of the flow are captured, while unsteady, time-dependant turbulent features are parameterized. The reduced computational costs compared to DNS allow simulations of complex phenomena such as flows through wind farms [44, 45].

However, the turbulent mixing processes and thus the recovery of the wakes are highly time-dependent. Time-dependent phenomena, such as the meandering of wakes and the streamwise-elongated meandering zones of high and low velocity in NBLs [47], highly influence the wind-farm power production [48]. Consequently, detailed, time-dependent simulations are necessary to understand the physical processes in wind farms.

Large-eddy simulations (LES) allow simulations of the temporal development and higher order statistics in flows in and around wind farms [6, 12, 49]. In LES, the large scales of the flow are explicitly resolved, while the effects of the small scales are modeled by sub-grid scale (SGS) models [50]. The higher accuracy compared to RANS is accompanied by higher computational costs, while the SGS modeling allows for faster simulations than DNS. Therefore, LES are a compromise between physical realizability and computational limits, as illustrated in figure 1.8.

The goal of microscale, high fidelity simulations of wind farms, such as LES, is to improve the understanding of the involved physical processes. Understanding these processes is necessary to improve computationally fast engineering models that are used to estimate the wake velocity inside wind farms. The engineering models require less computational resources and allow to study the power production of wind farms for various layouts and wind directions. Consequently, improving engineering models is necessary to optimize the layout of wind farms.

1.3.1 Modeling wind turbines in LES

The method used to model wind turbines and farms in numerical simulations is dependent on the research question, which determines the necessary grid and time resolution of the simulation. If the research question considers the structures in the near wake region, the turning of the blades has to be represented in detail by the numerical model. To fully resolve the flow around the blades in LES, body-fitted meshes are required, which are computationally very challenging [51, 52].

In practice, the turbine blades are often represented by so-called actuator lines. The actuator line model (ALM) parameterizes lift and drag forces that act on turbine blades by applying the blade-element theory [53]. These forces are calculated on a number of points, which are distributed over a line ranging from the hub to the tip (see figure 1.9a). The forces are projected on a volumetric grid surrounding the actuator line by applying a smearing function [54, 55] to avoid numerical instabilities. The lines are assumed to rotate with the rotor angular speed. As a result, the time step of the numerical simulations is often restricted, to guarantee that the actuator line does not move more than one grid cell per time step. Furthermore, structures in the near wake can only be resolved when a fine resolution is applied. Due to the high computational costs, these simulations are restricted to relatively small domain sizes in which only a small number of turbines can be simulated.

Aiming to allow for larger time steps and coarser resolutions, the actuator disk model with rotation (ADM-R) is suggested for the use in LES by Wu and Porté-Agel [56]. The basic idea of ADM-R is to distribute the lift and drag forces over the disk area that is swept by the blades. For this purpose, the

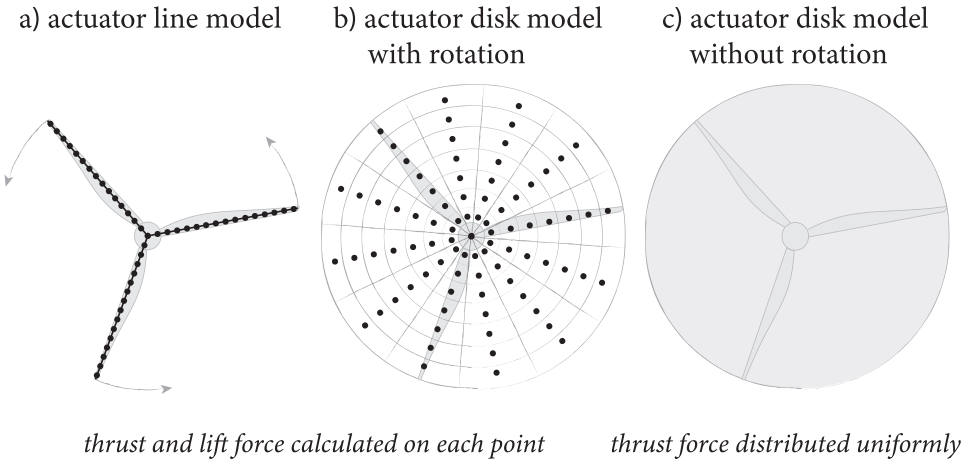

a) actuator line model

b) actuator disk model with rotation

c) actuator disk model without rotation

thrust and lift force calculated on each point

thrust force distributed uniformly

Figure 1.9 – Illustration of the a) actuator line method; b) actuator disk model with rotation and c) actuator disk model without rotation.

disk is represented by a number of rings, each including a number of segments [56], as shown in figure 1.9b. The force at each element is scaled by a solidity factor, which represents the fraction of time that a blade would need to pass one segment. Consequently, ADM-R gives similar predictions as ALM [57].

For simulations of large-scale wind farms where the focus lies on the far-wake regions, simulations are restricted to even coarser resolutions. For resolutions with a minimum of eight grid points per rotor diameter, the actuator disk model without rotation (ADM) can be used [12, 58]. The ADM calculates the thrust force and distributes it uniformly over the rotor area, as shown in figure 1.9c. The advantage of this method is that it is very fast and that the results of the actuator disk model do not depend strongly on the employed grid resolution, especially when a correction factor introduced by Shapiro et al. [59] is used. The model predicts the velocity, turbulence intensity and turbulence fluxes well, starting from a distance of 5 rotor diameters behind the turbine [56, 60]. Therefore, ADM is a good choice when the interest is in the far-wake region.

It is worth mentioning that simulations on larger scales, which use horizontal grid cells that are larger than the turbine diameter, make use of wind turbine parameterizations where the effect of multiple wind turbines is combined. Details on these approaches can be found in Rodrigo et al. [61] and Fischereit et al. [62].

1.4 A guide through the thesis

Modeling the ABL flow with or without including wind turbines requires a careful selection of several numerical methods and approximations. **Part I** of this thesis starts with a discussion on the choice between several SGS models in LES. Furthermore, the effect of selected mesoscale processes is modeled and investigated in microscale LES of wind farms. In **Part II** wind farm wakes and their impact on downstream positioned wind farms are analyzed and compared to engineering models. The objective of each chapter is introduced below.

1.4.1 Part I: Modeling sub-grid scales and mesoscale effects in large-eddy simulations

LES resolve the equations of motion for scales larger than the grid size, while smaller scale motions are modeled (see section 1.3). Consequently, the accuracy of LES is highly dependent on the SGS model used to parameterize these processes. In addition to the accuracy, the computational costs are dependent on the applied SGS model as well. In **chapter 2** of this thesis, three different SGS models, namely the Smagorinsky model, the Lagrangian-averaged scale-dependent (LASD) model, and the anisotropic minimum dissipation (AMD) model, are compared. In this chapter, the basic equations and numerical method of the in-house code that is used and further developed in the framework of this thesis are introduced. The comparison is performed based on neutral, stable and unstable boundary layers and results are compared to theories, observations and numerical simulations, where applicable. We answer the following question:

> *Comparing the Smagorinsky model, the LASD model and the AMD model, which SGS model is the most physically accurate and computationally efficient for LES of ABL flows?*

LES of wind farms often assume that the flow is driven by a constant pressure gradient and the wind angle relative to the wind farm remains constant [6, 49]. In **chapter 3**, we answer two main questions:

> *Can we incorporate dynamic wind directions from measurements or mesoscale models in LES in a straightforward way? How do dynamic wind direction changes affect the wind farm production?*

The driving pressure gradient, that arises from scales much larger than the size of the domains considered in this work, is neither constant in time nor with height. Phenomena such as flow transition between land and sea give rise to baroclinicity, i.e. height-dependent pressure gradients. In **chapter 4** we focus on the question:

> *How does negative shear baroclinicity affect wind farm performance in neutral, and stable ABLs?*

1.4.2 Part II: Wind farm wakes

The power production of wind farms is not only influenced by its own layout and the atmospheric conditions, but also by the surrounding terrain, including other wind farms and their wakes. In **chapter 5** we evaluate the ability of different engineering models to predict the wind farm wake recovery, using LES as a reference. To study the impact of the wind farm wake recovery on wind farm power production and its predictions, a setup with two wind farms that are positioned 10 km apart is considered. Based on a selection of four engineering models, our study finds answers to the following questions:

> *How well do engineering wake models capture the downstream development of wind farm wakes?*

In **chapter 6** LES are used to study the physics of wind farm wakes and their influence on downstream positioned wind farms in more detail. We answer the following questions:

> *How are the flow physics in and around a wind farm affected by the presence of an upstream farm? How does the power production of the downstream farm depend on the inter-farm distance and the wind farm layout?*

Finally, the findings of this research are briefly summarized and unanswered questions are highlighted in **chapter 7**. Furthermore, topics that fell outside the scope of this thesis are briefly explored with the aim to inspire future research.

Part I

Modeling sub-grid scales and mesoscale effects in large-eddy simulations

2

Large-eddy simulations of stratified atmospheric boundary layers: Comparison of different sub-grid scale models

The development and assessment of sub-grid scale (SGS) models for large-eddy simulations of atmospheric boundary layers is an active research area. In this study, we compare the performance of the classical Smagorinsky model, the Lagrangian-averaged scale-dependent (LASD) model, and the anisotropic minimum dissipation (AMD) model. The LASD model has been widely used in the literature for 15 years, while the AMD model was recently developed. Both the AMD and the LASD model allow three-dimensional variation of SGS coefficients and are therefore suitable to model heterogeneous flows over complex terrain or a wind farm. We perform a one-to-one comparison of these SGS models for neutral, stable, and unstable atmospheric boundary layers. We find that the LASD and the AMD models capture the logarithmic velocity profile and the turbulence energy spectra better than the Smagorinsky model. The

---

Adapted from publication: Srinidhi N. Gadde, **Anja Stieren**, and Richard J. A. M. Stevens, *Large-eddy simulations of stratified atmospheric boundary layers: Comparison of different subgrid models*, Boundary-Layer Meteorol. 178, 363–382 (2021), doi: 10.1007/s10546-020-00570-5.

performance analysis of the models reveals that the computational overhead of the AMD model and the LASD model compared to the Smagorinsky model are approximately 10% and 30% respectively. The LASD model has a higher computational and memory overhead because of the global filtering operations and Lagrangian tracking procedure, which can result in bottlenecks when the model is used in extensive simulations. These bottlenecks are absent in the AMD model, which makes it an attractive SGS model for large scale simulations of turbulent boundary layers.

2.1 Introduction

Large-eddy simulations (LES) have been instrumental in the study of turbulence in atmospheric boundary layers (ABLs) [63–65]. In LES, large-scale eddies are resolved and the effect of the sub-grid scale (SGS) eddies are parametrized. The most widely used SGS parametrization is the Smagorinsky approximation, in which the model coefficients are derived from theoretical arguments and empirical formulations [66]. A significant disadvantage of the Smagorinsky model is that the SGS stresses are assumed to be universal, isotropic, and scale-invariant, which makes the model unsuitable for anisotropic flows such as ABL flows. To overcome the limitations of the Smagorinsky model, ad-hoc wall damping functions, backscatter [67], and buoyancy corrections [68] have been proposed to account for the effects of wind shear and buoyancy.

Significant progress in SGS modelling was achieved with the introduction of the Germano identity [69]. The Germano identity relates stresses at different scales and facilitates the calculation of the Smagorinsky coefficients without ad-hoc formulations. This approach assumes scale-similarity, i.e. that the model coefficients do not vary with scale. However, scale-dependency is important in wall-bounded flows in which the grid-scale approaches the local integral scale, such that the SGS stresses contribute significantly to the total stress. Scale-dependent models allow for more accurate modelling of SGS stresses and therefore can capture the flow physics in wall-bounded flows better than the Smagorinsky model [70].

One class of scale-dependent models overcomes the limitation of scale similarity by calculating the model coefficients at different scales [71]. This calculation is performed by using two so-called test filters. When calculating SGS constants with this method numerical instabilities can arise [72]. To prevent this the model coefficients are averaged spatially [71] or in a Lagrangian way over fluid path-lines [73]. Planar averaging limits the coefficients to change only with height, while Lagrangian averaging allows for a three-dimensional variation of the SGS coefficients. For heterogeneous flows, such as flows over complex terrains or in extended wind farms, the three-dimensional variation of the model coefficient is necessary to model the flow physics accurately. It has been shown that the Lagrangian-averaged scale-dependent model (LASD) [73] is a more suitable choice for such heterogeneous flows than SGS models that rely on planar averaging of the model coefficients.

A new class of SGS models that does not involve any additional filtering operations has recently been developed. In this approach, the minimum dissipation to balance the turbulence production at scales smaller than the grid-scale is determined. These so-called minimum-dissipation models were initially developed for isotropic turbulence by Verstappen [74]. Further developments by Rozema et al. [75] extended the approach to anisotropic turbulence. This model is known as the anisotropic minimum dissipation (AMD) model. Recently, Abkar and Moin [76] incorporated buoyancy effects in the AMD model. The AMD model has been used successfully to model turbulent channel flows [75], neutral ABL flows with passive scalars [77], and thermally stratified ABLs [76]. The basic concept of the AMD model can be outlined as follows: The eddy viscosity in the minimum dissipation model is calculated by limiting the SGS eddies produced by the non-linear advective terms in the Navier–Stokes equation from becoming dynamically significant. This argument does not involve any specific assumptions about the energy transfer between different scales, the energy spectrum, turbulent energy cascades, or phenomenological arguments [74]. The dynamically significant part of the motion is confined to large eddies by damping the velocity gradient with an eddy viscosity. The eddy viscosity is calculated such that the energy transferred from the large eddies to the SGS is dissipated at a rate that ensures that the production of SGS eddies by the non-linear terms in the Navier–Stokes equations becomes dynamically irrelevant.

To understand the performance of the different SGS models it is necessary to test them under different conditions. Therefore, we compare the performance of the standard Smagorinsky model [66], the LASD model [73, 78, 79], and the AMD model [76] for different atmospheric conditions. We analyze the first- and second-order turbulence statistics and the surface similarity for a neutral, stable, and unstable ABL. This provides more insight into the performance of two distinct classes of scale-dependent models (i.e. the LASD and the AMD model) for different atmospheric conditions.

The primary consideration in evaluating the performance of a SGS model is how accurately the model can capture the relevant flow physics. However, practical considerations can also play a role in the selection of an appropriate SGS model. The Smagorinsky model is by far the easiest to implement, but the limited accuracy of the Smagorinsky model is a significant drawback [70]. Scale-dependent models can capture the flow physics more accurately than the Smagorinsky model. While the LASD model [73] has been used widely in the literature [12, 56, 80, 81], the AMD model has only been developed relatively recently [75–77]. While the LASD model has been shown to provide accurate predictions [82], it has some practical drawbacks. It is challenging to implement, due to the required filtering operations and Lagrangian averaging procedure that is employed. Due to the additional filtering operations, the LASD model generates a computational overhead, and the numerical implementation of the Lagrangian averaging involves numerous interpolation operations, which requires MPI communication between multiple processors. Besides, the LASD model has an additional memory overhead due to the requirement to store the time-histories of different quantities. These are all essential considerations for simulations performed on modern supercomputers. The AMD model, on the other hand, has low computational complexity and is straightforward to implement. Therefore, it is particularly interesting to see how the AMD model performs compared to the LASD model to assess whether it is a good alternative for the LASD model when considering large-scale simulations of ABLs.

The remainder of this chapter is structured as follows: In section 2.2 the governing equations, numerical method, and the three SGS models used in this study are introduced. In section 2.3 the performance of the different models is analyzed for neutral, stably, and unstably stratified boundary layers. We close with the conclusions in section 2.4.

2.2 Large-eddy simulations

In LES, turbulent motions larger than the grid scale are resolved and the SGS motions are parametrized. In a thermally stratified ABL, the Boussinesq approximation to model buoyancy leads to the following governing equations:

$$\partial_i \widetilde{u}_i = 0, \tag{2.1}$$

$$\partial_t \widetilde{u}_i + \partial_j \left(\widetilde{u}_i \widetilde{u}_j\right) = -\partial_i \widetilde{p} - \partial_j \tau_{ij} + g\beta(\widetilde{\theta} - \left\langle \widetilde{\theta} \right\rangle)\delta_{i3} + f\varepsilon_{ij3}(\widetilde{u}_j - G_j), \tag{2.2}$$

$$\partial_t \widetilde{\theta} + \widetilde{u}_j \partial_j \widetilde{\theta} = -\partial_j q_j, \tag{2.3}$$

where the tilde represents spatial filtering, $\langle\ \rangle$ represents planar averaging, $\widetilde{u}_i$ and $\widetilde{\theta}$ are the filtered velocity and potential temperature, respectively, $\widetilde{p}$ is the kinematic pressure, g is the acceleration due to gravity, $\beta = 1/\theta_0$ is the buoyancy parameter with respect to the reference potential temperature θ_0, δ_{ij} is the Kronecker delta, f is the Coriolis parameter, $G_j = (U_g, V_g)$ is the geostrophic wind speed, and ε_{ijk} is the alternating unit tensor. $\tau_{ij} = \widetilde{u_i u_j} - \widetilde{u}_i \widetilde{u}_j$ is the traceless part of the SGS stress tensor, and $q_j = \widetilde{u_j \theta} - \widetilde{u}_j \widetilde{\theta}$ is the SGS heat flux vector.

Wall-resolved LES are limited to moderate Reynolds numbers due to the very high computational expense [83]. Consequently, simulations of high Reynolds number ABL flows rely heavily on wall and SGS modelling. As it is impossible to resolve all the flow scales, an accurate representation of the SGS properties is crucial in these simulations [84]. It is common practice in LES to parametrize SGS stresses and fluxes using an eddy viscosity and an eddy diffusivity. Thus, the traceless part of the SGS stress and heat flux are modelled as:

$$\tau_{ij} - \frac{1}{3}\tau_{kk} = -2\nu_T \widetilde{S}_{ij} \quad = -2(C_{s,\Delta}\Delta)^2 |\widetilde{S}| \widetilde{S}_{ij}, \tag{2.4}$$

$$q_j = -\frac{\nu_T}{\mathrm{Pr}_{\mathrm{sgs}}} \partial_j \widetilde{\theta} = -(D_{s,\Delta}\Delta)^2 |\widetilde{S}| \partial_j \widetilde{\theta}, \tag{2.5}$$

where $\widetilde{S}_{ij} = \frac{1}{2}\left(\partial_j \widetilde{u}_i + \partial_i \widetilde{u}_j\right)$ represents the filtered strain rate tensor, ν_T is the eddy viscosity, and $\mathrm{Pr}_{\mathrm{sgs}}$ is the SGS Prandtl number. Equations 2.4 and 2.5 are generally known as the Smagorinsky model (1963). In any SGS model, ν_T and $\mathrm{Pr}_{\mathrm{sgs}}$ are not known a priori. They are modelled by the mixing length approximation, which includes the strain rates calculated using the grid scale velocities, where the eddy viscosity is modelled as $\nu_T = (C_{s,\Delta}\Delta)^2|\widetilde{S}|$ with the Smagorinsky coefficient $C_{s,\Delta}$ at the grid scale Δ, and $|S| = \sqrt{2\widetilde{S}_{ij}\widetilde{S}_{ij}}$ is the strain-rate magnitude. The eddy diffusivity is modelled as $\nu_T/\mathrm{Pr}_{\mathrm{sgs}} = (D_{s,\Delta}\Delta)^2|\widetilde{S}|$, where $D_{s,\Delta}$ is the Smagorinsky coefficient for the SGS heat flux. We emphasise that for the LASD and the AMD model, both $C_{s,\Delta}$ and $D_{s,\Delta}$ are dynamically calculated. However, for the Smagorinsky model $C_{s,\Delta}$ and $\mathrm{Pr}_{\mathrm{sgs}}$ are chosen constants, and it is worth mentioning that the results obtained using the Smagorinsky model are sensitive to the choice of these constants [85].

2.2.1 Smagorinsky Model

For LES of ABLs, the Smagorinsky coefficient $C_{s,\Delta}$ is determined using empirical formulations, field observations, and turbulence theory. Assuming the existence of an inertial range spectrum, Lilly [86] calculated that the Smagorinsky constant should be around 0.17 for homogeneous isotropic turbulence. To further account for the inhomogeneity of the flow, Moin and Kim [87] used ad-hoc wall damping functions in simulations of channel flows. This wall damping function was further modified by Mason and Thomson [67] using phenomenological arguments to account for the scale-dependence of the SGS coefficients as:

$$\frac{1}{(C_{s,\Delta}\Delta)^n} = \frac{1}{(C_{s0,\Delta}\Delta)^n} + \frac{1}{[\kappa(z+z_o)]^n}, \tag{2.6}$$

where $\kappa = 0.4$ is the von Kármán constant, $C_{s0,\Delta}$ is the mixing length away from the surface, $n = 2$ is the damping exponent, z is the distance from the surface, and z_o is the roughness height. In addition to $C_{s,\Delta}$, the value of the SGS Prandtl number $\mathrm{Pr}_{\mathrm{sgs}}$ has to be specified when thermal stratification is included. Several stability corrections have been proposed to account for the effect of thermal stability. The value of $\mathrm{Pr}_{\mathrm{sgs}}$ ranges from 0.44 for free convection, to 0.7 for neutral conditions, up to 1.0 for the critical Richardson number [88]. In our simulations we use $C_{s0,\Delta} = 0.17$ and $\mathrm{Pr}_{\mathrm{sgs}} = 0.5$ when using the Smagorinsky model. The values were chosen by trial and error such that the results closely match the results of the dynamic models. We note here that Porté-Agel et al. [71] used $C_{s0,\Delta} = 0.17$ in the simulation of similar pressure-driven neutral ABLs. In addition, the wall damping function proposed by Mason and Thomson [67] is applied, with a damping exponent $n = 2$.

2.2.2 Lagrangian-Averaged Scale-dependent Model

A significant drawback of the Smagorinsky model is that the model coefficients have to be specified a priori. Besides, the use of an ad-hoc wall damping function requires tuning of the constants on a case by case basis. Dynamic models overcome this limitation by computing the model coefficients based on the local flow properties [69]. In a dynamic model, the model coefficients are calculated by relating stresses at two different scales by using the Germano identity. The filtering at two different filter sizes is known as test filtering. The stresses at these two different scales are equated by using the Smagorinsky approximation. The error due to the Smagorinsky approximation is then minimized by averaging it over a plane [71], by dynamic localization [72], or averaging over fluid path-lines [89]. Inherent to the derivation of these models is the assumption of scale-invariance. However, this assumption is inappropriate when the flow is anisotropic. In the LASD model, to break the scale invariance, a second test filter is used, and the process of error minimization is carried out over fluid path-lines [73]. A similar process is employed for the calculations of the SGS heat flux. We refer to Bou-Zeid et al. [73] and Stoll and Porté-Agel [78, 79] for a detailed derivation of the LASD model for neutral and thermally stratified conditions, respectively.

If two test-filters of size 2Δ and 4Δ are used to relate stresses at two different scales, the scale-dependence parameter for the stresses γ and the heat flux γ_θ

are given by:

$$\gamma = \frac{C^2_{s,4\Delta}}{C^2_{s,2\Delta}} \quad \text{and} \quad \gamma_\theta = \frac{D^2_{s,4\Delta}}{D^2_{s,2\Delta}}, \tag{2.7}$$

where $C^2_{s,2\Delta}$ and $C^2_{s,4\Delta}$ are the calculated SGS coefficients at the filter sizes 2Δ and 4Δ, respectively. Assuming that γ and γ_θ are scale-invariant over the test-filter scale, i.e. $\gamma = C^2_{s,4\Delta}/C^2_{s,2\Delta} = C^2_{s,2\Delta}/C^2_{s,\Delta}$ and $\gamma_\theta = D^2_{s,4\Delta}/D^2_{s,2\Delta} = D^2_{s,2\Delta}/D^2_{s,\Delta}$ results in the model coefficients at grid scale Δ:

$$C^2_{s,\Delta} = \frac{C^2_{s,2\Delta}}{\max(\gamma, 0.125)} \quad \text{and} \quad D^2_{s,\Delta} = \frac{D^2_{s,2\Delta}}{\max(\gamma_\theta, 0.125)}. \tag{2.8}$$

Technically, γ and γ_θ can vary between 0 and ∞. However, when γ approaches zero the $C^2_{s,\Delta}$ values become vary large, which causes numerical instabilities. Following Bou-Zeid et al. [73] and Stoll and Porté-Agel [79] we clip the γ and γ_θ values to 0.125 to ensure numerical stability. This procedure does not impact the final statistics. It is worth mentioning here that the only tuning parameter used in this model is the Lagrangian averaging time scale, for which different choices are available [89]. The time scale is chosen following Bou-Zeid et al. [73], i.e. $T = 1.5\Delta(L_{ij}M_{ij}/M_{ij}M_{ij})^{-1/8}$, where $L_{ij} = \overline{\widetilde{u}_i\widetilde{u}_j} - \overline{\widetilde{u}_i}\;\overline{\widetilde{u}_j}$, and $M_{ij} = 2\Delta^2[\overline{|\widetilde{S}|\widetilde{S}_{ij}} - 4\gamma|\overline{\widetilde{S}}|\;\overline{\widetilde{S}_{ij}}]$. We note that the Lagrangian time scale used in the LASD model works very well for most cases [73].

2.2.3 Anisotropic minimum dissipation model

In a minimum dissipation model, the main requirement is that the energy of the sub-filter scales in a filter box Ω_b does not increase. The upper bound for this energy is obtained from the Poincaré inequality, which is given by:

$$\partial_t \int_{\Omega_b} \frac{1}{2}\tilde{u}'_i\tilde{u}'_i d\mathbf{x} \leq C_i \partial_t \int_{\Omega_b} \frac{1}{2}(\partial_i\tilde{u}_j)(\partial_j\tilde{u}_i) d\mathbf{x}, \tag{2.9}$$

where C_i is the modified Poincaré constant that controls the energy in the filter box. We refer to Abkar and Moin [76] for a detailed description of the model.

In the model, the eddy-viscosity and eddy-diffusivity are given by:

$$\nu_T = \frac{-(\hat{\partial}_k\widetilde{u}_i)(\hat{\partial}_k\widetilde{u}_j)\widetilde{S}_{ij} + \delta_{i3}\beta(\hat{\partial}_k\widetilde{u}_i)\hat{\partial}_k\left(\tilde{\theta} - \left\langle\tilde{\theta}\right\rangle\right)}{(\partial_l\widetilde{u}_m)(\partial_l\widetilde{u}_m)}, \tag{2.10}$$

and

$$\nu_\theta = \frac{-(\hat{\partial}_k \tilde{u}_i)(\hat{\partial}_k \tilde{\theta})\hat{\partial}_i \tilde{\theta}}{(\partial_l \tilde{\theta})(\partial_l \tilde{\theta})}, \tag{2.11}$$

respectively, where $\hat{\partial}_i = \sqrt{C_i}\delta_i\partial_i$ (for i = 1, 2, 3) is the scaled gradient operator. The model constants are obtained based on the argument that in a filter box the energy of the SGS eddies does not increase with time. Essentially, in the filter box, the minimum dissipation required to balance the production of scales smaller than the grid scale is used to calculate the SGS coefficients [74, 75, 77].

The value of the modified Poincaré constant depends on the used discretization method. It has been shown that $C_i = 1/12$ gives good results when a spectral method is used [75, 76]. Rozema et al. [75] found that for decaying turbulence simulations $C_i = 0.3$ provides good results when a second-order central finite difference method is used. For a fourth-order method $C_i = 0.212$ works well. Abkar and Moin [76] found that $C_i = 1/3$ works well for LES of thermally stratified boundary layers. We note here that Abkar and Moin [76] used a code similar to ours, i.e. pseudo-spectral in the horizontal direction and second-order central difference in the vertical direction. Following them, we use $C_i = 1/12$ along the horizontal direction and $C_i = 1/3$ in the vertical direction throughout this study.

2.2.4 Numerical method

We use a pseudo-spectral method and periodic boundary conditions in the horizontal directions and a second-order central difference scheme in the vertical direction. Time integration is performed using a second-order accurate Adams–Bashforth scheme. The aliasing errors resulting from the non-linear terms are prevented by using the 3/2 anti-aliasing rule [90]. Viscous terms are neglected as we consider very high Reynolds number flows. This code is based on work by Albertson and Parlange [91]. The computational domain is uniformly discretized with n_x, n_y, and n_z points, with grid sizes of $\Delta_x = L_x/n_x$, $\Delta_y = L_y/n_y$, and $\Delta_z = L_z/n_z$ in the streamwise, spanwise, and vertical directions, respectively. L_x, L_y and L_z are the dimensions of the computational domain in the streamwise, spanwise, and wall-normal direction. The computational planes are staggered in the vertical direction with the first vertical velocity plane at the ground. The first grid point for the streamwise and spanwise velocities and the potential temperature is located at $\Delta_z/2$ above the ground. Free-slip boundary conditions with zero vertical velocity are used at the top boundary.

The instantaneous shear stress and buoyancy flux at the surface, which form the boundary condition, are modelled with the Monin–Obukhov similarity theory [63, 92] using the resolved velocities and temperature at the first grid point, i.e.:

$$\tau_{xz|w} = -u_*^2\cos(\alpha) = -\left(\kappa\frac{\sqrt{\widetilde{u}^2+\widetilde{v}^2}}{\ln(0.5\Delta z/z_o)-\psi_M}\right)^2\cos(\alpha), \tag{2.12}$$

$$\tau_{yz|w} = -u_*^2\sin(\alpha) = -\left(\kappa\frac{\sqrt{\widetilde{u}^2+\widetilde{v}^2}}{\ln(0.5\Delta z/z_o)-\psi_M}\right)^2\sin(\alpha), \tag{2.13}$$

and

$$q_* = \frac{u_*\kappa(\theta_s-\tilde{\theta})}{\ln(0.5\Delta z/z_{os})-\psi_H}, \tag{2.14}$$

where $\tau_{xz|w}$, $\tau_{yz|w}$, and q_* are the instantaneous shear stress and buoyancy flux at the surface, respectively. Friction velocity is represented by u_*, and z_o is the roughness length for momentum. Filtered velocities at the first grid level in the streamwise and spanwise directions are represented by $\widetilde{u}$ and $\widetilde{v}$ respectively and $\alpha = \tan^{-1}(\tilde{v}/\tilde{u})$. Vertical grid size is denoted by Δz, θ_s is the potential temperature at the surface, and z_{os} is the thermal surface roughness. Stability corrections for momentum and temperature are denoted by ψ_M and ψ_H, respectively. In classical works, the thermal surface roughness is set to $z_{os} = z_o/10$ [93]. However, to facilitate easier comparison, we follow the reference cases Sullivan et al. [68] and Beare et al. [94], which use $z_{os} = z_o$, in the present study. For the convective boundary layer we follow Brutsaert [93] and set the stability corrections as follows:

$$\psi_M = 2\ln\left[\frac{1}{2}(1+\zeta)\right] + \ln\left[\frac{1}{2}(1+\zeta^2)\right] - 2\tan^{-1}[\zeta] + \pi/2, \tag{2.15}$$

$$\psi_H = 2\ln\left[\frac{1}{2}(1+\zeta^2)\right], \tag{2.16}$$

where $\zeta = (1-16z/L)^{1/4}$ and $L = -({u_*}^3\theta_0)/(\kappa g q_*)$ is the Obukhov length. For the stable boundary layer we use the stability correction suggested by Beare et al. [94]:

$$\psi_M = -4.8z/L, \tag{2.17}$$

$$\psi_H = -7.8z/L. \tag{2.18}$$

In addition to the surface stresses, the vertical gradients of the velocity at $z_1 = \Delta z/2$ are required for the calculation of SGS stress. They are given by the similarity formula:

$$\left(\frac{\partial \tilde{u}}{\partial z}\right)_{\Delta z/2} = \frac{u_* \cos(\alpha)}{\kappa \Delta z/2}, \tag{2.19}$$

$$\left(\frac{\partial \tilde{v}}{\partial z}\right)_{\Delta z/2} = \frac{u_* \sin(\alpha)}{\kappa \Delta z/2}. \tag{2.20}$$

It is worth mentioning here that the surface similarity relations (Eqs. 2.12, 2.13, and 2.14) are defined for the mean stresses and fluxes. However, Moeng [63] used this mean relation to calculate the ‘instantaneous’ stresses, which now is an established practice in the literature. However, this procedure also contributes to the logarithmic layer mismatch [95, 96]. To reduce the effect, Albertson [65] proposed calculating the mean gradients with the similarity theory and the fluctuations with finite differences. This technique has been used in our code. Furthermore, for the neutral boundary layer cases, the correction proposed by Porté-Agel et al. [71] is used to further reduce the effect of the log-layer mismatch.

To simplify the notation, the tilde representing the spatial filtering of the LES quantities is omitted hereafter.

2.3 Results and Discussion

Three canonical boundary layers with neutral, stable, and unstable temperature stratification are studied here. First, a mean pressure-driven neutral boundary layer is used to assess the performance of different models in truly neutral conditions. Second, we consider the Global Earth and Water Experiment (GEWEX) ABL Study (GABLS−1), which is a moderately stable stratified boundary layer [94]. Finally, an unstable convective boundary layer with a moderate capping inversion is considered [97].

2.3.1 Neutral boundary layer

We performed simulations of a neutral ABL over a rough homogeneous surface using the Smagorinsky, LASD, and AMD models. The Coriolis forces are neglected for this case, and the boundary layer is driven by an imposed pressure

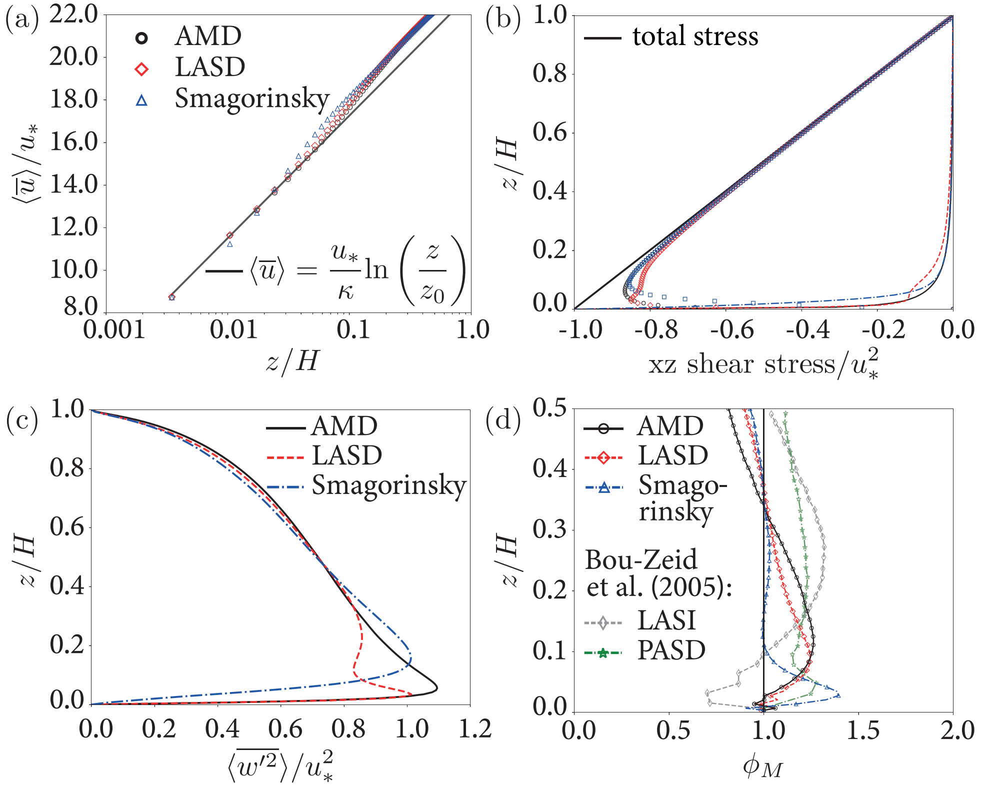

Figure 2.1 – Planar-averaged vertical profiles for simulations of the neutral boundary layer. (a) Mean velocity profile on a semi-logarithmic plot. (b) Resolved (markers), SGS (lines), and total shear stress (thick line) in the xz-direction. (c) Vertical velocity variance and (d) non-dimensional velocity gradient ϕ_M. Results from Bou-Zeid et al. [73] obtained with the LASI and the PASD models are also plotted for comparison.

gradient $1/\rho(\nabla p) = -u_*^2/H$, where H is the domain height. The domain length L and width W are both set to $2\pi H$. The domain is discretized with a grid of spacing $\Delta_x = \Delta_y = 2\pi\Delta_z$, where Δ_x, Δ_y, and Δ_z represent streamwise, spanwise, and vertical grid spacing, respectively. The computational domain is 1000 m in height and the grid spacing is $\Delta_x = \Delta_y = 43.630$ m and $\Delta_z = 6.944$ m. The roughness used to model the surface stresses is set to $z_o/H = 10^{-4}$. The simulations are run until the flow has reached a statistically stationary state. The set-up considered here is the same as in Bou-Zeid et al. [73].

The planar-averaged streamwise velocity obtained from the simulations using the different SGS models is presented in figure 2.1a. This velocity profile is expected to follow the logarithmic law $\langle \overline{u} \rangle (z) = u_*/\kappa \ln (z/z_o)$ in the surface layer, i.e. up to $z/H \approx 0.1 - 0.2$. The figure shows that the streamwise velocity profiles obtained from the AMD and the LASD models agree excellently with the logarithmic law in the surface layer. However, in agreement with previous studies [71, 73, 96], the velocity profile obtained from the simulation with the Smagorinsky model shows a mismatch with the logarithmic profile.

The resolved and modelled SGS stresses obtained from the simulations with different SGS models are presented in figure 2.1b. The figure shows that the ratio of the resolved to modelled stresses increases with the distance from the surface. For the AMD and the Smagorinsky models, the resolved stresses increase smoothly with increasing height [77]. However, in agreement with Bou-Zeid et al. [73], we find that the transition between the resolved and modelled stresses is very sharp in the LASD model. In all cases, the sum of the resolved and the modelled stresses follows the expected linear stress profile, which occurs at a steady state in the absence of Coriolis forces.

Figure 2.1c shows the planar-averaged vertical velocity variance calculated as $\left\langle \overline{w'^2} \right\rangle = \left(\left\langle \overline{w^2} \right\rangle + \langle \overline{\tau}_{zz} \rangle \right) - \langle \overline{w} \rangle \ \langle \overline{w} \rangle$. Further away from the surface the vertical velocity variance predicted by the LASD and the AMD model is nearly the same. However, in the surface layer ($z/H \lesssim 0.1 - 0.2$) there is a considerable difference in the variances obtained using the three models. The non-dimensional velocity gradient $\phi_M (z) = (\kappa z/u_*) \, \partial \langle \overline{u} \rangle / \partial z$ is presented in figure 2.1d. Results from the Lagrangian-averaged scale-independent model (LASI) and planar-averaged scale-dependent model (PASD) from Bou-Zeid et al. [73] are also included in the figure for better perspective. Higher ϕ_M values near the surface are caused by the log-layer mismatch [95] and the use of finite differences to calculate gradients. Close to the surface, ϕ_M values predicted by the LASD and the AMD models are closer to the theoretical value of 1 than the ones predicted by the Smagorinsky, LASI, and PASD models. This shows that the simulations with the AMD and the LASD model capture the logarithmic law in the surface layer ($z/H \lesssim 0.1 - 0.2$) better than the Smagorinsky model. Furthermore, near the surface the values of ϕ_M obtained from both the LASD and the AMD model are nearly equal, indicating a similar performance of the models.

To obtain further insight into the dissipation characteristics of the SGS models, we present the streamwise wavenumber spectra of the streamwise velocity for various heights above the surface in figure 2.2. The spectra is defined as $\int_0^\infty E_{11}(\kappa_1) d\kappa_1 = \overline{u'u'}/2$, where $E_{11}(\kappa_1)$ represents the spectral

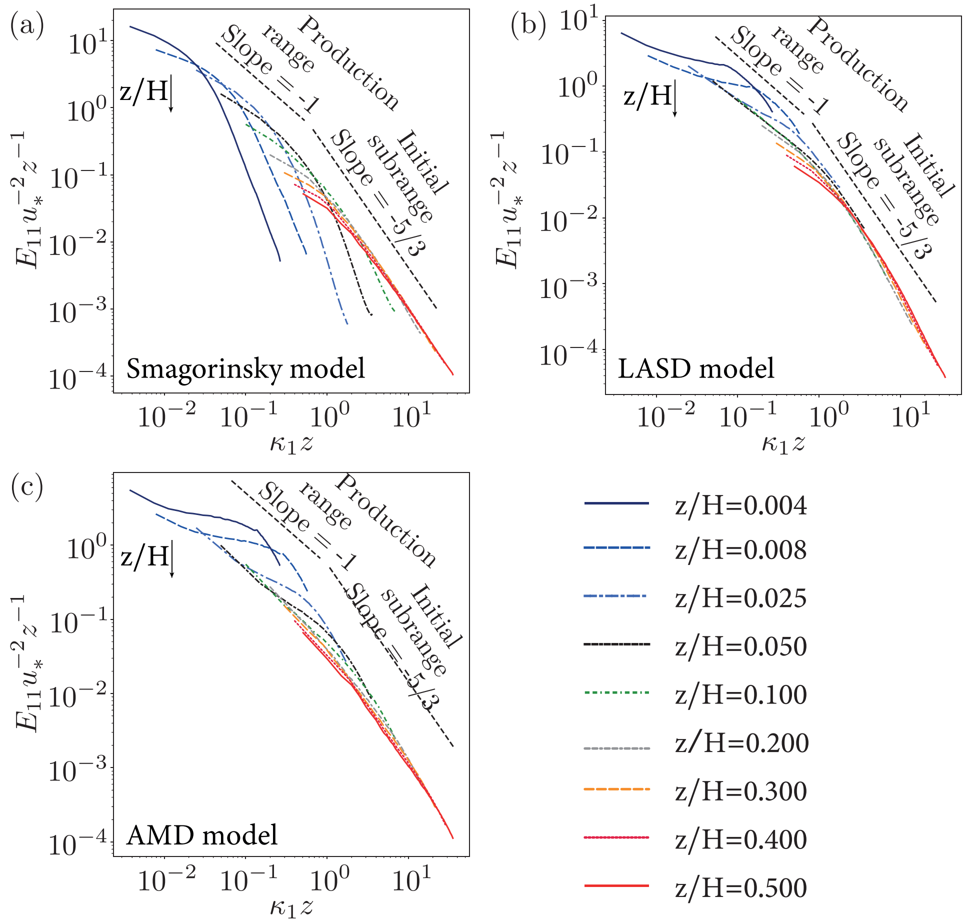

Figure 2.2 – Normalized streamwise wavenumber spectra of the streamwise velocity at different heights using (a) the Smagorinsky model, (b) the LASD model, and (c) the AMD model.

energy associated with wavenumber κ_1 and u' represents streamwise velocity fluctuations. In the inertial subrange (for $\kappa_1 z > 1$, where κ_1 is the streamwise wavenumber and z is the distance from the surface) the turbulence is unaffected by the flow configuration, dissipation, or viscosity. The flow in the inertial subrange is nearly isotropic and the spectrum generally follows the Kolmogorov $-5/3$ scaling [98]. Figure 2.2 shows that close to the surface the spectra obtained using the Smagorinsky model decay faster than $\kappa^{-5/3}$, while the LASD and

AMD models accurately capture the Kolmogorov scaling. This indicates that the Smagorinsky model is too dissipative close to the surface. In the production range ($\kappa_1 z < 1$) the turbulence is affected by the flow configuration [73, 99]. For a neutral ABL the production is expected to follow a κ^{-1} scaling [73]. Figure 2.2 shows that the LASD and AMD model capture the κ^{-1} scaling in the production range better than the Smagorinsky model. That the LASD and AMD model predict the spectra more accurately than the Smagorinsky model indicates that these scale-dependent models have better dissipation characteristics due to which the flow physics can be captured more accurately. A detailed comparison between the AMD and LASD model reveals that the LASD model captures the expected $\kappa^{-5/3}$ and κ^{-1} in the production and inertial subrange slightly better than the AMD model.

2.3.2 Stably stratified boundary layer

In this section, we study the GABLS-1 inversion capped boundary layer with a constant cooling rate at the surface. The potential temperature is initialized with the two layer temperature profile given by Beare et al. [94]:

$$\theta(z) = \begin{cases} 265\ \mathrm{K}, & 0 < z \leq 100\ \mathrm{m} \\ 265\ \mathrm{K} + (z - 100\ \mathrm{m}) \times 0.01\ \mathrm{K\ m^{-1}}, & z > 100\ \mathrm{m}. \end{cases} \tag{2.21}$$

The initial velocity is set to the geostrophic wind speed of 8 m s^{-1} everywhere except at the surface. Turbulence is triggered by adding random perturbations. A random noise term of magnitude 3% the geostrophic wind speed is added to velocities below 50 m, and for the temperature a noise term with an amplitude of 0.1 K is added. The reference temperature θ_0 is set to 263.5 K. The Coriolis parameter $f = 1.39 \times 10^{-4}$ s^{-1}, which corresponds to latitude 73^oN and the surface cooling rate is set to 0.25 K hour^{-1}. The simulations are performed in a computational domain of 400 m × 400 m × 400 m, which is discretized on an isotropic grid with a spacing of 2.08 m. Gravity waves are damped out by a Rayleigh damping layer with a strength of 0.0016 s^{-1} in the top 100 m of the computational domain [100]. The simulations were run for 9 h to ensure that quasi-equilibrium is reached. The statistics are gathered over the final hour. This is approximately equal to 400 large eddy turnover times $T = z_i/w_*$, where the velocity scale is $w_* = (g q_* z_i/\theta_0)^{1/3}$ and z_i is the boundary-layer height.

As theoretical results and experimental data are very limited, we also compare our results against the high-resolution results from Sullivan et al. [102] and Beare et al. [94]. Even though these high-resolution simulations provide a

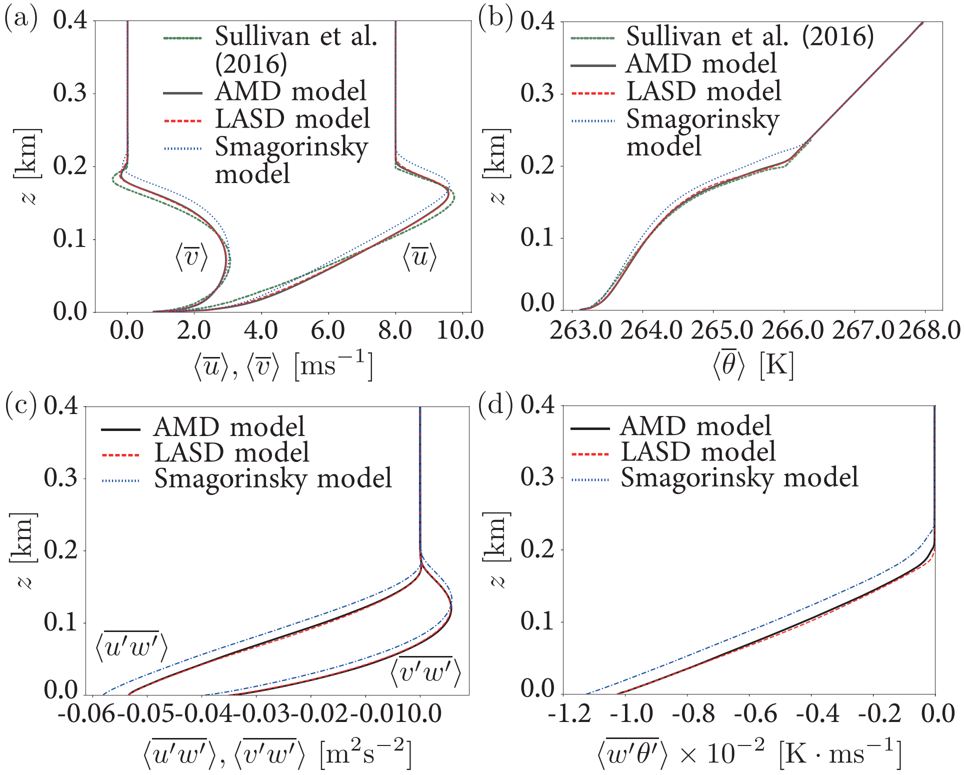

Figure 2.3 – Planar-averaged vertical profiles for the stable boundary layer simulations. (a) Streamwise and spanwise velocities, (b) potential temperature, (c) streamwise and spanwise momentum fluxes, and (d) the vertical heat flux.

Table 2.1 – Details of the stable boundary layer simulations. The columns from left to right give the case name, the isotropic grid resolution Δ, the friction velocity u_*, the boundary-layer height z_i, the surface heat flux q_*, and the momentum flux τ.

Simulation	Δ [m]	u_* [m s^{-1}]	z_i [m]	q_* [K $\cdot$ m s^{-1}]	τ [m^2 s^{-2}]
Smagorinsky model	2.08	0.265	176	-11.26×10^{-3}	0.070
AMD model	2.08	0.252	166	-10.24×10^{-3}	0.064
LASD model	2.08	0.253	166	-10.25×10^{-3}	0.064
Beare et al. [94]	1.00	0.256	149	-9.55×10^{-3}	0.066
Sullivan et al. [102]	0.39	0.255	-	-9.63×10^{-3}	0.065

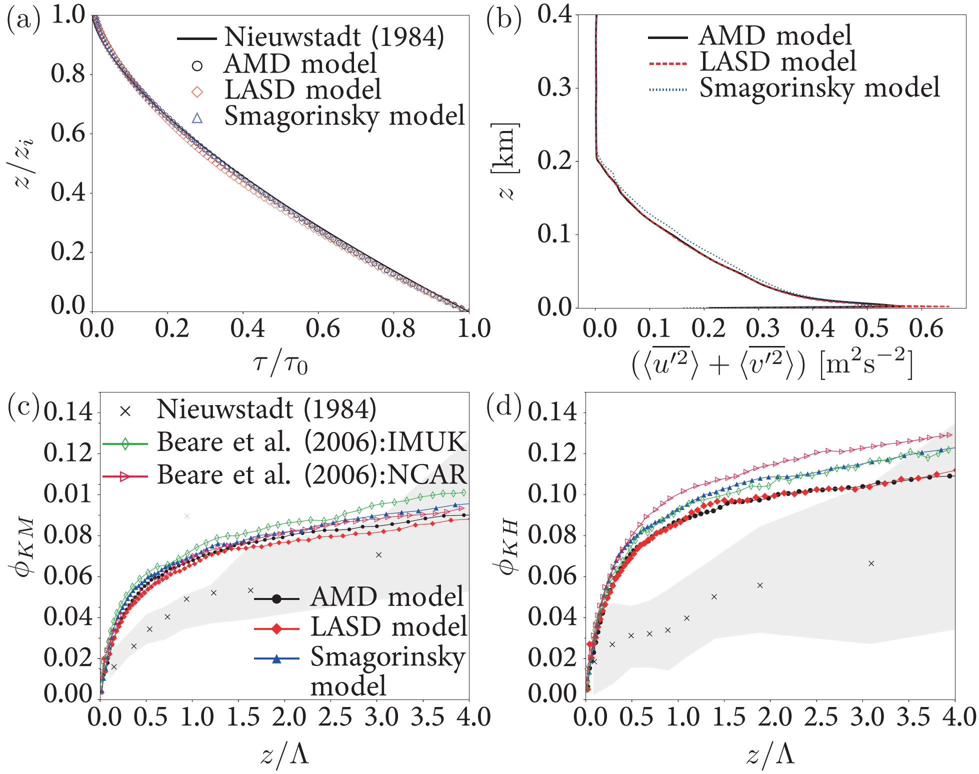

Figure 2.4 – Planar-averaged vertical profiles for the stable boundary layer simulations. (a) Normalized momentum flux, (b) horizontal velocity variance, (c) locally scaled momentum diffusivity and (d) locally scaled heat diffusivity. The experimental data by [101] are given for comparison.

useful reference, it is worth noting that these results still depend on the surface and SGS modelling. In Table 2.1 we compare various integral boundary layer properties obtained from our simulations with these high-resolution simulation results. We calculated the boundary-layer height z_i by determining the height where the mean stress falls below 5% of its surface value [94]. We note that Sullivan et al. [102] used a different method to determine the boundary-layer height. Therefore, to avoid confusion, any comparison to the boundary-layer height from their study is left out.

Beare et al. [94] report that the time-averaged buoyancy flux $g\theta_0^{-1}\langle w\theta\rangle$ ranges from -3.5×10^{-3} to -5.5×10^{-3} m^2 s^{-3}, which agrees well with the value of -3.8×10^{-3} m^2 s^{-3} that we find in our simulation with the LASD and

AMD model. In addition, Beare et al. [94] report that the mean momentum fluxes $\sqrt{\left\langle\overline{u'w'}\right\rangle^2 + \left\langle\overline{v'w'}\right\rangle^2}$ range from 0.06 to 0.08 $\mathrm{m}^2\ \mathrm{s}^{-2}$, which corresponds to a friction velocity of $0.24 - 0.28$ m s^{-1}. The mean momentum flux in our simulations varies between $0.064 - 0.069$ $\mathrm{m}^2\ \mathrm{s}^{-2}$, which corresponds to a friction velocity range of $0.252 - 0.265$ m s^{-1}. Hence, these values lie well within the range reported in the LES intercomparison study by Beare et al. [94]. A comparison of our simulation results with the high-resolution data presented by Beare et al. [94] and Sullivan et al. [102] shows that the AMD and LASD model provide more accurate predictions for the friction velocity, mean momentum fluxes, boundary-layer height, and the surface heat than the Smagorinsky model.

The surface-normal streamwise and spanwise velocity profiles are presented in figure 2.3a and reveal the pronounced super-geostrophic jet that is characteristic for the GABLS-1 case [94]. The figure shows that the LASD and the AMD model results agree better with the high-resolution results of Sullivan et al. [102] than the Smagorinsky model results. Figure 2.3b shows that the LASD and the AMD model results for the vertical temperature profile are closer to the high-resolution results by Sullivan et al. [102] than the corresponding Smagorinsky model results. The planar-averaged vertical momentum and heat flux are presented in figure 2.3c, d. In agreement with the integral properties presented in Table 2.1, we find that the results obtained using the AMD and LASD model agree excellently. In contrast, the momentum and buoyancy fluxes due to which the velocity and temperature profiles are not accurately captured with the Smagorinsky model.

In figure 2.4a we compare the mean momentum flux obtained from the simulations with the theoretical model proposed by Nieuwstadt [101]. This model states that the normalized vertical momentum profile is given by:

$$\frac{\tau}{\tau_0} = \left(1 - \frac{z}{z_i}\right)^{3/2}, \tag{2.22}$$

where the subscript 0 denotes the surface values and $\tau = \sqrt{\left\langle\overline{u'w'}\right\rangle^2 + \left\langle\overline{v'w'}\right\rangle^2}$. The fluxes are calculated by adding the resolved fluxes ($\left\langle\overline{u'w'}\right\rangle$ and $\left\langle\overline{v'w'}\right\rangle$) to the SGS fluxes ($\langle\overline{\tau}_{xz}\rangle$ and $\langle\overline{\tau}_{yz}\rangle$). Nieuwstadt [101] defined the boundary-layer height as the height where the turbulence is nearly zero. Therefore, only for this plot, the boundary-layer height is defined as the height where the turbulence is 1% of the surface values. Figure 2.4a shows that the mean momentum flux profiles obtained using all three SGS models agrees well with the theoretical prediction.

Figure 2.4b shows that the horizontal velocity variance $\left(\left\langle\overline{u'^2}\right\rangle + \left\langle\overline{v'^2}\right\rangle\right)$ with $\left\langle\overline{u'^2}\right\rangle = \left(\left\langle\overline{u^2}\right\rangle + \langle\overline{\tau}_{xx}\rangle - \langle\overline{u}\rangle\langle\overline{u}\rangle\right)$ and $\left\langle\overline{v'^2}\right\rangle = \left(\left\langle\overline{v^2}\right\rangle + \langle\overline{\tau}_{yy}\rangle - \langle\overline{v}\rangle\langle\overline{v}\rangle\right)$ obtained using the three SGS models is similar. We note that the kinetic energy obtained using the LASD model shows a sharp peak at the first grid point above the surface. We believe this peak is related to the sharp transition between the resolved and modelled stresses in the LASD (see figure 2.1b).

To assess the effectiveness of the different models in capturing the surface-layer similarity profiles we plot the locally scaled momentum,

$$\phi_{KM} = \frac{1}{\Lambda}\sqrt{\frac{\tau}{\left(\frac{\partial\langle\overline{u}\rangle}{\partial z}\right)^2 + \left(\frac{\partial\langle\overline{v}\rangle}{\partial z}\right)^2}}, \tag{2.23}$$

and the locally scaled heat diffusivity,

$$\phi_{KH} = \frac{1}{\Lambda\tau^{1/2}}\frac{-\left\langle\overline{w'\theta'}\right\rangle}{\frac{\partial\langle\overline{\theta}\rangle}{\partial z}}, \tag{2.24}$$

where $\Lambda = -\tau^{3/2}/\left(\kappa g\left\langle\overline{w'\theta'}\right\rangle\right)$ is the local Obukhov length (in figure 2.4c, d). Results obtained from two different models by Beare et al. [94], i.e. the IMUK (University of Hannover) and NCAR (National Center for Atmospheric Research) are also included in the figures to provide a better perspective. The crosses in the figure 2.4c, d represent the mean values, and the shaded areas show the standard deviation from the observations of the stable boundary layer by Nieuwstadt [101]. According to the local-scaling hypothesis of Nieuwstadt [101], the quantities ϕ_{KM} and ϕ_{KH} can be expressed as a function of z/Λ. We find that ϕ_{KM} and ϕ_{KH} reach a nearly constant value for large z/Λ, which is known as the z-less stratification regime. Beare et al. [94] report that the GABLS-1 boundary layer falls within the range of values (shaded region in figure 2.4c, d) seen in Nieuwstadt [101] observations. Our results are consistent with the findings by Beare et al. [94]. The overlap of the results in the shaded region shows that the results fall within the limits of the observation at high z/Λ, i.e. the z-less stratification limit. Our results are similar to the IMUK and NCAR results reported in the LES intercomparison of Beare et al. [94]. Overall, the results show that the LASD and the AMD models have similar performance, while the Smagorinsky model results are significantly different.

Table 2.2 – Details of the unstably stratified boundary layer simulations. The columns from left to right give the case name, the grid spacing in streamwise, spanwise, and vertical direction ($\Delta_x \times \Delta_y \times \Delta_z$), the friction velocity u_*, the Obukhov length L, and the boundary-layer height z_i. The high-resolution simulation using the LASD model, which is used as the reference, is performed on a grid with 960^3 nodes instead of a 480^3 grid.

Simulation	$\Delta_x \times \Delta_y \times \Delta_z$ [m]	u_* [m s^{-1}]	L [m]	z_i [m]
Smagorinsky model	10.41 × 10.41 × 4.16	0.573	-60.45	1021
AMD model	10.41 × 10.41 × 4.16	0.556	-55.26	1012
LASD model	10.41 × 10.41 × 4.16	0.571	-59.85	1016
High-resolution (LASD)	5.20 × 5.20 × 2.08	0.550	-53.31	1020
Moeng and Sullivan [97]	52.08 × 52.08 × 20.833	0.556	-57.20	1032
Abkar and Moin [76]	52.08 × 52.08 × 20.833	0.570	-59.20	1030

2.3.3 Unstably stratified boundary layer

Following Moeng and Sullivan [97], we performed simulations of an inversion capped convective boundary layer in a computational domain of 5 km × 5 km × 2 km on a 480^3 grid. The boundary layer is driven by a constant geostrophic wind of 10 m s^{-1} and the Coriolis parameter $f = 10^{-4}$ s^{-1}. The surface roughness for momentum and heat are set to 0.16 m. The surface was heated at the bottom with a constant surface buoyancy flux of $q_* = 0.24$ K·m s^{-1}. The reference potential temperature is set to $\theta_{\text{ref}} = 301.78$ K. The initial velocities are set to the geostrophic wind speed with randomly seeded uniform perturbations in the region $0 < z \leq 937$ m to spin up turbulence. The potential temperature is initialized with a three-layered structure:

$$\theta(z) = \begin{cases} 300\ \text{K}, & 0 < z \leq 937\ \text{m} \\ 300\ \text{K} + (z - 937\ \text{m}) \times \frac{8}{126}\ \text{K m}^{-1}, & 937\ \text{m} < z \leq 1063\ \text{m} \\ 308\ \text{K} + (z - 1063\ \text{m}) \times 0.003\ \text{K m}^{-1}, & z > 1063\ \text{m}. \end{cases}$$

The simulation reaches a quasi-stationary state in 10 large eddy turnover times $T = z_i/w_*$, where the convective velocity scale is $w_* = (gq_*z_i/\theta_{\text{ref}})^{1/3}$ and the boundary-layer height z_i is defined as the height at which the buoyancy flux is minimum [68]. The presented statistics are obtained from the time interval of $13T$ to $18T$.

Table 2.2 gives a summary of the simulation results, which are in good agreement with the results reported by Moeng and Sullivan [97] and Abkar and

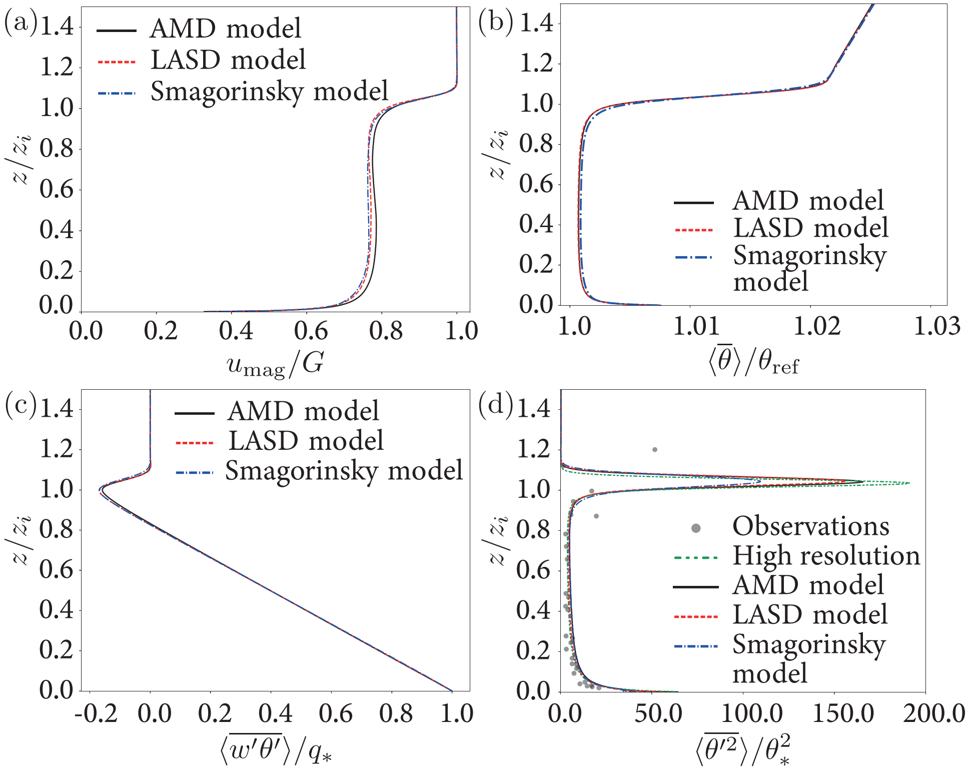

Figure 2.5 – Planar-averaged vertical profiles for the unstable boundary layer. (a) Mean velocity magnitude $u_{\mathrm{mag}} = \sqrt{\langle\overline{u}\rangle^2 + \langle\overline{v}\rangle^2}$, (b) potential temperature, (c) vertical heat flux, and (d) variance of the potential temperature $\langle\overline{\theta'^2}\rangle/\theta_*^2$, where $\theta_* = q_*/w_*$, compared to the observational data from the AMTEX experiment by Lenschow et al. [103] and the high-resolution reference simulation.

Moin [76]. As these studies only provide results obtained on coarser grids, we also performed a high-resolution reference simulation on a 960^3 grid using the LASD model. It is worth noting that the integral boundary layer properties obtained by this high-resolution simulation can still depend on the surface and SGS modelling. Nevertheless, it provides a useful reference to judge the performance of the different SGS models. The results in Table 2.2 show that the AMD model predicts a lower friction velocity, surface Obukhov length, and boundary-layer height than the LASD and the Smagorinsky model. Furthermore, the results obtained with different SGS models agree reasonably well with our high-resolution results and the studies of Moeng and Sullivan [97] and Abkar and Moin [76]. The results show that all the models predict values within an acceptable range and only minor variation is visible in the values of different quantities. Overall, all models perform well in predicting the friction velocity and boundary layer height.

Figure 2.5a shows the variation of the planar-averaged horizontal wind magnitude $u_{\text{mag}} = \sqrt{\langle \overline{u} \rangle^2 + \langle \overline{v} \rangle^2}$ normalized by the geostrophic wind velocity. In agreement with the lower friction velocity, the AMD model predicts a stronger velocity in the boundary layer than the LASD or Smagorinsky model. Figure 2.5b shows that the variation of the potential temperature $\left\langle \overline{\theta} \right\rangle / \theta_0$ with height, predicted using the LASD and AMD model, agrees excellently. Due to the intense turbulent mixing the velocity and temperature are almost constant in the mixed layer ($0.1 < z/z_i < 0.9$), which is a characteristic feature of convective boundary layers [97]. Overall, the AMD model is as effective as the LASD model in predicting the velocity and temperature profiles.

Figure 2.5c compares the vertical profiles of the horizontally averaged vertical heat flux $\left\langle \overline{w'\theta'} \right\rangle$. We observe that the heat flux decreases linearly over the boundary-layer height and reaches a minimum at the inversion layer height. The depth of the entrainment zone is defined as the region where $\left\langle \overline{w'\theta'} \right\rangle$ is negative. The Smagorinsky and the LASD model results show a wider entrainment region than the AMD results. This means that there is more turbulent mixing at the inversion height when the Smagorinsky and LASD model are used. In an unstable boundary layer the profile of the temperature fluctuations is expected to show a sharp maximum at the inversion height, where the entrainment flux becomes negative [103].

Figure 2.5d compares the temperature variance as a function of height obtained with the different models against the Air Mass Transformation Experiment (AMTEX) observational data by Lenschow et al. [103]. The profiles show a sharp peak in the temperature variance at the inversion layer height. The origin of this peak is described by Sullivan et al. [104], and a sharper peak corresponds to a smaller vertical extent of the entrainment zone. The AMD and LASD model results agree excellently and show a sharper peak than the Smagorinsky model results. The figure shows that the temperature variance obtained from the high-resolution reference simulation has an even sharper peak. This means that, for a given grid resolution, the Smagorinsky model strongly underestimates the temperature variance at the inversion layer when compared to the results of the LASD and AMD models. Therefore, we conclude that the LASD and the AMD model provide better predictions than

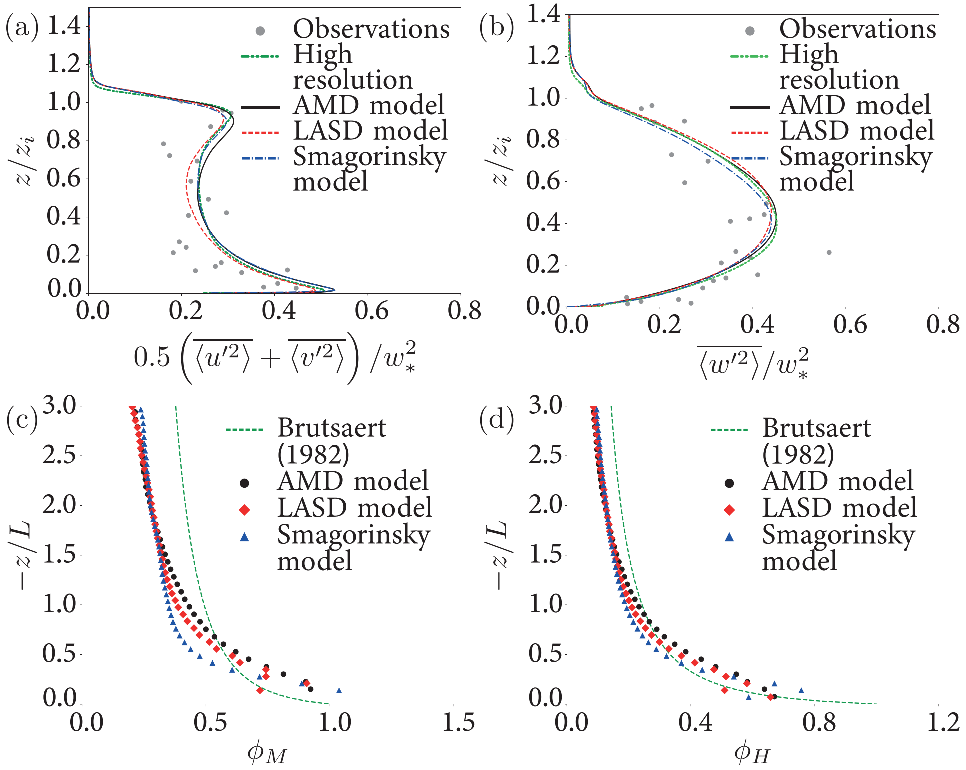

Figure 2.6 – Planar-averaged vertical profiles of the (a) horizontal and the (b) vertical velocity variance for the unstable boundary layer simulations compared to the AMTEX observational data by Lenschow et al. [103] and the high-resolution reference simulation. The planar-averaged vertical profiles for the (c) non-dimensional velocity gradient ϕ_M, and (d) non-dimensional temperature gradient ϕ_H.

the Smagorinsky model.

The vertical profiles of the horizontal velocity variance obtained using the three SGS models are compared in figure 2.6a. Although the results are nearly the same near the surface, there is a significant difference around the capping inversion $z/z_i \approx 1$. This difference is a consequence of the different depth of the entrainment zone, which we discussed above. Furthermore, the AMD model agrees better with the high-resolution reference data than the LASD and the Smagorinsky model results. Figure 2.6b shows that temperature profiles obtained using the LASD and AMD agree better with the high-resolution reference data than the corresponding Smagorinsky model results.

To assess the effectiveness of the model in capturing the surface-layer similarity profiles, we plot the non-dimensional shear,

$$\phi_M = \left(\frac{\kappa z}{u_*}\right)\frac{\partial u}{\partial z}, \tag{2.25}$$

and the non-dimensional temperature gradient,

$$\phi_H = \left(\frac{\kappa z}{\theta_*}\right)\frac{\partial \theta}{\partial z}, \tag{2.26}$$

where $\theta_* = q_*/u_*$. The vertical profiles of ϕ_M and ϕ_H are compared with the empirical formulations proposed by Brutsaert [93] in figure 2.6c, d. The empircal similarity profiles, which are applicable close to the surface ($-z/L < 1.5$) are $\phi_M = (1-16\zeta)^{-1/4}$ and $\phi_H = (1-16\zeta)^{-1/2}$. Figure 2.6c shows that both the LASD and the AMD model results are relatively similar when compared to the Smagorinsky model results. The deviation in the results from the empirical formulation is expected. This is similar to the deviation of the ϕ_M values from the theoretical value of 1 in the case of the neutral boundary layer, observed in figure 2.1d. Furthermore, we also observe the log-layer mismatch in the plots of non-dimensional shear. Figure 2.6d shows that the results from the different models agree equally well with the similarity profile. This is consistent with the observation of a similar temperature profile for all models (see figure 2.5b). For both quantities, ϕ_M and ϕ_H, we observe minor differences between the results obtained with the LASD and the AMD models.

2.4 Conclusions

In summary, we compared the performance of the Smagorinsky, the AMD [75–77], and the LASD model [73, 78, 79] for neutral, stable, and unstable conditions. For neutral conditions, we find that the LASD and the AMD models capture the logarithmic velocity profile and the streamwise wavenumber spectra of the streamwise velocity more accurately than the Smagorinsky model. For the stably stratified GABLS-1 boundary layer, we compared the results obtained using the different models with the higher resolution results of Sullivan et al. [102] and Beare et al. [94]. A comparison with these high-resolution results reveals that, on a relatively coarse grid, the LASD and the AMD model provide better predictions than the Smagorinsky model. Also for the unstably stratified boundary layer we find that the AMD and the LASD model results obtained on a relatively coarse grid agree better with the high-resolution reference than the corresponding Smagorinsky model result. Furthermore, in turbulent quantities such as the horizontal and vertical velocity variances, temperature variances, non-dimensional shear, and temperature gradients, the results obtained with the LASD and the AMD models are nearly the same, while the Smagorinsky model model results are significantly different.

From all the above, we conclude that, on a given grid resolution, the LASD and the AMD model capture the flow physics better than the Smagorinsky model. While the LASD model [73] has been successfully used for about 15 years [12, 56, 78, 81, 82] the AMD model was only developed recently [75–77]. Here we show, using a one-to-one comparison, that the LASD and AMD model provide similar results for neutral, stable, and unstable test cases. Both the AMD and LASD model provide three-dimensional variation of the SGS coefficients, which is essential when considering heterogeneous flows, such as flows over complex terrains or in extended wind farms. An inspection of the streamwise wavenumber spectra of the streamwise velocity suggests that the LASD model predicts the velocity spectra in the inertial and production range slightly better than the AMD model.

Our results suggest that the AMD model is nearly as good as the LASD model in simulations of horizontally homogeneous atmospheric boundary layers. In simulations of neutral boundary layers, the AMD model provides similar dissipation characteristics as the LASD model, which is established by a similar turbulence spectrum. The performance analysis of different sub-grid models on three grid sizes 240^3, 480^3, and 960^3 reveals that the computational overhead of the AMD model compared to the Smagorinsky model is 11.3% (240^3), 9.8% (480^3), 11.3% (960^3), while the corresponding numbers for the LASD model are 29.5% (240^3), 33.8% (480^3), 34.5% (960^3), respectively. The numbers show that the computational overhead of the LASD model is higher than the AMD model and increases slowly with grid size due to increased MPI communication related to the interpolations in the Lagrangian model calculations. Furthermore, we emphasise that the Lagrangian averaging in the LASD model requires the storage of time histories of various terms in the model, which requires at least 8 additional three-dimensional arrays and numerous two-dimensional temporary arrays.

As indicated in the introduction, we emphasize that the AMD model has several practical advantages and is more straightforward to implement than the LASD model. The reason is that the AMD model does not require filter operations or Lagrangian tracking of fluid parcels, which are required in the LASD model. The computational and memory overheads are essential considerations for simulations performed on modern supercomputers. Therefore, we conclude that the AMD model is an attractive alternative to the LASD model when considering large-scale LES of turbulent boundary layers. We have shown here that the results obtained with the AMD model are almost as good as the LASD model results. However, AMD model results depend on the modified Poincaré constant, which requires tuning in complex flow scenarios such as flow over cubes (urban boundary layer) or wind farms, while the LASD model is tuning free. In the future, it would be beneficial to study the performance of these models in the aforementioned complex flow scenarios.

3

Modeling dynamic wind direction changes in large-eddy simulations of wind farms[1]

The wind direction in atmospheric boundary layers changes continuously due to mesoscale weather phenomena. Developing accurate simulations of these changes is essential for understanding their effect on the performance of large wind farms. Our study introduces a new technique to model dynamic wind direction changes obtained from mesoscale simulations or field measurements in microscale large-eddy simulations. We propose a method in which the simulation domain is treated as a non-inertial rotating reference frame. The primary benefit of our approach is that it is straightforward to implement and reproduces desired wind direction changes excellently. We verified our approach in neutral atmospheric boundary layers and show that the observed boundary-layer characteristics for dynamic wind directions agree very well with those observed for constant mean wind directions when the wind direction is changed slowly such that the flow is quasi-stationary. Further, we show that atmospheric measurements of the wind direction can be reproduced by our method. To underline the importance of the method, we conclude with a representative scenario, which shows that dynamic wind direction changes can affect the performance of large wind farms.

---

[1] Adapted from publication: **Anja Stieren**, Srinidhi N. Gadde, and Richard J. A. M. Stevens, *Modeling dynamic wind direction changes in large eddy simulations of wind farms*, Renew. Energy **170**, 1342–1352 (2021), doi: 10.1016/j.renene.2021.02.018.

3.1 Introduction

With the increasing size of wind farms, there is a growing need to understand how wind farm performance is affected by changes in atmospheric conditions. The effect of atmospheric phenomena with scales that are much larger than the typical size of wind farms is still *terra incognita* [105, 106] and needs further exploration. In particular, changing wind directions can strongly influence the performance of wind farms as the wakes from upwind turbines can greatly affect the power production of downstream turbines, and this effect depends strongly on the wind direction [107–109]. While the effect of different mean wind directions on wind farm performance is well explored, the effect of dynamic wind direction changes, which originate from mesoscale weather phenomena, on wind farm performance is not well-understood and needs further investigation [6, 49, 110, 111].

Mesoscale simulations in which dynamic large-scale wind direction changes are accounted for, are usually restricted to horizontal resolutions larger than the turbine diameter [112–116]. Different parameterizations have been developed to represent wind farms in these mesoscale models. Commonly used models include the use of increased surface roughness to parametrize the effect of a wind farm [12, 117, 118], or a more detailed approach in which momentum is extracted, and turbulent kinetic energy is added at rotor height as proposed by Fitch et al. [119]. However, the horizontal resolution in these models is extremely coarse, due to which the interaction between the individual turbines cannot be investigated [120, 121].

These interactions are commonly studied in microscale large-eddy simulations (LES) of wind farms [6, 12, 49, 122]. However, a vast majority of these studies focus on small scale turbulence and consider cases in which the flow is forced to approach *steady-state* conditions [12, 56, 123]. Although these simulations provide great insights into the *steady-state* interaction of wind farms and atmospheric boundary layers (ABLs), they ignore the influence of large-scale effects such as the influence of dynamic wind direction changes on wind farm performance.

To simulate more realistic inflow conditions mesoscale forcings have to be included in the LES [106, 124–126]. This can be achieved by nesting the LES within a mesoscale simulation domain, e.g. by coupling LES to mesoscale models like the Weather Research and Forecasting model (WRF) [125, 127–134]. As mesoscale simulations do not resolve the turbulent structures up to the same scale as LES, this affects the LES modeling itself [61, 135–137]. An alternative approach [110, 111] is to represent the effect of mesoscale phenomena in the microscale simulation so that the LES modeling itself is not affected. The benefit of this approach is that it allows a direct comparison with LES results in which mesoscale effects are not included. This allows one to study the influence of these mesoscale effects, such as dynamic changes in the wind direction, independently.

To model the effect of dynamic wind direction changes obtained from field measurements or mesoscale simulations in LES, Munters et al. [110] proposed to use a concurrent precursor method [138] in which they rotate the horizontally periodic precursor domain.Chatterjee et al. [111] modified the method of Munters et al. [110] and proposed to rotate the inflow velocity vector instead of the precursor domain. They used data from LIDAR scans to model the effect of dynamic wind direction changes on the operation of the Alpha Ventus wind farm. Both studies revealed that dynamic-wind directions can significantly impact wind farm performance.

However, rotating the precursor simulation requires a sequence of geometrical interpolations and significant MPI communication. Here, we propose a more straightforward method to simulate dynamic wind direction changes in LES. Our approach is inspired by the use of a proportional-integral-derivative (PID) controller, which is used in wind farm simulations to keep the wind angle constant at a particular height [139–141]. We therefore treat the simulation domain as a non-inertial rotating reference frame, which is an attractive approach as it only requires small changes to the governing equations and is straightforward to implement. A major advantage of our approach is that it avoids the geometrical interpolations and associated computational overhead that is required in the previously considered methods [110, 111]. Besides, the methods discussed above [110, 111] require a concurrent precursor inflow technique, i.e. an additional concurrent simulation from which the inflow data for the wind farm simulation is sampled. This condition makes it impossible to perform simulations with periodic boundary conditions. Such simulations are, for example, used to perform simulations of infinite wind turbine arrays that are considered in the development of analytical wind farm models [12, 142]. In contrast, we will demonstrate that our method can be applied with and without a precursor method, allowing simulations of both finite and infinite wind farms.

The remainder of this chapter is organized as follows: a description of the governing equations used to model dynamic wind direction changes in LES is outlined in section 3.2. A validation of the approach for neutral ABLs is presented in section 3.3, and the method is applied to a representative scenario in section 3.4 in which dynamic wind direction changes affect the wind farm performance. The conclusions will be presented in section 3.5.

3.2 Rotation of the mean wind direction in LES

The simulations are performed using an updated version of the LES code developed by Calaf et al. [12], Albertson and Parlange [143]. The updated code has been successfully used to study neutral, stable, and unstable ABLs [138, 144], as well as the flow dynamics in extended wind farms [80, 81, 145, 146]. The governing equations are the filtered incompressible continuity and momentum equations. The aim is to include dynamic wind direction changes $\theta(t)$, which can be obtained by mesoscale simulations or field measurement data, in the LES. For this purpose, the reference frame is rotated with an angular velocity $\omega = 0.5\partial_t\theta(t)$ and corresponding non-inertial forces are added to equation (3.2). Here, the factor 0.5 can be explained as follows: half of the Coriolis acceleration arises due to the relative velocity and half due to the turning of the frame of reference [147]. As a consequence, the wind direction relative to a fixed axis is changed by an angle $\theta(t)$ in the time where the frame of reference rotates by an angle equal to $0.5\theta(t)$ (see, e.g., Persson [147]). The resulting equations are:

$$\partial_i \tilde{u}_i = 0, \tag{3.1}$$

$$\begin{aligned}\partial_t \tilde{u}_i + \partial_j \left(\tilde{u}_i \tilde{u}_j\right) = & -\partial_i \tilde{p}^* - \partial_j \tau_{ij} + f_i + \frac{\partial_i p_\infty}{\rho} \cdot \left[\cos\left(\theta\right)\delta_{i1} + \sin\left(\theta\right)\delta_{i2}\right] \\ & - 2\omega \tilde{u}_j \epsilon_{ij3}.\end{aligned} \tag{3.2}$$

Here, the tilde represents spatial filtering with a spectral cut-off filter at the LES grid scale Δ and $\tilde{u}_i$ represents the filtered velocity field components. $\tau_{ij} = \widetilde{u_i u_j} - \tilde{u}_i \tilde{u}_j$ is the trace-less part of the sub-grid scale (SGS) stress tensor and it is modeled with a standard Smagorinsky model [148] using a constant Smagorinsky coefficient $C_s = 0.16$ [86]. The trace of the SGS stress tensor is absorbed into the filtered modified pressure $\tilde{p}^+ = \tilde{p}/\rho - p_\infty/\rho - \tau_{kk}/3$, note that $\tilde{p}^*$ is defined below. The force f_i is added for modeling the effects of the wind turbines, which are parameterized using an actuator disk approach [12, 58]. Since the simulations are performed at very high Reynolds numbers we neglect viscous stresses [35], which is a common practice in LES of ABLs. The wall shear stress at the ground is modeled using the Monin-Obukhov similarity theory [63, 73]. We use a surface roughness of $z_0 = 0.1$ m. The boundary conditions at the top of the domain are zero vertical velocity and zero shear stress. The mean-pressure gradient $\partial_i p_\infty/\rho$ defines a reference friction velocity $u_* = -\sqrt{H p_\infty/\rho}$. Length and time scales are non-dimensionalized with the domain height H and H/u_*, respectively. To present the results in dimensional form, we assume that the incoming wind velocity at $z = 150$ m is 10 m/s, which is representative for the typical value observed in offshore conditions, see the Dutch Offshore Wind Atlas [149]. From this we obtain that $u_* \approx 0.5$ m/s [109], which means that each non-dimensional time unit corresponds to $t_{dim} = H/u_* = 2000$ s (≈ 0.56 h).

While the continuity equation (3.1) is rotational invariant, the momentum equation (3.2) is modified by adding the Coriolis force $2\omega\tilde{u}_j\epsilon_{ij3}$. Besides, the direction of the mean-pressure gradient, which is driving the flow, is aligned with the desired wind direction $\theta(t)$. In a non-inertial, rotating reference frame, in addition to the Coriolis force, the centrifugal force $-\omega^2 x_i(\delta_{i1} + \delta_{i2})$ and the Euler force $\epsilon_{ij3}x_j d\omega/dt$ are introduced [10]. The centrifugal force can be rewritten as a conservative force $-\omega^2 x_i(\delta_{i1} + \delta_{i2}) = -0.5(\partial_i\omega^2 x_i^2)(\delta_{i1} + \delta_{i2})$. Once rewritten as a conservative force, the centrifugal force is combined with the pressure term: $p^* = \tilde{p}^+ - 0.5\omega^2 x_i^2\,(\delta_{i1} + \delta_{i2})$. The Euler force is neglected here, as a periodic domain is considered and the distance to the axis of rotation, which is required for its calculation, is unknown.

Time integration is performed using a second-order accurate Adams-Bashforth scheme. Derivatives in the vertical direction are calculated using a second-order central finite difference scheme. In streamwise and spanwise directions a pseudo-spectral method is applied. Thus, doubly periodic boundary conditions are considered in the horizontal directions, which implies that an infinite wind farm is considered [12]. To model finite size wind farms we employ a concurrent precursor inflow method [138]. In this approach we sample flow data from a periodic turbulent ABL simulation performed in a precursor domain. The sampled data is introduced as inflow velocity into a *fringe* region of the wind farm simulation domain. To ensure a smooth transition between the velocity in the wind farm domain $u_{i,WF}$ and the inflow velocity sampled from the precursor simulation $u_{i,Pre}$ a symmetric weighing function $w(x)$ is applied in the *fringe* region:

$$\begin{aligned} u_{i,Fringe}(x,y,z,t) = {} & w(x)\; u_{i,Pre}(x,y,z,t) \\ & + (1 - w(x))\; u_{i,WF}(x = L_{start}, y, z, t), \end{aligned} \tag{3.3}$$

where:

$$w(x) = \begin{cases} \frac{1}{2}\left(1-\cos\left(\pi\frac{x-L_s}{\Delta_{\text{Fringe}}}\right)\right), & \text{if } x < L_s + \Delta_{\text{Fringe}} \\ 1, & \text{if } L_s + \Delta_{\text{Fringe}} \leq x \leq L_s + 2\Delta_{\text{Fringe}} \\ \frac{1}{2}\left(1-\cos\left(\pi\frac{x-L_s-2\Delta_{\text{Fringe}}}{\Delta_{\text{Fringe}}}\right)\right)+\frac{1}{2}, & \text{if } x > L_s + 2\Delta_{\text{Fringe}} \end{cases} \tag{3.4}$$

The parameter L_s sets the starting point of the fringe region. Here, we select $L_s = L_x - 0.2L_x$ such that the length of the fringe region is $\Delta_{\text{Fringe}} = 0.2L_x$, where L_x is the domain length in streamwise direction. Figure 3.1 shows the corresponding weighing function and figure 3.7 shows the fringe regions in the wind farm simulation domain. However, before we employ our method to a simulation of a representative wind farm, we first test its performance in a neutral ABL in section 3.3.

3.3 Dynamic wind direction changes in LES of neutral ABL

In section 3.3.1 we validate the proposed method to model dynamic wind direction changes in LES for flows that are quasi-stationary. In section 3.3.2 we show that our method can be used to reproduce the dynamic wind direction changes obtained from atmospheric field measurement data.

3.3.1 Validation of the approach

We perform LES of a neutral ABL to validate the described method to incorporate dynamic wind direction changes. The selected size is $L_x = L_y = 10$ km and $L_z = 1$ km, L_y, and L_z are the domain length in the spanwise, and vertical direction, respectively. The simulations are performed on a grid with

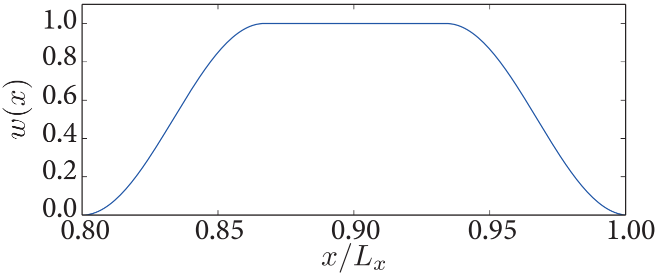

Figure 3.1 – The weighting function $w(x)$, defined by equation 3.4.

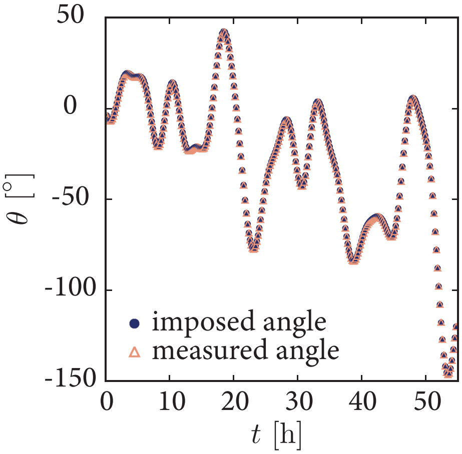

Figure 3.2 – Imposed and measured wind direction for the *random* wind direction case, see equation 3.5.

$256 \times 256 \times 48$ nodes. We perform three simulations in which the wind direction is changed linearly with time, i.e. $\theta(t) = \theta_0 t$ and consider different rotation speeds $\theta_0 = [9°/\mathrm{h}, 27°/\mathrm{h}, 54°/\mathrm{h}]$. In addition, the following combination of sines and cosines:

$$\begin{aligned}\theta(t) = &-1°t + [15° - 3°\sin(0.7°t/5°)\sin(2°t/5°) - 11°\cos(t)\sin(t/10°)\\ &- 15°\sin(2°t/15°) + \cos(1.5°t/5°) + \sin(t/2°) - 3°\cos(t/4.5°)],\end{aligned} \tag{3.5}$$

is considered to assess the performance for more or less *random* wind direction changes. These simulations are compared with a reference simulation with a constant wind direction.

Figure 3.2 confirms that the horizontal wind direction at hub-height $\langle\theta\rangle(t) = \tan^{-1}(\langle v\rangle(t)/\langle u\rangle(t))$ follows this imposed wind direction excellently. It is worth noting that this excellent overlap would not be achieved by only varying the driving pressure gradient, because a large phase-lag (up to several hours [110]) is visible between the pressure gradient and the mean wind direction when the additional Coriolis force is neglected [109].

A visualization of the horizontal velocity magnitude $u_h = \sqrt{u^2 + v^2}$ at mid box-height ($z = L_z/2$) is shown in figure 3.3. In the top row, the horizontal wind direction is rotated from $\theta = 0°$ to $\theta = 20°$ within 2.2 h. The visualizations reveal streamwise-elongated coherent structures typically observed in neutral ABL simulations [122]. For the 0° wind direction (left panel in figure 3.3), these structures are oriented parallel to the x-axis. When the mean wind direction is rotated the large-scale flow structures orient themselves with the

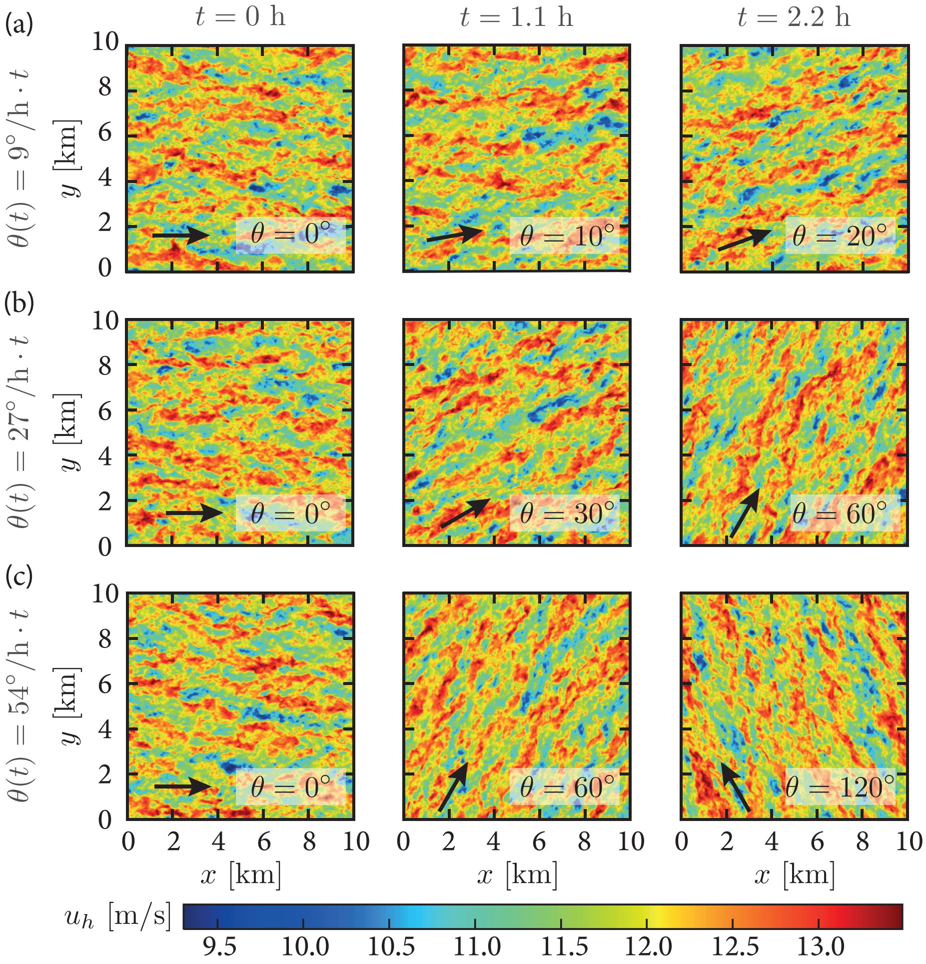

Figure 3.3 – The horizontal wind speed $u_h = \sqrt{u^2 + v^2}$ at mid-height $z = L_z/2$. Each column represents a different time instant. Each row corresponds to a different rotation rate: **a)** $\theta(t) = 9°/\mathrm{h} \cdot t$, **b)** $\theta(t) = 27°/\mathrm{h} \cdot t$, **c)** $\theta(t) = 54°/\mathrm{h} \cdot t$. Arrows indicate the horizontally averaged wind direction.

mean flow direction, and we do not observe any unusual stretching of the flow structures due to the rotation.

We also compare the time and horizontally averaged turbulent statistics obtained from the reference simulation to the simulation results in which the mean wind direction is dynamically rotated to validate the proposed method. The mean velocity u_h for the different rotation rates is depicted in figure 3.4(a).

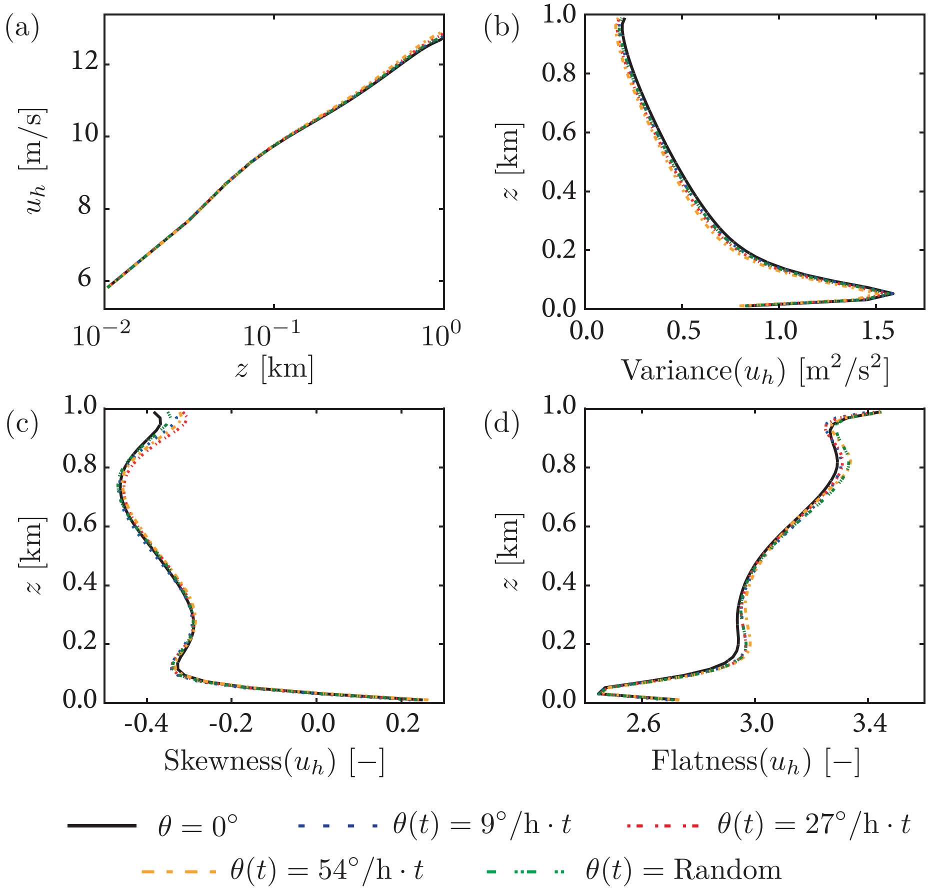

Figure 3.4 – **a)** Horizontally averaged velocity $u_h = \sqrt{u^2 + v^2}$ for a constant mean wind direction ($\theta = 0°$), linearly rotating wind direction ($\theta(t) = 9°/\mathrm{h} \cdot t$, $27°/\mathrm{h} \cdot t$, $54°/\mathrm{h} \cdot t$) and a *randomly* varying wind direction (see figure 3.2). **b)** Profiles of the variance, **c)** skewness and **d)** flatness of the horizontal velocity magnitude as function of z/H.

For all cases, the velocity profiles agree well with the reference result. We observe only small differences in the velocity at the top of the domain. This difference could be caused by slight variations in the large-scale structures when the flow is rotated. When the wind direction changes, the domain length in the flow direction continuously changes, see figure 3.3, and the high and low-velocity streaks tend to *adjust* themselves to this. In addition to this inevitable domain effect, the neglected Euler force might also cause these small differences when comparing the statistics with the constant mean wind

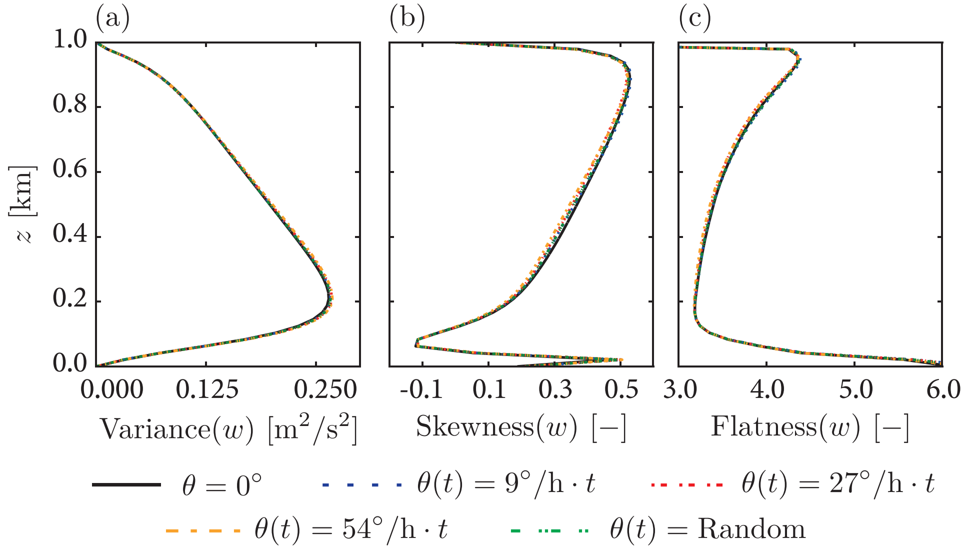

Figure 3.5 – **a)** Profiles of variance, **b)** skewness, and **c)** flatness of the vertical velocity magnitude as function of z/H.

direction case.

Figure 3.4(b) shows that the time and horizontally averaged variance of the horizontal velocity for the different rotation rates agrees well with the reference case. All the cases show the same trend, exhibiting a maximum close to the ground. The maximum indicates the height up to which the influence of the surface friction dominates. At this height, the skewness of the horizontal velocity, displayed in figure 3.4(c), turns from positive, super-Gaussian to sub-Gaussian at higher positions. While there are small quantitative differences for higher rotation rates, the qualitative trend is consistent. This consistency is also present for the flatness presented in figure 3.4(d). The flatness increases with height above the surface layer, corresponding to an increase in rare but extreme deviations from the mean velocity. This qualitative trend is the same for all rotation rates. It is worth mentioning here that the higher-order statistics, such as skewness and flatness, provide a stricter validation of the proposed method than lower-order statistics. The vertical velocity is zero at the bottom and top of the domain and shows a maximum at $z/H \approx 0.2$, see figure 3.5(a). The figure shows that the variance obtained from the simulation with changing wind direction agree very well with the reference case. Furthermore, the higher-order statistics such as skewness and flatness (figures 3.5(b)-(c)) only vary slightly

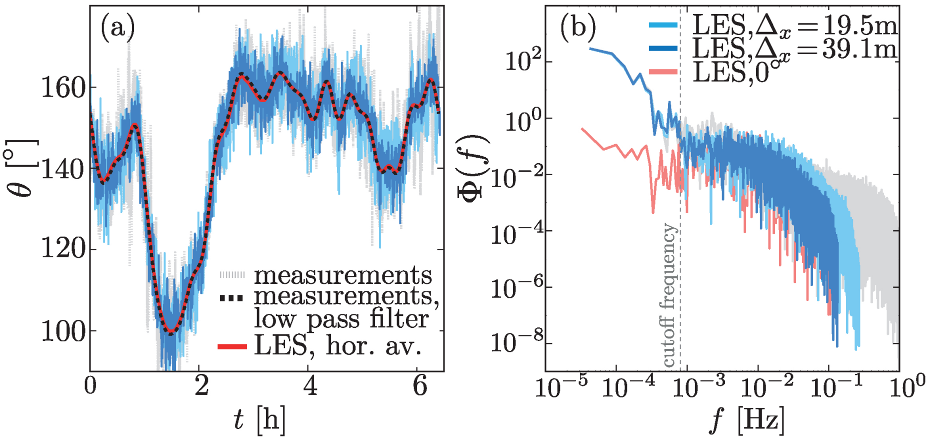

Figure 3.6 – **a)** Wind direction time series from measurements and LES. The low-pass filtered measurements serve as input data to the LES. The figure shows that the horizontally averaged wind direction from LES follows the imposed wind direction perfectly. **b)** Normalized power spectra of the wind direction determined from measurements and LES. The spectrum for a simulation with constant mean wind direction is also included, as an example, we consider 0°.

with increasing rotation rate.

Overall, the quantitative and qualitative results agree for all rotation rates, which indicates that the flow characteristics remain the same when the wind direction is rotated slowly. This validates that the non-inertial rotating reference frame method has been implemented correctly.

3.3.2 Comparison with field measurement data

To assess the ability of our method to represent dynamic wind direction changes from mesoscale weather phenomena into microscale LES, we compare the simulation results to field measurement data. In figure 3.6(a) we reproduce the wind direction measurements taken from a wind vane at a height of 87 m on the M5 meteorological mast at National Wind Technology Center [150], of National Renewable Energy Laboratory (NREL), for a 7 h period on the 1st of February, 2018 from 6 am to 1 pm. Figure 3.6(b) shows the corresponding power spectrum of the wind direction changes.

We performed LES of a neutral ABL in a domain of $L_x = L_y = 5$ km, and $L_z = 1$ km using a $128 \times 128 \times 48$ and a $256 \times 256 \times 96$ grid. Figure 3.6 shows that LES with a constant mean wind direction captures the high-frequency wind direction changes fairly accurately, especially considering that we perform neutral ABL simulations, instead of matching the atmospheric conditions of the observational data. The figure shows that the higher resolution simulation captures the high-frequency wind direction changes better. However, the low-frequency wind direction changes are not represented in the LES that considers a constant wind direction.

The low-frequency wind direction changes can be included in the LES using the low-pass filtered field measurement data as input to the LES. Here, the low-pass filter's cutoff frequency is chosen as 0.0008 Hz. In agreement with the results in section 3.3.1, we find in figure 3.6(a) that the mean wind direction of the LES perfectly follows the desired wind direction. More importantly, figure 3.6(b) shows that the spectrum of wind direction changes obtained from LES now accurately represents the entire frequency range. As intended, our approach models the low-frequency wind direction changes obtained from field observations, or a mesoscale simulation, while it does not affect the high-frequency range, which we assume to be represented accurately by our microscale LES. In the next section, we will apply our method to a representative scenario to demonstrate that these low-frequency wind direction changes can significantly affect the performance of extended wind farms.

3.4 Effect of dynamic wind direction changes on wind farm performance

3.4.1 Case Description

We perform LES of a symmetric wind farm with 6×6 turbines in a neutral ABL with the same surface roughness considered previously. Both the wind farm and the precursor domains have a size of $L_x = L_y = 7.5$ km and $L_z = 1$ km. The last 1.5 km of each horizontal direction is used as a fringe region. The wind farm layout is presented in figure 3.7. The simulations are performed on a uniform grid with $384 \times 384 \times 64$ nodes and are used to demonstrate that dynamic wind direction changes can significantly affect wind farm performance.

To demonstrate this we consider the following representative scenario with sinusoidal wind direction changes: $\theta(t) = 20^{\circ}\sin(2\pi t/T_{\theta})$ with $T_{\theta} = 0.6$ h and $T_{\theta} = 2.2$ h and 13 additional reference simulations in which a constant mean wind direction is considered, see figure 3.7. At each time step of the simulation, the wind turbines are rotated perpendicular to the local incoming

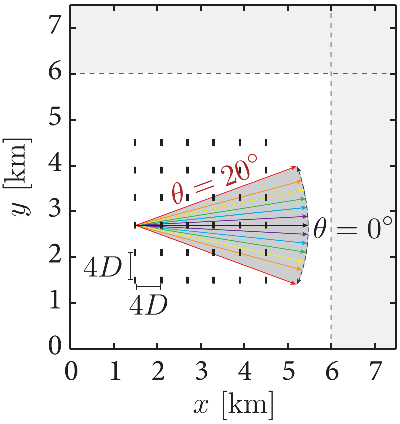

Figure 3.7 – Wind farm simulation domain. The locations of the turbines are indicated with black markers. The shaded regions indicate the fringe layers. The colored arrows depict the different constant mean wind direction cases (*black:* 0°, *violet:* ±3°, *blue:* ±6°, *green:* ±9°, *yellow:* ±12°, *orange:* ±15°, *red:* ±20°).

wind direction to ensure that there is no yaw misalignment. We note that this instantaneous rotation of the disks is idealistic as wind turbines adjust their orientation with respect to the incoming wind direction with a time delay [151]. This can lead to additional yaw effects, which are not included in our representative scenario. The turbines have a thrust coefficient of $C_T = 3/4$, a diameter of $D = 150$ m, a hub-height of $z_{hub} = 150$ m, and the distance to neighboring turbines is four turbine diameters in both horizontal directions. In the following, the total power production of the wind farm P_{tot} is normalized by taking into account the velocity at hub-height and the power obtained for the reference case (P_{ref}) with constant mean wind direction of $\theta = 0°$.

3.4.2 Hysteresis effects in wind farm power production

Figures 3.8(a) and (b) present the time-variation of the imposed and the measured wind direction at hub-height for the two cases under consideration. Circular markers indicate when the wind direction is $\theta = 0°$. Figures 3.8(c)-(d) depict the time-variation of the total power production of the wind farm. The circular markers denote the power at the time instant when $\theta = 0°$. Furthermore, the power production of two constant mean wind direction cases $\theta = 0°$ and $\theta = 15°$ are given as a reference. For time-varying wind directions, we observe that the power is mostly higher than for the case with a constant mean wind direction of 0° at both slow and fast rotation rates, see figures

3.8(c)-(d). This is due to the strong wake-effects for the $\theta = 0^\circ$ wind direction. Surprisingly, for fast wind direction changes (case $T_\theta = 0.6$ h, see figure 3.8(d)), the minimum power is not reached for $\theta = 0^\circ$. Instead, the power minima are reached after the wind direction passed $\theta = 0^\circ$. A comparison with the constant mean wind direction $\theta = 15^\circ$ reference case reveals that the wind farm power production can be a bit higher due to the effect of the dynamic wind direction changes.

Figure 3.9(a)-(b) display the wind farm power production as function of the wind direction θ. These results are obtained by binning the time-varying power production based on the instantaneous wind direction. A solid black line displays results that are binned over the entire simulation. Additionally, results are divided up into time periods during which $d\theta/dt > 0$ (red, dash-dotted line) and $d\theta/dt < 0$ (blue, dashed line), respectively. Each circle represents simulation results obtained with constant mean wind directions. Figure 3.9(a) shows that the wind farm power production agrees well with the results obtained from the constant mean wind direction cases when the wind direction changes slowly ($T_\theta = 2.2$ h). Due to the symmetric layout of the wind farm, the power production is symmetric around $\theta = 0^\circ$. The power production is lowest for $\theta = 0^\circ$ when the wind is aligned with the farm layout. The maximum inter-turbine spacing and thus maximum power production is reached at $\theta \approx 15^\circ$. The wind farm power production is nearly independent of the sign of the wind direction change $d\theta/dt$.

However, figure 3.9(b) shows that the wind farm power production depends on the sign of the wind direction change $d\theta/dt$ for faster rotation rates. For $d\theta/dt > 0$ the power production agrees well with the values obtained for constant mean wind directions with negative θ. In contrast, the power production is lower than for the constant mean wind direction cases for positive θ and the minimum power production is observed for $\theta \approx 3^\circ$. An exception is found between $\theta = 12^\circ$ and $\theta = 20^\circ$, where the power production is higher than for the constant mean wind direction cases. Due to the symmetric farm layout, a similar pattern is found for $d\theta/dt < 0$ with the symmetry axis positioned at $\theta = 0^\circ$. These hysteresis effects can be explained by examining the development of the wake between the turbine rows, as displayed in figure 3.10 and the corresponding movie (see the supplementary materials). The figure shows flow snapshots of the horizontal velocity magnitude normalized by the inflow-velocity for different wind directions. Each column represents one wind direction between $\theta = -9^\circ$ and $\theta = 9^\circ$. The top row displays snapshots of the horizontal velocity magnitude from simulations performed with a constant

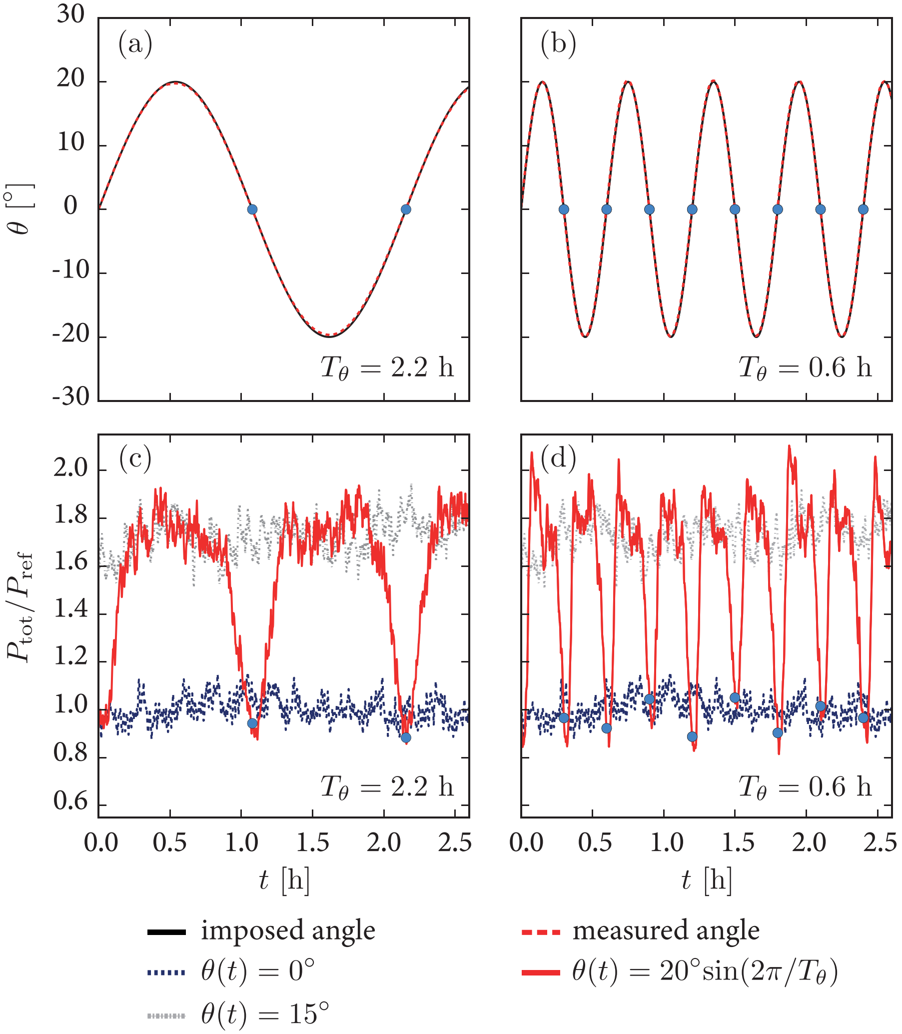

Figure 3.8 – **a) & b)** Imposed and measured wind directions at hub-height with $T_\theta = 2.2$ h and $T_\theta = 0.6$ h, respectively. Circular markers represent the reference wind direction $\theta = 0°$. **c) & d)** Corresponding normalized wind farm power production for $T_\theta = 2.2$ h and $T_\theta = 0.6$ h, respectively.

mean wind direction. In the lower rows, instantaneous flow fields for the same range of wind directions are shown for the simulation in which the wind direction varies with a period of $T_\theta = 0.6$ h. The difference between the middle and bottom rows is the direction in which the wind direction changes, i.e. from

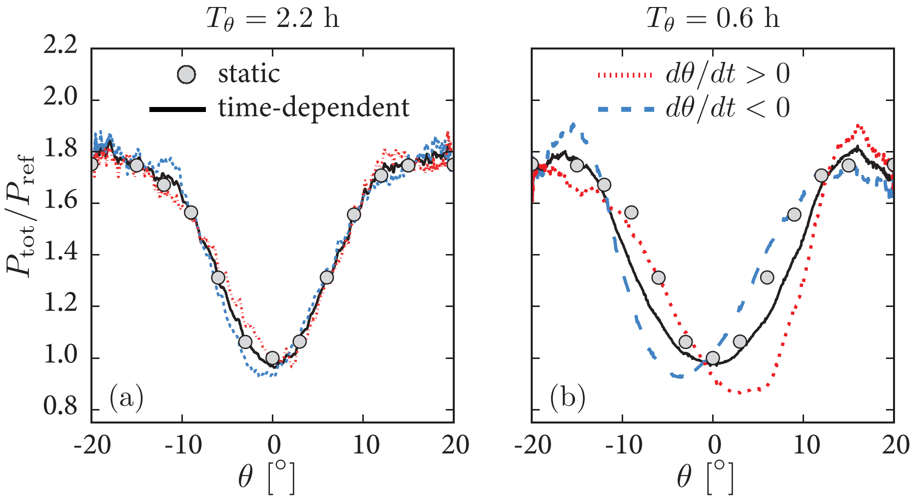

Figure 3.9 – Wind farm power production as a function of the horizontal wind direction for time-varying wind directions (lines), as well as a set of simulations with constant mean wind directions (circles). **a)** $T_\theta = 2.2$ h, **b)** $T_\theta = 0.6$ h.

$d\theta/dt > 0$ in the middle row and $d\theta/dt < 0$ in the bottom row.

For $d\theta/dt > 0$ the minimum power production is lower than for the 0° reference case and observed at $\theta \approx 3°$. When $d\theta/dt < 0$ the minimum is positioned at $\theta \approx -3°$. We note that also Munters et al. [110] found that the flow angle for which the minimum power production is observed can change when the wind direction changes dynamically. The observed effects for $d\theta/dt > 0$ can be explained by the low-velocity zones between the turbine rows, which originate from earlier time steps (see figure 3.10, middle row). Due to the fast rotation rate, the low-velocity zones between the turbine rows at $x > 3$ km did not mix with the incoming high-velocity inflow yet. Therefore, turbines at $x > 3$ km cannot entrain energy from the sides, which is possible for the constant mean $\theta = 0°$ wind direction case for which high-velocity wind-speed channels are formed between the turbines, see figure 3.10. Besides, we speculate that the dynamic wind direction changes may influence the vertical kinetic energy flux that brings down high-velocity wind from above the wind farm to the hub-height plane. In previous work it was namely observed that wakes recover faster when their inter turbine distance is smaller, which leads to a relatively strong wake recovery for the aligned configuration [152]. Unfortunately, as the vertical kinetic energy flux cannot be conditionally sampled on the wind direction, we cannot verify this hypothesis at the moment.

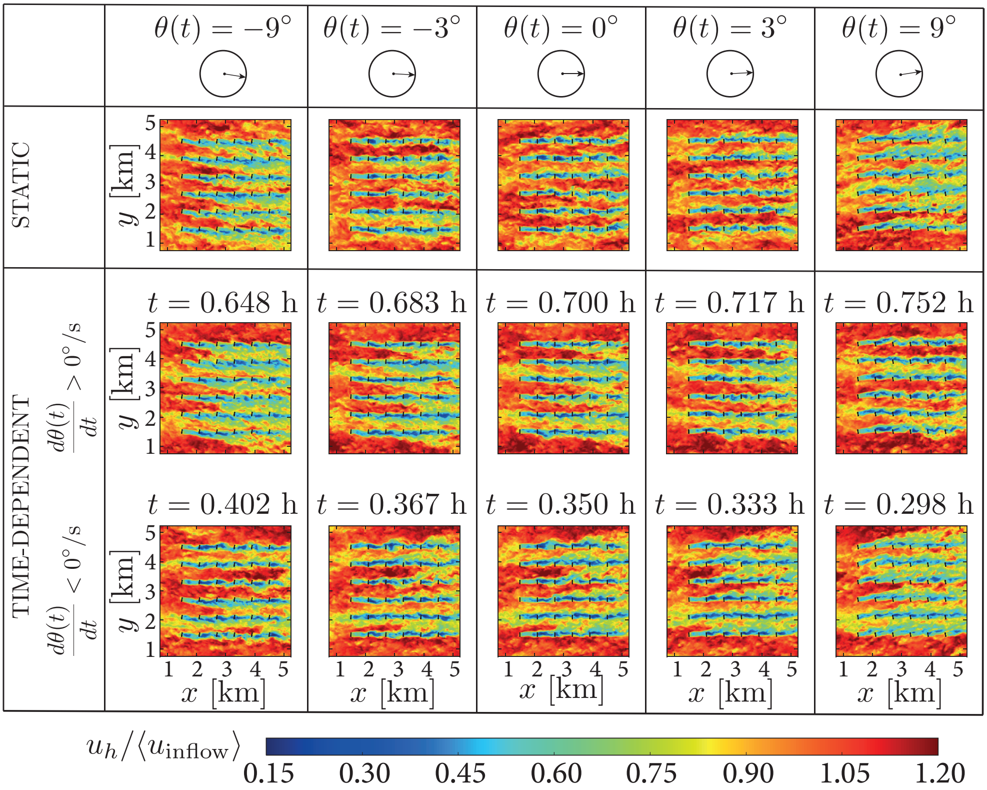

Figure 3.10 – Visualization of the horizontal velocity magnitude at hub-height $u_h = \sqrt{u^2 + v^2}$ normalized by the horizontally-averaged velocity in front of the farm. Each column represents a different wind angle. Top row: Simulations with constant mean wind directions. Middle and bottom row: Simulations in which the mean wind direction is varied $\theta(t) = 20° \sin(2\pi t/0.6h)$ for $d\theta/dt > 0°/s$ (Middle row) and $d\theta/dt < 0°/s$ (Bottom row). Note that time increases from right to left in the bottom row.

In the range of wind directions selected in this study ($\theta = [-20°, 20°]$), we observe that for $d\theta/dt > 0$ the power production at $\theta = 15°$ is higher than for the corresponding mean wind direction case. The movie shows that the turbines at $x > 3$ km and $y > 1.5$ km benefit from the high-velocity wind speed zones between the turbines (see the supplementary movie). However, when $d\theta/dt < 0$ or when the mean wind direction is static at $\theta = 15°$, the turbines in this region of the wind farm are continuously in the wakes created by upstream turbines.

The representative scenario considered above is presented to show that dynamic wind direction changes can significantly affect the performance of large wind farm. As we have shown, this can lead to the hysteresis effect in the power production. We emphasize that these effects will be wind farm-specific and will depend on wind farm design parameters and atmospheric flow conditions. For example, we would expect that the hysteresis effect will be more pronounced when the turbine thrust coefficient is higher. Besides, we expect hysteresis effects to increases with wind farm size in which longer length and time scales corresponding to the dynamic wind direction changes are more important than in smaller farms. Further studies are required to assess such effects in more detail.

3.5 Conclusions

We have presented a new technique to incorporate dynamic wind direction changes in LES of ABLs. The time evolution of the wind direction can be obtained from mesoscale simulations or field measurements. Our method is advantageous compared to previously considered methods [110, 111] as our approach only requires small changes to the governing equations and is easy to implement. Besides, our approach can be applied to simulations of infinite wind farms, which is not possible with previously considered methods [110, 111].

We performed neutral ABL simulations in which we varied the rotation rate of the wind direction to validate our approach. We find an excellent agreement between the imposed and simulated wind direction. We showed that the mean and higher-order flow statistics in the simulations with varying wind direction agrees very well with results obtained from a simulation with a constant mean wind direction when the flow direction is rotated slowly. Comparisons to measurement data demonstrate that our method produces a similar power spectrum of wind directions. This confirms that the non-inertial rotating reference frame is a good technique to model dynamic wind direction changes in LES.

Subsequently, we applied our method to a representative scenario to demonstrate some potential effects of dynamic wind direction changes on wind farm performance. We performed simulations for various wind directions and cases in which a sinusoidal wind direction variation ($\theta = 20°\sin(2\pi t/T_\theta)$ with a time periods of $T_\theta = 0.6$ h and $T_\theta = 2.2$ h) is enforced. In agreement with previous studies [110, 111], we show that dynamic wind direction changes can significantly affect the performance of wind farms. The presented demonstration case shows that dynamic wind direction changes can positively and negatively affect the wind farm power production.

However, we emphasize that further studies are required to better understand these effects. The observed hysteresis effect can, for example, depend on the wind farm design, atmospheric conditions, yaw misalignment with respect to the incoming flow direction, and the turbine thrust coefficient. In this work, we considered a neutral boundary layer situation, but we emphasize that there are no restrictions in extending the presented approach to stable and unstable boundary layer simulations. The present work focuses on modeling wind direction changes, but we note that other mesoscale phenomena like wind shear and temperature variations require further studies.

Link to the supplementary movie [153].

4

The impact of negative geostrophic wind shear on wind farm performance[1]

Baroclinicity, which leads to height-dependent driving pressure gradients, occurs in various situations such as the flow transition between land and sea, and sloping terrain. It has been shown that baroclinicity modifies the structure of the atmospheric boundary layer. For example, negative shear baroclinicity creates additional turbulence at higher elevations, which might influence the energy entrainment into large wind farms. Here, we use large-eddy simulations to study the effect of baroclinicity-induced negative shear on the wind farm power production and energy entrainment into a large wind farm. In agreement with literature, our simulations show that negative geostrophic wind shear significantly modifies the mean wind velocity in the atmospheric boundary layer. Specifically, for the cases considered in the study, the negative geostrophic shear causes a change in the mean velocity up to 2.3 m/s at hub-height, which greatly alters the wind farm power production. Additionally, we demonstrate with an energy budget analysis that a wind farm does not necessarily benefit from the additional turbulence created by the negative geostrophic wind shear. The reason for this is that the baroclinicity-induced negative shear alters the

---

[1] Adapted from: **Anja Stieren**, Jens H. Kasper, Srinidhi N. Gadde, and Richard J. A. M. Stevens, *The impact of negative geostrophic wind shear on wind farm performance*, accepted for publication in Phys. Rev. X Energy (2022)

height and strength of the low-level jet and creates an upward flux above the jet, limiting the energy entrainment into the wind farm. Our results show that wind resources are altered in the boundary layer due to negative geostrophic wind shear and should be considered in wind farm modeling and power forecasts.

4.1 Introduction

One of the uncertainties in wind farm power production is its dependency on the prevailing atmospheric conditions. For instance, energy entrainment into the turbine wakes from the atmosphere above plays a dominant role in the overall efficiency of a wind farm [6, 49]. Consequently, understanding the interaction between the atmospheric boundary layer (ABL) and wind farms is instrumental in increasing the wind farm's efficiency. However, the variety of phenomena occurring in the ABL makes its description and modeling highly complex. Some of these phenomena are variations in atmospheric stability [36, 92, 154–158], cloud formations [156, 159] and geostrophic wind [103, 160–166]. In this study, we will focus on the latter.

According to the thermal wind balance [167], horizontal temperature gradients can cause a variation in the geostrophic wind with height, which is known as baroclinicity [168]. A height-dependent geostrophic wind implies that the driving pressure gradient varies with height. However, this effect is often neglected in simulations of the ABL [36, 92, 154, 155, 169, 170] even though baroclinicity can play an important role in the atmospheric dynamics. For example, effects of baroclinicity can be significant in the transition between land and sea [158, 171], between ice and water [172], in sloping terrain [173] or close to mountain ranges [168]. The change in the geostrophic wind with height is governed by its alignment with the horizontal temperature gradient. Depending on this alignment, the pressure gradient can either increase or decrease in magnitude, or rotate with height. Since the wind direction is often governed by different factors than the direction of the temperature gradient, the specific effects of baroclinicity at a given site may vary. Here, we focus on the scenario wherein the geostrophic wind decreases with height without changing its direction, called *negative geostrophic shear*.

Negative geostrophic shear modifies the mean wind profile in the boundary layer and hence alters the available wind resources. Furthermore, a negative geostrophic shear promotes the formation of a wind maximum at low heights in stable conditions, the so-called low-level jet (LLJ) [168]. Negative shear baroclinicity introduces enhanced shear above the LLJ, which enhances the turbulence in the layer above the turbulence inversion [38, 168]. These processes affect the momentum and heat entrainment [162, 163, 165, 166]. Momen [174] recently discovered that the friction velocity, Obukhov length, shear production, and ABL height strongly depend on baroclinicity when weakly stable conditions prevail. For stronger atmospheric stability, when the lower part of the ABL

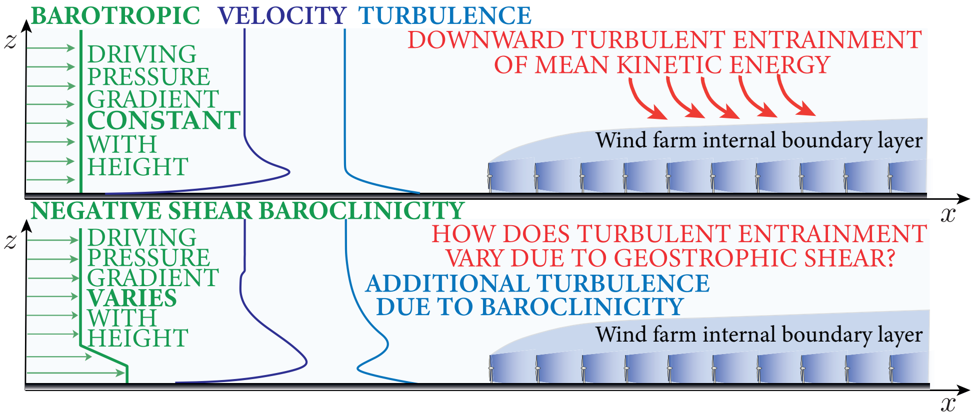

Figure 4.1 – Schematic, illustrating the research question under consideration, namely, how does negative geostrophic wind shear affect the power production of and the energy entrainment into a wind farm? The illustrated velocity and turbulence profiles indicate that shear-induced by baroclinicity creates additional turbulence at higher elevations. This is expected to affect the vertical entrainment of energy into the wind farm. Details on the simulations and the considered velocity profiles are provided in figures 4.2 and 4.3, respectively.

is decoupled from higher elevations due to the strong turbulence destruction, the dependency of these parameters on baroclinicity decreases [174]. Previous experiments and simulations have shown dependencies of the wind profiles on baroclinicity for neutral and unstable conditions as well [166, 171, 172, 175–180]. Recently, Ghannam and Bou-Zeid [181] introduced a correction to the logarithmic law predictions to account for baroclinicity effects in near neutral conditions. They use first-order closure principles to capture wind turning and baroclinicity effects.

As baroclinicity affects the structure of the ABL, it is expected to have a large impact on the performance of wind farms. The height and strength of the LLJ, which are highly influenced by baroclinicity, play an important role in the wake recovery inside wind farms [182–184]. Conangla and Cuxart [168] measured and simulated cases of negative geostrophic wind shear, where the LLJ is positioned at heights starting from 50 m and the turbulence kinetic energy increased above, i.e. between 75 and 250 m. Wind turbine rotors are typically positioned within this range of heights. The increased turbulence intensity that results from negative geostrophic wind shear is expected to influence the momentum transport in the ABL, and hence the ability of the wind farm to harvest energy from it.

However, how geostrophic shear influences the entrainment into wind farms is still unknown. To study the complex interaction of wind farms and turbulent ABL flows, Calaf et al. [12] proposed using large-eddy simulations (LES). The advantage of LES is that they capture temporal fluctuations and resolve large-scale flow features in the ABL, while the small-scale turbulence is parameterized using a sub-grid scale model (SGS) [170]. Thus, LES can accurately model the complex flows through wind farms. The first LES of wind farms assume neutral pressure-driven flow over flat terrain [12] and this simplification is still commonly used in the fundamental research on wind farm flows [80, 108, 185–188]. Studying flows under these controlled conditions is necessary to get more fundamental insight. While LES of wind farms in neutral pressure-driven flow have been shown to reproduce measurements [108], their results are not universally applicable. The reason for this is the underlying assumption in such simulations that the wind turbines reside in the inner region of the ABL and that outer layer effects are negligible. In later studies, outer layer effects like thermal stability [24, 122, 140, 189–194] and Coriolis force [81, 195, 196] received more attention. These studies highlighted the complexity of the interaction between wind farms and the ABL. In particular, they showed that the wake recovery and the energy entrainment into the wind farms are highly dependent on the atmospheric conditions, such as the height and strength of the capping inversion and the free-atmosphere stratification. Due to the high complexity of the interaction between ABL dynamics and wind farms, understanding the influence of atmospheric mesoscales on microscale processes was identified as one of the grand challenges in wind energy [105].

Recently, realistic flow conditions have been included in LES via data assimilation [125, 134], or by coupling LES to mesoscale models like the Weather Research and Forecasting model (WRF) [131, 132]. However, the complexity involved in these approaches makes it difficult to isolate and understand the effect of baroclinicity on wind farm performance. The present study aims to identify the differences in wind farm power production with and without a prevailing negative geostrophic shear. We especially want to find out how the altered velocity profile and the increased turbulence intensity due to negative shear baroclinicity affect the energy entrainment into the farm, see figure 4.1.

The remainder of this chapter is structured as follows. Section 4.2 discusses the simulation approach and the considered cases. The effect of negative geostrophic wind shear on atmospheric dynamics is addressed in section 4.3.

The effect of negative geostrophic wind shear on the flow in and around wind farms is studied in section 4.4, followed by an analysis of the entrainment fluxes (section 4.5) and the effect on the power production (section 4.6). We end with the conclusions and outlook in section 4.7.

4.2 Large-eddy simulations

We perform LES with an updated version of the code used by Albertson and Parlange [143]. The code was validated by Gadde et al. [144] and can accurately simulate thermally stratified ABLs and wind farm wakes [197]. The governing equations for the LES, in terms of the filtered quantities (denoted by a tilde), are the incompressible continuity equation, the equation of momentum conservation, and the transport equation for potential temperature:

$$\partial_i \tilde{u}_i = 0, \tag{4.1}$$

$$\begin{aligned} \partial_t \tilde{u}_i + \partial_j \left(\tilde{u}_i \tilde{u}_j\right) = -\partial_i \tilde{p}^* - \partial_j \tau_{ij} + g\beta\delta_{i3}\left(\tilde{\theta} - \left\langle\tilde{\theta}\right\rangle\right) \\ + \epsilon_{ij3} f_c \left(\tilde{u}_j - G_j\right) + f_i, \end{aligned} \tag{4.2}$$

$$\partial_t \tilde{\theta} + \tilde{u}_i \partial_i \tilde{\theta} = -\partial_i q_i. \tag{4.3}$$

Here, $i = 1, 2, 3$ correspond to the streamwise (x,u), spanwise (y,v), and vertical (z,w) directions, respectively. Furthermore, $\tilde{u}_i$ represents the filtered velocity field components and $\tilde{\theta}$ is the filtered potential temperature field. The Boussinesq approximation is applied to obtain the buoyancy term in equation (4.2), with gravitational constant g, Kronecker delta δ_{ij}, and buoyancy parameter $\beta = 1/\langle\tilde{\theta}\rangle$ with respect to the planar averaged potential temperature $\langle\tilde{\theta}\rangle$. Effects of resolved viscous stresses are neglected, since a very high Reynolds number flow is assumed. The SGS stress tensor is denoted by τ^t_{ij} and $\tau_{ij} = \widetilde{u_i u_j} - \tilde{u}_i \tilde{u}_j$ is its deviatoric, traceless part, while the trace of the SGS stress tensor $\tau^t_{kk}/3$ is absorbed into the filtered modified pressure $\tilde{p}^* = \tilde{p}/\rho_0 - p_\infty/\rho_0 + \tau^t_{kk}/3$ with the air density ρ_0. The SGS heat flux vector is given by $q_i = \widetilde{u_i \theta} - \tilde{u}_i \tilde{\theta}$. Both SGS deviatoric stress and SGS heat flux are modeled using an eddy diffusivity parameterization. Specifically, the anisotropic minimum dissipation model [77, 144] is applied. The model provides dynamic and scale-dependent SGS coefficients for modeling SGS turbulence. The geostrophic wind velocity is given by $G_i = -\epsilon_{ij3}\partial_j p_\infty / \left(\rho_0 f_c\right)$, where ϵ_{ij3} denotes the alternating unit tensor and f_c the Coriolis parameter. $\partial_i p_\infty$ is the driving mean pressure gradient, which is independent of height in barotropic conditions, but depends on height in baroclinic conditions.

The computational domain is discretized with n_x, n_y, and n_z points in the streamwise, spanwise, and vertical directions, respectively. A uniform grid is used in horizontal directions, with a corresponding grid spacing of $\Delta_x = L_x/n_x$ and $\Delta_y = L_y/n_y$, where L_x and L_y are the dimensions of the computational domain. In vertical direction the grid is uniform (with spacing Δ_z) up to a height z_{uni}. Beyond z_{uni} the grid is stretched up to the domain height L_z, using a hyperbolic tangent stretching function. The computational grid is staggered in vertical direction. The variables u, v, and θ are stored at the intervals $z_l^{\text{stag}} = (z_l + z_{l+1})/2$, with $l = 0, ..., n_z - 1$, whereas the vertical velocity w is stored in the nodes z_l.

Free-slip boundary conditions with zero vertical velocity are enforced at the top of the domain. A Rayleigh damping layer is used at the top of the domain to reduce the reflection of gravity waves that are triggered by the presence of the wind farm [100]. For the bottom boundary condition, the wall shear stress $\tau_{i3|w}$ and the buoyancy flux q_* at the surface are modeled using the Monin-Obukhov similarity theory [92]:

$$\tau_{i3|w} = -u_*^2 \frac{\tilde{u}_i}{\tilde{u}_r} = -\left[\frac{\tilde{u}_r \kappa}{\ln(z/z_0) - \psi_M}\right]^2 \frac{\tilde{u}_i}{\tilde{u}_r}, \tag{4.4}$$

$$q_* = \frac{u_* \kappa (\theta_{\text{s}} - \tilde{\theta})}{\ln(z/z_{0,\text{s}}) - \psi_H}, \tag{4.5}$$

where u_* is the frictional velocity, z_0 is the roughness height, $\kappa = 0.4$ is the von Kármán constant, $\tilde{u}_r = \sqrt{\tilde{u}^2 + \tilde{v}^2}$ is filtered velocity magnitude at the first grid level [73]. θ_{s} is the filtered potential temperature at the surface and $z_{0,\text{s}} = z_0/10$ [93] is the thermal surface roughness length. For stable boundary layers (SBL) the stability corrections for momentum $\psi_M = -4.8z/L$ and heat flux $\psi_H = -7.8z/L$ are used [94]. Here θ_0 is the reference potential temperature and $L = -(u_*^3\theta_0)/(\kappa g q_*)$ is the surface Obukhov length. For neutral boundary layers (NBLs) the buoyancy flux at the surface and the stability corrections are zero ($q_* = \psi_M = \psi_H = 0$).

Time integration is performed using a third-order accurate Adams-Bashforth scheme. Spatial derivatives in the vertical direction are calculated using a second-order central finite difference scheme. A pseudo-spectral method is applied in horizontal directions, resulting in periodic boundary conditions in horizontal directions. The concurrent precursor method [138] is employed to generate realistic, turbulent inflow conditions. This approach samples flow data from a periodic ABL simulation performed in a precursor domain. The sampled data is introduced as inflow velocity into a fringe region of the wind farm domain using a symmetric fringe function [153]. As the wind direction changes with height, a second fringe region is employed in spanwise direction. We employ a PI controller [139] to guarantee that the planar-averaged wind angle at hub-height is 0°. This is necessary as the wind veer depends on the stability conditions.

4.2.1 Wind turbine parameterization

The turbine force term f_i is implemented using the actuator line method [198, 199]. The turbine blades are represented by distributed body forces, calculated dynamically using the local flow velocity. The total force f_i comprises a lift and drag component, evaluated in a local coordinate frame (r, θ, x) before being transformed to the global frame (x, y, z). The local lift and drag forces, per unit span, are given by:

$$f_L = \frac{1}{2}\rho_0 C_L \tilde{u}_{\mathrm{rel}}^2 c, \qquad f_D = \frac{1}{2}\rho_0 C_D \tilde{u}_{\mathrm{rel}}^2 c, \tag{4.6}$$

respectively. Here, $\tilde{u}_{\mathrm{rel}} = \sqrt{\tilde{u}_\theta^2 + \tilde{u}_x^2}$ is the flow velocity relative to the blade, with circumferential velocity $\tilde{u}_\theta = \Omega r - \tilde{u}_y \cos(\theta) + \tilde{u}_z \sin(\theta)$. Furthermore, Ω is the rotational speed of the rotor and c is the local chord length. The lift and drag coefficients $C_L(\alpha)$ and $C_D(\alpha)$, at the local angle of attack $\alpha = \phi - \gamma$, are obtained from tabulated airfoil data. Here, ϕ is the angle between $\tilde{u}_\theta$ and $\tilde{u}_{\mathrm{rel}}$, while γ accounts for any twist and pitch contributions. A Gaussian projection, given by $\eta_\epsilon = \epsilon^{-3}\pi^{-3/2}\exp\left(-d^2/\epsilon^2\right)$, where ϵ denotes the kernel width and d is the distance to the considered actuator point, is used to smear the turbine force and avoid numerical instabilities. The kernel width ϵ for the force projection is related to the grid spacing via $\epsilon = 2\Delta_x$, based on initial testing, as well as the recommendation by Martínez-Tossas et al. [200]. For practical reasons, the rotor heads are oriented perpendicular to the x-direction rather than perpendicular to the local flow. In the appendix, we show that this does not influence the main findings of the study.

We note that the LES filtering tilde is omitted to simplify the notation in the remainder of this work.

4.2.2 Modeling Baroclinicity in LES

To evaluate the effects of baroclinicity on wind farm performance and wake development, we study cases with varying geostrophic wind profiles and boundary-layer stability. Baroclinicity is generated by surface temperature gradients, resulting in thermal winds within the ABL, which weaken aloft [172]. While the temperature gradients occur on very large horizontal scales, the geostrophic wind changes with height also on small horizontal scales. For instance, a temperature change of 1 K over 1000 km in horizontal direction can cause an increase in geostrophic velocity of 3 $\text{m s}^{-1}\,\text{km}^{-1}$ with height [175]. On the relatively small domain size considered here, we model the effect of baroclinicity by varying the geostrophic wind with height. As pointed out by Sorbjan [180], this is a relatively straightforward approach.

The boundary layer is driven by a geostrophic wind with magnitude G. Cases with constant G are known as *barotropic*, while cases where G is height-dependent are named *baroclinic*. The selection of the geostrophic wind velocity for the SBL cases in this study is inspired by the measurements of Conangla and Cuxart [168]. Conangla and Cuxart [168] observe and model negative shear baroclinicity in a SBL. Interestingly, they observe that the negative geostrophic wind shear gives rise to sharp changes in the LLJs and increased turbulence intensity aloft. The changes in the shape of the LLJ and the increased turbulence intensity above the LLJ are expected to change the energy transport in the ABL. The entrainment from above highly influences wind farm performance. Consequently, we are interested in how the increased turbulence intensity observed by Conangla and Cuxart [168] affects this entrainment process. Conangla and Cuxart [168] used a turbulent kinetic energy single-column model to show that the measured wind profiles could result from a baroclinic geostrophic wind profile as below:

$$G(z) = \begin{cases} G_0, & \text{if } z < z_s \\ G_0 - \frac{\Delta G}{\Delta z_s} \cdot (z - z_s), & \text{if } z_s \leq z \leq z_s + \Delta z_s \\ G_0 - \Delta G, & \text{if } z > z_s + \Delta z_s \end{cases} \tag{4.7}$$

Here, G_0 refers to the geostrophic velocity at the surface. All baroclinic cases under consideration have a negative shear layer in the geostrophic velocity profile. It is modeled by a linear vertical variation in the geostrophic wind of magnitude ΔG over a height of Δz_s, starting from a height z_s. In all cases, the geostrophic velocity is constant above an altitude of $z_s + \Delta z_s$, see also figure 4.2.

Additionally, we are interested in how negative geostrophic wind shear effects are different in SBLs and NBLs. Therefore, we drew inspiration from the study by Floors et al. [171] and simulations by Momen et al. [172] to design realistic NBL conditions with negative geostrophic shear, allowing us to study the wind farm performance under these conditions. The NBL cases are also constructed using equation 4.7.

Table 4.1 – Values for the geostrophic wind speed at the surface G_0 and at the top of the domain $G_0 - \Delta G$ for the different cases, see equation (4.7) and figure 4.2.

Case name	G_0 [m/s]	ΔG [m/s]	Δz_s [m]	z_s [m]
SBL Barotropic	10	0	0	0
SBL Baroclinic low	10	4	200	200
SBL Baroclinic high	14	4	200	200
NBL Barotropic	12	0	0	0
NBL Baroclinic low	12	3	1000	0
NBL Baroclinic high	15	3	1000	0

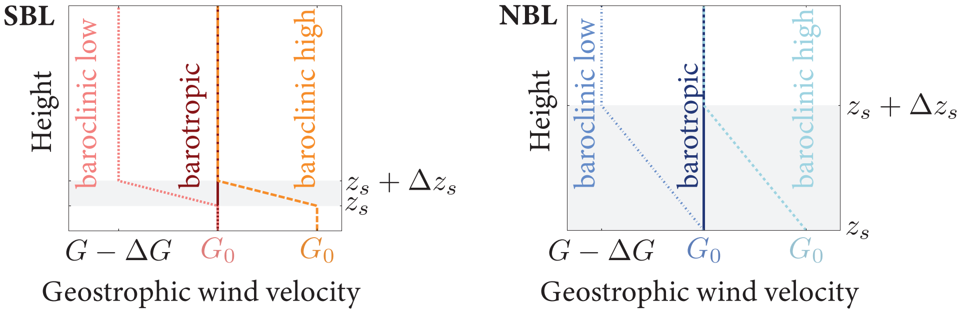

Figure 4.2 – Schematic of the geostrophic wind velocity with height in the baroclinic cases (equation 4.7).

4.2.3 Suite of LES

We consider a domain size of $L_x = 15.36$ km, $L_y = 4.8$ km and $L_z = 4.0$ km. Previous studies [197] confirmed that this domain size allows the turbulence statistics relevant to this study to be captured accurately. The domain is discretized using $1280 \times 640 \times 384$ grid points in streamwise, spanwise, and vertical directions, respectively. The streamwise and spanwise grid resolutions are $\Delta_x = 12$ m and $\Delta_y = 7.5$ m, respectively. The vertical grid spacing equals $\Delta_z = 5$ m up to $z_{\text{uni}} = 1.5$ km, and is thereafter stretched to a maximum of $\Delta_z = 59$ m at the top boundary. The fringe region covers the final 1.54 km in streamwise and 0.48 km in spanwise direction. The roughness length is $z_0 = 0.002$ m, corresponding to offshore conditions [201] and the reference potential temperature is $\theta_0 = 286$ K. The initial potential temperature profile contains a mixed layer with a constant potential temperature of θ_0 up to

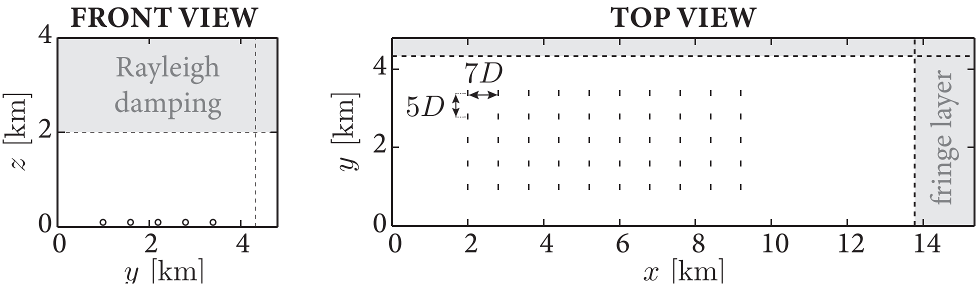

Figure 4.3 – Schematic of the simulation domain, showing the wind farm layout, the extent of Rayleigh damping layer and the fringe layers. Black circles and lines indicate the positions of the wind turbines.

1200 m. Starting from $z = 1200$ m, a capping inversion is implemented by increasing the potential temperature by 3 K over a height of 200 m. The free atmosphere is positioned above $z = 1400$ m with a stratification strength of 5 K/km. Furthermore, we apply a constant surface cooling of $C_r = 0.25$ K/h for the SBL cases, while the surface temperature is kept constant for the NBL cases. The Coriolis parameter is set to $f_c = 1.159 \cdot 10^{-4}\ \mathrm{s}^{-1}$ (corresponding to latitude $\Phi = 52°$). The details of the geostrophic wind used in the study and its variation with height are listed in table 4.1 and shown in figure 4.2, respectively. The magnitude of the geostrophic wind velocity for the barotropic cases was selected to achieve hub-height velocities around 10 m/s, which are typical for wind farms. The geostrophic wind velocities in the baroclinic cases match the barotropic velocities at the top or bottom. In this way, we can study how the actual velocity magnitude and LLJ height influence the result.

The initial wind profile is set equal to $G(z)$, see equation (4.7). Random perturbations are added to the velocity profile below 200 m to spin up turbulence. The amplitude of the perturbations has a maximum value of $10^{-5}G_0$ at the ground and decreases linearly with height. Similarly, random perturbations with a maximum magnitude of $10^{-5}\theta_0$ are added to the initial potential temperature profile. The boundary layer is assumed to be in a quasi-steady state when the velocity and other turbulent quantities have reached a steady state, and the temperature profile changes at a constant rate [202].

We perform the simulations in two stages. In the first stage, we perform a spin-up simulation in a domain of size $L_x/2 \times L_y/2 \times L_z$ for 7 hours. In the second stage, after the flow has reached a quasi-steady state, we use the domain periodicity to initialize the flow for the wind farm domain and activate

Table 4.2 – The columns from left to right indicate the case name, the LLJ height (z_{LLJ} [m]), the velocity at the LLJ height (v_{LLJ} [m/s]), velocity (V_{inflow} [m/s]) and turbulence intensity (TI [m]) at hub-height, frictional velocity (u_* [m/s]), Obukhov length (L [m]) and baroclinicity strength (S_0 [−]).

Case name	z_{LLJ}	v_{LLJ}	V_{inflow}	$\mathrm{TI}(z_{\mathrm{h}})$	u_*	L	S_0
SBL Barotropic	242	11.66	9.53	3.4%	0.258	141	-
SBL Baroclinic low	133	9.90	9.33	3.0%	0.243	126	2.40
SBL Baroclinic high	228	13.34	11.58	4.8%	0.341	243	1.71
NBL Barotropic	1043	12.88	10.71	6.3%	0.378	-	-
NBL Baroclinic low	447	10.92	9.7	6.3%	0.341	-	0.30
NBL Baroclinic high	628	13.95	12.00	6.6%	0.423	-	0.24

the wind turbines. The statistics are collected over 3 h starting from the 8th hour to the 11th hour.

We consider a wind farm with 10 × 5 wind turbines. A schematic of the setup is shown in figure 4.3. The turbines are positioned uniformly in an aligned layout, with a spacing of $s_x = 7D$ and $s_y = 5D$ in the streamwise and spanwise directions, respectively. We simulate turbines based on the National Renewable Energy Laboratory (NREL) 5 megawatt (MW) turbine [203], which has a rotor diameter of $D = 126$ m and a hub-height of $z_h = 90$ m. The tip-speed ratio (TSR) is fixed to $\lambda = 7.55$, which gives an optimal power coefficient C_p [203]. Consequently, the rotor rotational speed Ω is computed dynamically to accommodate the prescribed TSR. Dependent on the local inflow conditions, Ω varies from 6.7 to 13.4 rpm and the thrust coefficient lies between 0.84 and 0.87 in the simulations under consideration.

4.3 Boundary layer characteristics

Figure 4.4 shows the mean horizontal wind magnitude $v_g = \left\langle \sqrt{\overline{u}^2 + \overline{v}^2} \right\rangle$ for the SBL (a) and NBL (e). Here, ($\langle\cdot\rangle$) and ($\bar{\cdot}$) denote planar and temporal averaging, respectively. The geostrophic forcing (equation 4.7), is displayed by thin lines. The actual velocity matches the imposed geostrophic wind velocity $G_0 - \Delta G$ at heights above the capping inversion (shaded area in figure 4.4). This is expected as above the BL height, the turbulent friction is small,

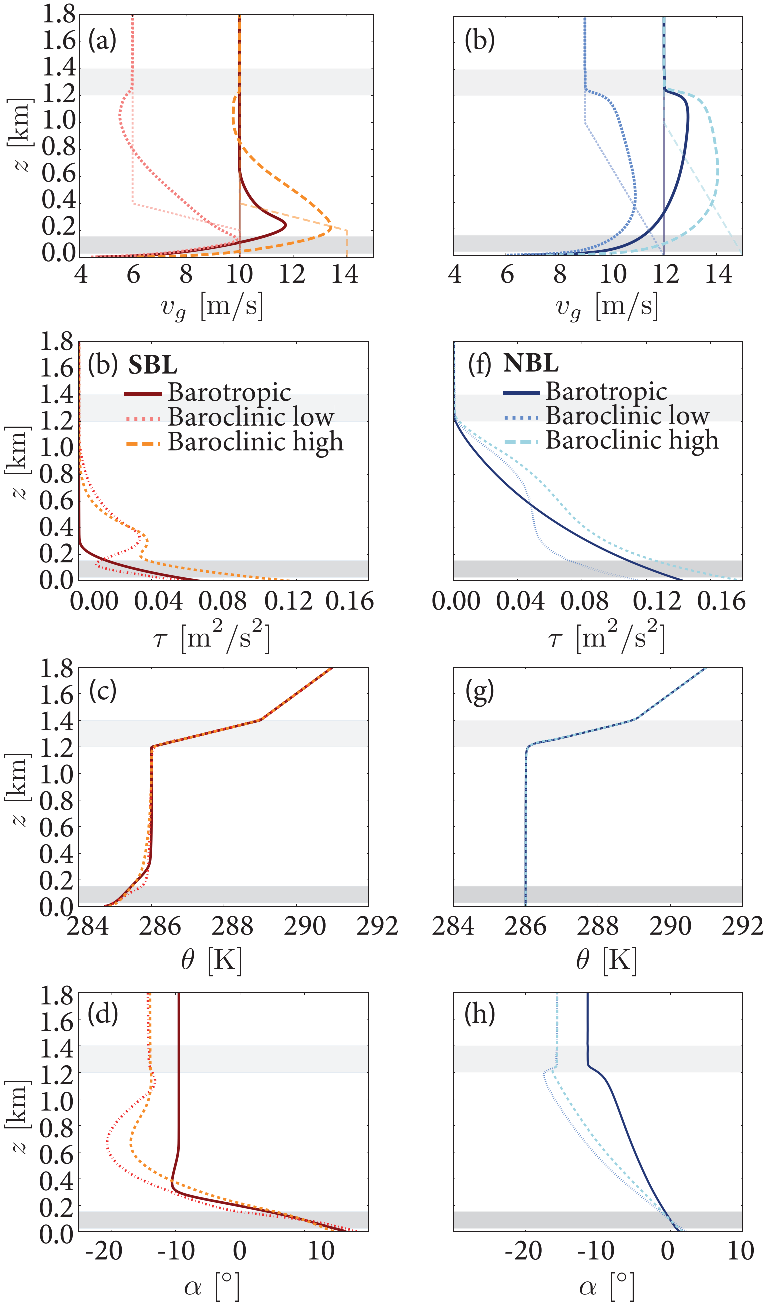

Figure 4.4 – (a & e) Horizontal velocity magnitude (thin lines show the geostrophic forcing, see also figure 4.2), (b & f) vertical momentum flux, (c & g) potential temperature, and (d & h) wind angle as a function of height for SBL and NBL cases, respectively. Grey shaded areas mark the heights that span the turbine blades and the capping inversion layer.

and the geostrophic balance between the Coriolis and pressure gradient force is reached. Below the capping inversion, the flow velocity strongly depends on the imposed geostrophic shear. Specifically, the jet strength depends on the local forcing strength; see also table 4.2. The jet height is lower for the baroclinic cases than for the barotropic cases. Similar observations were made by Momen et al. [172] and Conangla and Cuxart [168], who also simulated and measured geostrophic velocities with negative shear. To conclude, figures 4.4(a) and (e) show that negative shear baroclinicity greatly alters the mean wind profile in the ABL and hence the available wind resources for energy production.

Figure 4.4(b) & (f) show the magnitude of the planar-, temporally-averaged vertical kinematic momentum flux:

$$\tau = \sqrt{\left\langle \overline{u'w'} \right\rangle^2 + \left\langle \overline{v'w'} \right\rangle^2},$$

with $\left\langle \overline{u'w'} \right\rangle = \langle \overline{uw} \rangle + \langle \overline{\tau}_{xz} \rangle - \langle \overline{u} \rangle \cdot \langle \overline{w} \rangle$. In the barotropic cases, the vertical kinematic momentum flux has its maximum at the ground and monotonically decreases with increasing height, approaching zero aloft where the influence of the surface is negligible. In contrast, shear is not only generated at the surface, but also due to the changes in geostrophic wind in the baroclinic cases. Right above the LLJ, where $dG/dz < 0$, a local maximum of momentum flux forms. Such local maxima have been reported previously by Conangla and Cuxart [168], who conclude that the geostrophic shear increases the wind shear and turbulence production away from the surface. The flow above the LLJ is thus shear dominated. In the neutral cases, the differences between the baroclinic and barotropic cases are less pronounced than in the SBL cases. This could result from the enhanced turbulence (see table 4.1) and the lower imposed baroclinicity strength in the neutral cases.

To estimate the baroclinicity strength S_0, we follow the definition of Momen et al. [172]. For negative shear baroclinicity, where the geostrophic wind G does not change its direction with height, the baroclinicity strength is defined as:

$$S_0 = \frac{z_i}{G_0} \left(\frac{\partial G}{\partial z} \right)_{\max}. \tag{4.8}$$

Momen et al. [172] define the baroclinicity strength based on the gradient measured at the surface. However, as $(dG/dz) = 0$ in the SBL cases we define S_0 based on $(dG/dz)_{\max}$. Following Momen et al. [172], we approximate the ABL height z_i by the base height of the capping inversion layer, which is $z_i = 1200$ m for all cases.

The values for S_0 are listed in table 4.2. Thus the stable cases have a stronger baroclinicity than the neutral cases, while the baroclinicity is strongest in the *Baroclinic low cases*. The reason is that the gradient of the geostrophic wind compared to its absolute values is highest for the *Baroclinic high cases*. As a result, the local maximum in the total vertical momentum flux, that arises due to baroclinicity, is most pronounced for the *SBL Baroclinic low case*, where the baroclinicity strength is highest (see figure 4.4(b) & (f)).

The planar-averaged turbulence intensity at hub-height:

$$\mathrm{TI} = \frac{\left\langle \sqrt{\frac{1}{3}\left(\overline{u'^2} + \overline{v'^2} + \overline{w'^2}\right)} \right\rangle}{\left\langle \sqrt{\overline{u}^2 + \overline{v}^2 + \overline{w}^2} \right\rangle},$$

with $\overline{u'^2} = \overline{u^2} + \overline{\tau}_{xx} - \overline{u}^2$, is given in table 4.2. The *Baroclinic low* cases show a reduced or equal turbulence intensity in comparison to their respective barotropic cases, for which G_0 is the same. An increase in TI is observed for the *Baroclinic high* cases. In agreement with the time- and horizontal-averaged hub-height velocity at the inlet V_{inflow}, the friction velocity and the Obukhov length are lowest for the *Baroclinic low* cases and highest for the *Baroclinic high* cases (see table 4.2).

The planar- and temporally averaged potential temperature θ is shown in figure 4.4c & g. For the SBL, the surface is cooled such that a stable stratification exists near the surface, followed by a neutral temperature profile up to the capping inversion. Above the capping inversion, there is stable free-atmospheric stratification. In the NBL, the potential temperature is constant below the capping inversion, above which the atmosphere is stably stratified. There are only minor differences in the potential temperature profiles in barotropic and baroclinic cases.

Due to the imposed geostrophic shear, the Ekman spiral is altered, yielding different wind angles for different cases. Figure 4.4d & h show the mean wind angle $\alpha = \tan^{-1} \langle \overline{v} \rangle / \langle \overline{u} \rangle$. Note that, due to the applied wind-angle controller, the wind direction has a constant value of $\alpha = 0°$ at hub-height for all cases under consideration. Typically, the wind veer is more pronounced in a SBL than in a NBL, and stronger for cases with negative geostrophic shear. A changing wind veer can alter the spatial structure of the wakes [196] and is, consequently, important to take into consideration.

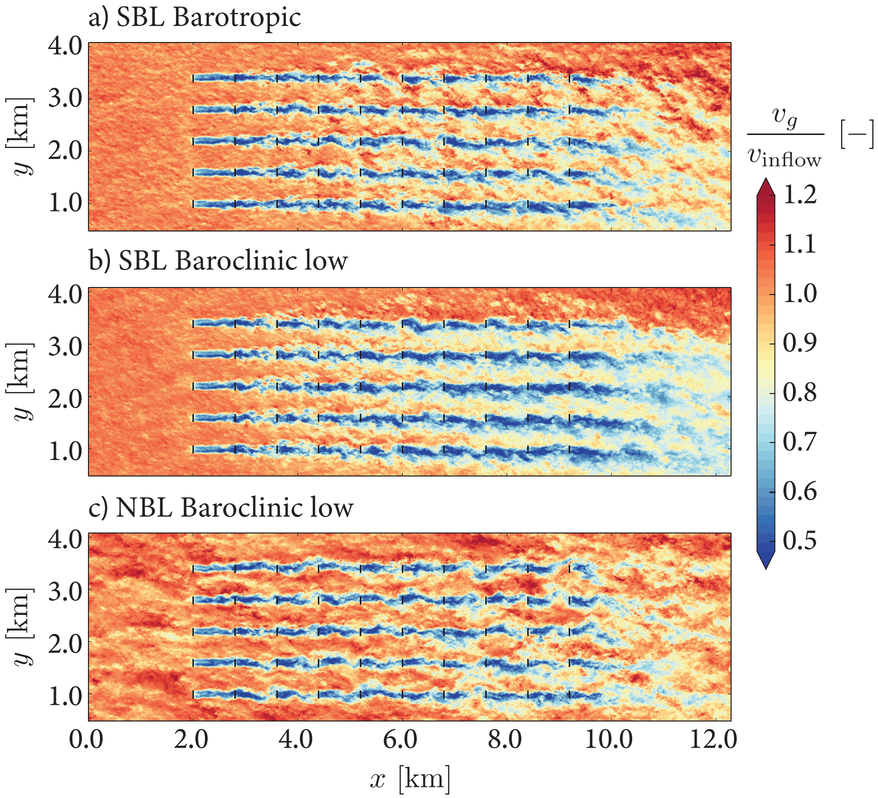

Figure 4.5 – (a-c) Instantaneous velocity at hub-height. Black lines indicate the position of turbines.

4.4 Effect of baroclinicity on the flow in and around wind farms

In the previous section, we showed that negative geostrophic shear alters the mean wind profile and causes a lower jet height. Furthermore, above the LLJ, additional shear and turbulence are created by baroclinicity. In the following, we examine how these changes affect the flow in and around a wind farm.

Figure 4.5 shows the instantaneous velocity at hub-height (x-y plane) for the (a) *SBL Barotropic*, (b) *SBL Baroclinic low*, and (c) *NBL Baroclinic low* cases. The wakes behind the first row for the *SBL Barotropic* and *SBL*

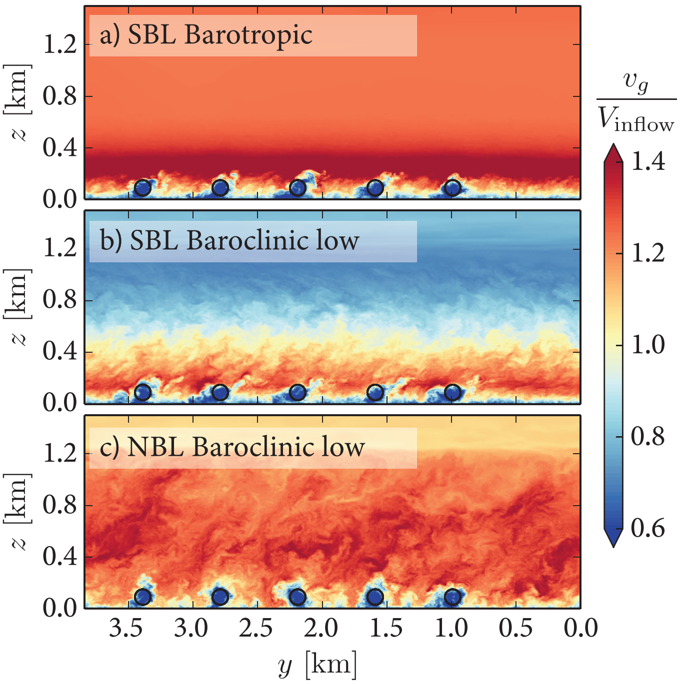

Figure 4.6 – y-z planes of the instantaneous velocity $1D$ behind the last turbine row. For clarity, only $z \leq 1.4$ km is shown here. Black circles indicate the position of turbines.

Baroclinic low cases are straight and have a similar velocity deficit. In contrast, the wakes in the second row seem to be shorter and meander stronger in the *SBL Baroclinic low* than in the *SBL Barotropic* case. Further downstream, the velocity deficit in the *SBL Baroclinic low* case is higher and persists longer than in the *SBL Barotropic* case. This difference is caused by the height of the LLJ, which is located above the turbines in the *SBL Barotropic* case, while it overlaps with the rotor swept area in the *SBL Baroclinic low* case. In the latter case, the first rows extract most of the energy from the LLJ, leaving fewer resources for downstream turbines. Furthermore, we observe a significant clockwise deflection of the wakes downstream. This is likely a result of downstream entrainment of momentum from the layer above [204, 205], where the flow direction is rotated (see figure 4.4d). In the NBL case (figure 4.5c), the atmospheric scales are larger and form high and low-velocity streaks.

Additionally, the turbulence intensity is higher in the NBL cases; see table 4.2. Consequently, the meandering of the wakes in the lateral direction is more pronounced.

Figure 4.6 show y-z planes of the instantaneous velocity at a distance of $1D$ behind the last turbine row. In the *SBL Barotropic* case (figure 4.5d) the flow above the LLJ is non-turbulent. However, in both baroclinic cases (figures 4.5e-f) the flow is more turbulent above the jet due to the geostrophic shear. Furthermore, due to the prevailing wind veer, the wakes are skewed significantly in the SBL cases [196]. In the NBL, this effect is less pronounced as the veer is much smaller. The jet in the NBL case is stretched up to a height of 1.2 km, and this layer is well mixed and more turbulent than in the SBL cases. For a further discussion of the effect of baroclinicity on the flow structures, we refer the reader to Momen et al. [172].

Figure 4.7 shows the time-averaged velocity, averaged over the spanwise extent of the wind farm, which clearly reveals the LLJ height. The LLJ is lowest in the *SBL Baroclinic low* case (figure 4.7b) in which it resides largely within the rotor swept area of the turbines. When the LLJ occurs roughly at hub-height, the first rows of the wind farm extract most of the momentum from the LLJ. Consequently, the energy that is available for downstream turbines is reduced significantly [183]. Figure 4.7b shows that the jet velocity is reduced towards the end of the farm. The effect is much less pronounced in the other cases, where the LLJ is positioned higher.

To show how this phenomenon affects the velocity at hub-height, we evaluate the velocity averaged over the spanwise extent of the wind farm, normalized by the inflow velocity, see figure 4.7d. For all cases, the velocity reduces significantly at the turbine locations, and there is a decreasing trend in the downstream direction over the length of the wind farm. Compared to all other cases, the *SBL Baroclinic low* case exhibits a greatly reduced downstream wake recovery. Furthermore, we observe that the wake behind the first turbine row recovers faster for the baroclinic cases, while the barotropic cases show increased wake recovery further downstream in the wind farm. Finally, the wake recovery is significantly slower in stable than in neutral conditions, in agreement with previous observations by Abkar and Porté-Agel [191]. The wake recovery further downstream in the wind farm depends strongly on the entrainment of energy from the flow above the wind farm [49]. Therefore, we analyze the entrainment fluxes to understand the slower wake recovery for baroclinic cases in the following section.

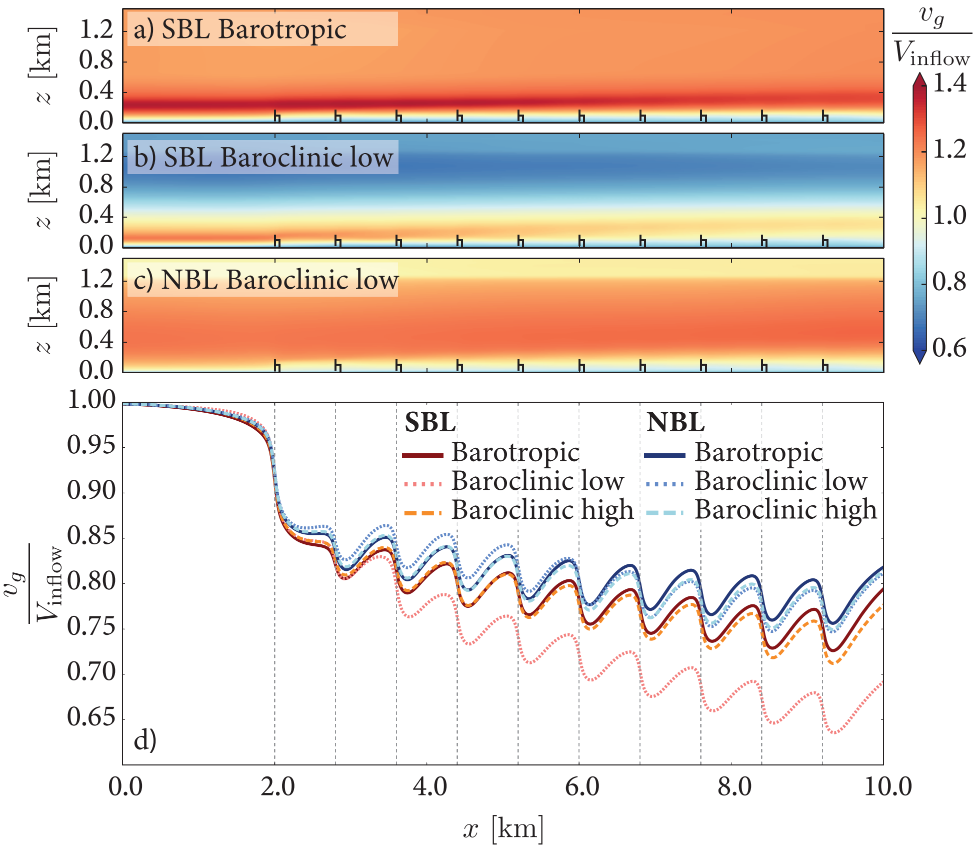

Figure 4.7 – Velocity, averaged over time and the spanwise extent of the wind farm. (a-c) Contour plots visualizing the height and strength of the LLJ. (d) Velocity at hub-height. Vertical dashed lines mark the positions of the turbines.

4.5 Energy budget analysis

To study how negative geostrophic wind shear affects entrainment fluxes and the power production of the turbines in the wind farm, we perform an energy budget analysis [23].

To obtain the total kinetic energy equation, the momentum equation 4.2 is first multiplied with u_i and then averaged over time. Subsequently, we integrate the resulting equation over a control volume to isolate the energy balance around each turbine row. We select control volumes V of size $s_x \times 5s_y \times D$ surrounding the center of each turbine row. The corresponding energy equation is given by:

$$
\begin{aligned}
\underbrace{\int_{\forall} \overline{f_i u_i} d\forall}_{\mathbb{P},\ \text{Turbine power}} &= \underbrace{\int_S \overline{u}_j \left(\frac{1}{2}\overline{u}_i \overline{u}_j + \frac{1}{2}\overline{u_i' u_j'} \right) dS_i}_{\mathbb{E}_{\mathrm{k}},\ \text{Kinetic energy flux}} + \underbrace{\int_S \left(\overline{u_i \tau_{ij}} \right) dS_i}_{\mathbb{T}_{\mathrm{sgs}},\ \text{SGS transport}} \\
&+ \underbrace{\int_S \left(\frac{1}{2}\overline{u_j' u_i' u_i'} + \frac{1}{2}\overline{u}_i \overline{u_i' u_j'} \right) dS_i}_{\mathbb{T}_{\mathrm{t}},\ \text{Turbulent transport}} + \underbrace{\int_S \left(\overline{p u_i} \right) dS_i}_{\mathbb{F},\ \text{Flow work}} \\
&- \underbrace{\int_{\forall} g\beta\delta_{i3} \left(\overline{u_i \theta} - \overline{u}_i \langle \theta \rangle \right) d\forall}_{\mathbb{B},\ \text{Buoyancy}} - \underbrace{\int_{\forall} \left(\overline{\tau_{ij} S_{ij}} \right) d\forall}_{\mathbb{D},\ \text{Dissipation}} \\
&- \underbrace{\int_{\forall} \left(f_c \overline{u}_i G_1 \delta_{i2} - f_c \overline{u}_i G_2 \delta_{i1} \right) d\forall}_{\mathbb{G},\ \text{Geostrophic forcing}} \\
&. \qquad (4.9)
\end{aligned}
$$

Here, $\mathbb{P}$ is the power production by a turbine row, and $\mathbb{E}_{\mathrm{k}}$ is the mean-flow transport of kinetic energy, including the mean-flow and resolved turbulent kinetic energy. $\mathbb{T}_{\mathrm{t}}$ and $\mathbb{T}_{\mathrm{sgs}}$ are the transport of momentum by resolved and SGS turbulent fluxes, respectively. The transfer of energy due to pressure fluctuations is represented by $\mathbb{F}$, while $\mathbb{B}$ is the turbulence destruction or production due to buoyancy, and $\mathbb{G}$ is the mean geostrophic forcing.

Figure 4.8 shows the energy budget analysis for the (a) *SBL Barotropic* and (b) *SBL Baroclinic low* cases, normalized by the power produced by the first row of turbines. For brevity, this analysis is only shown for the two cases that reveal the effect most pronounceable. The trends for the other cases are similar to the *SBL Barotropic* case. $\mathbb{P}$, $\mathbb{D}$, $\mathbb{G}$ and $\mathbb{B}$ are energy sinks, while $\mathbb{E}_k$ and $\mathbb{T}_{\mathrm{t}}$ are energy sources.

Using an energy budget analysis for wind farms with an infinite lateral size in barotropic NBLs, Allaerts and Meyers [23] and Cortina et al. [188] have shown that the kinetic energy contribution $\mathbb{E}_{\mathrm{k}}$ is highest at the first row and shows a decreasing trend over the length of the farm since the turbines extract kinetic energy from the flow. Meanwhile, the turbulent transport $\mathbb{T}_t$ increases as turbulent wakes form and interact behind the turbines. In figure 4.8 we observe the same trend and show, that for the *SBL Barotropic* case the turbulent transport $\mathbb{T}_{\mathrm{t}}$ becomes the dominant contribution, rather than $\mathbb{E}_{\mathrm{k}}$, starting from the fourth row. However, this transition takes place further downstream for the *SBL Baroclinic low* case because the lower jet height limits

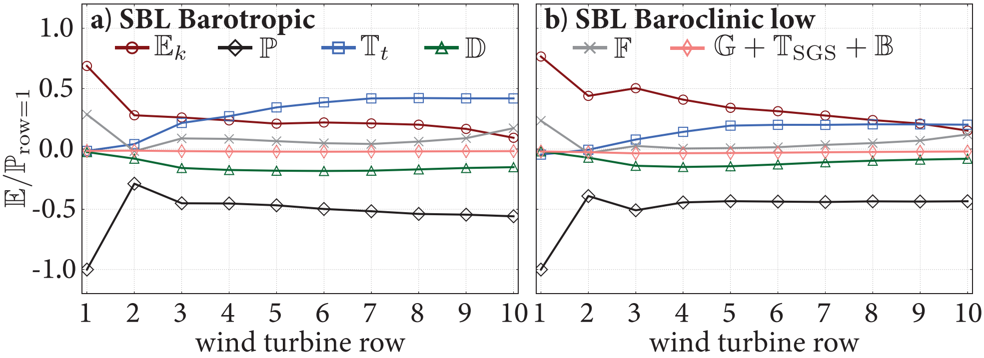

Figure 4.8 – Energy budget for the (a) *SBL Barotropic* and (b) *SBL Baroclinic low* cases, see table 4.1. All the terms are normalized by the power production of the first turbine row. The symbols in the legend are defined in equation 4.3.

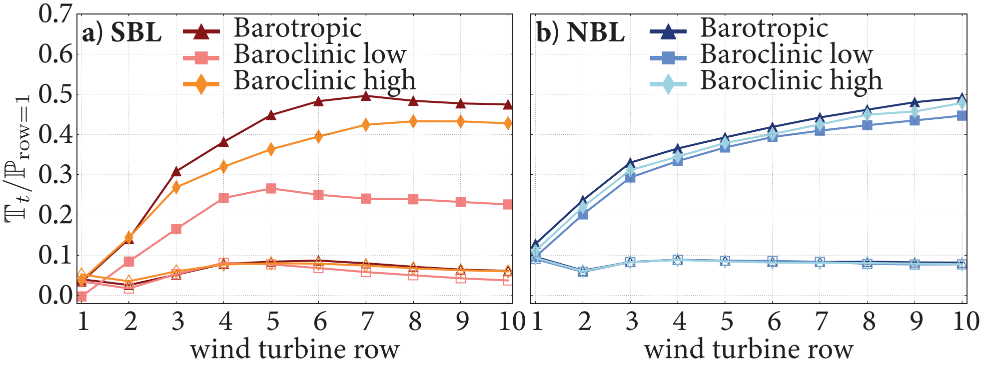

Figure 4.9 – Integrated entrainment flux over top and bottom planes of the control volume. Lines with filled and open symbols represent $\mathbb{T}_t$ on the top and bottom plane, respectively.

the energy entrainment into the wind farm. Abkar and Porté-Agel [206] and Cortina et al. [188] have shown that the transition point, at which $\mathbb{T}_\mathrm{t}$ starts exceeding $\mathbb{E}_\mathrm{k}$, depends on the wind farm layout, while Abkar and Porté-Agel [206], Cortina et al. [15], Wu and Porté-Agel [24] and Gadde and Stevens [197] further showed that that the transition point also depends on the atmospheric stratification. Particularly, $\mathbb{T}_\mathrm{t}$ is higher for denser wind farms [14, 188, 206] and for lower atmospheric stability [15, 24, 197, 206]. Furthermore, Gadde and

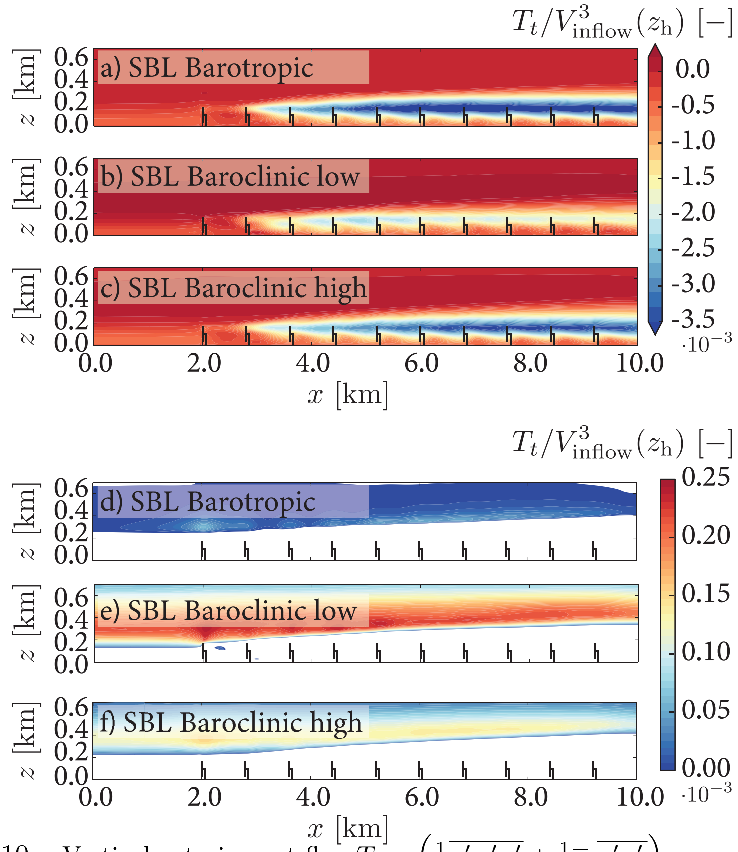

Figure 4.10 – Vertical entrainment flux $T_t = \left(\frac{1}{2}\overline{u_j' u_i' u_i'} + \frac{1}{2}\overline{u}_i\overline{u_i' u_j'}\right)$ averaged over the spanwise wind farm extent, normalized by the inflow velocity at hub-height. In panels (d-f) a different color map range than in (a-c) is used to visualize the positive flux above the jet. Regions with values outside the plotted range are shown in white.

Stevens [183] showed that $\mathbb{T}_\mathrm{t}$ is highly dependent on the height of the low-level jet. In the *SBL Baroclinic low* case, the lower jet height limits the energy entrainment into the wind farm and consequently the vertical energy transport from above only becomes dominant further downstream in the wind farm.

To demonstrate the reduced energy entrainment from above for the *SBL Baroclinic low* case, we show the integrated vertical entrainment flux through the top $(z_h + D/2)$ and bottom $(z_h - D/2)$ planes of the control volume in figure 4.9. In both SBL and NBL cases, the barotropic cases exhibit more entrainment from above than the baroclinic cases. The entrainment is smallest

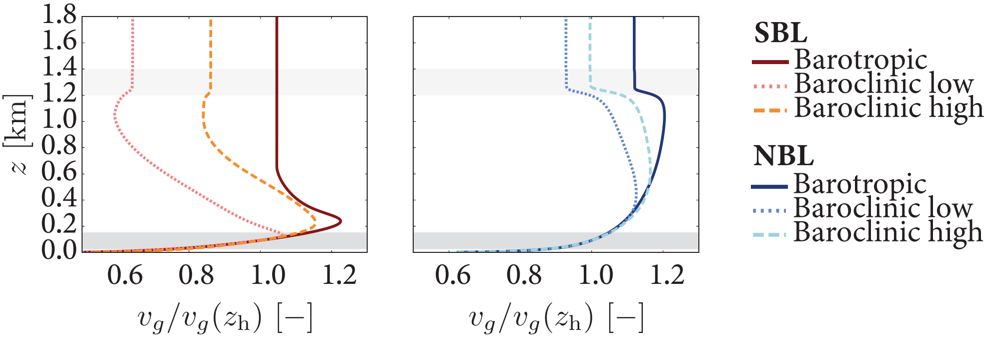

Figure 4.11 – Horizontal inflow velocity magnitude normalized by the velocity at hub-height.

for the *SBL Baroclinic low* case, where the LLJ is lowest and resides within the rotor swept area. The entrainment flux from below is much smaller than from above and almost unaffected by baroclinicity.

The decreased downward flux in the SBL baroclinic cases is also visualized in figure 4.10. The figure shows the vertical energy flux averaged over the spanwise wind farm extent, normalized by the inflow velocity at hub-height. The figure reveals that downward flux reaches higher elevations in the downstream direction, forming an internal boundary layer (IBL).

The reason for the lower entrainment from above in the baroclinic cases is two-fold: (i) The velocity above the turbines, relative to the velocity at hub-height, is higher for the barotropic case than for the baroclinic cases (see figure 4.11 in which we normalize the velocity by the hub-height velocity, the representative for power production of the first turbine ro). Consequently, there is relatively less momentum available for downward entrainment in baroclinic cases. (ii) The negative shear in the baroclinic cases gives rise to upward turbulent flux, which reduces the net energy entrainment into the wind farm. The reason is that the turbulence and shear profiles above the nose of the LLJ are different in the barotropic and baroclinic conditions, see figure 4.4a, b and f. The baroclinic cases have a larger negative shear above the wind maximum than the barotropic cases. The term $\overline{u'w'}\frac{\partial u}{\partial z}$ in the energy budget has to be negative to produce turbulence. For the baroclinic cases there is a large negative shear above the nose of the jet, i.e. $\frac{\partial u}{\partial z} < 0$, which results in a positive vertical entrainment flux aloft i.e. $\overline{u'w'} > 0$.

This upwards (positive) entrainment flux due to the negative shear is clearly visible in figure 4.10 (d-f). The highest upwards flux outside the IBL of the wind

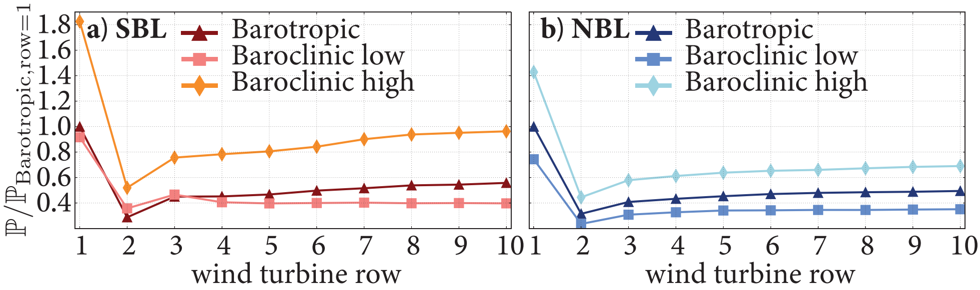

Figure 4.12 – The row-averaged power normalized with the barotropic case.

farm is observed for the *SBL Baroclinic low* case, while the vertical entrainment outside the IBL of the wind farm is negligible in the *SBL Barotropic case*.

In summary, the presence of a wind farm in the ABL creates a momentum deficit region and therefore causes a downward entrainment flux in the presence of positive mean shear in the ABL [12–14, 207]. However, the large negative shear created by the baroclinicity in the SBL counteracts this effect and therefore reduces the net entrainment downwards. The upward turbulent flux changes the momentum transfer from the jet and hinders downward energy entrainment into the wind farm.

We note that none of the cases considered in this study reaches a fully developed wind farm regime, where the statistical properties of the flow are constant along the streamwise direction such that the energy available at the wind turbine locations must be entrained entirely from the layers above [12–14, 16–18]. In contrast to infinitely wide wind farms considered in previous studies [12, 14, 16–18, 193], wind farms with a finite spanwise size (see also e.g. [108, 110, 190, 197, 208]) are expected to be influenced by entrainment from the sides due to the prevailing wind veer. Wu and Porté-Agel [24] and Allaerts and Meyers [23] assume that a fully developed region might not be reached in various atmospheric conditions even for large wind farms. However, Cortina et al. [188] states that the flow physics is very similar to the physics in fully developed regimes, once $\mathbb{T}_t$ dominates.

4.6 Wind farm power production

Figure 4.12 shows the power production normalized by the power production of its first row of the barotropic reference case. We observe that the total power

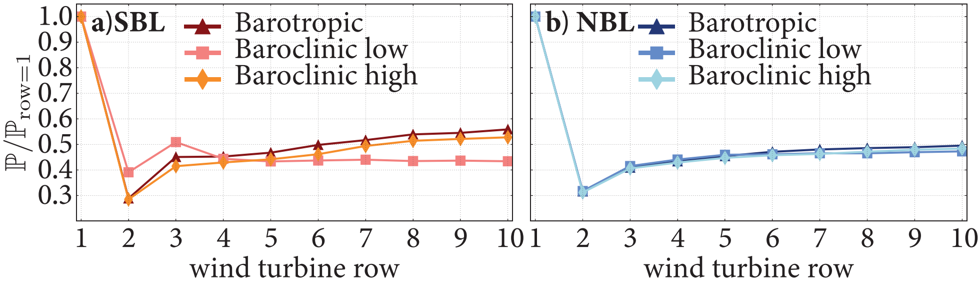

Figure 4.13 – The row-averaged power normalized with the power production of each first row.

production strongly depends on the baroclinicity. To be specific, the *Baroclinic high* cases have the same geostrophic wind at high elevations as the *Barotropic* cases. Here, baroclinicity leads to higher wind velocities at hub-height and consequently the highest power production. The *SBL Barotropic* case and the *SBL Baroclinic low* case have similar velocities at hub-height, as shown in table 4.2. However, the trend in power production is quite different, which will be discussed below. This figure highlights that baroclinicity alters the mean wind profile in the ABL and thereby affects the wind energy available for extraction by the turbines. Consequently, including baroclinicity effects in numerical and analytical models that are used to design wind farms is crucial to obtaining accurate performance predictions.

Figure 4.13 shows the wind farm power production, normalized by the power production of its first turbine row for the (a) SBL and (b) NBL cases. Behind the first row, the wind turbine wakes cause a strong drop in power production. The *SBL Baroclinic low* case has the highest normalized power production for the second and third rows. This is caused by the high kinetic energy of the LLJ, which resides at turbine rotor height in this case, as shown in figure 4.8b. Further downstream, the power production of the *SBL Baroclinic low* case is lowest due to the previously discussed lack of energy entrainment from above. The normalized power production of the *SBL Baroclinic high* case is slightly below the reference barotropic case. For the NBL cases (figure 4.13b), the effect of the negative geostrophic wind shear on the normalized power production is negligible. This is because the wind profile in the region directly above the wind farm is similar in the barotropic and baroclinic cases, see figure 4.11. Relevant differences in the available momentum above the wind farm are only observed above approximately 400m. Consequently, the entrainment into the wind farm is only slightly lower for the baroclinic cases than for the barotropic case (figure 4.9).

4.7 Conclusion

We performed LES to study the effects of negative shear baroclinicity on wind farm performance in stable and neutral ABLs. We find that even modest negative geostrophic wind shear of 3 m s^{-1} $mathrmkm^{-1}$ with height can greatly alter wind farm power production, as geostrophic wind shear modifies the mean wind profile in the ABL significantly (see figures 3(a) and (e) and figure 4.11). For the *Baroclinic* cases considered in this study, which either had the same geostrophic wind velocity at the surface or the top of the domain as the *Barotropic* cases, the velocities at hub-height differed by up to 2.3 m/s. An increase in the geostrophic wind near the surface relative to barotropic conditions can significantly increase the velocity at hub-height and, consequently, the absolute power production of a wind farm (the *Baroclinic high* cases). Meanwhile, a reduction of the geostrophic wind aloft with respect to barotropic conditions can lower the LLJ to turbine height (the *SBL Baroclinic low* case). In that case, normalized power production increases for the first turbine rows, but decreases significantly for downstream rows, as less momentum is available above the wind farm for downward entrainment.

The negative geostrophic wind shear does not only alter the mean velocity profile, but also modifies turbulence in the ABL. To be specific, the negative geostrophic wind shear increases turbulence and vertical momentum fluxes at higher altitudes. Typically, additional turbulence aloft is considered beneficial for the performance of extended wind farms as it can aid wake recovery and entrainment. However, an energy budget analysis reveals that negative shear baroclinicity reduces entrainment into the wind farm. In fact, the negative shear creates a positive turbulent flux above the LLJ and causes an upward transport of momentum. This limits the entrainment of energy from the jet into the wind farm and ultimately hinders the performance of turbines further downstream in the wind farm.

The observed alterations of wind resources and turbulence in the ABL and resulting changes in wind farm power production indicate that baroclinicity should be considered in wind farm modeling and power production forecasts. Therefore, future studies are required to incorporate the effects of negative shear baroclinicity in analytical models. Furthermore, it will be important to investigate different forms of baroclinicity [172, 174], resulting from different alignment between pressure and temperature gradients. This includes positive shear, as well as thermal advection. Besides, it is important to note that there are no physical constraints on the relative orientation between ΔT and ΔP and ΔT might vary with height [172]. Consequently, it will be relevant to investigate the impact of non-linear changes in the magnitude of the geostrophic wind velocity with height and to consider the time-dependent geostrophic wind effect.

4.8 Appendix

Here, we show the time-averaged version of figure 4.5 to give a reference flow field in figure 4.14. The figure shows the time-averaged velocity at hub-height for the (a) *SBL Barotropic*, (b) *SBL Baroclinic low*, and (c) *NBL Baroclinic low* cases. Starting from the third turbine row, the velocity deficit in the *SBL Baroclinic low* case is higher than in the *SBL Barotropic* case. In addition to the phenomena discussed for the instantaneous flow field in figure 4.5, the turning of the wakes is clearly visible in both stable cases. The strongest wake turning (5°) is observed in the last turbine row for the *SBL Baroclinic low* cases. For the *NBL Baroclinic low*, the wind veer is less, namely 1.5° in front of the last row.

To verify that the fixed orientation of the rotor heads perpendicular to the x-direction in our simulations do not affect our findings, we performed simulations on a coarse grid with a resolution of $\Delta x = 24$ m, $\Delta y = 15$ m, $\Delta z = 5$ m using actuator disks, for the stable cases. Figure 4.15 shows the power production for the stable cases: 1. the rotor heads are oriented perpendicular to the x-direction, and 2. the rotor heads are oriented perpendicular to the local flow angle. The difference in total power production between the two cases is small ($\langle\overline{P}\rangle_{\mathrm{tot,local-angle}}/\langle\overline{P}\rangle_{\mathrm{tot,x-aligned}} \leq 2.5\%$) and, most importantly, the same trends were observed when comparing baroclinic and barotropic cases.

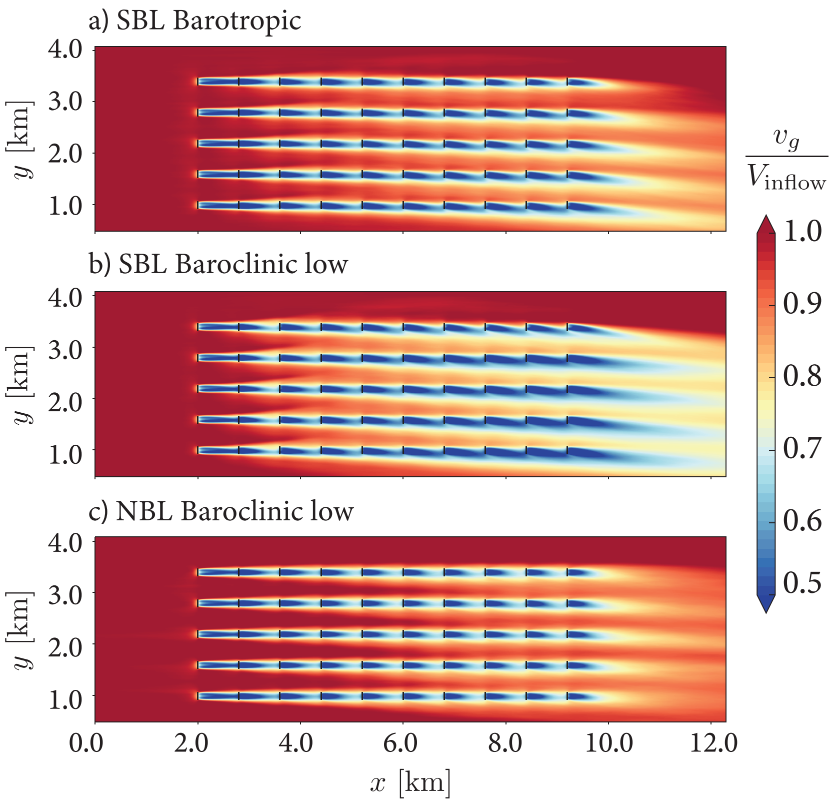

Figure 4.14 – Time-averaged velocity at hub-height. Black lines indicate the turbine positions.

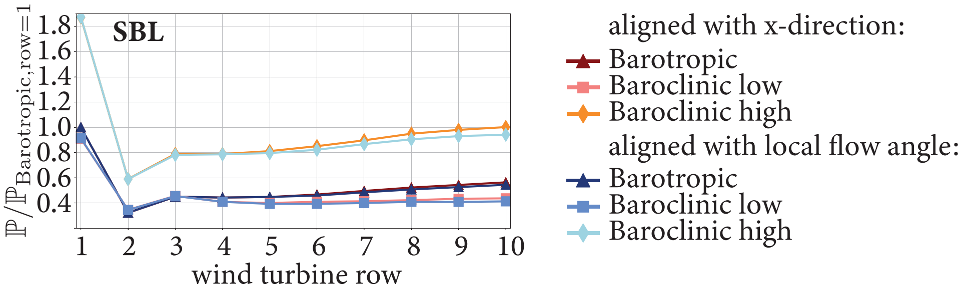

Figure 4.15 – The row-averaged power normalized with the barotropic case where the orientation of the rotor heads is perpendicular to the x-direction and perpendicular to the local flow angle. These simulation were performed on a coarse grid with a resolution of $\Delta x = 24$ m, $\Delta y = 15$ m, $\Delta z = 5$ m using actuator disks.

Part II

Wind farm wakes

5

Evaluating wind farm wakes in large-eddy simulations and engineering models[1]

We study wind farm wakes with large-eddy simulations (LES) and use these results for the evaluation of engineering models such as the Jensen model, the coupled wake boundary layer model (CWBL), the Turbulence Optimized Park model (TurbOPark), and the wind farm model developed by Niayifar and Porté-Agel (Energies 9, 741 (2016)). We study how well these models capture the wake effects between two aligned wind farms with 72 turbines separated by 10 kilometers in a neutral boundary layer. We find that all considered models over-predict the wind farm wake recovery compared to what is observed in LES. The TurbOPark model predictions on the wind farm wake effect are closest to the LES results for the scenario considered here.

---

[1] Adapted from publication: **Anja Stieren** and Richard J. A. M. Stevens, *Evaluating wind farm wakes in large eddy simulations and engineering models*, J. Phys. Conf. Ser., 1934:012018. (2021), doi: 10.1088/1742-6596/1934/1/012018.

5.1 Introduction

Due to the increasing number of offshore wind farms, studies of low-velocity zones far downstream of wind farms, also known as wind farm wakes, are of utmost importance [209]. Measurements of these wakes are performed with diverse methods such as Synthetic Aperture Radar (SAR) [210–214], Doppler radar [214, 215], Laser Imaging Detection And Ranging (LIDAR) [34], research air-crafts [216–219], and supervisory control and data acquisition (SCADA) power data [220]. Long-distance wind farm wakes have been observed up to 55 km in stable atmospheric conditions, up to 35 km in neutral conditions, and up to 10 km in unstable conditions [34]. Additionally, Reynolds-averaged Navier–Stokes solver (RANS) [221], large-eddy simulation (LES) [222], and Weather Research and Forecasting (WRF) simulations [34, 218] have shown that wind farms can influence each other. As a consequence, long-distance wakes behind wind farms have to be considered when planning new farms in the vicinity of existing ones.

Engineering models are widely used in this planning process. Their main advantage is that they are computationally efficient and can evaluate a wide range of possible scenarios. Due to these advantages, various wake models are continuously developed [6, 49]. The most simple wake model goes back to Jensen [223] who assumed a linear wake growth. More recent wake models consider more details, e.g. the model of Bastankhah and Porté-Agel [224] relies on the conservation of mass and momentum and predicts a more realistic Gaussian wake shape. Furthermore, different superposition methods have been proposed to account for wake interactions. These interactions are modeled by considering either a linear superposition of the velocity deficits [225, 226] or a linear superposition of the energy deficits [227, 228]. Besides, one can consider the wake deficit with respect to the incoming upstream wind speed [225, 227], or with respect to the incoming flow speed for that turbine [226, 228].

While these models are extensively tested for wind farms, the ability of these models to accurately capture the interaction between different wind farms is still relatively unknown. Hansen et al. [220] compared the wind farm wake effects predicted by engineering models with SCADA data, the WRF mesoscale model, and computational fluid dynamics models and highlighted the necessity of further investigations to achieve more robust predictions. Recently, Nygaard et al. [28] introduced the Turbulence Optimized Park (TurbOPark) model that is designed to model the interaction between wind farms. The TurbOPark model combines the Jensen [223] and the Katić et al. [227] superposition method, often referred to as the Park model, and improves on this modeling approach by accounting for the turbulence intensity in the wind farm as described by the model by Frandsen et al. [229]. Nygaard et al. [28] found that the wind farm power output predicted by TurbOPark agrees favorably with SCADA data for the neighboring offshore wind farms Humber Gateway and Westernmost Rough.

In this work, we compare the predictions by the Jensen model, the TurbOPark model, the coupled wake boundary layer (CWBL) model, and the model developed by Niayifar and Porté-Agel [226] for the wind farm wake development against results from a reference LES. In the LES we consider two aligned wind farms with 72 turbines that are separated by 10 km. In the remainder of this chapter, we first summarize the different engineering models and the LES. Subsequently, we present the comparison between the LES results and model predictions before discussing the conclusions.

5.2 Engineering models

5.2.1 Jensen model

The Jensen model [223] is a simple, classical wake model. The fundamental assumption of the model is that the width of the wake behind a wind turbine increases linearly with the downstream distance. Following Jensen [223] the velocity u_w in the wake of a turbine is expressed by:

$$u_w(x') = u_\infty \left[1 - \frac{D^2}{D_w(x')^2}\left(1 - \sqrt{1 - C_T}\right)\right]. \tag{5.1}$$

Here u_∞ is the incoming free stream velocity, and x' is the downstream distance with respect to the turbine. The turbines are assumed to be actuator disks with a rotor diameter D and the thrust coefficient $C_T = 4a(1-a)$ with the induction factor a. The wake diameter growth rate D_w is assumed to be linear:

$$D_w(x') = D + 2k_w x', \tag{5.2}$$

where

$$k_w = \frac{\kappa}{\ln(z_{\text{hub}}/z_0)} \tag{5.3}$$

is the wake expansion coefficient estimated based on the logarithmic wind profile. Here z_0 is the surface roughness, z_{hub} the turbine hub-height and κ the von Kármán constant [230].

To account for the wake interactions the Jensen model [223] is combined with the Katić et al. [227] superposition model, which sums up the squared velocity deficits [227], i.e.

$$u(x,y) = u_\infty - \sqrt{\sum_i \left(u_\infty - u_w^i(x,y)\right)^2}. \tag{5.4}$$

Here the summation i is over all turbine wakes at that location. The power of each turbine P_T, normalized by the power of the turbines in first row P_1, is estimated as

$$\frac{P_T}{P_1} = \left(\frac{\langle u(x_T)\rangle_{\text{disk}}}{u_\infty}\right)^3, \tag{5.5}$$

where the brackets $\langle\ \rangle$ stand for an average over the turbine disk and x_T is the turbine position.

5.2.2 Coupled wake boundary layer model

The Jensen model is one of the so-called *bottom-up* models in which wake deficits are combined using some superposition model to account for the wake interactions. The CWBL model [145, 231] suggests to improve the Jensen model by coupling it to the Calaf et al. [12] *top-down* model such that the predictions from the Jensen and the *top-down* model are consistent in the fully developed regime of the wind farm. The *top-down* model parameterizes the wind farm, instead of the individual turbines, using an increased surface roughness $z_{0,\text{hi}}$. This model is based on the assumption of two constant momentum flux layers, one above the turbine hub-height and one below. Each has a characteristic friction velocity and surface roughness, such that the velocity at hub-height is given as

$$\frac{\langle \overline{u}(z_{\text{hub}})\rangle}{\langle \overline{u}_\infty(z_{\text{hub}})\rangle} = \frac{\ln(\delta_{\text{IBL}}/z_0)}{\ln(\delta_{\text{IBL}}/z_{0,\text{hi}})} \ln\left[\left(\frac{z_{\text{hub}}}{z_{0,\text{hi}}}\right)\left(1+\frac{D}{2z_{\text{hub}}}\right)^{\gamma}\right]\left[\ln\left(\frac{z_{\text{hub}}}{z_0}\right)\right]^{-1}, \tag{5.6}$$

where δ_{IBL} is the height of the internal boundary layer in the fully developed regime of the wind farm, $\gamma = \nu_w^*/(1+\nu_w^*)$ and $\nu_w^* \approx 28\sqrt{\pi C_T/(8 w_f s_x s_y)}$. Here w_f indicates the effective wake area coverage in the fully developed regime of the wind farm. The roughness length of the wind farm is defined as:

$$\begin{aligned} z_{0,\mathrm{hi}} =& z_{\mathrm{hub}} \cdot \left(1+\frac{D}{2z_{\mathrm{hub}}}\right)^{\gamma} \\ & \cdot \exp\left(-\left[\frac{\pi C_T}{8 w_f s_x s_y \kappa^2} + \left(\ln\left[\frac{z_{\mathrm{hub}}}{z_0}\left(1-\frac{D}{2z_{\mathrm{hub}}}\right)^{\gamma}\right]\right)^{-2}\right]^{-1/2}\right). \end{aligned} \quad (5.7)$$

The value of w_f and the value of the wake coefficient in the fully developed regime of the wind farm $k_{w,\infty}$ are determined and updated iteratively until the turbine velocity in the fully developed regime of the wind farm is the same (up to a tolerance of 0.1%) in the Jensen (equation (5.4)) and the *top-down* model (equation (5.6)). The effects of the entrance region of the wind-farm are considered by assigning a wake coefficient to the wake originating from each individual turbine:

$$k_{w,T} = k_{w,\infty} + (k_w - k_{w,\infty}) \exp\left(-\zeta m\right), \quad (5.8)$$

where m is the number of turbine wakes that overlaps with the turbine of interest and $\zeta = 1$ is determined empirically. k_w is the wake expansion coefficient in the entrance region of the wind farm, see equation (5.3). For further details we refer to Stevens et al. [145].

5.2.3 Turbulence Optimized Park model

Nygaard et al. [28] extended the Park model based on the idea that the wake expansion rate is dependent on turbulence intensity. To estimate the turbulence intensity behind a wind turbine, the sum of the ambient turbulence intensity I_∞ and the wake added turbulence I_w is considered:

$$I(x') = \sqrt{I_\infty^2 + I_w^2(x')}, \quad (5.9)$$

$$I_w(x') = \frac{1}{c_1 + c_2 \frac{x'/D}{\sqrt{C_T}}}. \quad (5.10)$$

The wake added turbulence is described empirically with the constants $c_1 = 1.5$ and $c_2 = 0.8$ [232]. Assuming that the wake diameter growth rate increases linearly with the turbulence intensity $dD_w(x')/dx' = AI(x')$, results in the following wake expansion rate:

$$D_w(x') = D + \frac{AI_\infty D}{\beta}\left(\sqrt{(\alpha+\beta x'/D)^2+1} - \sqrt{1+\alpha^2} - \ln\left[\frac{\left(\sqrt{(\alpha+\beta x'/D)^2+1}+1\right)\alpha}{\left(\sqrt{1+\alpha^2}+1\right)(\alpha+\beta x'/D)}\right]\right) \tag{5.11}$$

with $\alpha = c_1 I_\infty$ and $\beta = c_2 I_\infty/\sqrt{C_T}$ and the model calibration constant $A = 0.6$ [28]. TurbOPark incorporates equation (5.11) into the calculation of the wake deficit in equation (5.2). Further, a prefactor u_0/u_∞ is added in front of the $\sqrt{1-C_T}$ term in equation (5.1) to take the normalized rotor-averaged inflow wind speed at each turbine position into account. Nygaard et al. [28] set the turbine thrust coefficient based on the velocity at the turbine, which is calculated iteratively based on the wakes induced by upstream turbines and the induced wind farm blockage. This effect is neglected here as the reference LES considers a constant value for C_T. We note that Nygaard et al. [28] couple TurbOPark with a wind farm blockage model [28], which is not considered here.

5

5.2.4 Niayifar and Porté-Agel (2016) model

Based on the assumption of a wake velocity deficit with an axisymmetric, self-similar Gaussian shape and using conservation of mass and momentum, Bastankhah and Porté-Agel [224] describe the velocity in a wake as

$$u_w(x',y') = u_0\left[1 - \left(1 - \sqrt{1 - \frac{C_T D^2}{8\sigma(x')^2}}\right)\exp\left(-\frac{y'^2}{2\sigma(x')^2}\right)\right]. \tag{5.12}$$

Here u_0 is the local average inflow velocity in front of each turbine [233], which is different from u_∞ in equations (5.1) and (5.4). y' is the spanwise distance with respect to the turbine center. The standard deviation of the Gaussian velocity deficit is:

$$\sigma(x') = k_w^*(x')x + 0.2D\sqrt{b} \tag{5.13}$$

with $b = \frac{1+\sqrt{1-C_T}}{2\sqrt{1-C_T}}$. The growth rate $k_w^*(x')$ is linked to the turbulence intensity by the empirical expression [226]:

$$k_w^*(x') = 0.3837 \cdot I(x') + 0.003678. \tag{5.14}$$

The turbulence intensity is determined using equation (5.9) in combination with the empirical model for the added turbulence intensity proposed by Crespo and Hernández [234]:

$$I_w(x') = 0.73 a^{0.8325} I_\infty^{0.0325} \left(\frac{x'}{D}\right)^{-0.32}. \tag{5.15}$$

Note that equation (5.15) is only valid in the range $0.065 < I_\infty < 0.14$, $5 < x'/D < 15$ and $0.1 < a < 0.4$ [234]. Further, Niayifar and Porté-Agel [226] only consider the turbulence intensity from the closest upstream turbine, i.e. the wake added streamwise turbulence intensity at turbine j is given by the maximum of the added streamwise turbulence intensity induced by turbine k at turbine j: $I_{w_j} = \max\left(I_{w_{kj}} \cdot 4A_w/\pi D^2\right)$. Here A_w indicates the intersection between the wake and the rotor area. We note that the wake velocity (equation (5.12)) is only defined starting from approximately two rotor diameters downstream of each turbine [224]. Considering that the inter-turbine distance in a wind farm is typically much larger this does not affect the model applicability. In contrast to the previous models the wake interaction is modeled as [226]:

$$u(x,y) = u_\infty - \sum_i \left(u_0 - u_w^i(x,y)\right). \tag{5.16}$$

Different from Katić et al. [227] (equation (5.4)), Niayifar and Porté-Agel [226] consider the local mean inflow velocity u_0 in front of each turbine instead of the velocity in front of the farm u_∞. Furthermore, this method considers a linear superposition of velocity deficit instead of a linear superposition of the energy deficit [227].

5.3 Large-eddy simulations

We perform LES of a neutral atmospheric boundary layer (ABL) flow driven by a geostrophic wind. The LES data is used as a reference to evaluate the ability of the various engineering models to capture the development of the wind farm wake. The used LES code is an updated version of the code developed by Albertson and Parlange [143]. The governing equations are the filtered, incompressible continuity and Navier-Stokes equations:

$$\partial_i \tilde{u}_i = 0, \tag{5.17}$$

$$\partial_t \tilde{u}_i + \partial_j \left(\tilde{u}_i \tilde{u}_j\right) = -\partial_i \tilde{p}^* - \partial_j \tau_{ij} - \epsilon_{ijk} f_{c,j} (\tilde{u}_k - G_k) + f_i \tag{5.18}$$

Here the tilde represents spatial filtering with a spectral cut-off filter at the LES grid-scale Δ and $\tilde{u}_i$ represents the filtered velocity field components. $\tau_{ij} = \widetilde{u_i u_j} - \tilde{u}_i\tilde{u}_j$ is the trace-less part of the sub-grid scale (SGS) stress tensor and it is modeled with the anisotropic minimum dissipation model [77] with a Pointcaré constant of $C_i = 1/12$ in horizontal and $C_i = 1/3$ in vertical directions. The trace of the SGS stress tensor is absorbed into the filtered modified pressure $\tilde{p}^+ = \tilde{p}/\rho - p_\infty/\rho + \tau_{kk}/3$. The Coriolis parameter is given by $f_c = (0, 2\Omega\mathrm{cos}(\Phi), 2\Omega\mathrm{sin}(\Phi))$ with the Earth's rotation angular speed $\Omega = 7.3{\cdot}10^{-5}$ rad/s and the latitude $\Phi = 52°$. G is the geostrophic wind velocity with a magnitude of $|G| = 11$ m/s. The effect of the wind turbines is added as a body force f_i using an actuator disk approach [12]. Effects of resolved viscous stresses are neglected, since a very high Reynolds number limit is assumed. The wall shear stress at the ground is modeled using the Monin-Obukhov similarity theory [63]. The boundary conditions at the top of the domain are zero vertical velocity and zero shear stress. Time integration is performed using a second-order accurate Adams-Bashforth scheme. Derivatives in the vertical direction are calculated using a second-order central finite difference scheme. In the horizontal directions a pseudo-spectral method is applied, and therefore a concurrent precursor inflow method is used to remove periodicity and generate the inlet ABL flow [138]. To ensure that the incoming wind direction at hub-height is aligned with the x-axis, we apply a proportional-integral controller [139, 140]. This simulation approach has recently been validated for various benchmark cases, see Gadde et al. [144], Gadde and Stevens [146], and Stieren et al. [153].

5.4 Computational setup

The computational domain has a size of $L_x = 54$ km, $L_y = 7.2$ km, and $L_z = 4$ km, in the streamwise, spanwise, and vertical direction, respectively. The domain is resolved on a grid with $1800 \times 480 \times 480$ nodes. This results in a resolution of $\Delta_x = 30$ and $\Delta_y = 15$ m in the streamwise and spanwise directions. A stretched grid with a constant $\Delta_z = 5$ m up to $z = 1.5$ km and larger grid cells above is employed. The fringe region in the concurrent precursor method is $\Delta x_{\mathrm{Fringe}} = 3$ km in streamwise direction and $\Delta y_{\mathrm{Fringe}} = 1$ km in spanwise direction. We use a surface roughness of $z_0 = 0.002$ m, which is a typical value for offshore conditions. We consider two aligned wind farms with 12×6 turbines. The inter turbine spacing is $s_x = 7D$ in streamwise and $s_y = 5D$ in spanwise direction. The first wind farm is positioned 7 km downstream of the inflow region, and the distance between the wind farms is 10 km. The turbines have a diameter of $D = 120$ m and a hub-height $z_{\text{hub}} = 100$m. The thrust coefficient is $C_T = 3/4$ and $a = 1/4$.

The boundary layer in the precursor domain of the LES reaches a quasi–steady state with a fully developed turbulent flow after 8.7 hours. Subsequently, the simulation in both domains is continued concurrently for two more hours before the statistics are collected in 5 additional hours. From the LES we obtain that the ambient turbulence intensity at hub-height is $I_\infty(z_{\text{hub}}) = \sigma_u/u_h = 9.02\%$. The internal boundary layer height (δ_{IBL}), based on the height where the time-averaged velocity is 99% of the incoming flow speed at that height, is about 700 meters at the end of the second wind farm. This height is used in the CWBL calculations. To conclude, we mention that all engineering model calculations are only performed at hub-height.

5.5 Results

Figure 5.1 shows the time-averaged velocity at hub-height obtained from the LES and the four engineering models under consideration. Figure 5.1(a) shows that the wakes of the individual turbines are distinguishable up to 6 km downstream of the wind farm. Further downstream, the individual wakes merge into a more homogeneously mixed wind farm wake. Similar observations have been made by synthetic aperture and dual-Doppler radar measurements [34, 215]. Further, these observations [34, 215] and the LES show that the wind farm wake does not expand much beyond the spanwise extent of the wind farm. We note that the spanwise variations in the wind farm wakes are caused by the streamwise elongated rolls in the ABL [235].

Figure 5.1(b-e) show that the various models qualitatively capture the trends that individual wakes can be observed up to a certain distance behind the farm, after which a more homogeneous wind farm wake is formed. Additionally, the figure reveals clear differences between the analytical models and the LES. A comparison of the different panels shows that the Jensen, CWBL, and Niayifar and Porté-Agel [226] models strongly overpredict the recovery rate of the wind farm wake. The Jensen model prediction gives a stronger wake deficit directly behind the wind farm, due to which the stronger wind farm wake recovery only becomes apparent further downstream of the wind farm. The TurbOPark model captures the wind farm wake recovery observed in the LES most accurately.

In figure 5.2 we show the velocity at hub-height, averaged over the spanwise

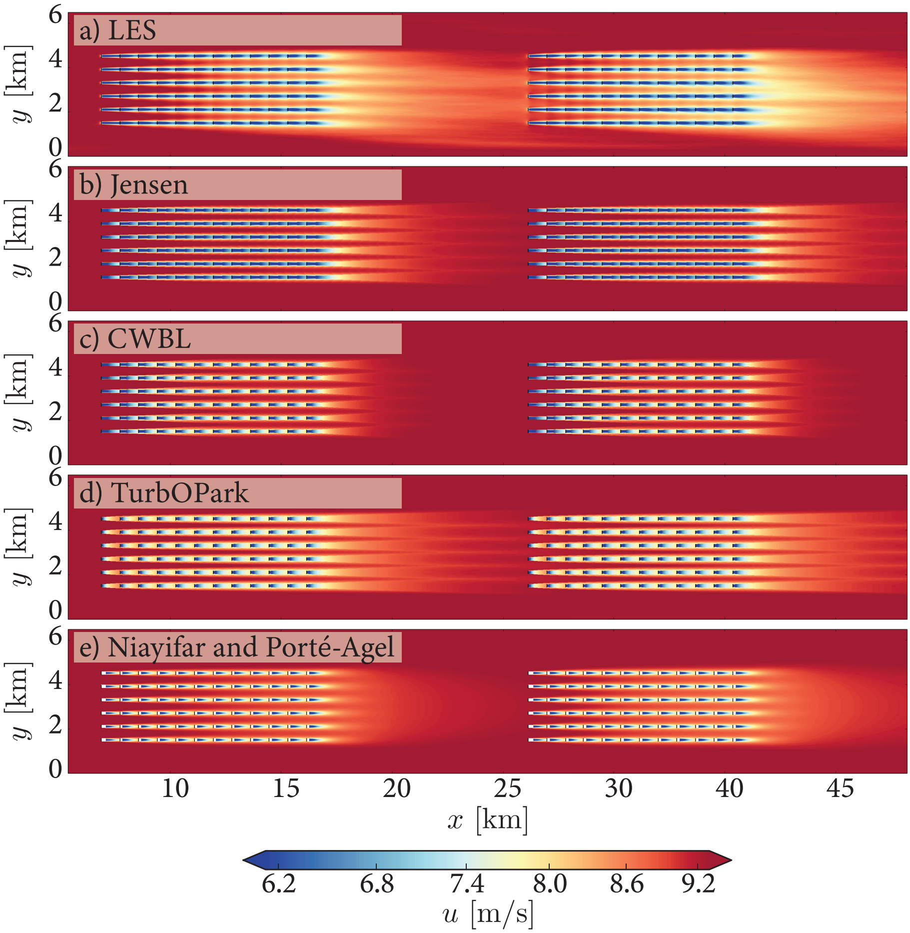

Figure 5.1 – Time-averaged streamwise velocity at hub-height from **a)** LES, **b)** Jensen, **c)** CWBL, **d)** TurbOPark, and **e)** the Niayifar and Porté-Agel [226] model. Please note that the white regions are a result of employed wake model, which is not defined in the region directly behind the turbine [226].

locations where the turbines are located. In agreement with the studies by Christiansen and Hasager [210] and Wu and Porté-Agel [24] the velocity deficit at 10 km downwind of the farm, i.e. where the second farm starts, is about 6% of the velocity in front of the first farm. Interestingly, the LES and the analytical models only show slightly lower velocities behind the second farm than in the wake of the first farm. Additionally, this figure shows that all considered models overestimate the recovery of the wind farm wake behind

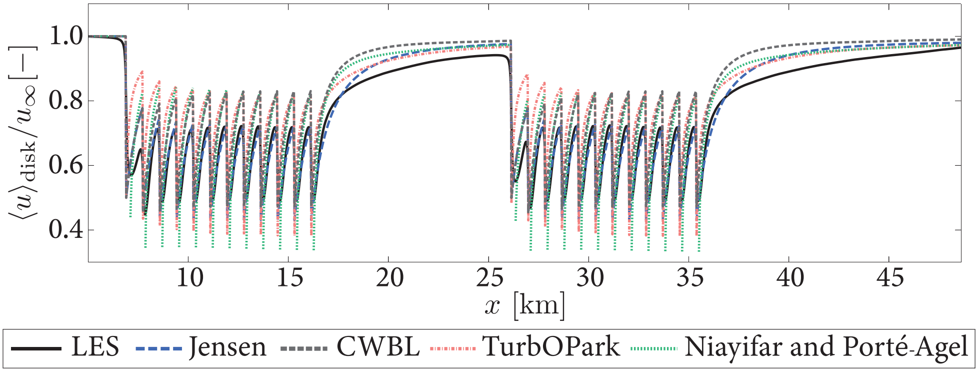

Figure 5.2 – Time-average streamwise velocity at hub-height averaged over the spanwise locations where the turbines are located.

both farms when compared to the LES. The Jensen model captures the wake deficit inside the wind farm reasonably accurately. As a result, the Jensen model estimates the wind farm wake quite well up to 1 km downstream of the wind farm, while it underestimates the wind farm wake further downstream. The other models overpredict the wake deficit inside the wind farm and consequently also overestimate the wind farm wake recovery. The TurbOPark model predictions for the wind farm wake recovery are closest to the LES results for the scenario considered here.

Figure 5.3 compares the wind turbine power output as a function of downstream position obtained from the models and LES for the first and second wind farm. The LES results in this figure reveal that the power output of the second farm's first row is about 14% lower than the power production of the first row of the first farm. In agreement with the wind farm wake recovery discussed above, all models significantly overestimate the production of the first row of the second farm. Particularly the reduction in power output of the second farm's first row compared to the power output of the first row of the first farm is about 9% for the TurbOPark model, 8% for the Niayifar and Porté-Agel [226], 7% for the Jensen and 4% for the CWBL model. Consequently, the TurbOPark model captures the effect of the wind farm wake most accurately. Furthermore, the Niayifar and Porté-Agel [226] model most accurately represents the power production as a function of downstream direction. However, in contrast to the CWBL and Niayifar and Porté-Agel [226] model, the TurbOPark overestimates the production in the entrance region of

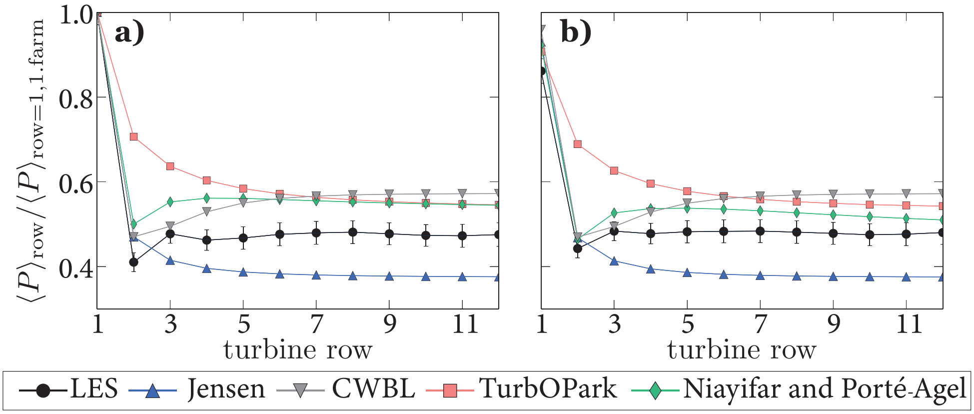

Figure 5.3 – Comparison of the power output as function of downstream direction obtained from the models for **a)** the first and **b)** the second wind farm. The results are normalized by the power production of the first row of the first farm. Error bars are the standard deviation of the power production per row over time.

the wind farm. Overall, the TurbOPark, CWBL, and Niayifar and Porté-Agel [226] model predictions are closer to the LES results than the Jensen model.

5.6 Conclusions

In this study, we performed LES of a wind farm cluster with two wind farms separated by 10 km and evaluated the performance of four engineering models taking the LES results as a reference. An important finding is that all considered models overestimate the wind farm wake recovery compared to what is observed in LES. From the models considered here, the TurbOPark model provides the best estimate for the recovery of the wind farm wake. However, it is essential to emphasize that more work is required to assess the performance and the capability of various engineering models to capture wind farm wake effects, as only one scenario is considered in this study.

6

Impact of wind farm wakes on flow structures in and around downstream wind farms[1]

We performed large-eddy simulations in a neutral atmospheric boundary layer (ABL) to study the interaction between two identical wind farms with 72 turbines each. We demonstrate that the wind farm wake created by the upstream farm affects the entire flow in and around the downstream farm. The vertical entrainment fluxes above the downstream wind farm are strengthened, resulting in a faster wind farm wake recovery behind the downstream farm. These findings illustrate that interaction between extended wind farms affects flow structures beyond the wind farm scale. Furthermore, we demonstrate that wind farm wakes can reduce the power production of turbines throughout the downstream wind farms. We additionally observe that a staggered wind farm extracts more energy from the flow and thus creates a stronger wind farm wake than an aligned wind farm.

---

[1] Adapted from publication: **Anja Stieren** and Richard J. A. M. Stevens, *Impact of wind farm wakes on flow structures in and around downstream wind farms*, Flow, 2, E21, (2022), doi: 10.1017/flo.2022.15.

6.1 Introduction

The number of wind farms is increasing due to the growing demand for renewable energy. In 2020 the total installed capacity in Europe was 220 GW, and an additional 105 GW is expected in the coming five years [236]. Especially in offshore regions, wind farms are often clustered as the space in shallow water depths is limited [218, 221]. Furthermore, the transport of the generated electricity is facilitated by clustering wind turbines. However, closely spaced wind farms negatively affect each other's performance as wind farm wakes, i.e. regions of velocity deficit and increased turbulence intensity, have been observed to persists far downstream wind farms [34, 237]. The wind farm wake development depends on the prevailing atmospheric conditions, as well as the size and layout of the wind farm [34, 194, 218, 221, 238], such that our fundamental understanding of wind farm wakes is still limited and is not well captured in wind farm design and siting tools [6, 239]. This emphasizes the importance of studying the impact of wind farm wakes on downstream wind farms.

To study long-distance wakes behind wind farms, measurements or numerical simulations need to cover a large spatial area. As an example, wind farm wakes have been observed with satellite synthetic aperture radar (SAR) measurements [210, 211, 213, 214]. Recently, Schneemann et al. [34] used SAR measurements to detect wind farm wakes up to 55 km downstream of a wind farm cluster with more than 250 turbines in a stably stratified atmosphere. The average velocity deficit 55 km downstream of the cluster was observed to be 21% with clear transition regions separating wake and free flow. Wind farm wakes are longer in stable atmospheric conditions for which the turbulence intensity is low. In neutral and especially unstable conditions, the turbulence intensity is higher, such that the wake recovery is faster [34, 237]. SAR observations by Christiansen and Hasager [210] of wind farms with up to 80 wind turbines report an average velocity deficit of 2% at a downstream distance of 5 km for unstable and of 20 km for near-neutral conditions. The differences compared to the study of Schneemann et al. [34] suggest that the atmospheric conditions and the wind farm layout influence the recovery rate of wind farm wakes. This hypothesis was confirmed by Platis et al. [218] who used airborne data to study long-distance wakes [216, 218]. For wind farms with different layouts and sizes in the North sea, they reveal that a smaller inter-turbine spacing results in a lower velocity directly behind the wind farm and an increased wake length.

In contrast to field measurements, numerical simulations make it possible to study the flow under well-controlled and reproducible conditions. Simulations allow for a better physical understanding of the development of wind farm wakes and how atmospheric flow conditions affect this process. The study of wind farm wakes and their influence on downstream positioned wind farms requires large numerical domains. Consequently, simulations of the interaction between large-scale wind farms have primarily been performed in mesoscale models using wind farm parameterizations [119, 240]. Lundquist et al. [209] used mesoscale simulations to show that wind farm wakes can have a significant impact on the performance of downstream farms. Additionally, Lundquist et al. [209] compared predicted and actual capacity factors of situations with and without wind farm wake effects to show the economic consequences of wake effects. Recently, Akhtar et al. [241] applied mesoscale simulations to analyze the annual wind speed variations in the North Sea over ten years. They conclude that wind farm wake effects can reduce the capacity factor by about 20% when wind farms are placed within 7 km of each other.

Mesoscale simulations and Reynolds-averaged Navier–Stokes (RANS) are often used to validate and optimize engineering models [218]. Examples of engineering models used to model wind farm wakes can be found in Emeis [242], Nygaard et al. [28], Stieren and Stevens [239], and Cañadillas et al. [237]. However, the horizontal resolution in mesoscale simulations is often larger than the wind turbine diameter [112–115], and smaller domain sizes are required to obtain finer resolution. RANS simulations have been used to study the wake behind wind farms and the interaction between wind farms, revealing the importance of the Coriolis force on the relevant scales for wind farm interaction [205, 220, 243]. In contrast to RANS and mesoscale simulations, more detailed large-eddy simulations (LES) capture temporal fluctuations and resolve large-scale flow features in an atmospheric boundary layer (ABL), while the small-scale turbulence is parameterized using a sub-grid scale model. LES have been shown to accurately capture wind turbine wake interaction in an unsteady anisotropic turbulent atmosphere. However, due to high computational cost, most LES have focused on individual wind turbines or wind farms, not the interaction between wind farms [6, 49]. Recently, Maas and Raasch [194] performed LES to study wind farm wakes in the German Bight. They observe that wind farm wakes are longer when the ABL is lower or when the inter turbine spacing in the farm is smaller. They find that, depending on the atmospheric conditions, the velocity deficit of the wind farm wake can be observed up to 100 km behind the wind farm, while the enhanced turbulence intensity can be observed up to 20 km downstream.

Here, we use LES to study the impact of a wind farm wake on a downstream wind farm. For this purpose, we perform LES and systematically increase the distance between two identical wind farms, each consisting of 72 wind turbines. Representative for existing and planned wind farm clusters in the North Sea, the distance between the wind farms is varied between 5 and 15 km [194, 237]. We note that these distances also correspond to the optimal wind farm spacing of 4 to 14 km suggested by Frandsen et al. [244]. Considering two identical wind farms allows us to directly compare the power production of turbines in the first and downstream wind farm. Only in this way we can study the impact of the wind farm wake on the power production of turbines in the downstream wind farm. Furthermore, we study the impact of the wind farm layout on the interaction between wind farms by considering aligned and staggered wind farms. This allows us to show, in agreement with previous studies [218], that the observed interaction between wind farms depends on the wind farm layout. The simulations are performed for neutral ABL conditions driven by a geostrophic wind. Such an ABL configuration is representative for cloudy days, near sunset or sunrise, and for ABLs formed offshore [245]. The remainder of this chapter is structured as follows. In section 6.2 we introduce the LES modeling framework and the considered wind farm layout. In section 6.3 we present the results, and the conclusions are discussed in section 6.4.

6.2 Large-eddy simulations

The simulations are performed using the LES code initially developed by Albertson and Parlange [143], which is continuously updated and tested [144, 153]. The governing equations are the filtered continuity equation and momentum-conservation equation:

$$\partial_i \tilde{u}_i = 0, \tag{6.1}$$

$$\partial_t \tilde{u}_i + \partial_j \left(\tilde{u}_i \tilde{u}_j \right) = -\partial_i \tilde{p}^* - \partial_j \tau_{ij} - \epsilon_{ijk} f_{c,j} (\tilde{u}_k - G_k) + \tilde{f}_i \tag{6.2}$$

where u is the velocity and $i = 1, 2, 3$ correspond to the streamwise (x,u), spanwise (y,v), and vertical (z,w) direction and component, respectively. The tilde indicates that a filtered velocity field is considered, and δ_{ij} is the Kronecker delta. The viscous stresses are neglected as we consider very high Reynolds number atmospheric flow, and the sub-grid stresses (SGS) are modeled through $\tau_{ij} = \widetilde{u_i u_j} - \tilde{u}_i \tilde{u}_j$. The trace of the SGS stress tensor is absorbed into the filtered modified pressure $\tilde{p}^* = \tilde{p}/\rho_0 - p_\infty/\rho_0 + \tau_{kk}/3$, where $\tilde{p}$ is the pressure and ρ_0 is the air density. The SGS deviatoric stress is modeled using the anisotropic minimum dissipation model [77] with a Pointcaré constant of $C_i = 1/\sqrt{12}$ in horizontal and $C_i = 1/\sqrt{3}$ in vertical direction, respectively. A mean pressure gradient $\partial_i p_\infty$, which is related to the geostrophic wind velocity as $G_i = -\epsilon_{ij3}\partial_j p_\infty / \left(\rho_0 f_c\right)$, drives the flow in the ABL (ϵ_{ijk} denotes the alternating unit tensor). The Coriolis parameter is given by $f_c = (0, 2\Omega\text{cos}(\Phi), 2\Omega\text{sin}(\Phi))$ with the rotation angular speed Ω and latitude Φ.

The wind turbines are modeled as actuator disks [12]. The thrust force exerted by a wind turbine on the flow is approximated as:

$$F_t = -\frac{1}{8}\rho_0 C_T' \langle \overline{u}^T \rangle^2_{\text{disk}} \pi D^2 \tag{6.3}$$

where $\left\langle \overline{u}^T \right\rangle_{\text{disk}}$ is the disk-averaged velocity and $C_T' = C_T/(1-a)^2$ includes the thrust coefficient $C_T = 0.75$ and the induction factor $a = 0.25$. The streamwise and spanwise components of the turbine force are included in equation 6.2 as $\tilde{f}_1 = F_t\text{cos}\phi$ and $\tilde{f}_2 = F_t\text{sin}\phi$ with the angle ϕ between actuator disk and x-axis. Wu and Porté-Agel [56] demonstrated that the actuator disk model provides an adequate representation of the overall wake structure behind the wind turbines starting from three diameters downstream of the turbine. This agreement was confirmed by Stevens et al. [60], who validated the actuator disk model and actuator line model against experimental data. Here, we also use the actuator disk model correction factor introduced by Shapiro et al. [59]. Therefore, the actuator disk model is considered to be sufficiently accurate to capture the large-scale flow phenomena studied here.

Time integration is performed using a second-order accurate Adams-Bashforth scheme. Derivatives in the vertical direction are calculated using a second-order central finite difference scheme, and in the horizontal directions a pseudo-spectral method is applied. The computational domain is discretized with n_x, n_y, and n_z points in streamwise, spanwise, and vertical directions. The grid sizes in horizontal direction are $\Delta_x = L_x/n_x$, $\Delta_y = L_y/n_y$, where L_x and L_y are the dimensions of the computational domain. The computational grid is vertically staggered such that the first vertical velocity plane is located at the ground and the first grid point for u, v, and θ is located at $z/2$. No-slip and free-slip boundary conditions with zero vertical velocity are used at the top and bottom boundaries, respectively. The wall shear stress $\tau_{i3|w}$ at the ground is modeled using the Monin-Obukhov similarity theory [63] such that $\tau_{i3|w} = -\left[\tilde{u}_r \kappa / \ln(z/z_0)\right] \frac{\tilde{u}_i}{\tilde{u}_r}$, where z_0 is the roughness length, κ is the von Kármán constant, and $\tilde{u}_r = \sqrt{\tilde{u}^2 + \tilde{v}^2}$ is filtered velocity magnitude at the first grid level [73]. We use a surface roughness of $z_0 = 0.002$ m, which is a typical

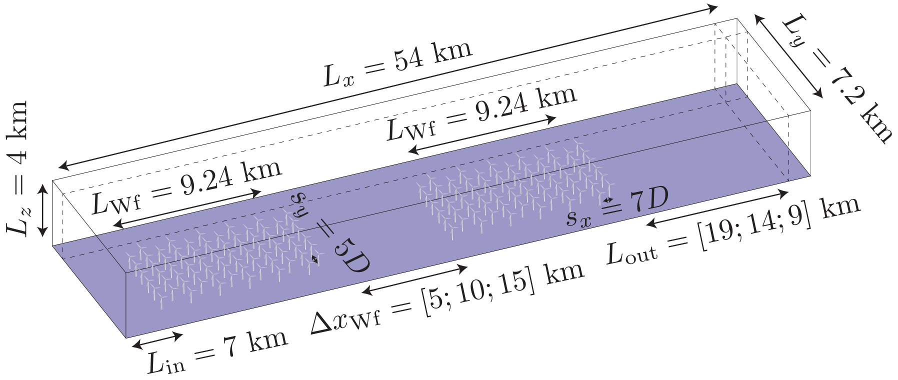

Figure 6.1 – Schematic of the computational domain, showing the wind farm layout and the fringe layer configuration. The distance between the farms Δx_{Wf} is varied from 5 to 15 km.

case name	arrangement of turbines	distance in between farms
stag-5km	staggered	5 km
stag-10km	staggered	10 km
stag-15km	staggered	15 km
align-10km	aligned	10 km
stag-align-10km	staggered & aligned	10 km

Table 6.1 – The case names are constructed as follows: the first part denotes the layout and the second part denotes the distance between the wind farms.

value for offshore conditions [201].

A schematic of the considered wind farm configuration is shown in figure 6.1. The main simulation domain includes two wind farms consisting of 12 × 6 wind turbines. The upstream wind farm is positioned 7 km downstream of the inflow region, and the distance between the wind farms is varied from 5 to 15 km, see table 6.1. The wind turbines have a diameter of $D = 120$ m and the hub-height is $z_h = 100$ m. The distance between the wind turbines is $s_x = 7D$ and $s_y = 5D$ in the streamwise and spanwise direction, respectively. The wind turbines are either fully aligned with the incoming wind or in a staggered layout. This results in a wind farm length $L_{\mathrm{Wf}} = 9.24$ km and a wind farm width $W_{\mathrm{Wf}} = 3.12$ km for the aligned layout and $W_{\mathrm{Wf}} = 3.42$ km for the staggered layout. In this work we use Wf as an abbreviation for wind farm.

Wf1 and Wf2 denote the upstream and downstream wind farm, respectively. Both the wind farm and the precursor domain have a size of $L_x = 54$ km, $L_y = 7.2$ km and $L_z = 4.0$ km, which is discretized on a $1800 \times 480 \times 480$ grid. The vertical resolution is 5 m up to a height of 1.5 km and grid stretching is applied above. The actuator disks are resolved with 24 grid points in vertical and 8 grid points in spanwise direction. This resolution has been shown to be sufficient by Wu and Porté-Agel [246] and Stevens et al. [60].

Realistic atmospheric inflow conditions are generated by the concurrent precursor method [138]. This approach samples flow data from a periodic turbulent ABL simulation performed in a precursor domain. The sampled data is introduced as an inflow condition into a fringe region of the wind farm simulation domain, see figure 6.1, and we apply shifted periodic boundary conditions to reduce the effect of persistent large-scale structures in the atmospheric inflow [235]. Nevertheless, some remnants of these large-scale structures are still visible in the results.

Furthermore, we apply a proportional-integral controller [139, 140] to guarantee that the planar-averaged wind angle at hub-height is 0° and aligned with the wind farm geometry. In addition, as the wind direction changes with height, we use a symmetric fringe function [153]. The simulations are performed with the Earth's rotation angular speed $\Omega = 7.3 \cdot 10^{-5}$ rad/s and for a latitude $\Phi = 52^\circ$, which is representative for the Dutch North Sea area. The geostrophic-wind velocity G is assumed to be constant, thus representing barotropic conditions, with a value of 11 m/s. The direction of the geostrophic-wind velocity is from West to East [195]. The simulations are started from an initial wind profile that is set equal to the geostrophic wind, and uniformly distributed random perturbations are added below 50 m to spin up turbulence. The perturbations have an amplitude of 3% of the geostrophic wind. These spin-up simulations are performed in a domain size of $L_x = 27$ km, $L_y = 3.6$ km and $L_z = 4.0$ km. After 8.7 hours a quasi-steady state is reached and then the domain size is increased to $L_x = 54$ km, $L_y = 7.2$ km and $L_z = 4.0$ km, which is possible due to the periodic boundary conditions. Subsequently, the precursor and wind farm simulations are continued concurrently for two additional hours. The statistical data is collected over five hours, corresponding to approximately three flow-through times.

Validations of the employed domain length and width, as well as the considered averaging time are provided in the appendix. For example, we performed an additional simulation in a wider domain to verify that the presented findings are not affected by the domain size. We find that the wind farm power

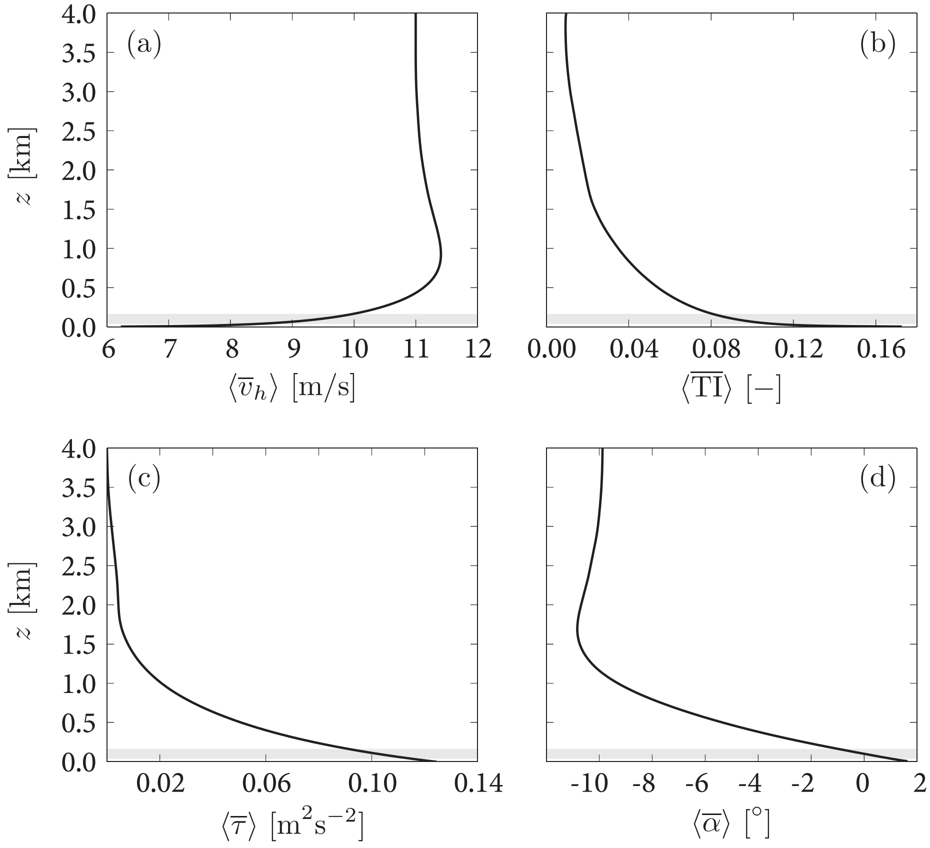

Figure 6.2 – Temporally and horizontally-averaged inflow conditions. (a) Horizontal velocity magnitude, (b) turbulence intensity, (c) vertical momentum flux, and (d) wind angle as a function of height. The shaded area indicates the vertical extent of the wind turbines.

production of the upstream and downstream farms is reduced by 1.5% when the domain size is doubled due to the decreased flow blockage. It is important to emphasize that this affects the upstream and downstream farms in a similar way and does not affect the main physics much.

6.2.1 Boundary layer characteristics

Figure 6.2 presents the time and planar-averaged atmospheric inflow conditions obtained from the precursor simulation. The horizontal velocity magnitude $\langle \overline{v}_h \rangle = \left\langle \sqrt{\overline{u}^2 + \overline{v}^2} \right\rangle$, where $\langle\ \rangle$ is the planar average and the overbar represents the temporal average, is shown in figure 6.2 (a). The tilde representing filtering is dropped in the remainder of the paper for simplicity. The velocity at hub-height is 9.5 m/s and the highest velocity, due to the formation of a weak low-level jet, is 11.4 m/s at 0.93 km. The horizontal turbulence intensity is defined as $\langle \overline{\mathrm{TI}} \rangle = \left\langle \sqrt{\overline{u'^2} + \overline{v'^2}} \right\rangle / \langle \overline{v}_h \rangle$ and is 9% at hub-height. The vertical profile of the turbulence intensity is presented in figure 6.2 (b). Figure 6.2 (c) shows the planar-averaged vertical momentum flux, which is defined as $\langle \overline{\tau} \rangle = \langle \sqrt{(\overline{u'w'})^2 + (\overline{v'w'})^2} \rangle$ with $\overline{u'w'} = \overline{uw} + \overline{\tau_{xz}} - \overline{u}\,\overline{w}$ and $\overline{v'w'} = \overline{vw} + \overline{\tau_{yz}} - \overline{v}\,\overline{w}$. The boundary layer height is $z_i = 1.73$ km, which is defined as the height where the mean stress is 5% of its surface value ($z_{0.05}$) followed by a linear extrapolation, i.e. $z_i = z_{0.05}/0.95$ [202]. The wind angle $\langle \overline{\alpha} \rangle = \tan^{-1}\left(\langle \overline{v} \rangle / \langle \overline{u} \rangle \right)$ as a function of height is shown in figure 6.2 (d), which shows that $\langle \overline{\alpha} \rangle$ changes from 1.02° at $z_h - D/2$ to $\langle \overline{\alpha} \rangle = -0.91°$ at $z_h + D/2$, resulting in a wind veer over the vertical extent of the rotor of 2°.

6.3 Results

6.3.1 Flow adjustment in and around the wind farms

Figure 6.3 (a) shows the instantaneous horizontal velocity magnitude at hub-height for case stag-10km. The figure shows that the wakes meander downstream and form a wind farm wake, creating the inflow condition for the downstream wind farm. We also refer to the corresponding supplementary movie. Figure 6.3 (b) displays the velocity $1D$ downstream of the last row of the upstream wind farm. The strongest wake deficits are in the center, suggesting that energy is entrained from the sides as the wake deficit is less pronounced at the edges. Above the wind turbines, it is visible that the flow is rotated in the clockwise direction; see also figure 6.2 (d). This effect is even more visible in figure 6.3 (c), which shows the flow $1D$ behind the last row of the downstream wind farm. A comparison between figures 6.3 (b) and 6.3 (c) shows that the velocity 1D behind the downstream wind farm is lower than 1D behind the upstream farm. This indicates that the velocity deficit is stronger behind the downstream farm. This effect is further analyzed below, see in

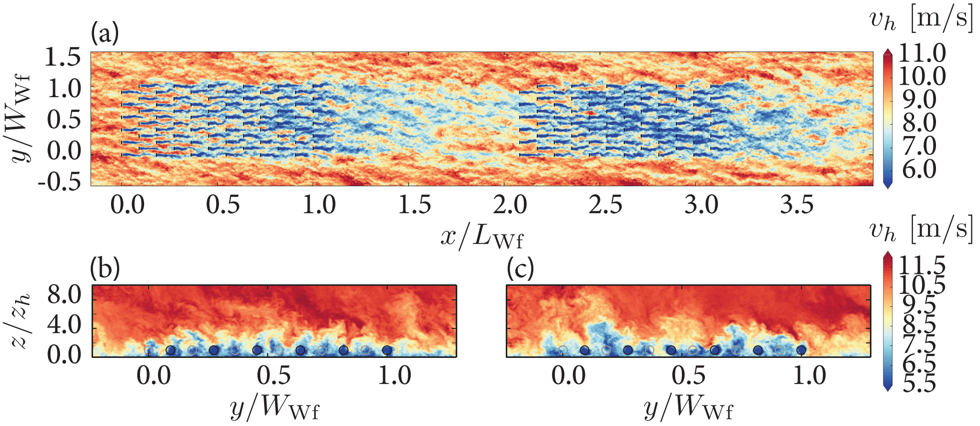

Figure 6.3 – Instantaneous horizontal velocity magnitude $v_h = \sqrt{u^2 + v^2}$ (a) at hub-height, (b) $1D$ behind the last row of the upstream wind farm, and (c) $1D$ behind the last row of the downstream farm. The positions of the wind turbines are marked by (a) black lines and (b-c) circles. Circles indicate the spanwise-vertical location of the turbines for uneven (grey) and even (black) turbine rows.

particular figure 6.6 (a), which analyzes the wind strength throughout the wind farm.

Figure 6.4 (a)-(c) show the time-averaged horizontal velocity magnitude at hub-height for the staggered wind farms that are separated by 5 km, 10 km and 15 km, respectively. Obviously, the flow inside the upstream wind farm is nearly identical for all cases, while the figure clearly shows that the velocities in the downstream wind farm are higher when the distance between both farms is increased from 5 to 15 km. The wind farm wake is most intense directly behind the farm where it spans the total width of the wind farm. Further downstream, the wind farm wake recovers from the sides and spans a narrower region. This effect was also observed by Schneemann et al. [34], and in section 6.3.4 we will see that this wind farm wake characteristic is visible in the power production of the downstream farm.

Figure 6.4 (d) shows that in an aligned wind farm high-velocity wind speed regions are formed in between the turbine columns, which are not observed in the staggered wind farm. A comparison between figure 6.4 (b) and (d) reveals that this affects the wind farm wake recovery as the individual wakes are visible behind the aligned wind farm while the wind farm wake behind the staggered farm is more homogeneous. Consequently, the spanwise averaged

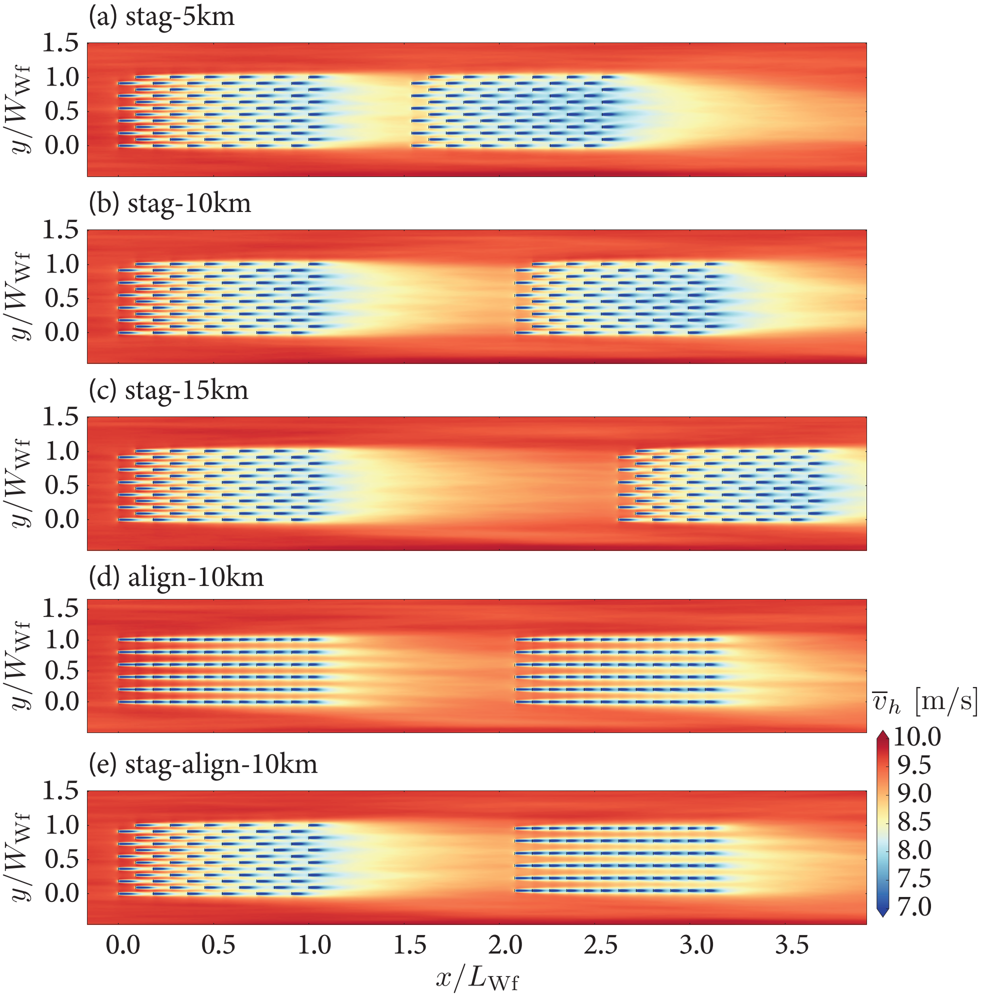

Figure 6.4 – Time-averaged horizontal velocity magnitude at hub-height.

velocity deficit behind the upstream wind farm is smaller behind the aligned wind farm than behind the staggered wind farm, see figure 6.5. This is related to the observation that the staggered wind farm produces more energy than the aligned wind farm, i.e. the larger energy extraction creates a stronger wind farm wake.

When only the downstream farm is aligned, while the upstream farm is staggered (see figure 6.4 (e)), the velocity in between the columns of the downstream

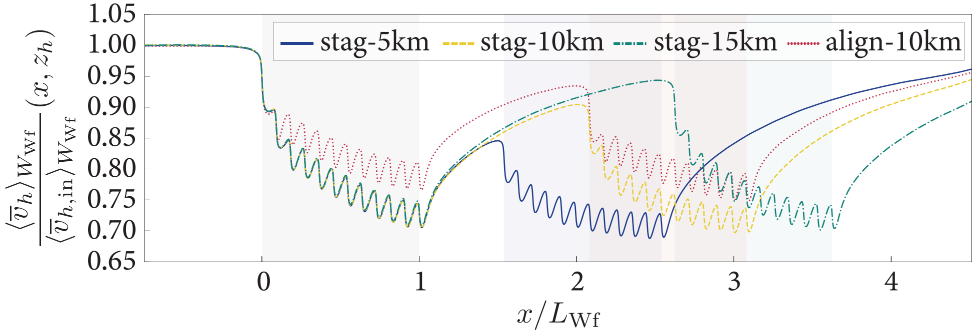

Figure 6.5 – Horizontal velocity magnitude at hub-height normalized by its inflow value averaged over the spanwise extent of the wind farm. The shaded regions indicate the streamwise location of each farm.

farm is lower compared to the case where both farms are aligned. Towards the end of the downstream farm, the differences between case stag-align-10km and align-10km decrease. The wind farm wake behind the downstream wind farm in case stag-align-10m seems to be slightly more homogeneous than in case align-10km. In all cases, the wind farm wakes are slightly deflected in the negative spanwise direction, which could result from the wind veer resulting from the Coriolis forces [81, 205, 247]. However, the effect is quite small, since the veer in the atmosphere is small (see figure 6.2 (d)).

Figure 6.5 reveals that the wake deficit of the wind farm wake decreases with increasing distance from the upstream farm until the induction zone of the downstream wind farm is reached. Consequently, the velocity in front of the downstream wind farm is lowest for case stag-5km and highest for case stag-15km. Note, that we did not include case stag-align-10km in this figure and in some of the following figures. The reason is that the wind farm width is different for the aligned and staggered wind farms, such that case stag-align-10km can not be analyzed and compared directly with the other cases.

Therefore, to study the velocities around the wind farms in more detail, we compare the flow statistics inside and behind the wind farms by introducing a virtual origin, such that $x = 0$ indicates the location of the first row of each farm, in figure 6.6. Panel (a) shows that the inflow velocity measured 1 km ($0.1/L_\mathrm{Wf}$) in front of the downstream wind farm is 83% of the undisturbed inflow velocity for case stag-5km, 90% for case stag-10km, and 94% for case stag-15km. For the aligned wind farm (figure 6.7 (a)) the velocity value

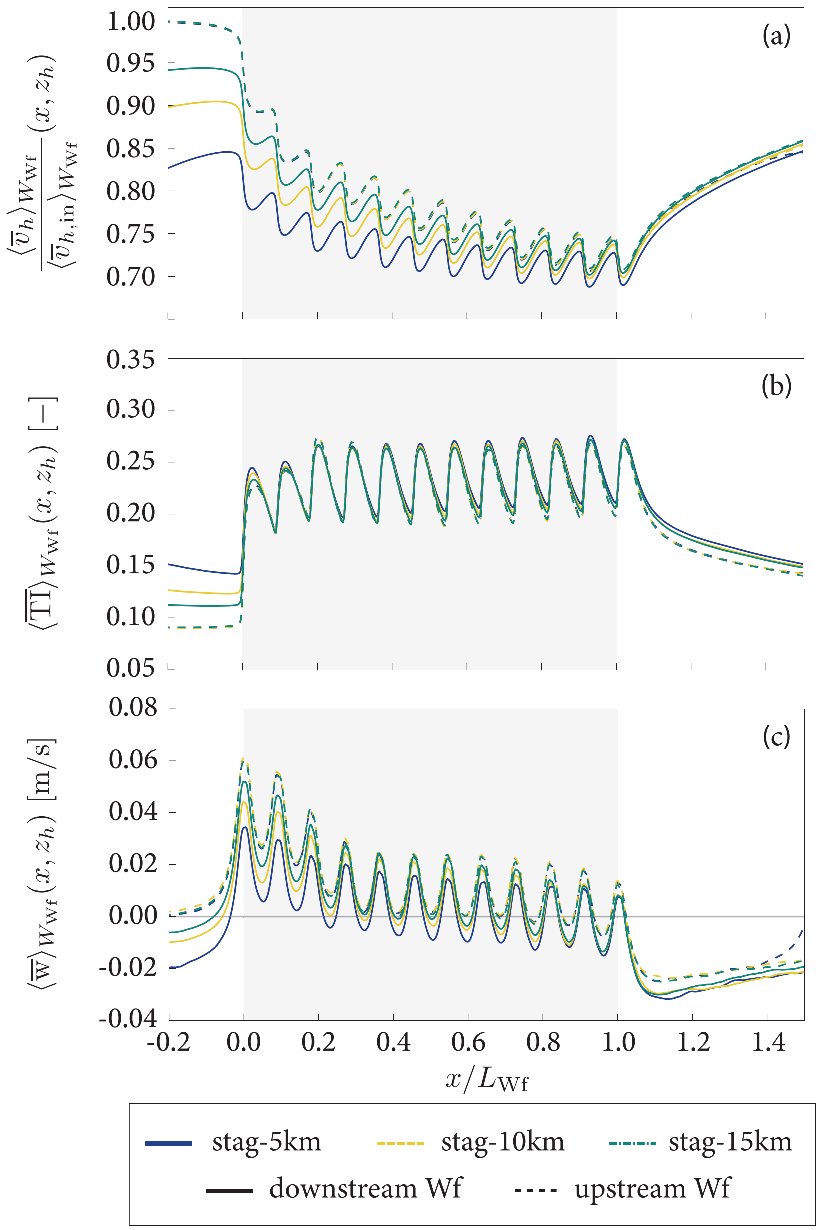

Figure 6.6 – (a) Horizontal velocity magnitude normalized by the inflow velocity, (b) turbulence intensity, and (c) vertical velocity at hub-height, averaged over time and the spanwise extent of the wind farm for the different wind farms, see the legend. The wind farm length normalizes the x-axis, and the origin indicates the location of the first row of each farm. The shaded area indicates the wind farm position.

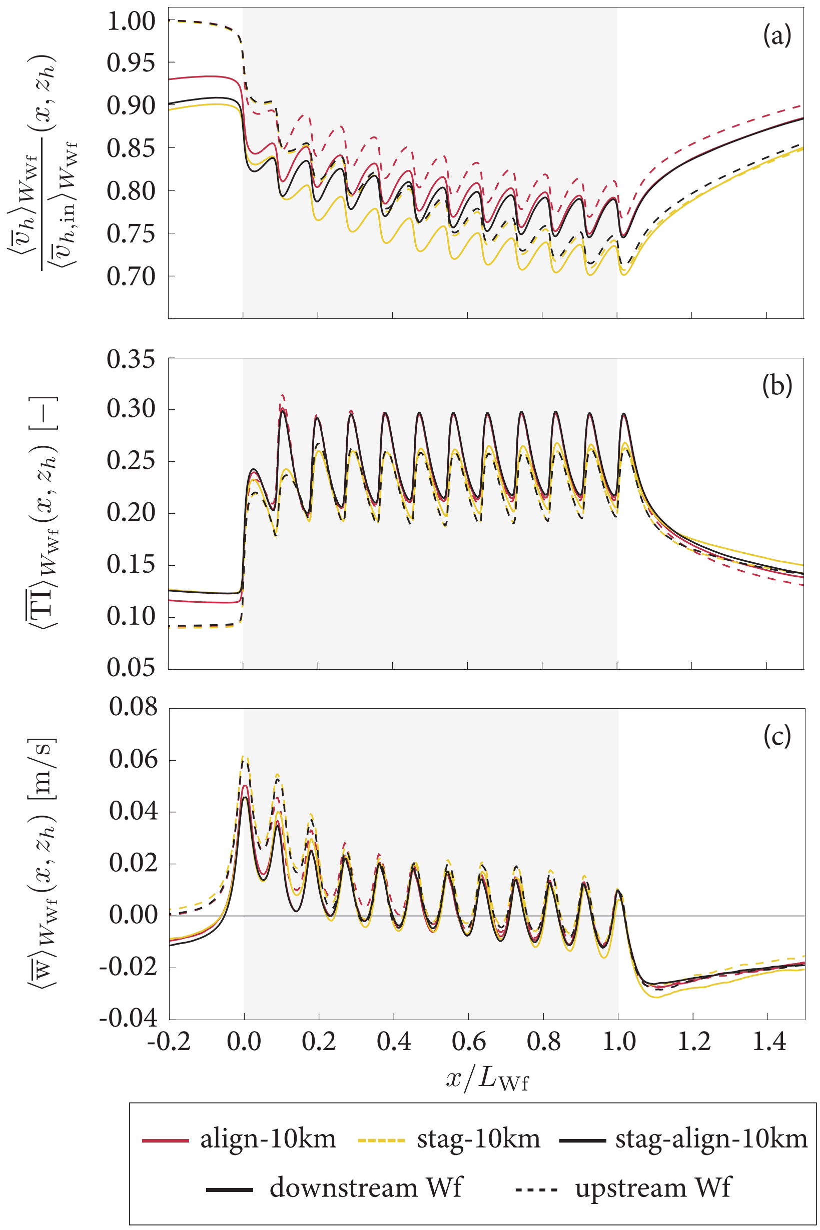

Figure 6.7 – (a) Horizontal velocity magnitude normalized by the inflow velocity, (b) turbulence intensity, and (c) vertical velocity at hub-height, averaged over time and the spanwise extent of the aligned wind farms. The wind farm length normalizes the x-axis, and the origin indicates the location of the first row of each farm. The shaded area indicates the wind farm position.

1 km ($0.1/L_{\mathrm{Wf}}$) in front of the downstream wind farm is 93% of the inflow for case align-10km and 90% in case stag-align-10km. Overall, this indicates that the wind farm wake behind a staggered wind farm is stronger. This means that the effect of the wind farm wake on the downstream wind farm is most pronounced in the entrance region of the downstream wind farm and becomes less noticeable further downstream in the wind farm. Furthermore, we note that the wind farm wake recovery behind the upstream wind farm is slightly faster for case stag-15km and case stag-align-10km (see figure 6.7(a)) when compared to the cases stag-5km and stag-10km. This effect could be caused by a reduced blockage effect when the downstream farm is narrower and produces less power (case stag-align-10km) or when the downstream farm is positioned further away (case stag-15km). However, the statistical variation between simulations may also play a role as there is no appreciable difference between the wind farm wake recovery for cases stag-5km and stag-10km even though the spacing between the farms is increased. Finally, figures 6.6 and 6.7 reveal that at the end of the wind farm, the wind velocities in the downstream farm are only about 3% lower than in the upstream farm.

Wind farm wakes are characterized by the velocity deficit and increased turbulence intensity. The turbulence intensity at hub-height averaged over the wind farm width is displayed in figure 6.6 (b) and 6.7 (b). In case stag-5km the turbulence intensity in front of the downstream wind farm is about 60% higher than in the upstream wind farm. Higher turbulence intensity is known to allow for faster wake recovery but also affects the loads on wind turbines [6, 49]. While the inflow for the downstream farm has much higher turbulence levels, the differences in turbulence intensity observed inside the upstream and downstream farms are limited. However, interestingly, the turbulence intensity behind the downstream wind farm is always a bit higher than behind the upstream wind farm. This suggests that, although the wakes of the closest turbines dominate the turbulence intensity inside the wind farm, the wake behind the downstream wind farm seems to be slightly amplified by the remnants of the wind farm wake that originates from the upstream farm. The turbulence intensity behind the wind farm with an aligned layout dissipates faster than behind a staggered wind farm.

In contrast to the turbulence intensity behind the wind farms, the turbulence intensity inside the wind farms is higher in the aligned than in the staggered layout. In the aligned layout, the distance between consecutive downstream turbines is smaller than in the staggered layout. The smaller inter turbine spacing allows less room for the turbulent kinetic energy from the wakes to

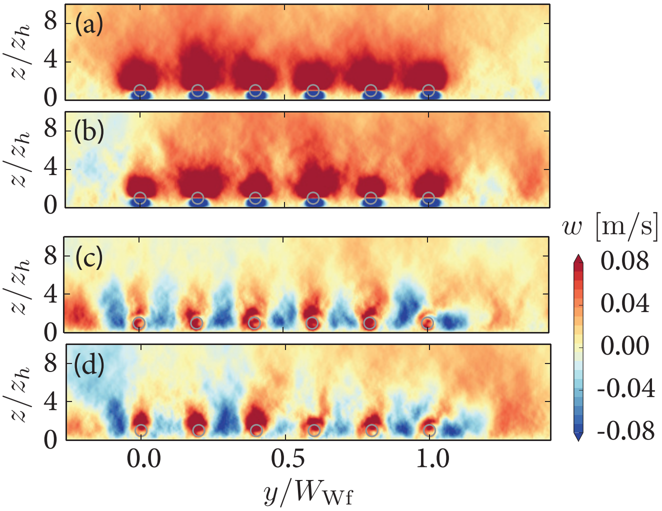

Figure 6.8 – Time-averaged vertical velocity at the first row of the (a) upstream and (b) downstream wind farm, and at the last row of the (c) upstream, and (d) downstream wind farm for case align-10km. Grey circles denote the wind turbine positions.

dissipate. Consequently, the turbulence intensity is higher in aligned wind farms than in staggered wind farms [24, 246, 248].

Figure 6.6 (c) and 6.7 (c) show that the vertical velocity averaged over the wind farm width at hub-height is zero in front of the induction zone of the upstream wind farm, which starts at $x/L_{Wf} = -0.2$, before the flow is deflected over the wind farm [24]. The reason for the positive velocity above the turbines is that the wind turbines deflect the flow over the wind farm. The negative vertical velocity behind the wind farm results from the flow deflection around the farm and the negative vertical kinetic energy flux that is created by the wind turbine wakes.

Figures 6.8 (a) and (b) show the time-averaged vertical velocity at the entrance of the upstream and downstream farm, respectively. A comparison between both panels reveals that the wind farm wake of the upstream farm creates negative vertical velocity patches on the sides of the downstream farm. Furthermore, these panels show that the flow deflection over the farm is most pronounced directly above the turbines and smaller for the downstream farm than for the upstream farm. Figure 6.9 further confirms that the weaker inflow for the downstream farm results in a reduced flow deflection over that farm.

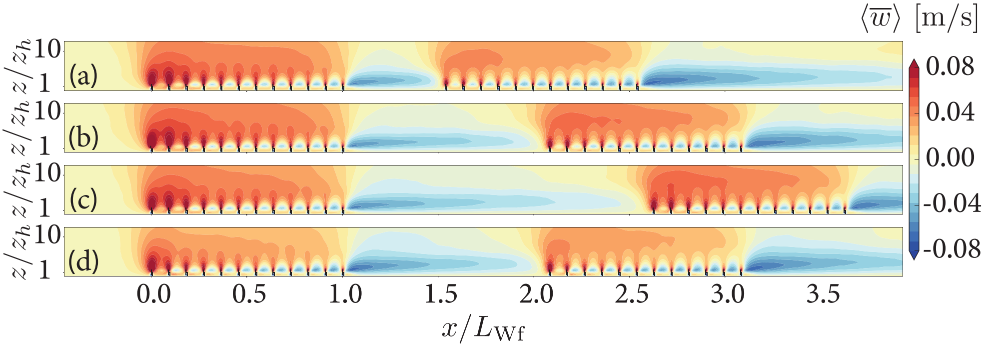

Figure 6.9 – The vertical velocity, averaged over time and the spanwise wind farm extent for cases (a) stag-5km, (b) stag-10km, (c) stag-15km, and (d) align-10km. The vertical extent is magnified by a factor 2 to increase the visibility.

The reduced flow deflection is caused by the negative vertical velocity in the wake of the upstream farm. Figure 6.8 (c) and (d) show that in the last turbine row, the vertical velocity is only positive directly above each turbine. In between the turbines the vertical velocity is negative, due to the downward vertical kinetic energy flux, which brings the high-velocity wind from above the wind farm downwards. This effect becomes stronger further downstream in the wind farm, leading to the observation of negative velocities between the turbine columns. We note that the negative vertical velocity created by the downwards flux further downstream in the wind farm is observed in figures 6.6 (c), 6.7 (c) and 6.9. The local patches of positive vertical velocity are due to the local flow deflection over each turbine.

In the following, we examine how the flow structure in and above the downstream wind farm compares to the upstream farm to study how the wind farm wake affects the flow in the downstream farm. The difference in vertical velocities averaged over the width of the upstream and downstream wind farms is shown in figure 6.10 for cases (a) stag-5km and (b) stag-15km. As expected, the difference in the vertical velocities between the upstream and downstream wind farms is higher when the distance between the farms is smaller. The differences are largest above the first turbine row and reflect the decreased flow deflection over the downstream farm discussed above. The corresponding ratio of the horizontal velocity magnitudes is shown in figure 6.11 (a) and (b), which reveals that the difference between the flow strength in the upstream and the downstream wind farm decreases with increasing distance in the farm. At the end of the farm the largest difference are observed above the farm, instead of

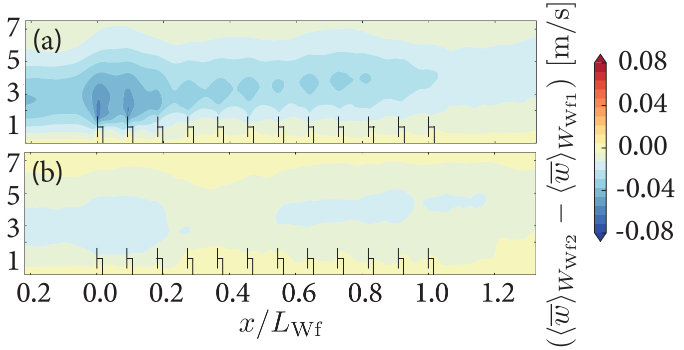

Figure 6.10 – The differences between the time-averaged vertical velocity in the downstream and upstream farm averaged over the wind farm width W_{Wf} for case (a) stag-5km and (b) stag-15km.

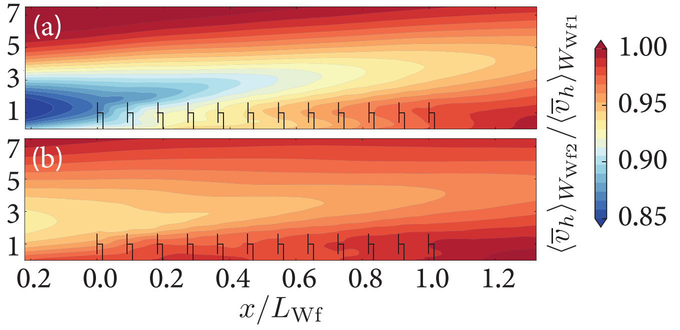

Figure 6.11 – The ratio of time-averaged horizontal wind speed in the downstream farm compared to the corresponding upstream farm averaged over the wind farm width W_{Wf} for case (a) stag-5km and (b) stag-15km.

inside the farm. A more quantitative representation of the spanwise averaged velocity at various locations in and around the upstream and downstream wind farm can be found in figure 1 of the appendix. The fact that the differences are largest above the wind farm emphasizes the need to investigate the flow above the wind farm in more detail, which we do in the next section.

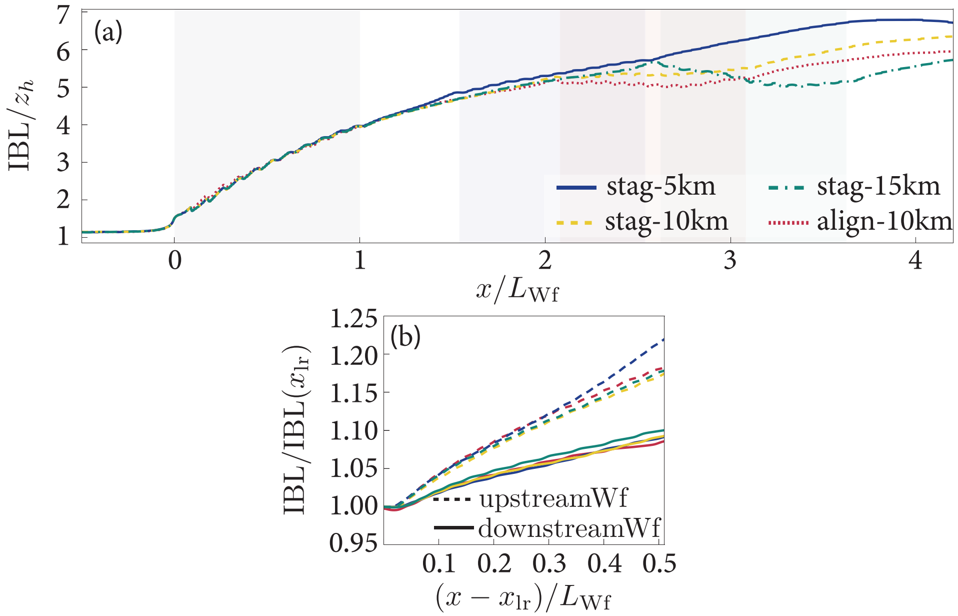

Figure 6.12 – (a) Internal boundary layer height (IBL) with the shaded areas representing the position of each wind farm. (b) IBL behind each wind farm, normalized by the IBL above the last row.

6.3.2 Wind farm boundary layer

To quantify the effect of the upstream wind farm on the flow above the downstream wind farm we study the internal boundary layer (IBL) development above both farms. As we showed in figure 6.5 the flow is decelerated due to the momentum extraction by the wind turbines at the entrance of a wind farm. The flow deflection over the farm causes an upward momentum flux leading to the growth of an IBL [229]. Here we define the IBL as the height where the time-averaged horizontal velocity magnitude is 97% of the planar-averaged inflow velocity at the same height [197]. The minimum height of the IBL is set to the height of the wind turbine top ($z_h + D/2$). Note, that the threshold of 97% is arbitrary. As an example, Wu and Porté-Agel [246] used a threshold of 99% instead of 97% and Stevens [186] define the IBL height based on the height where the vertical energy flux reaches the value in the inflow. Figure 6.12 shows that the IBL height above the upstream wind farm is comparable for all cases under consideration. Behind the downstream wind farm the IBL growth is almost identical for all cases under consideration (see figure 6.12 (b)), but significantly less than behind the upstream wind farm.

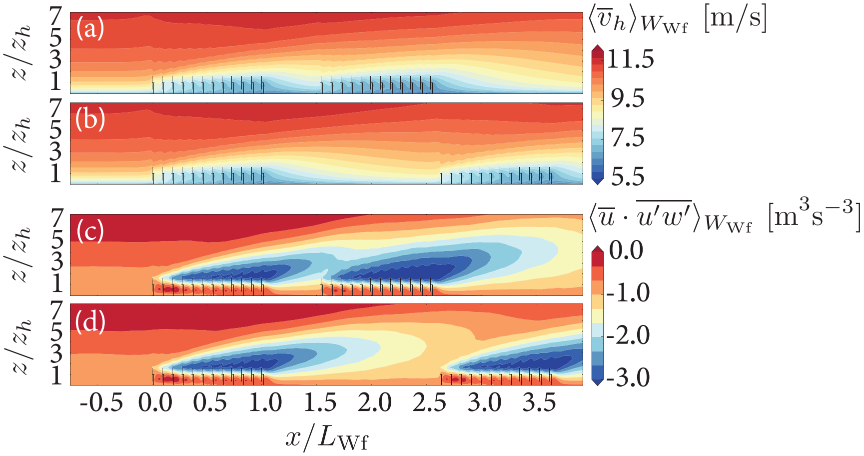

Figure 6.13 – The horizontal velocity magnitude (a,b) and vertical energy flux (c,d) averaged over the spanwise wind farm extent for cases stag-5km (a,c) and stag-15km (b,d).

The slower increase of the IBL height at the start of the downstream wind farm in case stag-5km and the decrease of the IBL height in case stag-15km can be explained by the formation of a second IBL that is formed at the start of the downstream wind farm, see figure 6.13 (a) and (b). The figure shows the IBL development, which is formed as the velocity deficit of the wake diffuses upwards with downstream direction. The corresponding vertical kinetic energy flux $\left\langle \overline{u} \cdot \overline{u'w'} \right\rangle$ is displayed in figure 6.13 (c) and (d). It is clearly visible that the energy entrainment above the downstream wind farm is increased by the presence of the upstream wind farm, especially for case stag-5km when the downstream distance between the wind farms is relatively small.

Figure 6.14 shows that just above the farm the energy entrainment in the entrance region is higher in the downstream farm. However, in the nearly fully developed regime the flux is similar in both farms. At a height of 400 m the absolute value of the vertical kinetic energy flux starts to increase at roughly $0.4 \cdot L_{\mathrm{Wf}}$ behind the first turbine row due to the IBL that is formed at the start of the wind farm. The absolute value of the kinetic energy flux is generally higher above the downstream farm than above the upstream farm. This can be explained by the flux created by the wake of the upstream farm, which is *superimposed* with the new flux created by the downstream farm itself, see figure 6.13. These results confirm that the impact of the wake of the upstream farm is most pronounced at higher elevations.

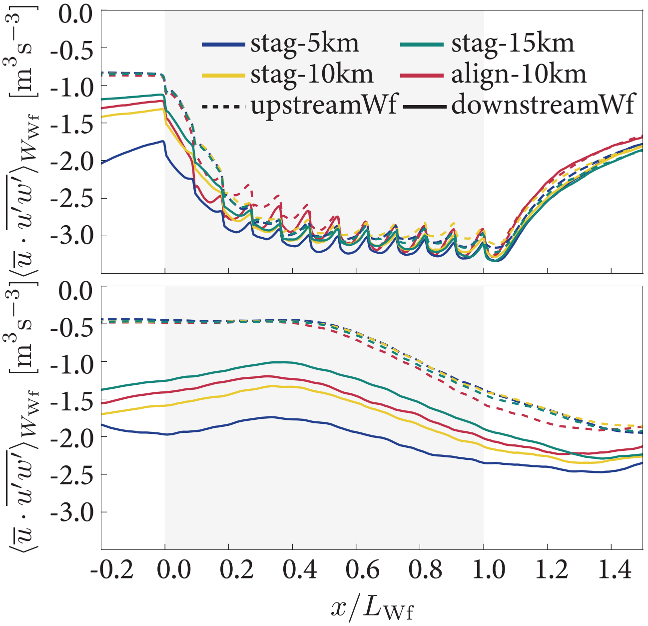

Figure 6.14 – The vertical kinetic energy flux, averaged over time and the spanwise wind farm extent at (a) $h = 160$ m and (b) $h = 400$ m. The shaded area indicates the wind farm position.

6.3.3 Wind farm wake characteristics

To study the wind farm wake layout in more detail, figure 6.15 (a) shows the horizontal inflow velocity at hub-height, averaged from $x = 10D$ to $2D$ in front of each wind farm. While the variations of the inflow velocity in front of the upstream wind farm are uniformly distributed, the signature of the wind farm width is visible in front of the downstream wind farm. The strongest velocity deficit is positioned around $y \approx 0.5W_\mathrm{Wf}$ and decreases towards the edge of the wind farm wake. The recovery is not symmetric because of the wind veer caused by the Coriolis force. This effect is less pronounced for the staggered wind farm layout than for the aligned layout due to the difference in the wind farm layout and width. The last row of the wind farm has turbines positioned from $y = 0.09W_\mathrm{Wf}$ to $1W_\mathrm{Wf}$ while the previous row has turbines positioned from $y = 0$ to $0.91W_\mathrm{Wf}$. As a consequence of this layout, the wake and also turbulence intensity is stronger at $y = 1/W_\mathrm{Wf}$ than at $0/W_\mathrm{Wf}$. As a result, the wake of the staggering wind farms is shifted towards the positive y-direction,

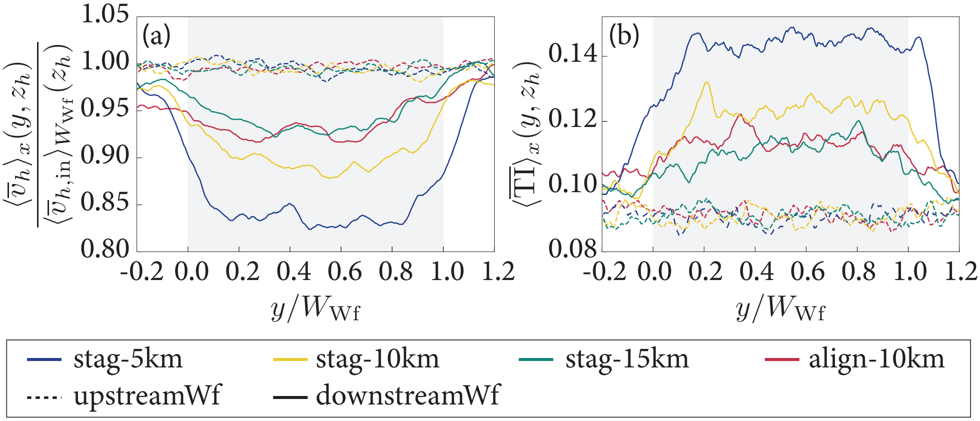

Figure 6.15 – (a) Horizontal inflow velocity and (b) turbulence intensity at hub-height. The average is taken from $x = 10D$ to $2D$ in front of each wind farm. The shaded area represent the wind farm position.

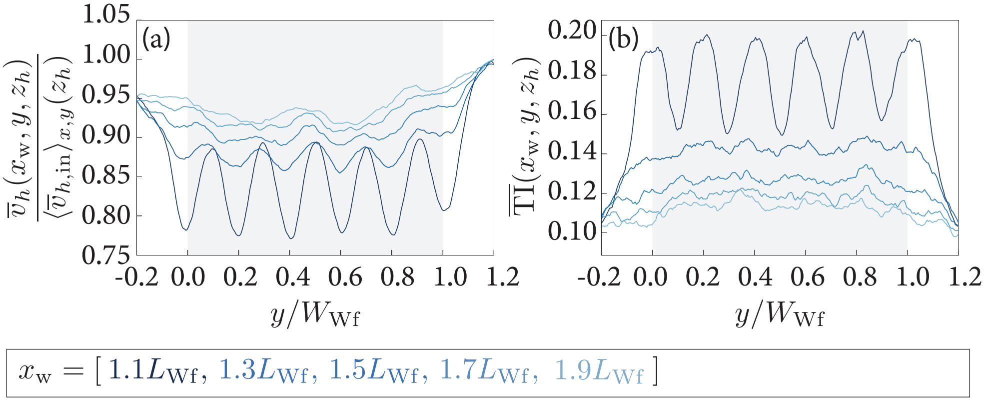

Figure 6.16 – (a) Horizontal velocity and (b) turbulence intensity at hub-height behind each wind farm for case align-10km. The shaded area represent the wind farm position.

which gives a false impression of a clockwise wake deflection.

While the extent of the wind farm width can be determined from the velocity deficit in figure 6.15, the positions of the individual wind turbines are not visible. Nygaard and Newcombe [215] and Schneemann et al. [34] reported that a wind farm wake does not include the characteristics of individual wind

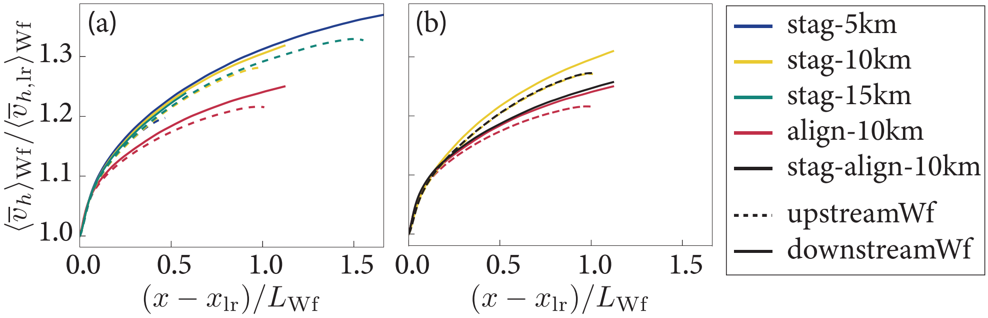

Figure 6.17 – Horizontal velocity magnitude at hub-height normalized with the velocity at 1.5D behind the last turbine row (x_{lr}) and averaged over the spanwise extent of either (a) each wind farm or (b) the aligned wind farm.

turbine wakes. In Nygaard and Newcombe [215] this status was reached 6 km downstream of the wind farm. Figure 6.16 shows that for the aligned wind farm (case align-10km) the characteristics of individual wind turbine wakes are not visible anymore starting from $x \approx 1.5L_{\mathrm{Wf}} \approx 14.13$ km downstream of the wind farm. The signature of the individual wind turbines disappear faster in the profile of the turbulence intensity (figure 6.16 (b)). However, even though the signature of the wind turbines disappears quickly, the turbulence intensity is still elevated at the entrance of the downstream wind farm (figure 6.15 (b)). Thus the increased turbulence intensity in wind farm wakes may increase the unsteady turbulence loading of turbines in the downstream farm [6, 49]. As previously discussed, the signature of the individual wind turbines disappears faster for the staggered layout than for the aligned layout (see figure 6.3).

Figure 6.17 confirms that wind farm wakes recover faster behind the downstream wind farm than behind the upstream wind farm. The figure displays the velocity averaged over the wind farm width, normalized by the velocity measured 1.5D behind the last turbine row. The fastest wake recovery is observed behind the downstream wind farm in case stag-5km. The slowest wake recovery is observed for the aligned case for which the turbulence intensity in the wind farm wake is lowest. The wake recovers faster behind the downstream farm than behind the upstream farm, as it benefits from the vertical kinetic energy flux created by both wind farms. The wake behind the aligned wind farm recovers similarly, but slightly faster when the upstream wind farm is staggered (case stag-align-10km) than when the upstream wind farm is aligned (case align-10km), see figure 16 (b).

6.3.4 Wind farm power production

The previous sections showed that an upstream positioned wind farm influences the velocities and energy entrainment in and around the downstream farm. Here, we investigate the wind farm wake effect on power production of a downstream farm. Figures 6.18 (a) and (c) show the power production per row, normalized by the power produced by the first row of the upstream farm for each case. In the staggered cases, the first two wind turbine rows produce almost the same power since the wind turbines are not positioned in the wake of upstream turbines. Behind the second row, the power production decreases drastically to 66% of the first row, and subsequently decreases gradually towards 53% at the end of the wind farm. In the aligned case, the strongest drop in power production occurs behind the first row as expected. Behind the second row, the power production increases slightly up to 47% of the first-row production due to energy entrainment from above.

Due to the wake effect of the upstream farm, the first row of the downstream wind farm produces only 67% (stag-5km), 78% (stag-10km), 87% (stag-15km), 86% (align-10km) and 81% (stag-align-10km) of the first row of the upstream wind farm. For the staggered cases, the second row of the downstream wind farm has a slightly higher power production than the first row due to the additional downstream distance (840 m) behind the upstream farm, which allows the wind farm wake to recover more. The relative production of the first row of the downstream aligned farm is comparable to the performance of the first row of the staggered wind farm when the distance between the farms is 15 km instead of 10 km. The reason for this difference is that staggered wind farms form a stronger wake. For case stag-align-10km the power production of the first row is slightly higher than for the case stag-10km. This may be caused by the smaller wind farm blockage effect of the downstream aligned wind farm, or due to statistical variations between simulations.

All wind turbines in the entrance region of the downstream staggered wind farms have a lower power production than the corresponding rows of the upstream farm due to the incoming wake. The power production of the wind turbines further downstream approaches the values of the corresponding rows of the upstream farm. For case stag-15km the production of the third and subsequent rows is similar to the corresponding rows of the upstream farm. For case stag-5km, only the power production of the last row is similar in the upstream and downstream farm. In contrast, we find that for aligned wind farms the power production of turbines in the second row and beyond is not affected by the wind farm wake. This shows, that the power production

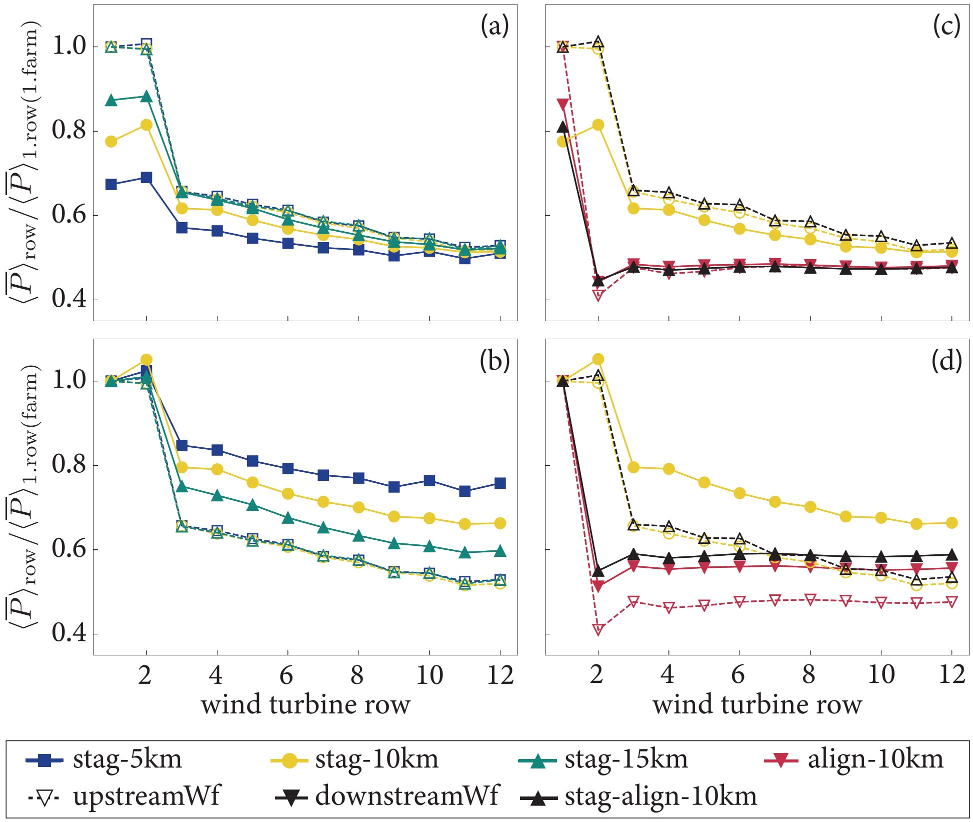

Figure 6.18 – (a & c) Power production per row normalized by the performance of the first row of the upstream farm. (b & d) Power production per row normalized by the first row of the farm itself.

of the turbines in aligned wind farms is mainly determined by the wake and entrainment effects caused by the turbines placed directly upstream.

Figures 6.18 (b) and (d) show the power production of each wind farm normalized by the power of the first row of the farm itself. In the entrance region, the normalized power production is higher in the downstream farm than in the upstream one. This further illustrates the effect of the upstream wind farm wake on the power production of the downstream farm. Analytical models, that are widely used in the planning process of wind farms, do not model the effect of the upstream farm on the downstream farm accurately [6, 239]. Figures 6.18 (b) and (d) show that it is crucial to take the wind

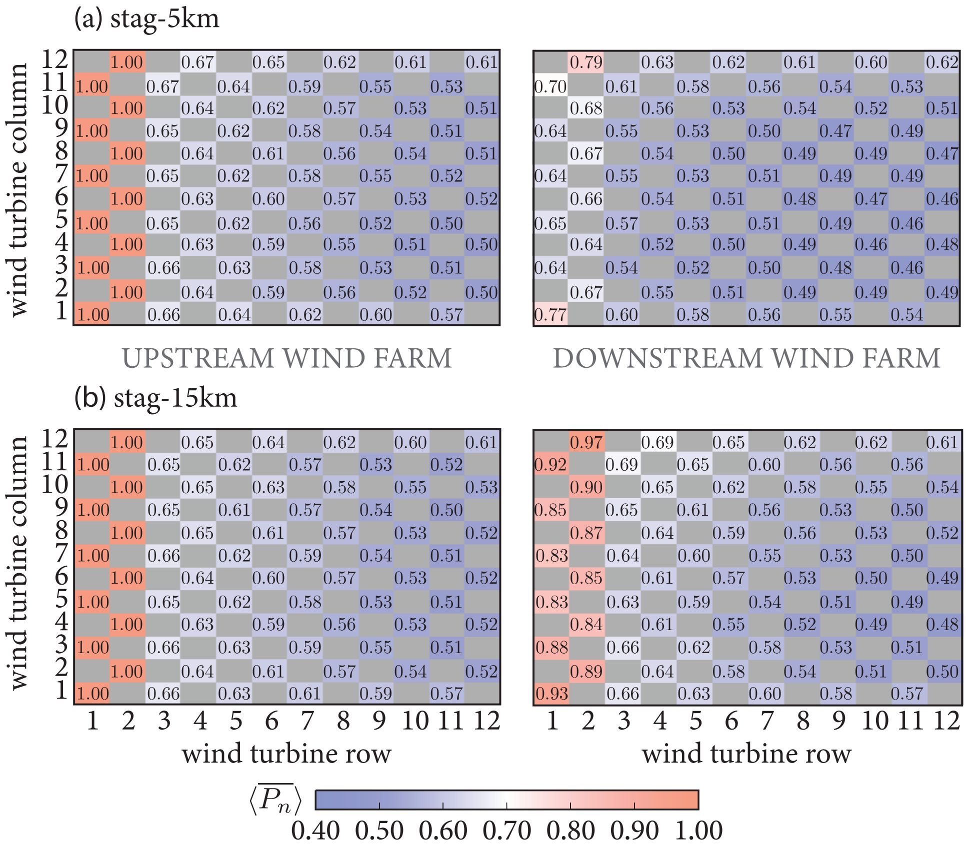

Figure 6.19 – Map of turbine power production $\langle P_\mathrm{n} \rangle$ for case (a) stag-5km and (b) stag-15km. All the entries have been normalized by the power of the turbines in the first or second row of the respective column.

farm wake effects into account, as the wind farm wake can strongly affect the performance of turbines throughout the wind farm, and not just of turbines on the first row. The reason for this effect is the large-scale interaction between the two wind farms discussed above.

Figure 6.19 (a) and (b) show maps of the power production of each wind turbine normalized by the production of the first turbine of the corresponding column. The power map visualizes that the lowest power production is in the inner wind turbine columns (i.e. columns 3-10) of the wind farm, while the outer columns (i.e. columns 1-2, and 11-12) profit from the wake recovery from the sides. Furthermore, the figure shows that column 12 of the downstream wind farm produces more than column 1. This effect is caused by the wind veer due to which turbines in column 12 benefit from the energy entrainment of less disturbed flow from above compared to the turbines in column 1.

6.4 Conclusion

We use LES to study the interaction between two identical wind farms in a neutral ABL driven by a geostrophic wind. We demonstrate that the wake generated by the upstream farm has a pronounced influence on the flow development inside and around the downstream farm and find that the interaction between the wind farms affects flow structures beyond the wind farm scale. The vertical kinetic energy flux created by the wake of the upstream wind farm increases the wind turbine wake recovery in the entrance region of the downstream farm. Furthermore, we find that the remnants of the upstream wind farm wake increase the wind farm wake recovery behind the downstream farm. This effect is stronger when the distance between the wind farms is smaller.

The distance over which interaction between wind farms can be observed depends on the length of the wind farm wake. We note that different methods have been used to define the length of a wind farm wake. Cañadillas et al. [237] determine the wake length as the distance behind the last turbine row at which the velocity has recovered to 95% of the inflow velocity, while Maas and Raasch [194] select a value of 90%. The variety of definitions stems from uncertainties in inflow velocities in field measurement observations and the limited area for which the wind farm wake is measured or simulated. However, we emphasize that such thresholds are arbitrary and note that a wake deficit of 5 or 10% has a significant effect on the power production of turbines in the downstream wind farm. Hence, the wind farm wake length reported in literature should be considered with caution as interactions between wind farms are likely to occur on larger length scales. Furthermore, we emphasize that wind farm wake lengths depend on the specific case under consideration. In this study, we focused on a setup where two wind farms are positioned behind each other in alignment with the wind direction. However, the impact of the upwind farm on the downwind farm's energy production will depend on atmospheric conditions such as the wind direction, the wind speed, and stability.

We find that the velocity deficit of the wind farm wake is mainly observed directly behind the wind farm, i.e. the wake expansion to the side is limited [34, 237]. Furthermore, the velocity deficit and increased turbulence intensity of individual turbines are visible directly behind the wind farm. However, the signature of individual wakes disappears further downstream when the wind farm wake becomes approximately uniform [215]. We observe a slight asymmetry in the wake strength due to the wind veer. The turbulence intensity in the wind farm wake becomes uniform faster than the velocity deficit. This process occurs faster behind a staggered wind farm than behind an aligned array. The wind farm layout (and consequently the wind direction) also affect the wind farm wake recovery. We find that a staggered wind farm's higher energy extraction from the boundary layer leads to a stronger wind farm wake than behind an aligned farm. However, the wind farm wake behind a staggered wind farm recovers faster than behind an aligned wind farm due to the higher turbulence intensity in the wind farm wake.

We demonstrate that wind farm wakes can impact the power production of all turbines in the downstream wind farm. For the staggered wind farms under consideration, the power production of the first row of the downstream wind farm is reduced by 33% when the distance is 5 km and by 13% when the distance is 15 km. As the wind farm wake increases the vertical kinetic energy flux in the downstream farm, the production of turbines further downstream converges towards the power production of the corresponding turbines in the upstream farm. This means that the development of the power production with downstream direction in the wind farm is very different in the upstream and downstream farm. Interestingly, in aligned wind farms, the wind farm wake primarily affects the power production of the first row of the downstream farm. In aligned wind farms the power production of turbines seems to depend mainly on the wake and entrainment effects caused by the directly upstream turbines. These observations agree with previous studies that analyzed the production data of neighboring wind farms and compared them to engineering models [249]. Further comparison with engineering wind farm models reveals that the models do not sufficiently capture the interactions between wind farms [239]. We believe that the difficulty in modeling these effects stems from the observed large-scale interactions between the wind farms. Our work further underlines the importance of detailed LES to study the interaction between wind farms.

Link to the supplementary movie [250].

6.5 Appendix

This section includes an additional analysis on the velocity and momentum flux profiles throughout the wind farms in section 6.5.1. The following sections give an overview of the effects of the grid resolution (section 6.5.2), the domain size (section 6.5.3), and the simulation time (section 6.5.4).

6.5.1 Development of the velocity and momentum flux profiles throughout the wind farms

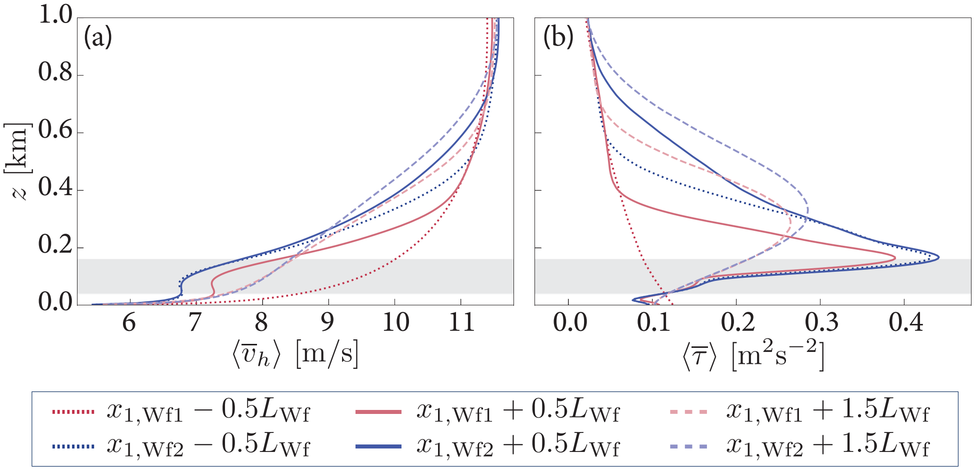

Figure 6.20 – (a) Velocity and (b) momentum flux profiles at various positions in and around the upstream (Wf1) and downstream wind farm (Wf2) averaged over time and the spanwise extent of the wind farm for case stag-5km.

Figure 10 and figure 12 (a,b) in chapter 6 show the time-averaged horizontal wind speed (averaged over the wind farm width) to compare the flow in and around the upstream and downstream wind farm. For a more quantitative comparison, figure 6.20 shows the spanwise averages of the velocity and momentum flux over the width of the wind farm at locations in front ($x_{1,\mathrm{Wf}} - 0.5L_{\mathrm{Wf}}$), in the center ($x_{1,\mathrm{Wf}} + 0.5L_{\mathrm{Wf}}$) and behind ($x_{1,\mathrm{Wf}} + 1.5L_{\mathrm{Wf}}$) each wind farm. Note, that the velocity at $0.5L_{\mathrm{Wf}}$ in front of the downstream wind farm (figure 6.20(a)) is lower than for the upstream farm at hub-height and above the wind farm. The same holds for the velocity deficit in the center of the wind farms (at $0.5L_{\mathrm{Wf}}$). Behind the wind farm, differences between upstream and downstream farm are mostly visible above the turbines. Similar to the velocity profile, the largest differences in momentum flux (figure 6.20(b)) between upstream and downstream farm are observed above the turbines. The momentum flux is generally higher in and above the downstream farm.

6.5.2 Effect of grid resolution

To show that our main findings are not sensitive to the employed grid resolution, we performed two simulations for case stag-10km from chapter 6, one with a resolution of $\Delta x = 30$ m, $\Delta x = 15$ m, $\Delta z = 5$ m (original resolution in chapter 6) and a second simulation using a coarser resolution $\Delta x = 40$ m, $\Delta x = 20$ m, $\Delta z = 10$ m, see figure 6.21. For the latter, a smaller domain size is used to save computational resources. In the smaller domain, the first row of the upstream wind farm starts at 5 km instead of 7 km, and the last row is closer to the fringe region. In section 6.5.3 we further confirm that this does not affect the results. Figure 6.21 shows that there are only small differences between the simulations performed on different resolutions, showing that the results are not sensitive to the grid resolution.

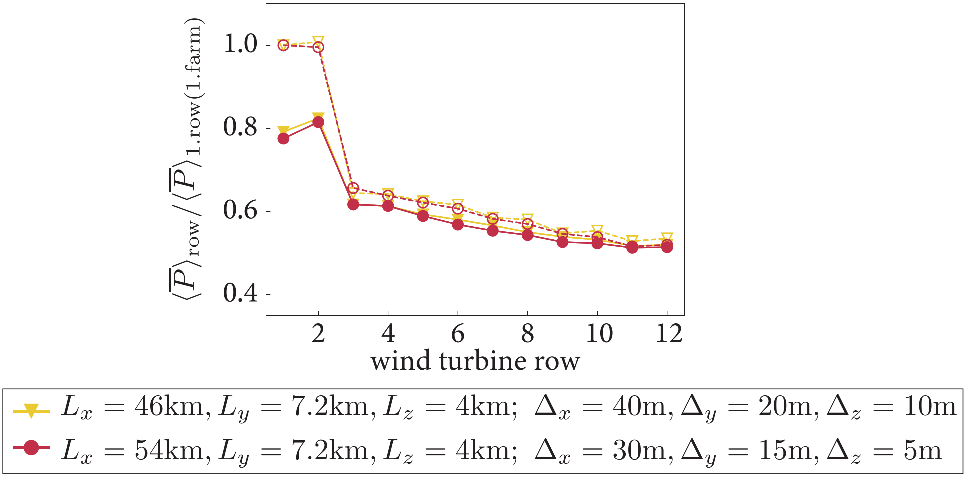

Figure 6.21 – Comparison of simulations performed using different grid resolutions, the standard resolution used in chapter 6: $\Delta_x = 30$ m, $\Delta_y = 15$ m, $\Delta_z = 5$ m and a coarser mesh: $\Delta_x = 40$ m, $\Delta_y = 20$ m, $\Delta_z = 10$ m. Shown is the power production per row normalized by the performance of the first row of the upstream farm. Empty symbols: upstream farm; filled symbols: downstream farm.

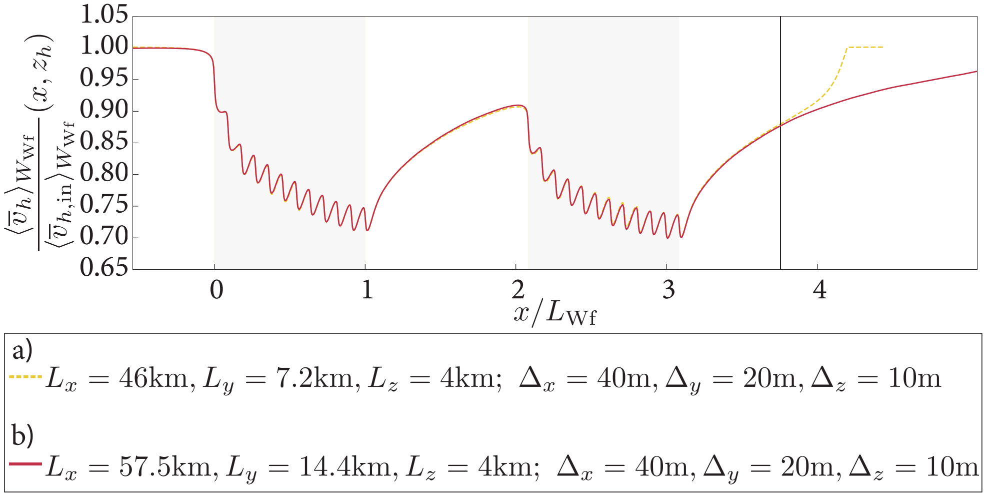

Figure 6.22 – Horizontal velocity magnitude at hub-height normalized by its inflow value averaged over the spanwise extent of the wind farm. The shaded regions indicate the streamwise location of each farm. Comparison of simulations for case stag-10km performed using different domain lengths, using the coarser $\Delta_x = 40$ m, $\Delta_y = 20$ m, $\Delta_z = 10$ m mesh. Distances to fringe region a) 10 km (comparable to case stag-15km); b) 15.5 km (comparable to case stag-10km). The black line indicates the position 4 km in front of the fringe region in the shorter domain. All plots in chapter 6 end at least at this position.

6.5.3 Effect of domain size

In the following test cases, the resolution is coarser ($\Delta_x = 40$ m, $\Delta_y = 20$ m, $\Delta_z = 10$ m) than the resolution used in chapter 6 ($\Delta_x = 30$ m, $\Delta_y = 15$ m, $\Delta_z = 5$ m) to reduce the computational costs. In section 2 we showed this does not affect the results. For the same reason, a shorter domain ($L_x = 46$ km) is considered and the first wind turbine row is positioned at $x = 5$ km, instead of $x = 7$ km (manuscript). The wind farm layout is staggered and the distance in between the farms is 10 km (case stag-10km). In section 6.5.3 and 6.5.3 we study the effect of the domain length and width, respectively.

Effect of domain length

Figure 6.22 compares the velocity profile averaged over the spanwise extent of the wind farms for two cases: a) a domain length of 46 km and b) a domain

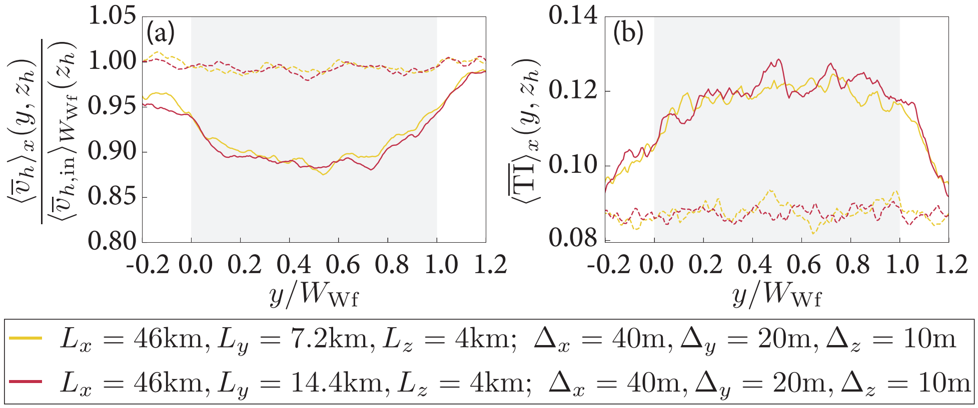

Figure 6.23 – Comparison of simulations for case stag-10km performed on domains with different width, using the coarser $\Delta_x = 40$ m, $\Delta_y = 20$ m, $\Delta_z = 10$ m mesh. The domain width is varied from $L_y = 7.2$ km to $L_y = 14.4$ km. (a) Horizontal inflow velocity and (b) turbulence intensity at hub-height. The average is taken from $x = 10D$ to $2D$ in front of each wind farm. The shaded area represent the wind farm position. Dashed lines: upstream farm; solid lines: downstream farm.

length of 57.5 km. As a result the last row is placed at either a) 10 km in front of the fringe region (comparable to case stag-15km) or b) 15.5 km in front of the fringe region (comparable to case stag-10km). The black line indicates the position 4 km in front of the fringe region in the shorter domain. Up to that position, there are only minor differences between the two cases. In chapter 6, all plots end at least 4 km in front of the fringe region. This test confirms that presented results inchapter 6 are not affected by the used domain length.

Effect of domain width

To test the effect of the domain width, two cases are considered: a) $L_y = 7.2$ km and b) $L_y = 14.4$ km. Figure 6.23, which is comparable to figure 14 from chapter 6, shows only minor variations in the inflow conditions for each wind farm.

Figure 6.24 shows that the time-averaged horizontal velocity magnitude at hub-height is comparable in both domains. However, high and low velocity streaks that are typical for neutral conditions [235] are visible in both domains. Figure 6.25 shows the difference in the velocity profile between the two cases and figure 6.26 shows the difference in power production. The power production in the wider domain is lower than in the smaller domain as there is less blockage. We quantified the difference in total power production between the small and large domain to be 1.5% (i.e. $\frac{\langle P\rangle_{\mathrm{Wf1,wide}}}{\langle P\rangle_{\mathrm{Wf1narrow}}} = 0.985$ and $\frac{\langle P\rangle_{\mathrm{Wf2,wide}}}{\langle P\rangle_{\mathrm{Wf2,narrow}}} = 0.986$).

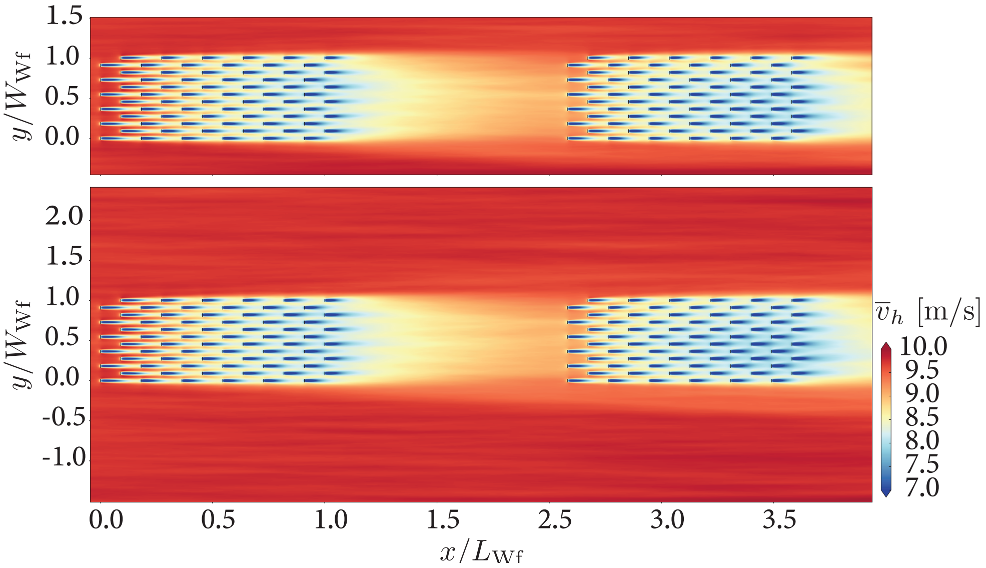

Figure 6.24 – Comparison of simulations for case stag-10km performed on domains with different width, using the coarser $\Delta_x = 40$ m, $\Delta_y = 20$ m, $\Delta_z = 10$ m mesh. The domain width is varied from $L_y = 7.2$ km to $L_y = 14.4$ km. Time-averaged horizontal velocity magnitude at hub-height.

6.5.4 Convergence of time-averaged statistics

To test the convergence of the time-averaged statistics we performed two simulations (on the same coarse grid as the test cases performed above) once time-averaged over 5 hours and once over 10 hours. The simulations considered in the main manuscript are performed for 5 hours. Figure 6.27 shows that the averaged velocity profiles become smoother after additional averaging. However, the main findings remain unchanged, which is further confirmed in figure 6.28.

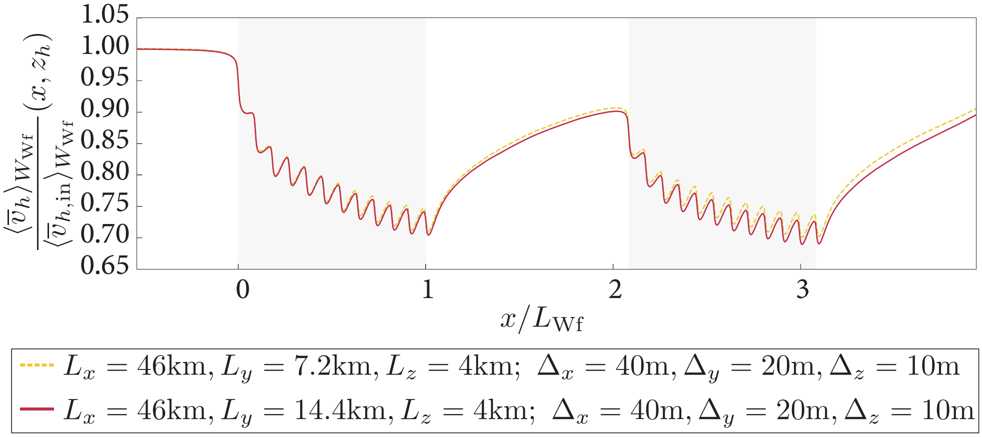

Figure 6.25 – Comparison of simulations for case stag-10km performed on domains with different width, using the coarser $\Delta_x = 40$ m, $\Delta_y = 20$ m, $\Delta_z = 10$ m mesh. The domain width is varied from $L_y = 7.2$ km to $L_y = 14.4$ km. Horizontal velocity magnitude at hub-height normalized by its inflow value averaged over the spanwise extent of the wind farm. The shaded regions indicate the streamwise location of each farm.

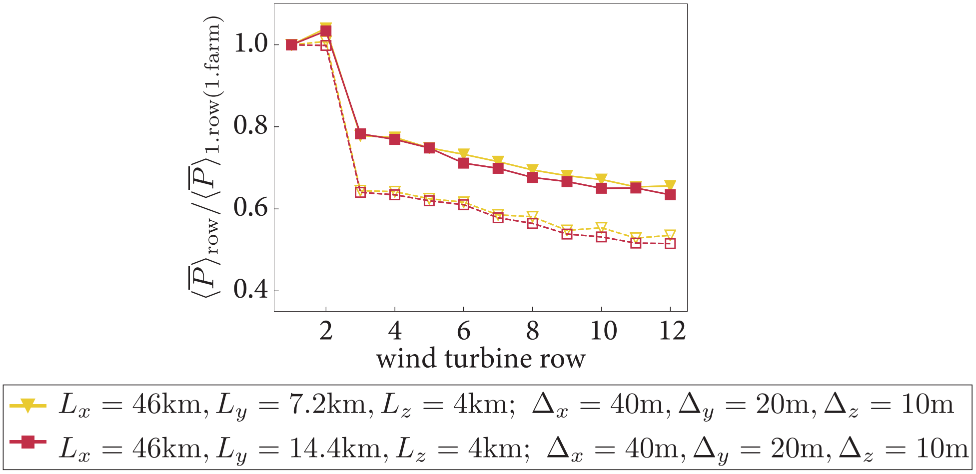

Figure 6.26 – Comparison of simulations for case stag-10km performed on domains with different width, using the coarser $\Delta_x = 40$ m, $\Delta_y = 20$ m, $\Delta_z = 10$ m mesh. The domain width is varied from $L_y = 7.2$ km to $L_y = 14.4$ km. Power production per row normalized by the first row of the farm itself. Empty symbols: upstream farm; filled symbols: downstream farm.

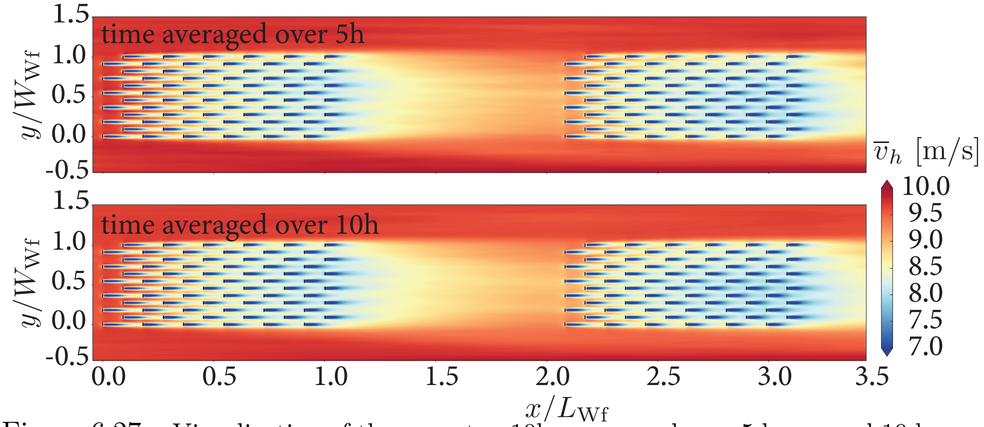

Figure 6.27 – Visualization of the case stag-10km averaged over 5 hours and 10 hours.

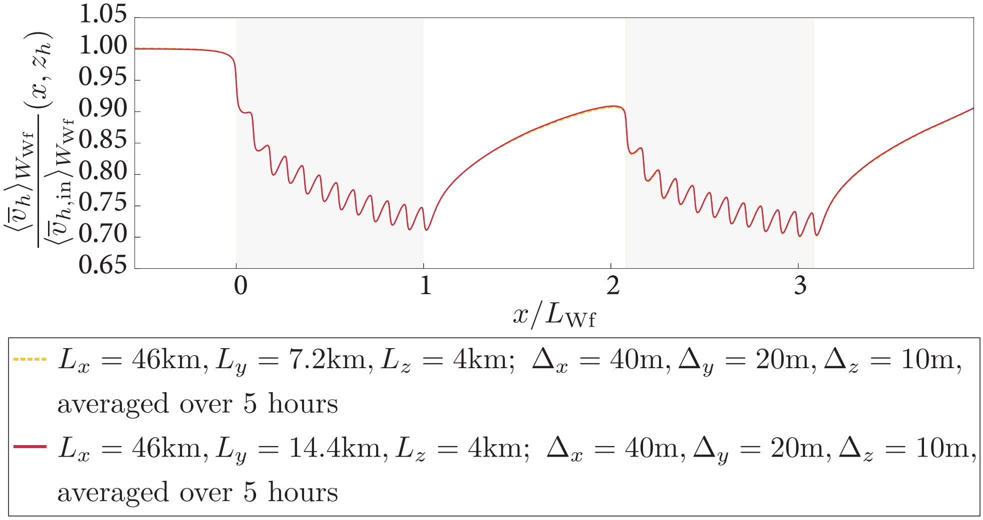

Figure 6.28 – Comparison of case stag-10km time-averaged over 5 hours and 10 hours. Horizontal velocity magnitude at hub-height normalized by its inflow value averaged over the spanwise extent of the wind farm. The shaded regions indicate the streamwise location of each farm.

7

Conclusions and Perspectives

In this thesis we used large-eddy simulations (LES) to model the atmospheric boundary layer (ABL) and its interaction with wind farms. We have compared three sub-grid scale (SGS) models for different atmospheric stability conditions (chapter 2) and modeled and investigated the impact of selected mesoscale processes in microscale LES of wind farms (chapter 3 & 4). Furthermore, we showed that engineering models cannot fully reproduce the wind farm wake recovery observed in LES (chapter 5). In addition, we demonstrated that the interaction between wind farms affects flow scales beyond the wind farm scale, such that the recovery of a wind farm wake is altered by the presence of an upstream farm (chapter 6). In this conclusion and perspective chapter, we briefly answer the research questions posed in the introduction and pose various questions that originate from our results.

7.1 Sub-grid scales and mesoscale effects in microscale large-eddy simulations

In **part I** of this thesis, we studied different methods to model the processes on sub-grid scales (SGS) and modeled and investigated the impact of selected mesoscale processes in microscale LES of wind farms.

> *In **chapter 2**, we showed that LES using either the anisotropic minimum dissipation (AMD) or the Lagrangian-averaged scale-dependent (LASD) SGS model agree better with measurements and theoretical predictions than LES using the Smagorinsky model for neutral, stable, and unstable conditions. Furthermore, we showed that the AMD model has less memory and computational overhead than the LASD model and hence is more suitable for large scale computations on modern supercomputers.*

However, in the cases considered here, the computational overhead of the AMD model compared to the Smagorinsky model is still about 11%. Further reducing this overhead while guaranteeing high quality results, low memory overhead and a straightforward implementation would be valuable for future simulations of the ABL on modern supercomputers. Additionally, the AMD model results depend on the modified Poincaré constant, which needs to be adjusted for more complex conditions. For instance, future studies and validation for flows over complex terrain would be beneficial.

> *In **chapter 3**, we introduced a method to include dynamic wind direction changes, originating from mesoscale atmospheric flow phenomena, in microscale LES. We showed that these dynamic wind direction changes can positively and negatively affect the power production of wind farms.*

Investigating the interaction between mesoscale and microscale processes remains one of the grand challenges in wind energy [105, 126]. As a next step, our method can be used to further develop and evaluate the representation of dynamic wind direction effects on power production in engineering wake models. Recently, von Brandis et al. [251] incorporated mesoscale background fields into the Fraunhofer IWES wind farm and wake modeling software *Farm Layout Program in Python (flappy)*. Their study highlights the importance of considering wind direction changes in the modeling of wind farms, especially if multiple wind farms within close proximity of each other are considered [251].

In addition to the evaluation of engineering models, our method can be used to evaluate the parameterization of wind farms in mesoscale models, such as in the Weather Research and Forecasting (WRF) [62, 119]. Evaluating these parameterizations for dynamic wind direction changes is important, as the parameterizations model the effect of multiple turbines in one horizontal grid cell [119]. Consequently, the individual turbine wakes cannot interact and a correct representation of the turbine wake effects for multiple wind directions is non-trivial. For example, Abkar and Porté-Agel [252] have proposed a model which incorporates the effect of different static wind directions and the wind farm layout in WRF. However, their approach requires preliminary simulation results and has to be optimized to be of practical use [253]. Since mesoscale simulations are becoming more important for planning large scale wind farms, the microscale knowledge gained from LES should be used to further improve the parameterization of wind turbine wake interactions in these mesoscale simulations [62].

Furthermore, recent studies have shown that our dynamic wind direction controller is already applied in LES studies of wind turbine control algorithms such as torque, pitch and yaw controls [254]. With control algorithms, the power production of wind farms can be increased, for example, by forcing yaw misalignment that can deflect the wind turbine wake away from downstream turbines. Additional to the maximization of power production, wind farm control can also improve the stability of the electrical power grid and reduce the wind turbine loads, leading to lower maintenance costs and wind turbine lifetime. Wind farm control has also been identified as one of the grand challenges in wind energy [105]. Influencing the wakes and turbulence in order to optimize the wind turbine interactions is especially challenging when the wind direction changes dynamically. LES are especially useful for validation of new control algorithms, since the inflow conditions are known and controlled [254]. Consequently, our method will be useful for the development and a more comprehensively evaluation of new wind farm control techniques.

Wind energy is dependent on the local meteorological conditions such as topography, stratification, and interesting phenomenon such as low-level jets or baroclinicity. We studied one such phenomena named baroclinicity. To be specific, we investigated the effects of negative geostrophic wind shear, which is one form of baroclinicity, on wind farm performance.

> *In* ***chapter 4****, we showed that negative shear creates an upward flux above the low-level jet which limits the energy entrainment into the wind farm.*

However, negative geostrophic wind shear is only one form of baroclinicity. In future work, we plan to study the impact of different forms of baroclinicity on wind farm performance, including positive shear, as well as thermal advection [172, 174]. We expect that the varying distributions of shear in the ABL will affect the entrainment and consequently the turbine wake recovery in wind farms.

7.2 Wind farm wakes

In **part II** of this thesis, we studied wind farm wakes and their impact on downstream wind farms with LES and various engineering models.

> *In **chapter 5** we revealed, that all engineering models under consideration, namely the Jensen model [223, 227], the coupled wake boundary layer model (CWBL) [145, 231], the Turbulence Optimized Park model (TurbOPark) [28], and the wind farm model developed by Niayifar and Porté-Agel [226], overestimate the wind farm wake recovery compared to LES observations. For the scenario considered here, the TurbOPark model predictions on the wind farm wake effect on a downstream wind farm are closest to the LES results.*

It is worth mentioning that this finding is in agreement with a recent study by Fischereit et al. [255], who compared wake effects in and behind wind farms measured by SCADA data with the results from the mesoscale model WRF, RANS, and three engineering models (namely the models by Jensen [223], Bastankhah and Porté-Agel [224], and Zong and Porté-Agel [233]). Fischereit et al. [255] find relative good agreement in wake recovery predictions between RANS, WRF and SCADA. In contrast, all engineering models over-predict the wind farm wake recovery, which was also found in our study. To increase the applicability of the engineering models to wind farm wake recovery predictions, additional models have to be developed for the wind farm wake recovery. Then, the new wind farm wake recovery models could be coupled to the aforementioned engineering wake models.

> *In **chapter 6** we showed, that the performance of the leading row of the downstream farm is highly impacted by the wake of the upstream farm. The impact increases with decreasing distance in between the wind farms. In addition to the distance in between the wind farms, the wake recovery is dependent on the layout of the wind farm. Stronger wind farm wakes are found for staggered than for aligned wind farms. Furthermore, the wake recovery of the downstream wind farm is affected by the upstream farm.*

In addition to the LES study of wind farm wakes presented in this thesis, other mesoscale flow phenomena have to be taken into account when studying wind farm wakes. For example, von Brandis et al. [251] discovered that the mesoscale wind direction can change by more than 7° when considering distances of 5-100 km. These wind direction changes can have a significant impact on the interaction between wind farms.

Furthermore, future studies should investigate how new wind farms that are built in proximity to existing wind farms affect wind farm blockage and gravity waves. Wind farm blockage is the wind speed reduction in front of the wind farm due to the placement of downstream turbines. It has been shown that turbines in the leading row of a wind farm produce less power compared to a free-standing turbine and that this effect is largest under stable conditions [30, 41, 256]. Velocity reductions due to blockage are much smaller than wake effects, ranging in the order of a few percentage points. This makes the quantification of blockage quite difficult. Additionally, field measurements of blockage are challenging since determining the inflow velocity is non-trivial and uncertainties are difficult to quantify [256]. Furthermore, a recent study has shown difficulties in studying wind farm blockage with numerical methods and in wind tunnels [30]. Bleeg and Montavon [30] namely show that the domain width has to be extremely large to avoid numerical blockage effects. Nevertheless understanding wind farm blockage is crucial as a failure to capture the effect leads to systematic errors in the wind farm power predictions. The construction of wind farms close to each other might increase the blockage effect drastically and further investigation of this topic is required.

Wind farm induced gravity waves form in stable conditions as the wind farm displaces flow upwards. When the potential temperature increases with height, a cold anomaly forms as a consequence of the upwards motion. The cold anomaly above causes a high pressure anomaly below, in the induction region of the wind farm, resulting in a lower velocity in front of the farm [41, 257]. The restoring forces of stable boundary layers force vertically perturbed air parcels back to their original height which triggers an inertia and gravity driven oscillation, known as a gravity wave [257]. Although wind farm induced gravity waves have a much smaller amplitude than the gravity waves caused by mountains [258], the pressure gradients influence the power production of wind farms [41, 257, 259]. Whether these waves improve or hinder the wind farms productivity depends on the atmospheric conditions, in particular, the ratio of the wind speed to wave speed in the capping inversion [23, 24, 41, 259, 260].

The nature of gravity waves triggered by neighboring wind farms remains a relevant topic. Although not presented here, additional simulations indicate that the magnitude of gravity waves increases significantly when a new wind farm is constructed downstream of an existing wind farm. Further studies should compare the velocity and pressure fields for three cases: 1. without the presence of wind farms, 2. with only one wind farm and 3. with more than one wind farm. However, the numerical investigation of wind farm induced gravity waves requires a large numerical domain length, width and height to prevent domain effects. When applying inflow methods, such as the concurrent-precursor method, domain-induced gravity waves might be generated in stable ABLs, which can affect the velocity and pressure fields drastically [261]. The recently developed fringe-region technique by Lanzilao and Meyers [261] shows promising results in reducing gravity waves that are triggered by the numerical domain. Thus, interesting studies on gravity waves triggered by wind farms, varying the distances in between the wind farms and the atmospheric conditions, can be performed in future works.

Scientific output

Publications in peer-reviewed journals

1. S. N. Gadde, **A. Stieren**, and R. J. A. M. Stevens
   Large-eddy simulations of stratified atmospheric boundary layers: Comparison of different subgrid models,
   Boundary-Layer Meteorol. 178, 363–382 (2021), doi:10.1007/s10546-020-00570-5.
   See chapter 2 of this thesis.
2. **A. Stieren**, S. N. Gadde, and R. J. A. M. Stevens
   Modeling dynamic wind direction changes in large-eddy simulations of wind farms,
   Renewable Energy **170** 013305 (2021), doi: 10.1016/j.renene.2021.02.018.
   See chapter 3 of this thesis.
3. **A. Stieren**, J. H. Kasper, S. N. Gadde, and R. J. A. M. Stevens
   The impact of negative geostrophic wind shear on wind farm performance,
   Accepted for publication in PRX Energy (2022).
   See chapter 4 of this thesis.
4. **A. Stieren** and R. J. A. M. Stevens
   Impact of wind farm wakes on flow structures in and around downstream wind farms,
   Flow, 2, E21 (2022), doi: 10.1017/flo.2022.15.
   See chapter 6 of this thesis.

Publications in peer-reviewed conference proceedings

1. **A. Stieren** and R. J. A. M. Stevens
   Evaluating wind farm wakes in large-eddy simulations and engineering models,
   J. Phys. Conf. Ser. 1934:012018 (2021), doi:10.1088/1742-6596/1934/1/012018.
   See chapter 5 of this thesis.

Contributed talks

- A brief introduction to Turbulence, **A. Stieren** and J. B. Will, Whirling Winds and Swirling Steams - Symposium S.V. Arago (Lunch discussion), Enschede, The Netherlands. February 2019.
- Modeling of wind farms. **A. Stieren** and J. M. I. Strickland. Physics of Fluids chair information day. Enschede, The Netherlands, February, 2020
- Large-eddy simulations of wind farm wakes. **A. Stieren** and R. J. A. M. Stevens. *Wind Energy Science Conference*, online. May 2021.
- Evaluating wind farm wakes in large-eddy simulations & engineering models. **A. Stieren** and R. J. A. M. Stevens. *Wake Conference*, online. June, 2021.
- Modeling wind direction changes in large-eddy simulations using a rotating reference frame. **A. Stieren**, S. N. Gadde, and R. J. A. M. Stevens. *13th International ERCOFTAC symposium on engineering, turbulence, modelling and measurements*, online. September 2021.
- Large-eddy simulations of wind farm wakes. **A. Stieren** and R. J. A. M. Stevens. *NWO Physics@Veldhoven - Physics Connects*, online. January 2022.
- Impact of wind farm wakes on downstream wind farms. **A. Stieren** and R. J. A. M. Stevens. *Max Planck Center Meeting 2022*, Boekelo, The Netherlands. March 2022.
- Effect of geostrophic wind shear on wind farm performance studied with large-eddy simulations. **A. Stieren**, J. H. Kasper, S. N. Gadde and R. J. A. M. Stevens. *47th windgroup meeting at KNMI.* March 2022.
- Impact of wind farm wakes on downstream wind farms. **A. Stieren** and R. J. A. M. Stevens. *Burgers Symposium 2022*, Lunteren, The Netherlands. June 2022.
- Impact of wind farm wakes on downstream wind farms. **A. Stieren** and R. J. A. M. Stevens. *MESA+ meeting 2022*, Enschede, The Netherlands. June 2022.
- Impact of wind farm wakes on downstream wind farms, **A. Stieren** and R. J. A. M. Stevens, *14th European Fluid Mechanics Conference-EFMC14*, Athens, Greece, September 2022

Posters

- Modeling wind direction changes with LES using a rotating reference frame. **A. Stieren**, S. N. Gadde, and R. J. A. M. Stevens. *15th EAWE PhD Seminar*, Nantes, France. November 2019.

Supervised student projects

- Bachelor thesis, *Investigating the effects of spanwise and streamwise spacing of turbines on the turbulence intensity throughout a wind farm.* (11/20-03/21)
- Bachelor thesis, *The impact of wind farm size on wind farm wakes.* (11/21-03/22)

Teaching experience

- Teaching assistant for the 3^{rd} year Bachelor course *Physics of Fluids* for the study Applied Physics in Twente. (2019)
- Teaching assistant for the 1^{st} year Master course *Mathematical and Numerical Physics* for the study Applied Physics in Twente. (2019-2021)

References

[1] T. Ackermann and L. Söder. Wind energy technology and current status: a review. *Renew. Sust. Energ. Rev.*, 4(4):315–374, 2000. doi:10.1016/S1364-0321(00)00004-6.

[2] T. J. Price. James Blyth - Britain's first modern wind power pioneer. *Wind. Eng.*, 29(3):191–200, 2005. doi:10.1260/030952405774354921.

[3] GE RENEWABLE ENERGY. Haliade-X offshore wind turbine, 2022. `https://www.ge.com/renewableenergy/wind-energy/offshore-wind/haliade-x-offshore-turbine` (last access: 12 June 2022).

[4] London Array. About London Array, 2022. `https://londonarray.com/` (last access: 12 June 2022).

[5] T. Burton, D. Sharpe, N. Jenkins, and E. Bossanyi. *Wind Energy Handbook*. John Wiley & Sons, New York, 2001.

[6] F. Porté-Agel, M. Bastankhah, and S. Shamsoddin. Wind-turbine and wind-farm flows: A review. *Boundary-Layer Meteorol.*, 74:1–59, 2020. doi:10.1007/s10546-019-00473-0.

[7] F. Lanchester. A contribution to the theory of propulsion and the screw propeller. *Trans. Inst. Naval Arch.*, 57:98–116, 1915. doi:10.1111/j.1559-3584.1915.tb00408.x.

[8] A. Betz. Schraubenpropeller mit geringstem Energieverlust. *Göttinger Nachrichten*, pages 193–213, 1919.

[9] F. P. Incropera, D. P. DeWitt, T. L. Bergman, and A. S. Lavine. *Fundamentals of heat and mass transfer*, volume 6. Wiley New York, 1996. ISBN:047131272X.

[10] P. K. Kundu and I. M. Cohen. *Fluid mechanics.* Elsevier, 2001. ISBN:9780124059351.

[11] S. B. Pope. *Turbulent Flows.* Cambridge University Press, Cambridge, 2000. doi:10.1017/CBO9780511840531.

[12] M. Calaf, C. Meneveau, and J. Meyers. Large eddy simulations of fully developed wind-turbine array boundary layers. *Phys. Fluids*, 22:015110,

2010. doi:10.1063/1.3291077.

[13] R. B. Cal, J. Lebrón, L. Castillo, H. S. Kang, and C. Meneveau. Experimental study of the horizontally averaged flow structure in a model wind-turbine array boundary layer. *J. Renew. Sustain. Energy*, 2:013106, 2010. doi:10.1063/1.3289735.

[14] C. VerHulst and C. Meneveau. Large eddy simulation study of the kinetic energy entrainment by energetic turbulent flow structures in large wind farms. *Phys. Fluids*, 26:025113, 2014. doi:10.1063/1.4865755.

[15] G. Cortina, M. Calaf, and R. B. Cal. Distribution of mean kinetic energy around an isolated wind turbine and a characteristic wind turbine of a very large wind farm. *Phys. Rev. Fluids*, 1(7):074402, 2016. doi:10.1103/PhysRevFluids.1.074402.

[16] H. Lu and F. Porté-Agel. On the impact of wind farms on a convective atmospheric boundary layer. *Boundary-Layer Meteorol.*, 157(1):81–96, 2015. doi:10.1007/s10546-015-0049-1.

[17] D. Yang, C. Meneveau, and L. Shen. Large-eddy simulation of offshore wind farm. *Phys. Fluids*, 26:025101, 2014. doi:10.1063/1.4863096.

[18] M. Abkar and F. Porté-Agel. The effect of free-atmosphere stratification on boundary-layer flow and power output from very large wind farms. *Energies*, 6(5):2338–2361, 2013. doi:https://doi.org/10.3390/en6052338. doi:10.3390/en6052338.

[19] D. Medici, S. Ivanell, J.-Å Dahlberg, and P. H. Alfredsson. The upstream flow of a wind turbine: blockage effect. *Wind Energy*, 14(5):691–697, 2011. doi:10.1002/we.451.

[20] A. R. Meyer Forsting and N. Troldborg. The effect of blockage on power production for laterally aligned wind turbines. *J. Phys. Conf. Ser.*, 625 (1):012029, 2015. doi:10.1088/1742-6596/625/1/012029.

[21] T. Nishino and S. Draper. Local blockage effect for wind turbines. *J. Phys. Conf. Ser.*, 625(1):012010, 2015. doi:10.1088/1742-6596/625/1/012010.

[22] A. R. Meyer Forsting, N. Troldborg, and M. Gaunaa. The flow upstream of a row of aligned wind turbine rotors and its effect on power production. *Wind Energy*, 20(1):63–77, 2017. doi:10.1002/we.1991.

[23] D. Allaerts and J. Meyers. Boundary-layer development and gravity waves in conventionally neutral wind farms. *J. Fluid Mech.*, 814:95–130, 2017. doi:10.1017/jfm.2017.11.

[24] K. L. Wu and F. Porté-Agel. Flow adjustment inside and around large finite-size wind farms. *Energies*, 10(12):2164, 2017. doi:10.3390/en10122164.

[25] A. Segalini and J.-Å Dahlberg. Global blockage effects in wind farms. *J. Phys. Conf. Ser.*, 1256(1):012021, 2019. doi:10.1088/1742-6596/1256/1/012021.

[26] A. Segalini and J.-Å Dahlberg. Blockage effects in wind farms. *Wind Energy*, 23(2):120–128, 2020. doi:10.1002/we.2413.

[27] J. M. I. Strickland and R. J. A. M. Stevens. Effect of thrust coefficient on the flow blockage effects in closely-spaced spanwise-infinite turbine arrays. *J. Phys. Conf. Ser.*, 1618:062069, 2020. doi:10.1088/1742-6596/1618/6/062069.

[28] N. G. Nygaard, S. T. Steen, L. Poulsen, and J. G. Pedersen. Modeling cluster wakes and wind farm blockage. *J. Phys. Conf. Ser.*, 1618:062072, 2020. doi:10.1088/1742-6596/1618/6/062072.

[29] M. Popescu and T. Flåtten. A Study of Blockage Effects at the Wind Turbine and Wind Farm Scales. *Energies*, 14(19):6124, 2021. doi:10.3390/en14196124.

[30] J. Bleeg and C. Montavon. Blockage effects in a single row of wind turbines. *J. Phys. Conf. Ser.*, 2265(2):022001, 2022. doi:10.1088/1742-6596/1618/6/062054.

[31] J. M. I. Strickland and R. J. A. M. Stevens. Investigating wind farm blockage in a neutral boundary layer using large-eddy simulations. *Eur. J. Mech. B. Fluids*, pages 303–314, 22. doi:10.1016/j.euromechflu.2022.05.004.

[32] A. Sebastiani, A. Peña, N. Troldborg, and A. Meyer Forsting. Evaluation of the global-blockage effect on power performance through simulations and measurements. *Wind Energy Sci.*, 7(2):875–886, 2022. doi:10.5194/wes-7-875-2022.

[33] K. Slavik, C. Lemmen, W. Zhang, O. Kerimoglu, K. Klingbeil, and K. W. Wirtz. The large-scale impact of offshore wind farm structures on pelagic primary productivity in the southern North Sea. *Hydrobiologia*, 845(1): 35–53, 2019. doi:10.1007/s10750-018-3653-5.

[34] J. Schneemann, A. Rott, M. Dörenkämper, G. Steinfeld, and M. Kühn. Cluster wakes impact on a far-distant offshore wind farm's power. *Wind Energy Science*, 5(1):29–49, 2020. doi:10.5194/wes-5-29-2020.

[35] R. B. Stull. *An Introduction to Boundary Layer Meteorology*. Kluwer Academic publishers, Boston, 1988. doi:10.1007/978-94-009-3027-8.

[36] A. K. Blackadar. Boundary layer wind maxima and their significance for the growth of nocturnal inversions. *Bull. Am. Meteorol. Soc.*, 38(5): 283–290, 1957. doi:10.1175/1520-0477-38.5.283.

[37] A. J. Thorpe and T. H. Guymer. The nocturnal jet. *Q. J. R. Meteorol. Soc.*, 103(438):633–653, 1977. doi:10.1002/qj.49710343809.

[38] A.-S. Smedman, M. Tjernström, and U. Högström. Analysis of the turbulence structure of a marine low-level jet. *Boundary-Layer Meteorol.*, 66(1-2):105–126, 1993. doi:10.1007/BF00705462.

[39] J. A. Businger and H. Charnock. Boundary layer structure in relation to larger-scale flow: some remarks on the JASIN observations. *Phil. Trans. R. Soc. A*, 308(1503):445–449, 1983. doi:10.1098/rsta.1983.0014.

[40] J. R. Garratt. *The Atmospheric Boundary Layer.* Cambridge University Press, Melbourne, 1992. doi:10.1016/0012-8252(94)90026-4.

[41] D. Allaerts and J. Meyers. Gravity waves and wind-farm efficiency in neutral and stable conditions. *Boundary-Layer Meteorol.*, 166:269, 2018. doi:10.1007/s10546-017-0307-5.

[42] J. F. Ainslie. Calculating the flow field in the wake of wind turbines. *J. Wind Eng. Ind. Aerodyn.*, 27:213–224, 1988. doi:10.1016/0167-6105(88)90037-2.

[43] G. P. van den Berg. *The sound of high winds. The effect of atmospheric stability on wind turbine sound and microphone noise.* PhD thesis, University of Groningen, 2006. PhD Thesis.

[44] L. J. Vermeer, J. N. Sørensen, and A. Crespo. Wind turbine wake aerodynamics. *Progress in Aerospace Sciences*, 39:467–510, 2003. doi:10.1016/S0376-0421(03)00078-2.

[45] B. Sanderse, S. P. van der Pijl, and B. Koren. Review of computational fluid dynamics for wind turbine wake aerodynamics. *Wind Energy*, 14: 799–819, 2011. doi:10.1002/we.458.

[46] J. Hart. Comparison of turbulence modeling approaches to the simulation of a dimpled sphere. *Procedia Eng.*, 147:68–73, 2016. doi:10.1016/j.proeng.2016.06.191.

[47] G. S. Young, D. A. R. Kristovich, M. R. Hjelmfelt, and R. C. Foster. Rolls, streets, waves, and more: A review of quasi-two-dimensional structures in the atmospheric boundary layer. *Bull Am Meteorol Soc*, 83(7):997–1002, 2002. doi:10.1175/1520-0477(2002)083<0997:RSWAMA>2.3.CO;2.

[48] A. Önder and J. Meyers. On the interaction of very-large-scale motions in a neutral atmospheric boundary layer with a row of wind turbines. *J. Fluid Mech.*, 841:1040–1072, 2018. doi:10.1017/jfm.2018.86.

[49] R. J. A. M. Stevens and C. Meneveau. Flow structure and turbulence in wind farms. *Annu. Rev. Fluid Mech.*, 49:311–339, 2017. doi:10.1146/annurev-fluid-010816-060206.

[50] S. B. Pope. Ten questions concerning the large-eddy simulation of turbulent flows. *New J. Phys.*, 6(1):35, 2004. doi:10.1088/1367-2630/6/1/035.

[51] A. Mittal, K. Sreenivas, L. K. Taylor, L. Hereth, and C. B. Hilbert. Blade-resolved simulations of a model wind turbine: effect of temporal convergence. *Wind Energy*, 19(10):1761–1783, 2016. doi:10.1002/we.1949.

[52] M. de Oliveira, R. C. Puraca, and B. S. Carmo. Blade-resolved numerical simulations of the NREL offshore 5 MW baseline wind turbine in full scale: A study of proper solver configuration and discretization strategies. *Energy*, page 124368, 2022. doi:10.1016/j.energy.2022.124368.

[53] H. Glauert. *The Elements of Aerofoil and Airscrew Theory*. Cambridge University Press, Cambridge, 1926.

[54] J. N. Sørensen, S. W. Z. Shen, and X. Munduate. Analysis of wake states by a full-field actuator disc model. *Wind Energy*, 1(2):73–88, 1998. doi:10.1002/(SICI)1099-1824(199812)1:2<73::AID-WE12>3.0.CO;2-L.

[55] R. Mikkelsen. *Actuator disc methods applied to wind turbines*. PhD thesis, PhD thesis, Technical University of Denmark, 2003. ISBN:7-7475-296-0.

[56] Y.-T. Wu and F. Porté-Agel. Large-eddy simulation of wind-turbine wakes: Evaluation of turbine parametrisations. *Boundary-Layer Meteorol.*, 138:345–366, 2011. doi:10.1007/s10546-010-9569-x.

[57] T. Revaz and F. Porté-Agel. Large-Eddy Simulation of Wind Turbine Flows: A New Evaluation of Actuator Disk Models. *Energies*, 14(13): 3745, 2021. doi:10.3390/en14133745.

[58] Á. Jiménez, A. Crespo, and E. Migoya. Application of a LES technique to characterize the wake deflection of a wind turbine in yaw. *Wind Energy*, 13:559–572, 2010. doi:10.1002/we.380.

[59] C. R. Shapiro, D. F. Gayme, and C. Meneveau. Filtered actuator disks: Theory and application to wind turbine models in large eddy simulation. *Wind Energy*, 22(10):1414–1420, 2019. doi:10.1002/we.2376.

[60] R. J. A. M. Stevens, L. A. Martínez-Tossas, and C. Meneveau. Comparison of wind farm large eddy simulations using actuator disk and actuator line models with wind tunnel experiments. *Renewable Energy*, 116:470–478, 2018. doi:10.2514/6.2016-1261.

[61] J. S. Rodrigo, R. A. C. Arroyo, P. Moriarty, M. Churchfield, B. Kosović, Branko, P. E. Réthoré, K. S. Hansen, A. N. Hahmann, J. D. Mirocha, and D. Rife. Mesoscale to microscale wind farm flow modeling and evaluation. *Wiley Interdiscip. Rev. Energy Environ*, 6(2):e214, 2017. doi:10.1002/wene.214.

[62] J. Fischereit, R. Brown, X. G. Larsén, J. Badger, and G. Hawkes. Re-

view of Mesoscale Wind-Farm Parametrizations and Their Applications. *Bound.-Layer Meteorol.*, 182(2):175–224, 2022. doi:10.1007/s10546-021-00652-y.

[63] C.-H. Moeng. A large-eddy simulation model for the study of planetary boundary-layer turbulence. *J. Atmos. Sci.*, 41:2052–2062, 1984. doi:10.1175/1520-0469(1984)041<2052:ALESMF>2.0.CO;2.

[64] A. Andren, A. R. Brown, P. J. Mason, J. Graf, U. Schumann, C.-H. Moeng, and F. T. M. Neuwstadt. Large-eddy simulation of a neutrally stratified boundary layer: A comparison of four computer codes. *Q. J. R. Meteorol. Soc.*, 120:1457–1484, 1994. doi:10.1002/qj.49712052003.

[65] J. D. Albertson. *Large Eddy Simulation of Land-Atmosphere Interaction.* PhD thesis, University of California, 1996.

[66] J. Smagorinsky. The role of numerical modeling. *Bull. Am. Meteorol. Soc.*, 48:89–93, 1967. url: jstor.org/stable/26249982.

[67] P. J. Mason and D. J. Thomson. Stochastic backscatter in large-eddy simulations of boundary layers. *J. Fluid Mech.*, 242:51–78, 1992. doi:10.1063/1.3291077.

[68] P. P. Sullivan, J. C. McWilliams, and C.-H. Moeng. A subgrid-scale model for large-eddy simulation of planetary boundary-layer flows. *Boundary-Layer Meteorol.*, 71:247–276, 1994. doi:10.1007/BF00713741.

[69] M. Germano, U. Piomelli, P. Moin, and W. H. Cabot. A dynamic subgrid-scale eddy viscosity model. *Phys. Fluids A*, 3:1760–1765, 1991. doi:10.1063/1.857955.

[70] C. Meneveau and J. Katz. Scale-invariance and turbulence models for large-eddy simulations. *Annu. Rev. Fluid Mech.*, 32:1–32, 2000. doi:10.1146/annurev.fluid.32.1.1.

[71] F. Porté-Agel, C. Meneveau, and M. B. Parlange. A scale-dependent dynamic model for large-eddy simulation: application to a neutral atmospheric boundary layer. *J. Fluid Mech.*, 415:261–284, 2000. doi:10.1017/S0022112000008776.

[72] S. Ghosal, T. S. Lund, P. Moin, and K. Akselvoll. A dynamic localization model for large-eddy simulation of turbulent flows. *J. Fluid Mech.*, 286: 229–255, 1995. doi:10.1017/S0022112095000711.

[73] E. Bou-Zeid, C. Meneveau, and M. B. Parlange. A scale-dependent Lagrangian dynamic model for large eddy simulation of complex turbulent flows. *Phys. Fluids*, 17:025105, 2005. doi:10.1063/1.1839152.

[74] R. Verstappen. When does eddy viscosity damp subfilter scales sufficiently? *J. Sci. Comp.*, 49(1):94, 2011. doi:10.1007/s10915-011-9504-4.

[75] W. Rozema, H. J. Bae, P. Moin, and R. Verstappen. Minimum-dissipation models for large-eddy simulation. *Phys. Fluids*, 27(8):085107, 2015. doi:10.1063/1.4928700.

[76] M. Abkar and P. Moin. Large eddy simulation of thermally stratified atmospheric boundary layer flow using a minimum dissipation model. *Boundary-Layer Meteorol.*, 165(3):405–419, 2017. doi:10.1007/s10546-017-0288-4.

[77] M. Abkar, H. Bae, and P. Moin. Minimum-dissipation scalar transport model for large-eddy simulation of turbulent flows. *Phys. Rev. Fluids*, 1 (4):041701, 2016. doi:10.1103/PhysRevFluids.1.041701.

[78] R. Stoll and F. Porté-Agel. Effects of roughness on surface boundary conditions for large-eddy simulation. *Boundary-Layer Meteorol.*, 118: 169–187, 2006. doi:10.1007/s10546-005-4735-2.

[79] R. Stoll and F. Porté-Agel. Large-eddy simulation of the stable atmospheric boundary layer using dynamic models with different averaging schemes. *Boundary-Layer Meteorol.*, 126:1–28, 2008. doi:10.1007/s10546-007-9207-4.

[80] M. Zhang, M. G. Arendshorst, and R. J. A. M. Stevens. Large eddy simulations of the effect of vertical staggering in extended wind farms. *Wind Energy*, 22(2):189–204, 2019. doi:10.1002/we.2278.

[81] S. N. Gadde and R. J. A. M. Stevens. Effect of Coriolis force on a wind farm wake. *J. Phys. Conf. Ser.*, 1256:012026, 2019. doi:10.1088/1742-6596/1256/1/012026.

[82] R. J. A. M. Stevens, M. Wilczek, and C. Meneveau. Large eddy simulation study of the logarithmic law for high-order moments in turbulent boundary layers. *J. Fluid Mech.*, 757:888–907, 2014. doi:10.1017/jfm.2014.510.

[83] U. Piomelli. Wall-layer models for large-eddy simulations. *Prog. Aerosp. Sci.*, 44(6):437–446, 2008. doi:10.1016/j.paerosci.2008.06.001.

[84] P. Sagaut. *Large eddy simulation for incompressible flows: an introduction*. Springer Science & Business Media, Berlin, 2006. doi:10.1007/b137536.

[85] X. Shi, F. K. Chow, R. L. Street, and G. H. Bryan. An evaluation of LES turbulence models for scalar mixing in the stratocumulus-capped boundary layer. *J. Atmos. Sci.*, 75(5):1499–1507, 2018. doi:10.1175/JAS-D-17-0392.1.

[86] D. K. Lilly. The representation of small-scale turbulence in numerical simulation experiments. *Proc. IBM Sci. Comp. Symp. on Environmental Sciences*, 1967. doi:10.5065/D62R3PMM.

[87] P. Moin and J. Kim. Numerical investigation of turbulent channel flow.

J. Fluid Mech., 118:341–377, 1982. doi:10.1017/S0022112082001116.

[88] P. J. Mason and A. R. Brown. On subgrid models and filter operations in large eddy simulations. *J. Atmos. Sci.*, 56(13):2101–2114, 1999. doi:10.1175/1520-0469(1999)056<2101:OSMAFO>2.0.CO;2.

[89] C. Meneveau, T. S. Lund, and W. H. Cabot. A Lagrangian dynamic subgrid-scale model of turbulence. *J. Fluid Mech.*, 319:353–385, 1996. doi:10.1017/S0022112096007379.

[90] C. Canuto, M. Y. Hussaini, A. Quarteroni, and T. A. Zang. *Spectral Methods in Fluid Dynamics*. Springer, Berlin, 1988. doi:10.1007/978-3-642-84108-8.

[91] J. D. Albertson and M. B. Parlange. Natural integration of scalar fluxes from complex terrain. *Adv. Water Resour.*, 23(3):239–252, 1999. doi:10.1016/S0309-1708(99)00011-1.

[92] A. S. Monin and A. M. Obukhov. Basic laws of turbulent mixing in the surface layer of the atmosphere. *Tr. Akad. Nauk SSSR Geophiz. Inst.*, 24(151):163–187, 1954. url:gibbs.science/efd/handouts/monin_obukhov_1954.pdf.

[93] W. Brutsaert. *Evaporation into the atmosphere: theory, history and applications*, volume 1. Springer Science & Business Media, 1982. doi:10.1007/978-94-017-1497-6.

[94] R. J. Beare, M. K. Macvean, A. A. M. Holtslag, J. Cuxart, I. Esau, J.-C. Golaz, M. A. Jimenez, M. Khairoutdinov, B. Kosović, D. Lewellen, T. S. Lund, J. K. Lundquist, A. Mccabe, A. F. Moene, Y. Noh, S. Raasch, and P. Sullivan. An intercomparison of large eddy simulations of the stable boundary layer. *Boundary-Layer Meteorol.*, 118:247–272, 2006. doi:10.1007/s10546-004-2820-6.

[95] J. G. Brasseur and T. Wei. Designing large-eddy simulation of the turbulent boundary layer to capture law-of-the-wall scaling. *Phys. Fluids*, 22:021303, 2010. doi:10.1063/1.3319073.

[96] X. I. A. Yang, H. I. Park, and P. Moin. Log-layer mismatch and modeling of the fluctuating wall stress in wall-modeled large-eddy simulations. *Phys. Rev. Fluids*, 2(10):104–601, 2017. doi:10.1103/PhysRevFluids.2.104601.

[97] C.-H. Moeng and P. P. Sullivan. A comparison of shear- and buoyancy-driven planetary boundary layer flows. *J. Atmos. Sci.*, 51:999–1022, 1994. doi:10.1175/1520-0469(1994)051<0999:ACOSAB>2.0.CO;2.

[98] A. S. Monin and A. M. Yaglom. *Statistical Fluid Mechanics, Vol. 1. Mechanics of Turbulence*. The MIT Press, Cambridge, Massachusetts, 1971. ISBN:9780486458830.

[99] A. E. Perry, S. M. Henbest, and M. Chong. A theoretical and experimental study of wall turbulence. *J. Fluid Mech.*, 165:163–199, 1986. doi:10.1017/S002211208600304X.

[100] J. B. Klemp and D. K. Lilly. Numerical simulation of hydrostatic mountain waves. *J. Atmos. Sci.*, 35(1):78–107, 1978. doi:10.1175/1520-0469(1978)035<0078:NSOHMW>2.0.CO;2.

[101] F. T. M. Nieuwstadt. The turbulent structure of the stable, nocturnal boundary layer. *J. Atmos. Sci.*, 41(14):2202–2216, 1984. doi:10.1175/1520-0469(1984)041<2202:TTSOTS>2.0.CO;2.

[102] P. P. Sullivan, J. C. Weil, E. G. Patton, H. J. J. Jonker, and D. V. Mironov. Turbulent winds and temperature fronts in large-eddy simulations of the stable atmospheric boundary layer. *J. Atmos. Sci.*, 73(4):1815–1840, 2016. doi:10.1175/JAS-D-15-0339.1.

[103] D. H. Lenschow, J. C. Wyngaard, and W. T. Pennell. Mean-field and second-moment budgets in a baroclinic, convective boundary layer. *J. Atmos. Sci.*, 37:1313–1326, 1980. doi:10.1175/1520-0469(1980)037<1313:MFASMB>2.0.CO;2.

[104] P. P. Sullivan, C.-H. Moeng, B. Stevens, D. H. Lenschow, and S. D. Mayor. Structure of the entrainment zone capping the convective atmospheric boundary layer. *J. Atmos. Sci.*, 55:3042–3064, 1998. doi:10.1175/1520-0469(1998)055<3042:SOTEZC>2.0.CO;2.

[105] P. Veers, K. Dykes, E. Lantz, S. Barth, C. L. Bottasso, O. Carlson, A. Clifton, J. Green, P. Green, H. Holttinen, D. Laird, V. Lehtomäki, J. K. Lundquist, J. Manwell, M. Marquis, C. Meneveau, P. Moriarty, X. Munduate, M. Muskulus, J. Naughton, L. Pao, J. Paquette, J. Peinke, A. Robertson, J. Sanz Rodrigo, A. Maria Sempreviva, J. C. Smith, A. Tuohy, and R. Wiser. Grand challenges in the science of wind energy. *Science*, 366(6464):eaau2027, 2019. doi:10.1126/science.aau2027.

[106] S. E. Haupt, B. Kosović, W. Shaw, L. K. Berg, M. Churchfield, J. Cline, C. Draxl, B. Ennis, E. Koo, R. Kotamarthi, L. Mazzaro, J. Mirocha, P. Moriarty, D. Muñoz-Esparza, E. Quon, R. K. Rai, M. Robinson, and G. Sever. On bridging a modeling scale gap: Mesoscale to microscale coupling for wind energy. *Bull. Am. Meteorol. Soc.*, 100(12):2533–2550, 2019. doi:10.1175/BAMS-D-18-0033.1.

[107] F. Porté-Agel, Y.-T. Wu, and C. H. Chen. A numerical study of the effects of wind direction on turbine wakes and power losses in a large wind farm. *Energies*, 6:5297–5313, 2013. doi:10.3390/en6105297.

[108] Y.-T. Wu and Fernando Porté-Agel. Modeling turbine wakes and

power losses within a wind farm using LES: An application to the Horns Rev offshore wind farm. *Renewable Energy*, 75:945–955, 2015. doi:10.1016/j.renene.2014.06.019.

[109] R. J. A. M. Stevens and C. Meneveau. Temporal structure of aggregate power fluctuations in large-eddy simulations of extended wind-farms. *J. Renew. Sustain. Energy*, 6:043102, 2014. doi:10.1063/1.4885114.

[110] W. Munters, C. Meneveau, and J. Meyers. Turbulent inflow precursor method with time-varying direction for large-eddy simulations and applications to wind farms. *Boundary-Layer Meteorol.*, 159(2):305–328, 2016. doi:10.1007/s10546-016-0127-z.

[111] T. Chatterjee, N. W. Cherukuru, Y.T. Peet, and R. J. Calhoun. Large eddy simulation with realistic geophysical inflow of Alpha Ventus wind farm: a comparison with LIDAR field experiments. *J. Phys. Conf. Ser*, 1037(7):072056, 2018. doi:10.1088/1742-6596/1037/7/072056.

[112] S. Baidya-Roy. Simulating impacts of wind farms on local hydrometeorology. *J. Wind Eng. Ind. Aerodyn.*, 99(4):491–498, 2011. doi:10.1016/j.jweia.2010.12.013.

[113] S. K. Siedersleben, A. Platis, J. K. Lundquist, B. Djath, A. Lampert, K. Bärfuss, B. Cañadillas, J. Schulz-Stellenfleth, J. Bange, and T. Neumann. Turbulent kinetic energy over large offshore wind farms observed and simulated by the mesoscale model WRF (3.8.1). *Geosci. Model Dev*, 13, 2020. doi:10.5194/gmd-13-249-2020.

[114] C. Draxl. *On the predictability of hub height winds.* PhD thesis, DTU Wind Energy, 2012. ISBN:978-87-550-3932-2.

[115] D. Carvalho, A. Rocha, M. Gómez-Gesteira, and C. Santos. A sensitivity study of the WRF model in wind simulation for an area of high wind energy. *Environ. Model. Softw.*, 33:23–34, 2012. doi:10.1016/j.envsoft.2012.01.019.

[116] W. Y. Y. Cheng, Y. Liu, A. J. Bourgeois, Y. Wu, and S. E. Haupt. Short-term wind forecast of a data assimilation/weather forecasting system with wind turbine anemometer measurement assimilation. *Renewable Energy*, 107:340–351, 2017. doi:10.1016/j.renene.2017.02.014.

[117] D. Keith, J. DeCarolis, D. Denkenberger, D. Lenschow, S. Malyshev, S. Pacala, and P. J. Rasch. The influence of large-scale wind power on global climate. *Proc. Natl. Acad. Sci. USA*, 101:16115, 2004. doi:10.1073/pnas.0406930101.

[118] L. A. Ivanova and E. D. Nadyozhina. Numerical simulation of wind farm influence on wind flow. *Wind Engineering*, 24(4):257–269, 2000.

doi:10.1260/0309524001495620.

[119] A. C. Fitch, J. B. Olson, J. K. Lundquist, J. Dudhia, A. K. Gupta, J. Michalakes, and I. Barstad. Local and mesoscale impacts of wind farms as parameterized in a mesoscale NWP model. *Mon. Weather Rev.*, 140:3017–3038, 2012. doi:10.1175/MWR-D-11-00352.1.

[120] F. Chatterjee, D. Allaerts, U. Blahak, J. Meyers, and N. P. M. van Lipzig. Evaluation of a wind-farm parametrization in a regional climate model using large eddy simulations. *Q. J. R. Meteorol. Soc.*, 142(701): 3152–3161, 2016. doi:10.1002/qj.2896.

[121] M. Abkar, A. Sharifi, and F. Porté-Agel. Large-eddy simulation of the diurnal variation of wake flows in a finite-size wind farm. *J. Phys. Conf. Ser.*, 625:012031, 2015. doi:10.1088/1742-6596/625/1/012031.

[122] M. Calaf, M. B. Parlange, and C. Meneveau. Large eddy simulation study of scalar transport in fully developed wind-turbine array boundary layers. *Phys. Fluids*, 23:126603, 2011. doi:10.1063/1.3663376.

[123] J. P. Goit, W. Munters, and J. Meyers. Optimal coordinated control of power extraction in LES of a wind farm with entrance effects. *Energies*, 9:29, 2016. doi:10.3390/en9010029.

[124] F. J. Zajaczkowski, S. E. Haupt, and K. J. Schmehl. A preliminary study of assimilating numerical weather prediction data into computational fluid dynamics models for wind prediction. *J. Wind Eng. Ind. Aerodyn.*, 99(4):320–329, 2011. doi:10.1016/j.jweia.2011.01.023.

[125] D. Allaerts, E. Quon, C. Draxl, and M. Churchfield. Development of a Time–Height Profile Assimilation Technique for Large-Eddy Simulation. *Boundary-Layer Meteorol.*, 176(3):329–348, 2020. doi:10.1007/s10546-020-00538-5.

[126] S. E. Haupt, L. Berg, M. Churchfield, B. Kosović, J. Mirocha, and W. Shaw. Mesoscale to Microscale Coupling for Wind Energy Applications: Addressing the Challenges. *J. Phys. Conf. Ser.*, 1452:012076, 2020. doi:10.1088/1742-6596/1452/1/012076.

[127] J. K. Lundquist, J. D. Mirocha, and B. Kosović. Nesting large-eddy simulations within mesoscale simulations in WRF for wind energy applications. In *Proceedings of the Fifth International Symposium on Computational Wind Engineering, Chapel Hill, NC, May*, pages 23–27, 2010.

[128] C. Talbot, E. Bou-Zeid, and J. Smith. Nested mesoscale large-eddy simulations with WRF: Performance in real test cases. *J. Turb.*, 13: 1421–1441, 2012. doi:10.1175/JHM-D-11-048.1.

[129] J. Mirocha, B. Kosović, and G. Kirkil. Resolved turbulence characteristics

in large-eddy simulations nested within mesoscale simulations using the Weather Research and Forecasting Model. *Mon. Weather Rev.*, 142(2): 806–831, 2014. doi:10.1175/MWR-D-13-00064.1.

[130] K. Rai, L. K. Berg, B. Kosović, S. E. Haupt, J. D. Mirocha, B. L. Ennis, and C. Draxl. Evaluation of the impact of horizontal grid spacing in terra incognita on coupled mesoscale–microscale simulations using the WRF framework. *Mon. Weather Rev.*, 147(3):1007–1027, 2019. doi:10.1175/MWR-D-18-0282.1.

[131] J. Sanz Rodrigo, M. Churchfield, and B. Kosović. A methodology for the design and testing of atmospheric boundary layer models for wind energy applications. *Wind Energy Science*, 2(1):35–54, 2017. doi:10.5194/wes-2-35-2017.

[132] J. Schalkwijk, H. J. J. Jonker, A. P. Siebesma, and F. C. Bosveld. A year-long large-eddy simulation of the weather over Cabauw: An overview. *Mon. Weather Rev.*, 143(3):828–844, 2015. doi:10.1175/MWR-D-14-00293.1.

[133] R. Heinze, C. Moseley, C. M. Böske, S. Muppa, V. Maurer, S. Raasch, and B. Stevens. Evaluation of large-eddy simulations forced with mesoscale model output for a multi-week period during a measurement campaign. *Atmos. Chem. Phys.*, 17:7083–7109, 2017. doi:10.5194/acp-17-7083-2017.

[134] C. Draxl, D. Allaerts, E. Quon, and M. Churchfield. Coupling Mesoscale budget components to large-eddy simulations for wind-energy applications. *Boundary-Layer Meteorol.*, 179(1):73–98, 2021. doi:10.1007/s10546-020-00584-z.

[135] S. E. Haupt, R. Kotamarthi, Y. Feng, J. D. Mirocha, E. Koo, R. Linn, B. Kosović, B. Brown, A. Anderson, M. J. Churchfield, C. Draxl, E. Quon, W. Shaw, L. Berg, R. Rai, and B. L. Ennis. Second year report of the atmosphere to electrons mesoscale to microscale coupling project: Nonstationary modeling techniques and assessment. Technical report, Pacific Northwest National Lab.(PNNL), Richland, WA (United States), 2017. doi:10.2172/1573811.

[136] D. Muñoz-Esparza, B. Kosović, J. Van Beeck, and J. Mirocha. A stochastic perturbation method to generate inflow turbulence in large-eddy simulation models: Application to neutrally stratified atmospheric boundary layers. *Phys. Fluids*, 27(3):035102, 2015. doi:10.1063/1.4913572.

[137] D. Muñoz-Esparza and B. Kosović. Generation of inflow turbulence in large-eddy simulations of nonneutral atmospheric boundary layers with the cell perturbation method. *Mon. Weather Rev.*, 146(6):1889–1909,

2018. doi:10.1175/MWR-D-18-0077.1.

[138] R. J. A. M. Stevens, J. Graham, and C. Meneveau. A concurrent precursor inflow method for large eddy simulations and applications to finite length wind farms. *Renewable Energy*, 68:46–50, 2014. doi:10.1016/j.renene.2014.01.024.

[139] A. Sescu and C. Meneveau. A control algorithm for statistically stationary large-eddy simulations of thermally stratified boundary layers. *Q. J. R. Meteorol. Soc.*, 140(683):2017–2022, 2014. doi:10.1002/qj.2266.

[140] D. Allaerts and J. Meyers. Large eddy simulation of a large wind-turbine array in a conventionally neutral atmospheric boundary layer. *Phys. Fluids*, 27:065108, 2015. doi:10.1063/1.4922339.

[141] M. F. Howland, A. S. Ghate, and S. K. Lele. Influence of the horizontal component of Earth's rotation on wind turbine wakes. *J. Phys. Conf. Ser.*, 1037:072003, 2018. doi:10.1088/1742-6596/1037/7/072003.

[142] J. Meyers and C. Meneveau. Optimal turbine spacing in fully developed wind farm boundary layers. *Wind Energy*, 15:305–317, 2012. doi:10.1002/we.469.

[143] J. D. Albertson and M. B. Parlange. Surface length-scales and shear stress: implications for land-atmosphere interaction over complex terrain. *Water Resour. Res.*, 35:2121–2132, 1999. doi:10.1029/1999WR900094.

[144] S. N. Gadde, A. Stieren, and R. J. A. M. Stevens. Large-eddy simulations of stratified atmospheric boundary layers: Comparison of different subgrid models. *Boundary-Layer Meteorol.*, 178:363–382, 2021. doi:10.1007/s10546-020-00570-5.

[145] R. J. A. M. Stevens, D. F. Gayme, and C. Meneveau. Generalized coupled wake boundary layer model: applications and comparisons with field and LES data for two real wind farms. *Wind Energy*, 19(11):2023–2040, 2016. doi:10.1002/we.1966.

[146] S. N. Gadde and R. J. A. M. Stevens. Interaction between low-level jets and wind farms in a stable atmospheric boundary layer. *Phys. Rev. Fluids*, 6:014603, 2021. doi:10.1103/PhysRevFluids.6.014603.

[147] A. Persson. How do we understand the Coriolis force? *Bull. Am. Meteorol. Soc.*, 79(7):1373–1386, 1998. doi:10.1175/1520-0477(1998)079<1373:HDWUTC>2.0.CO;2.

[148] J. Smagorinsky. General circulation experiments with the primitive equations: I. The basic experiment. *Mon. Weather Rev.*, 91(3):99–164, 1963. doi:10.1175/1520-0493(1963)091<0099:GCEWTP>2.3.CO;2.

[149] I. Wijnant, B. van Ulft, B. van Stratum, J. Barkmeijer, J. Onvlee,

C. de Valk, S. Knoop, S. Kok, G. Marseille, H. K. Baltink, and A. Stepek. The dutch Offshore Wind Atlas (DOWA): Description of the dataset, Tech. Rep. TR-380. Technical report, Royal Netherlands Meteorological Institute (KNMI), 2019. Available at: `https://www.dutchoffshorewindatlas.nl`.

[150] NWTC Information Portal. NWTC 135-m Meteorological Towers Data Repository, 2016. `https://nwtc.nrel.gov/135mData` (last access: 12 December 2020).

[151] E. Simley, P. Fleming, and J. King. Design and analysis of a wake steering controller with wind direction variability. *Wind Energy Science*, 5(2):451–468, 2020. doi:10.5194/wes-5-451-2020.

[152] R. J. A. M. Stevens, D. F. Gayme, and C. Meneveau. Effects of turbine spacing on the power output of extended wind-farms. *Wind Energy*, 19: 359–370, 2016. doi:10.1002/we.1835.

[153] A. Stieren, S. N. Gadde, and R. J. A. M. Stevens. Modeling dynamic wind direction changes in large eddy simulations of wind farms. *Renewable Energy*, 170:1342–1352, 2021. doi:10.1016/j.renene.2021.02.018.

[154] J. W. Deardorff. Numerical investigation of neutral and unstable planetary boundary layers. *J. Atmos. Sci.*, 29(1):91–115, 1972. doi:https://doi.org/10.1175/1520-0469(1972)029<0091:NIONAU>2.0.CO;2.

[155] S. K. Shah and E. Bou-Zeid. Direct numerical simulations of turbulent Ekman layers with increasing static stability: Modifications to the bulk structure and second-order statistics. *J. Fluid Mech.*, 760:494–539, 2014. doi:10.1017/jfm.2014.597.

[156] J. R. Garratt. The atmospheric boundary layer. *Earth-Sci. Rev.*, 37(1-2): 89–134, 1994. doi:10.1016/0012-8252(94)90026-4.

[157] J. C. Kaimal and J. J. Finnigan. *Atmospheric boundary layer flows: their structure and measurement.* Oxford university press, 1994. ISBN:9780195062397.

[158] L. Mahrt. Stably stratified atmospheric boundary layers. *Annu. Rev. Fluid Mech.*, 46:23–45, 2014. doi:10.1146/annurev-fluid-010313-141354.

[159] D. Randall, S. Krueger, C. Bretherton, J. Curry, P. Duynkerke, M. Moncrieff, B. Ryan, D. Starr, M. Miller, W. Rossow, G. Tselioudis, and B. Wielicki. Confronting models with data: The GEWEX cloud systems study. *Bull. Am. Meteorol. Soc.*, 84(4):455–469, 2003. http://www.jstor.org/stable/26216834.

[160] L. R. Hoxit. Planetary boundary layer winds in baroclinic

conditions. *J. Atmos. Sci.*, 31(4):1003–1020, 1974. doi:1520-0469(1974)031<1003:PBLWIB>2.0.CO;2.

[161] S. P. S. Arya and J. C. Wyngaard. Effect of baroclinicity on wind profiles and the geostrophic drag law for the convective planetary boundary layer. *J. Atmos. Sci.*, 32(4):767–778, 1975. doi:10.1175/1520-0469(1975)032<0767:EOBOWP>2.0.CO;2.

[162] A. Smedman. Observations of a multi-level turbulence structure in a very stable atmospheric boundary layer. *Boundary-Layer Meteorol.*, 44 (3):231–253, 1988. doi:10.1007/BF00116064.

[163] A. R. Brown. Large-eddy simulation and parametrization of the baroclinic boundary-layer. *Q. J. R. Meteorol. Soc.*, 122(536):1779–1798, 1996. doi:10.1002/qj.49712253603.

[164] A. R. Brown. Large-eddy simulation and parametrization of the effects of shear on shallow cumulus convection. *Bound.-Layer Meteorol.*, 91(1): 65–80, 1999. doi:10.1023/A:1001836612775.

[165] R. M. Banta, R. K. Newsom, J. K. Lundquist, Y. L. Pichugina, R. L. Coulter, and L. Mahrt. Nocturnal low-level jet characteristics over Kansas during CASES-99. *Boundary-Layer Meteorol.*, 105(2):221–252, 2002. doi:10.1023/A:1019992330866.

[166] G. D. Hess. The neutral, barotropic planetary boundary layer, capped by a low-level inversion. *Boundary-Layer Meteorol.*, 110(3):319–355, 2004. doi:10.1023/B:BOUN.0000007248.42321.d5.

[167] W. D. Smyth and J. R. Carpenter. *Instability in geophysical flows*. Cambridge University Press, 2019. doi:10.1017/9781108640084.

[168] L. Conangla and J. Cuxart. On the turbulence in the upper part of the low-level jet: an experimental and numerical study. *Boundary-Layer Meteorol.*, 118(2):379–400, 2006. doi:10.1007/s10546-005-0608-y.

[169] V. W. Ekman. On the influence of the Earth's rotation on ocean-currents. *Archive for Mathematics, Astronomical Physics*, 2:1–52, 1905. URL:jhir.library.jhu.edu/handle/1774.2/33989.

[170] R. Stoll, J. A. Gibbs, S. T. Salesky, W. Anderson, and M. Calaf. Large-eddy simulation of the atmospheric boundary layer. *Bound.-Layer Meteorol.*, 177(2):541–581, 2020. doi:10.1007/s10546-020-00556-3.

[171] R. Floors, A. Peña, and S. E. Gryning. The effect of baroclinicity on the wind in the planetary boundary layer. *Q. J. R. Meteorol. Soc.*, 141(687): 619 – 630, 2015. doi:10.1002/qj.2386.

[172] M. Momen, E. Bou-Zeid, M. B. Parlange, and M. Giometto. Modulation of mean wind and turbulence in the atmospheric boundary layer by

baroclinicity. *J. Atmos. Sci.*, 75(11):3797–3821, 2018. doi:10.1175/JAS-D-18-0159.1.

[173] J. R. Holton. The diurnal boundary layer wind oscillation above sloping terrain. *Tellus*, 19(2):200–205, 1967. doi:10.3402/tellusa.v19i2.9766.

[174] M. Momen. Baroclinicity in stable atmospheric boundary layers: Characterizing turbulence structures and collapsing wind profiles via reduced models and large-eddy simulations. *Q. J. R. Meteorol*, 148:76–96, 2022. doi:10.1002/qj.4193.

[175] S. S. Zilitinkevich and I. N. Esau. The effect of baroclinicity on the equilibrium depth of neutral and stable planetary boundary layers. *Q. J. R. Meteorol. Soc.*, 129(595):3339–3356, 2003. doi:10.1256/qj.02.94.

[176] S. S. Zilitinkevich and I. N. Esau. Resistance and heat-transfer laws for stable and neutral planetary boundary layers: Old theory advanced and re-evaluated. *Q. J. R. Meteorol. Soc.*, 131(609):1863–1892, 2005. doi:10.1256/qj.04.143.

[177] S. Basu, J. Vinuesa, and A. Swift. Dynamic LES modeling of a diurnal cycle. *J. Appl. Meteorol. Climatoly*, 47(4):1156–1174, 2008. doi:10.1175/2007JAMC1677.1.

[178] V. Kumar, G. Svensson, A. A. M. Holtslag, C. Meneveau, and M. B. Parlange. Impact of surface flux formulations and geostrophic forcing on large-eddy simulations of diurnal atmospheric boundary layer flow. *J. Appl. Meteorol. Climatol.*, 49(7):1496–1516, 2010. doi:10.1175/2010JAMC2145.1.

[179] J. G. Pedersen, M. Kelly, S. E. Gryning, and B. Brümmer. The effect of unsteady and baroclinic forcing on predicted wind profiles in Large Eddy Simulations: Two case studies of the daytime atmospheric boundary layer. *Meteorol. Z.*, 22(6):661–674, 2013. doi:10.1127/0941-2948/2013/0477.

[180] Z. Sorbjan. Large-eddy simulations of the baroclinic mixed layer. *Boundary-Layer Meteorol.*, 112:57–80, 2004. doi:10.1023/B:BOUN.0000020161.99887.b3.

[181] K. Ghannam and E. Bou-Zeid. Baroclinicity and directional shear explain departures from the logarithmic wind profile. *Q. J. R. Meteorol. Soc.*, 147(734):443–464, 2021. doi:10.1002/qj.3927.

[182] A. Doosttalab, D. Siguenza-Alvarado, V. Pulletikurthi, Y. Jin, H. Bocanegra Evans, L. P. Chamorro, and L. Castillo. Interaction of low-level jets with wind turbines: On the basic mechanisms for enhanced performance. *J. Renew. Sustain. Energy*, 12(5):053301, 2020. doi:10.1063/5.0017230.

[183] S. N. Gadde and R. J. A. M. Stevens. Effect of turbine-height on wind farm performance in the presence of a low-level jet. *J. Renew. Sustain.*

Energy, 13:013305, 2021. doi:10.1063/5.0026232.

[184] J. A. Aird, R. J. Barthelmie, T. J. Shepherd, and S. C. Pryor. WRF-simulated low-level jets over Iowa: characterization and sensitivity studies. *Wind Energy Sci.*, 6(4):1015–1030, 2021. doi:10.5194/wes-6-1015-2021.

[185] J. Meyers and C. Meneveau. Flow visualization using momentum and energy transport tubes and applications to turbulent flow in wind farms. *J. Fluid Mech.*, 715:335–358, 2013. doi:10.1017/jfm.2012.523.

[186] R. J. A. M. Stevens. Dependence of optimal wind-turbine spacing on wind-farm length. *Wind Energy*, 19:651–663, 2016. doi:10.1002/we.1857.

[187] J. P. Goit and J. Meyers. Optimal control of energy extraction in wind-farm boundary layers. *J. Fluid Mech.*, 768:5–50, 2015. doi:10.1017/jfm.2015.70.

[188] G. Cortina, V. Sharma, R. Torres, and M. Calaf. Mean kinetic energy distribution in finite-size wind farms: A function of turbines' arrangement. *Renew. Energy*, 148:585–599, 2020. doi:10.1016/j.renene.2019.10.148.

[189] H. Lu and F. Porté-Agel. Large-eddy simulation of a very large wind farm in a stable atmospheric boundary layer. *Phys. Fluids*, 23:065101, 2011. doi:10.1063/1.3589857.

[190] M. Dörenkämper, B. Witha, G. Steinfeld, D. Heinemann, and M. Kühn. The impact of stable atmospheric boundary layers on wind-turbine wakes within offshore wind farms. *J. Wind Eng. Ind. Aerodyn.*, 144:146–153, 2015. doi:10.1016/j.jweia.2014.12.011.

[191] M. Abkar and F. Porté-Agel. Influence of atmospheric stability on wind-turbine wakes: A large-eddy simulation study. *Phys. Fluids*, 27:035104, 2015. doi:10.1063/1.4913695.

[192] J. S. Na, E. Koo, E. K. Jin, R. Linn, S. C. Ko, D. Muñoz-Esparza, and J. S. Lee. Large-eddy simulations of wind-farm wake characteristics associated with a low-level jet. *Wind Energy*, 21(3):163–173, 2018. doi:10.1002/we.2152.

[193] N. Ali, N. Hamilton, M. Calaf, and R. B. Cal. Turbulence kinetic energy budget and conditional sampling of momentum, scalar, and intermittency fluxes in thermally stratified wind farms. *J. Turbul.*, 20(1):32–63, 2019. doi:10.1080/14685248.2018.1564831.

[194] O. Maas and S. Raasch. Wake properties and power output of very large wind farms for different meteorological conditions and turbine spacings: A large-eddy simulation case study for the German Bight. *Wind Energy Science*, 7(2):715–739, 2022. doi:10.5194/wes-2021-83.

[195] M. F. Howland, A. S. Ghate, and S. K. Lele. Influence of the geostrophic

wind direction on the atmospheric boundary layer flow. *J. Fluid Mech.*, 883:A39, 2020. doi:10.1017/jfm.2019.889.

[196] M. Abkar and F. Porté-Agel. Influence of the Coriolis force on the structure and evolution of wind turbine wakes. *Phys. Rev. Fluids*, 1: 063701, 2016. doi:10.1103/PhysRevFluids.1.063701.

[197] S. N. Gadde and R. J. A. M. Stevens. Interaction between low-level jets and wind farms in a stable atmospheric boundary layer. *Phys. Rev. Fluids*, 6:014603, 2021. doi:10.1103/PhysRevFluids.6.014603.

[198] J. N. Sørensen and W. Z. Shen. Numerical modeling of wind turbine wakes. *J. Fluids Eng.*, 124:393, 2002. doi:10.1115/1.1471361.

[199] L. Liu, L. Franceschini, D. F. Oliveira, F. C. C. Galeazzo, B.S. Carmo, and R. J. A. M. Stevens. Evaluating the accuracy of the actuator line model against blade element momentum theory in uniform inflow. *Wind Energy*, 25:1046–1059, 2022. doi:10.1002/we.2714.

[200] L. A. Martínez-Tossas, M. J. Churchfield, and C. Meneveau. Large eddy simulation of wind turbine wakes: detailed comparisons of two codes focusing on effects of numerics and subgrid modeling. *J. Phys. Conf. Ser.*, 625:012024, 2015. doi:10.1088/1742-6596/625/1/012024.

[201] M. Golbazi and C. L. Archer. Methods to Estimate Surface Roughness Length for Offshore Wind Energy. *Adv. Meteorol.*, 2019:5695481, 2019. doi:10.1155/2019/5695481.

[202] B. Kosović and J. A. Curry. A Large Eddy Simulation Study of a Quasi-Steady, Stably Stratified Atmospheric Boundary Layer. *J. Atmos. Sci.*, 57:1052–1068, 2000. doi:10.1175/1520-0469(2000)057<1052:ALESSO>2.0.CO;2.

[203] J. Jonkman, S. Butterfield, W. Musial, and G. Scott. *Definition of a 5-MW Reference Wind Turbine for Offshore System Development*. National Renewable Energy Laboratory, Golden, Colorado, 2009. doi:10.2172/947422.

[204] S. N. Gadde, L. Liu, and R. J. A. M. Stevens. Effect of low-level jet on turbine aerodynamic blade loading using large-eddy simulations. *J. Phys. Conf. Ser.*, 1934:012001, 2021. doi:https://doi.org/10.1088/1742-6596/1934/1/012001.

[205] M. P. van der Laan and N. N. Sørensen. Why the Coriolis force turns a wind farm wake clockwise in the northern hemisphere. *Wind Energy Science*, 2:285–294, 2017. doi:10.5194/wes-2-285-2017.

[206] M. Abkar and F. Porté-Agel. Mean and turbulent kinetic energy budgets inside and above very large wind farms under

conventionally-neutral condition. *Renewable Energy*, 70:142–152, 2014. doi:10.1016/j.renene.2014.03.050.

[207] N. Hamilton, H. S. Kang, C. Meneveau, and R. Bayoán Cal. Statistical analysis of kinetic energy entrainment in a model wind turbine array boundary layer. *J. Renew. Sustain. Energy*, 4(6):063105, 2012. doi:10.1063/1.4761921.

[208] I. Sood, E. Simon, A. Vitsas, B. Blockmans, G. C. Larsen, and J. Meyers. Comparison of Large Eddy Simulations against measurements from the Lillgrund offshore wind farm. *Wind Energy Sci.*, pages 1–31, 2022. 10.5194/wes-2021-153.

[209] J. K. Lundquist, K. K. DuVivier, D. Kaffine, and J. M. Tomaszewski. Costs and consequences of wind turbine wake effects arising from uncoordinated wind energy development. *Nat. Energy*, 4(1):26–34, 2019. doi:10.1038/s41560-018-0281-2.

[210] M. B. Christiansen and C. B. Hasager. Wake effects of large offshore wind farms identified from satellite SAR. *Remote Sens. Environ.*, 98 (2-3):251–268, 2005. doi:10.1016/j.rse.2005.07.009.

[211] C. B. Hasager, P. Vincent, J. Badger, M. Badger, A. D. Bella, A. Peña, R. Husson, and P. J. H. Volker. Using satellite sar to characterize the wind flow around offshore wind farms. *Energies*, 8:5413–5439, 2015. doi:10.3390/en8065413.

[212] B. Djath, J. Schulz-Stellenfleth, and B. Cañadillas. Impact of atmospheric stability on X-band and C-band synthetic aperture radar imagery of offshore windpark wakes. *J. Renew. Sustain. Energy*, 10(4):043301, 2018. doi:10.1063/1.5020437.

[213] B. Djath and J. Schulz-Stellenfleth. Wind speed deficits downstream offshore wind parks–A new automised estimation technique based on satellite synthetic aperture radar data. *Meteorol. Zeitschrift*, 28(6):499–515, 2019. doi:10.1127/metz/2019/0992.

[214] T. Ahsbahs, N. G. Nygaard, A. Newcombe, and M. Badger. Wind Farm Wakes from SAR and Doppler Radar. *Remote Sens.*, 12(3):462, 2020. doi:10.3390/rs12030462.

[215] N. G. Nygaard and A. C. Newcombe. Wake behind an offshore wind farm observed with dual-Doppler radars. *J. Phys. Conf. Ser.*, 1037:072008, 2018. doi:10.1088/1742-6596/1037/7/072008.

[216] A. Platis, S. K. Siedersleben, J. Bange, A. Lampert, K. Bärfuss, R. Hankers, B. Cañadillas, R. Foreman, J. Schulz-Stellenfleth, B. Djath, T. Neumann, and S. Emeis. First in situ evidence of wakes in the far field behind

offshore wind farms. *Sci. Rep.*, 8(1):1–10, 2018. doi:10.1038/s41598-018-20389-y.

[217] S. K. Siedersleben, A. Platis, J. K. Lundquist, A. Lampert, K. Bärfuss, B. Cañadillas, B. Djath, J. Schulz-Stellenfleth, J. Bange, T. Neumann, and S. Emeis. Evaluation of a wind farm parametrization for mesoscale atmospheric flow models with aircraft measurements. *Meteorol. Zeitschrift*, 27(5):401–415, 2018. doi:10.1127/metz/2018/0900.

[218] A. Platis, M. Hundhausen, M. Mauz, S. Siedersleben, A. Lampert, K. Bärfuss, B. Djath, J. Schulz-Stellenfleth, B. Canadillas, T. Neumann, S. Emeis, and J. Bange. Evaluation of a simple analytical model for offshore wind farm wake recovery by in situ data and Weather Research and Forecasting simulations. *Wind Energy*, 24:212–228, 2020. doi:10.1002/we.2568.

[219] A. Lampert, K. Bärfuss, A. Platis, S. Siedersleben, B. Djath, B. Cañadillas, R. Hunger, R. Hankers, M. Bitter, T. Feuerle, H. Schulz, T. Rausch, M. Angermann, A. Schwithal, J. Bange, J. Schulz-Stellenfleth, T. Neumann, and S. Emeis. In situ airborne measurements of atmospheric and sea surface parameters related to offshore wind parks in the German Bight. *Earth Syst. Sci. Data*, 12(2):935–946, 2020. doi:10.5194/essd-12-935-2020.

[220] K. S. Hansen, P. E. Réthoré, J. Palma, B. G. Hevia, J. Prospathopoulos, A. Peña, S. Ott, G. Schepers, A. Palomares, M. P. van der Laan, and P. Volker. Simulation of wake effects between two wind farms. *J. Phys. Conf. Ser.*, 625:012008, 2015. doi:10.1088/1742-6596/625/1/012008.

[221] N. G. Nygaard. Wakes in very large wind farms and the effect of neighbouring wind farms. *J. Phys. Conf. Ser.*, 524:012162, 2014. doi:10.1088/1742-6596/524/1/012162.

[222] O. Eriksson, S. P. Breton, K. Nilsson, and S. Ivanell. Impact of wind veer and the Coriolis force for an idealized farm to farm interaction case. *Appl. Sci.*, 9(5):922, 2019. doi:10.3390/app9050922.

[223] N. O. Jensen. A note on wind generator interaction. *Risø-M-2411, RisøNational Laboratory, Roskilde*, 1983. ISBN:87-550-0971-9.

[224] M. Bastankhah and F. Porté-Agel. A new analytical model for wind-turbine wakes. *Renewable Energy*, 70:116–123, 2014. doi:10.1016/j.renene.2014.01.002.

[225] P. B. S. Lissaman. Energy effectiveness of arbitrary arrays of wind turbines. *J. Energy*, 3(6):323–328, 1979. doi:10.2514/3.62441.

[226] A. Niayifar and F. Porté-Agel. Analytical modeling of wind farms: A new approach for power prediction. *Energies*, 9:741, 2016.

doi:10.3390/en9090741.

[227] I. Katić, J. Højstrup, and N. O. Jensen. A simple model for cluster efficiency. *European Wind Energy Association Conference and Exhibition, 7-9 October 1986, Rome, Italy*, pages 407–410, 1986. https://orbit.dtu.dk/en/publications/a-simple-model-for-cluster-efficiency.

[228] S. G. Voutsinas, K. G. Rados, and A. Zervos. On the analysis of wake effects in wind parks. *J. Wind Eng. Ind. Aerodyn.*, 14:204, 1990. https://www.jstor.org/stable/43749429.

[229] S. Frandsen, R. J. Barthelmie, S. Pryor, O. Rathmann, S. Larsen, J. Højstrup, and M. Thøgersen. Analytical modeling of wind speed deficit in large offshore wind farms. *Wind Energy*, 9:39–53, 2006. doi:10.1002/we.189.

[230] S. Frandsen. On the wind speed reduction in the center of large clusters of wind turbines. *J. Wind Eng. Ind. Aerodyn.*, 39:251–265, 1992. doi:10.1016/0167-6105(92)90551-K.

[231] R. J. A. M. Stevens, D. F. Gayme, and C. Meneveau. Coupled wake boundary layer model of wind-farms. *J. Renew. Sustain. Energy*, 7: 023115, 2015. doi:10.1063/1.4915287.

[232] S. T. Frandsen. *Turbulence and turbulence-generated structural loading in wind turbine clusters.* Risø report R-1188 (Roskilde, Denmark), 2007. https://www.risoe.dk/rispubl/VEA/veapdf/ris-r-1188.pdf.

[233] H. Zong and F. Porté-Agel. A momentum-conserving wake superposition method for wind farm power prediction. *J. Fluid Mech.*, 889:A8, 2020. doi:10.1017/jfm.2020.77.

[234] A. Crespo and J. Hernández. Turbulence characteristics in wind-turbine wakes. *J. Wind Eng. Ind. Aerodyn.*, 61:71, 1996. doi:10.1016/0167-6105(95)00033-X.

[235] W. Munters, C. Meneveau, and J. Meyers. Shifted periodic boundary conditions for simulations of wall-bounded turbulent flows. *Phys. Fluids*, 28:025112, 2016. doi:10.1063/1.4941912.

[236] I. Komusanac, G. Brindley, D. Fraile, and L. Ramirez. Wind energy in Europe 2020: Statistics and the outlook for 2021-2025. *Wind Europe*, 2021. https://windeurope.org.

[237] B. Cañadillas, R. Foreman, V. Barth, S. Siedersleben, A. Lampert, A. Platis, B. Djath, J. Schulz-Stellenfleth, J. Bange, S. Emeis, and T. Neumann. Offshore wind farm wake recovery: Airborne measurements and its representation in engineering models. *Wind Energy*, 23(5):1249–

1265, 2020. doi:10.1002/we.2484.

[238] B. Cañadillas, M. Beckenbauer, J. J. Trujillo, M. Dörenkämper, R. Foreman, T. Neumann, and A. Lampert. Offshore wind farm cluster wakes as observed by long-range-scanning wind lidar measurements and mesoscale modeling. *Wind Energy Sci.*, 7(3):1241–1262, 2022. doi:10.5194/wes-2021-159.

[239] A. Stieren and R.J.A.M. Stevens. Evaluating wind farm wakes in large eddy simulations and engineering models. *J. Phys. Conf. Ser.*, 1934: 012018, 2021. doi:https://doi.org/10.1088/1742-6596/1934/1/012018.

[240] M. L. Mayol, A. C. Saulo, and A. D. Otero. Farm to farm wake interaction in WRF: impact on power production. *J. Phys. Conf. Ser.*, 1934(1): 012017, 2021. doi:10.1088/1742-6596/1934/1/012017.

[241] N. Akhtar, B. Geyer, B. Rockel, P. S. Sommer, and C. Schrum. Accelerating deployment of offshore wind energy alter wind climate and reduce future power generation potentials. *Sci. Rep.*, 11(1):1–12, 2021. doi:10.1038/s41598-021-91283-3.

[242] S. Emeis. *Wind energy meteorology: atmospheric physics for wind power generation*. Springer, 2018. doi:10.1007/978-3-642-30523-8.

[243] M. P. van der Laan, K. S. Hansen, N. N. Sørensen, and P. E. Réthoré. Predicting wind farm wake interaction with RANS: an investigation of the Coriolis force. *J. Phys. Conf. Ser.*, 524:1–12, 2015a. doi:10.1088/1742-6596/625/1/012026.

[244] S. Frandsen, R. Barthelmie, S. Pryor, O. Rathmann, S. Larsen, J. Højstrup, P. Nielsen, and M. L. Thoegersen. *The necessary distance between large wind farms offshore - study*. Number 1518(EN). Denmark. Forskningscenter Risø. Risø-R, 2005. ISBN:87-550-3447-0.

[245] U. Högström, J. C. R. Hunt, and A. S. Smedman. Theory and measurements for turbulence spectra and variances in the atmospheric neutral surface layer. *Boundary-Layer Meteorol.*, 103(1):101–124, 2002. doi:10.1023/A:1014579828712.

[246] Y. T. Wu and F. Porté-Agel. Simulation of turbulent flow inside and above wind farms: Model validation and layout effects. *Boundary-Layer Meteorol.*, 146:181–205, 2013. doi:10.1007/s10546-012-9757-y.

[247] M. F. Howland, A. S. Ghate, and S. K. Lele. Coriolis effects within and trailing a large finite wind farm. *AIAA Scitech 2020 Forum*, page 0994, 2020. doi:10.2514/6.2020-0994.

[248] Y. T. Wu, C. Y. Lin, and T. J. Chang. Effects of inflow turbulence intensity and turbine arrangements on the power generation efficiency of large

wind farms. *Wind Energy*, 23(7):1640–1655, 2020. doi:10.1002/we.2507.

[249] N. G. Nygaard and S. D. Hansen. Wake effects between two neighbouring wind farms. *J. Phys. Conf. Ser.*, 753:032020, 2016. doi:10.1088/1742-6596/753/3/032020.

[250] A. Stieren and R. J. A. M. Stevens. Impact of wind farm wakes on flow structures in and around downstream wind farms. *Flow*, 2:E21, 2022. doi:10.1017/flo.2022.15.

[251] A. von Brandis, G. Centurelli, J. Schmidt, L. Vollmer, B. Djath, and M. Dörenkämper. An investigation of mesoscale wind direction changes and their consideration in engineering models. *Wind Energy Sci. Discuss.*, pages 1–28, 2022. doi:10.5194/wes-2022-21.

[252] M. Abkar and F. Porté-Agel. A new wind-farm parameterization for large-scale atmospheric models. *J. Renew. Sustain. Energy*, 7:013121, 2015. doi:10.1063/1.4907600.

[253] J. C. Y. Lee and J. K. Lundquist. Evaluation of the wind farm parameterization in the Weather Research and Forecasting model (version 3.8.1) with meteorological and turbine power data. *Geosci. Model. Dev.*, 10: 4229–4244, 2017. doi:10.5194/gmd-10-4229-2017.

[254] G. W. Qian, Y. P. Song, and T. Ishihara. A control-oriented large eddy simulation of wind turbine wake considering effects of Coriolis force and time-varying wind conditions. *Energy*, 239:121876, 2022. doi:10.1016/j.energy.2021.121876.

[255] J. Fischereit, K. Schaldemose Hansen, X. G. Larsén, M. P. van der Laan, P. E. Réthoré, and J. P. Murcia Leon. Comparing and validating intra-farm and farm-to-farm wakes across different mesoscale and high-resolution wake models. *Wind Energy Sci.*, 7(3):1069–1091, 2022. doi:10.1007/s10546-021-00652-y.

[256] J. Schneemann, F. Theuer, A. Rott, M. Dörenkämper, and M. Kühn. Offshore wind farm global blockage measured with scanning lidar. *Wind Energy Science*, 6(2):521–538, 2021. doi:10.5194/wes-6-521-2021.

[257] R. B. Smith. Gravity wave effects on wind farm efficiency. *Wind Energy*, 13(5):449–458, 2010. doi:10.1002/we.366.

[258] R. B. Smith. Linear theory of stratified hydrostatic flow past an isolated mountain. *Tellus*, 32(4):348–364, 1980. doi:10.3402/tellusa.v32i4.10590.

[259] L. Lanzilao and J. Meyers. A new wake-merging method for wind-farm power prediction in the presence of heterogeneous background velocity fields. *Wind Energy*, 25(2):237–259, 2022. doi:10.1002/we.2669.

[260] D. Allaerts and J. Meyers. Sensitivity and feedback of wind-

farm-induced gravity waves. *J. Fluid Mech.*, 862:990–1028, 2019. doi:10.1017/jfm.2018.969.

[261] L. Lanzilao and J. Meyers. An improved fringe-region technique for the representation of gravity waves in large-eddy simulation with application to wind farms. *arXiv preprint arXiv:2205.10612*, 2022.

Summary

In this thesis we study the interaction of wind turbine wakes inside and in between wind farms with large-eddy simulations (LES). One of the main challenges is the large range of length scales involved in atmospheric boundary layer (ABL) flows. When studying flows through wind farms, the simulation domain of a LES is limited to a few hundred square kilometers. ABL simulations with these domain sizes are often referred to as microscale simulations. This naming highlights that mesoscale processes, such as different weather phenomena, cannot be explicitly simulated in these domains. On the other hand, the microscale simulation domains used to simulate flows through wind farms do not allow to explicitly resolve the smallest turbulent eddies that range in the order of millimeters.

Part I of this thesis focuses on the modeling of sub-grid scale (SGS) phenomena and on the modeling of processes on scales beyond the numerical domain size. First, in **chapter 2**, we focus on the small scales which are modeled in LES using SGS models. We compare three SGS models, namely the Smagorinsky model, the Lagrangian-averaged scale-dependent (LASD) model, and the recently developed anisotropic minimum dissipation (AMD) model in neutral, stable, and unstable ABLs. In contrast to the Smagorinsky model, the AMD and the LASD model allow three-dimensional variations of SGS coefficients and are therefore suitable to model heterogeneous flows over complex terrain or wind farms. Compared to observations and theoretical expectation, both models capture the flow physics better than the Smagorinsky model. The advantage of the LASD model is that it is tuning free, while the AMD model depends on modifications of the Poincaré constant. However, the disadvantage of the LASD compared to the AMD model is that it requires global filtering operations and Lagrangian tracking procedures with a large computational and memory overhead. Consequently, the AMD model, which is more straightforward to implement than the LASD model, is an attractive SGS model for computational intensive simulations of ABLs.

In **chapter 3** the focus is on dynamic wind direction changes, which origi-

nate on scales beyond the domain size and are consequently not incorporated in standard microscale wind farm simulations. We introduce a new method to include dynamic wind direction changes from field measurements or mesoscale simulations in microscale LES. Our approach treats the simulation domain as a non-inertial rotating reference frame and is straightforward to implement. Based on field measurements, we show that the method reproduces atmospheric wind direction changes in neutral ABLs. Simulations of a wind farm show, that dynamic wind directions change the total power production compared to constant wind directions.

Dynamic wind direction changes are only one example of large scale effects that are often neglected in microscale simulations and engineering models of wind farms. Another example are variations in the driving pressure gradient with height, also known as baroclinicity. Baroclinicity arises due to horizontal temperature gradients, which occur in scenarios such as the transition between land and sea, between ice and water, in sloping terrain or in association with mountain ranges. In **chapter 4** we study the impact of negative shear baroclinicity on wind farm performance. Negative geostrophic wind shear strongly influences the available wind resources and causes an increase in turbulence at higher elevations. The power production of wind farms is especially affected under stable atmospheric conditions. In the stable atmospheric boundary layer (SBL) the negative shear creates an upward flux above the low-level jet that limits the energy entrainment into the wind farm. This contrasts the assumption that atmospheric turbulence aids the energy entrainment into wind farms. Therefore, it is essential to account for atmospheric baroclinicity and incorporate its effects in wind farm design tools.

In **Part II** we investigate the impact of wind farm wakes on downstream wind farms and evaluate the representation of wake recovery in engineering models in a neutral boundary layer. Improving the physical understanding of wind farm wake recovery is of utmost importance, since wind farms strongly affect each others performance.

In **chapter 5** we study how well the wake effects between two wind farms are captured by engineering models such as the Jensen model, the coupled wake boundary layer model (CWBL), the Turbulence Optimized Park model (TurbOPark), and the wind farm model developed by Niayifar and Porté-Agel (Energies 9, 741 (2016)). We find that all considered models overestimate the wind farm wake recovery compared to what is observed in LES. Predicted wind farm wake effects with the TurbOPark model are closest to the LES results for the scenario considered in this study, which includes two aligned wind farms with 72 turbines. These results show, that current engineering models have to be improved to be suitable in the planning and design of new wind farms in the proximity of existing ones.

To study the wind farm wake impact on downstream wind farms in more detail, the layout of the wind farms and the distance in between the farms is varied in **chapter 6**. The wake of the upstream farm reduces the performance of the leading row of the downstream farm by up to 33% when the distance between the farms is 5 km and up to 13% when the distance is 15 km. The power production of turbines further downstream in the wind farm is closer to the performance of the corresponding turbines in the upstream farm. Reason for this is the vertical entrainment fluxes which are strengthened above the downstream wind farm. For the same reason, the wind farm wake recovery behind the downstream farm is faster. These findings illustrate that interaction between extended wind farms affects flow structures beyond the wind farm scale, which makes the modeling of wind farm interaction in engineering models challenging. Additionally, the wake recovery is dependent on the layout of the wind farm, i.e. stronger wind farm wakes are found for staggered than for aligned wind farms. These results show why the representation of wind farm wake recovery in engineering models is complicated. Besides the enhanced turbulence in turbine wakes, a parameterization for the vertical kinetic energy flux is required to accurately model wind farm wakes in neutral ABLs.

Finally, in **chapter 7**, we summarize what was learned regarding the research questions posed in **chapter 1** and provide more detailed perspectives.

In brief

In this thesis, we developed and employed high-fidelity LES to study the interaction between wind farms and atmospheric flows. We find that the wind farm power production is strongly influenced by various mesoscale phenomena, such as dynamic wind direction changes and baroclinicity, and by the presence of neighboring wind farms. Furthermore, we demonstrate that computationally more efficient numerical models, which are used for wind farm design, do not capture all of these effects. Therefore, we conclude that these wind farm design models must be updated to include the effect of the mesoscale flow phenomena and the interaction between wind farms.

Samenvatting

In dit proefschrift onderzoeken we de interacties tussen windturbinezoggen binnen en tussen windparken, aan de hand van grote-wervelsimulaties, beter bekend als large eddy simulaties (LES). Een van de voornaamste uitdagingen is het grote scala aan lengteschalen die van betekenis zijn voor luchtstromingen in de atmosferische grenslaag (ABL). In LES van windparken is de grootte van het numerieke domein doorgaans gelimiteerd tot een paar honderd vierkante kilometer. Simulaties van de ABL met dergelijke domeingroottes worden microschaalsimulaties genoemd. Deze naamgeving benadrukt dat mesoschaalprocessen, zoals de vorming van het weer, niet expliciet kunnen worden gesimuleerd in deze domeinen. Anderzijds is de gridresolutie van LES doorgaans niet hoog genoeg om de kleinste turbulente wervels, met groottes in de orde van millimeters, te kunnen simuleren.

Deel I van dit proefschrift richt zich op het modelleren van fenomenen op sub-gridschaal (SGS) en het modelleren van processen op schalen groter dan de domeingroottes van de simulaties. In **hoofdstuk 2** focussen we eerst op de kleinste schalen, welke in LES gemodelleerd worden door SGS-modellen. We vergelijken drie verschillende SGS-modellen, namelijk het Smagorinsky-model, het Lagrangiaans-gemiddelde schaalafhankelijke (LASD)-model en het recent ontwikkelde anisotrope minimale dissipatie (AMD)-model, in simulaties van neutrale, stabiele en onstabiele grenslagen. In tegenstelling tot het Smagorinsky-model, laten de AMD- en LASD-modellen driedimensionale variatie van de SGS-coëfficiënt toe, waardoor deze geschikter zijn voor het modelleren van heterogene stromingen langs oneffen terrein en door windparken. Deze twee modellen representeren de stromingsfysica beter dan het Smagorinsky-model. Voordeel van het LASD-model is dat deze geen kalibratie behoeft, terwijl het AMD-model afhankelijk is van de gekozen waarde voor de Poincaré-constante. Echter, het LASD-model vereist globale filteroperaties en Lagrangiaanse trackingprocedures, welke gepaard gaan met grote reken- en geheugenoverhead. Daarnaast is het AMD-model eenvoudiger te implementeren. Derhalve is dit model uiteindelijk het meest geschikt voor rekenintensieve simulaties van de atmosferische grenslaag.

In **hoofdstuk 3** onderzoeken we dynamische veranderingen van de windrichting, die ontstaan op een schaal groter dan het simulatiedomein en doorgaans dus niet worden meegenomen in de microschaalsimulaties van windparken. We introduceren een nieuwe methode om dynamische veranderingen in windrichting, verkregen uit experimenten of mesoschaalsimulaties, mee te nemen in LES. In deze methode wordt het simulatiedomein als een roterend niet-inertiaalstelsel beschouwd, wat eenvoudig valt te implementeren. Met behulp van veldmetingen tonen we aan dat onze methode atmosferische veranderingen in windrichting nauwkeurig kan simuleren. Uit windparksimulaties maken we op dat een dynamische windrichting invloed heeft op het totale vermogen dat een windpark levert.
Naast dynamische veranderingen van de windrichting zijn er meerdere grote meteorologische effecten die vaak verwaarloosd worden in microschaalsimulaties en modellen van windparken. Een ander voorbeeld zijn veranderingen van de drijvende drukgradiënt met hoogte, zogenoemde barocliniciteit. Barocliniciteit ontstaat als gevolg van horizontale temperatuurgradiënten, welke voorkomen nabij, onder andere, overgangen tussen land en zee, en zee en ijs, nabij heuvelachtige landschappen en nabij berggebieden. In **hoofdstuk 4** onderzoeken we de invloed van een specifieke vorm van barocliniciteit, namelijk negatieve geostrofische windschering, op het vermogen dat windparken leveren. Negatieve geostrofische windschering beïnvloedt sterk hoeveel wind er beschikbaar is en resulteert in een toename van turbulentie op grotere hoogten. De elektriciteitsproductie verandert met name in stabiele atmosferische condities. In stabiele grenslagen zorgt een negatieve windgradiënt voor een opwaartse flux boven het windmaximum, waardoor neerwaarts impulstransport naar het windpark wordt gelimiteerd. Dit contrasteert met de doorgaans gemaakte aanname dat atmosferische turbulentie impulstransport versterkt. Daarom is het essentieel dat de effecten van atmosferische barocliniciteit worden meegenomen in ontwerptools voor windparken.

In **deel II** bestuderen we de invloeden van windparkzoggen op windparken daarachteren evalueren we hoe zoggen herstellen volgens bestaande modellen in een neutrale grenslaag. Het verbeteren van dergelijke modellen is van uiterst belang, gezien windparken elkaars elektriciteitsproductie sterk beïnvloeden.

In **hoofdstuk 5** onderzoeken we of de effecten van zoggen tussen twee windparken accuraat worden vertegenwoordigd in bestaande modellen, waaronder het Jensen-model, het gekoppelde zog-grenslaag (CWBL)-model, het turbulentie-geoptimaliseerde park (TurbOPark)-model, en het windparkmodel ontwikkeld door Niayifar en Porté-Agel (Energies 9, 741 (2016)), in vergelijking met LES. We observeren dat alle bovengenoemde modellen het herstel van de windparkzoggen overschatten in verhouding tot LES. De voorspelde zogeffecten van het TurbOPark model komen het meest overeen met de LES-resultaten, voor het scenario beschouwd in dit onderzoek, bestaande uit twee uitgelijnde windparken met elk 72 turbines. De resultaten tonen aan dat huidige modellen verbeterd dienen te worden, om bruikbaar te zijn voor het plannen en ontwerpen van nieuwe windparken gelegen naast bestaande windparken.

Om de zogeffecten op stroomafwaartsgelegen windparken in meer detail te onderzoeken, variëren we de windparkindeling en afstand tussen turbines in **hoofdstuk 6**. Het zog van een stroomopwaartsgelegen windpark verlaagt het vermogen geleverd door de eerste turbinerij van een stroomafwaartsgelegen windpark met 33%, als de afstand tussen beide parken 5 km bedraagt, en met 13% wanneer deze 15 km bedraagt. Voor de volgende turbinerijen zijn de verschillen in vermogen tussen beide windparken aanmerkelijk lager. De onderliggende oorzaak is dat het verticale transport van impuls boven het stroomafwaartsgelegen windpark is versterkt. Hierdoor herstelt het zog achter dit windpark zich ook sneller. Deze bevindingen illustreren dat de interactie tussen windparken invloed heeft op turbulente structuren op een grotere schaal dan die van een windpark zelf, wat het modelleren van windparkinteracties zeer uitdagend maakt. Daarnaast is het herstel van zoggen afhankelijk van de indeling van een windpark. Uitgelijnde windparken leiden tot sterkere zoggen dan windparken met een gespreide indeling. Deze resultaten laten zien waarom het gecompliceerd is het herstel van zoggen te modelleren met bestaande modellen. Naast de verhoogde turbulentie in de zoggen, is een parametrisatie van de verticale kinetische energieflux vereist om windparkzoggen in neutrale ABL's nauwkeurig te kunnen modelleren.

Tot slot wordt in **hoofdstuk 7** samengevat welke kennis is opgedaan met betrekking tot de onderzoeksvragen uit **hoofdstuk 1** en worden gedetailleerdere perspectieven behandeld.

In het kort

In dit proefschrift hebben we hoogstaande LES ontwikkeld en toegepast om de interactie tussen windparken en luchtstromen in de atmosfeer te onderzoeken. We concluderen dat het door windparken geleverde vermogen sterk afhangt van verscheidene mesoschaalprocessen, zoals dynamische veranderingen van de windrichting en barocliniciteit, en de aanwezigheid van naburige windparken. Verder tonen we aan dat vereenvoudigde numerieke modellen, welke veelal worden gebruikt voor het ontwerpen van windparken, niet in staat zijn al deze effecten te reproduceren. Daarom concluderen we dat dergelijke ontwerptools voor windparken uitgebreid dienen te worden, zodat deze ook mesoschaaleffecten en de interactie tussen windparken omvatten.

Zusammenfassung

In dieser Dissertation entwickeln und nutzen wir Large-Eddy Simulationen (LES) um die Entwicklung und Wechselwirkung von Windschatten hinter Windturbinen und Windparks zu untersuchen. Eine der größten Herausforderungen in diesen Simulationen ist die große Variation von Skalen, welche in Strömungen in der atmosphärischen Grenzschicht vorhanden sind. Für LES von Strömungen durch Windparks ist die Größe der numerischen Simulationsdomänen auf mehrere hundert Quadratkilometer beschränkt. Simulationen der atmosphärischen Grenzschicht in dieser Größenordnung werden oft als Mikroskalen-Simulationen bezeichnet. Diese Bezeichnung verdeutlicht, dass in diesen Simulationsdomänen Prozesse auf Mesoskalen, wie zum Beispiel die Wetterbildung, nicht explizit simuliert werden. Andererseits ist die Auflösung der Mikroskalen-Simulationsdomänen, in welchen Strömungen durch Windparks simuliert werden, immernoch nicht klein genug, um die kleinsten turbulenten Verwirbelungen, welche die Größenordnung einiger Millimeter haben, aufzulösen.

Im **ersten Teil** dieser Dissertation werden Phänomene, die auf den Skalen unterhalb der numerischen Auflösung (SGS) stattfinden, sowie Prozesse, die auf größeren Skalen als der numerischen Domäne stattfinden modelliert. In **Kapitel 2**, werden die Skalen untersucht, welche in LES über SGS-Modelle parametrisiert werden. Hierbei vergleichen wir drei SGS-Modelle in neutralen, stabilen and unstabilen atmosphärischen Grenzschichten: das Smagorinsky-Modell, das Lagrangian-averaged scale-dependent (LASD) Modell, und das kürzlich entwickelte anisotropic minimum dissipation (AMD) Modell. Im Gegensatz zu dem Smagorinsky-Modell, erlauben das AMD- und das LASD-Modell dreidimensionale Variationen der SGS Koeffizienten und sind somit geeignet inhomogene Strömungen über komplexen Topografien oder Windparks zu modellieren. Das LASD-Modells benötigt keine Verfeinerung der Modellparameter, während das AMD-Modell von der Pointcaré Konstante abhängig ist. Der Nachteil des LASD-Modells im Vergleich zum AMD-Modell ist dagegen die Notwendigkeit von globalen Filter-Operationen und dem Lagrange Algorithmus,

welcher einzelne Partikel verfolgt. Letztere führen zu großen Rechenzeit- und Speicher-Overheads. Dementsprechend ist das AMD Model, welches einfacher zu implementieren ist als das LASD-Modell, ein attraktives SGS-Modell für aufwändige Computersimulationen von atmosphärischen Grenzschichten.

In **Kapitel 3** liegt der Fokus auf dynamischen Änderungen der Windrichtung. Diese enstehen auf Skalen, welche größer als die numerische Domäne sind und demzufolge nicht in Windpark Simulationen von Mikroskalen integriert sind. Wir stellen eine neue Methode vor, um dynamische Änderung der Windrichtungen von Feldmessungen oder Mesoskalen-Simulationen in Mikroskalen-LES zu modellieren. In unserem Ansatz wird die Simulationsdomäne als ein trägheitsloses, rotierendes Bezugssystem behandelt, was eine einfache Implementierung erlaubt. Anhand von Feldmessungen zeigen wir, dass unsere Methode atmosphärische Windrichtungsänderungen in neutralen atmosphärischen Grenzschichten reproduziert. Angewandt in Simulationen von Windparks zeigen wir, dass dynamische Windrichtungsänderungen die Gesamtstromproduktion im Vergleich zu statischen Windrichtungen beeinflussen.

Dynamische Windrichtungsänderungen sind nur ein Beispiel von Effekten auf Mesoskalen, die in Mikroskalen-Simulationen und Ingenieurmodellen oft vernachlässigt werden. Ein weiteres Beispiel sind Variationen des Druckgradienten mit der Höhe, sogenannte Baroklinität. Diese Baroklinität entsteht durch horizontale Temperaturgradienten, welche sich beispielsweise an Küsten, Eisschelfen, an abfallenden Terrain oder Gerbirgsketten bilden. In **Kapitel 4** untersuchen wir den Einfluss von negativen geostrophischen Windscherungen, einer Form von Baroklinität, auf das Leistungsvermögen von Windparks. Negative geostrophische Windscherungen beeinflussen die verfügbaren Windressourcen und führen zu einem Anstieg der Turbulenzen in höheren Leveln. Unter stabilen atmosphärischen Bedingungen ist die Stromproduktion von Windparks besonders von Windscherungen beeinflusst. Das liegt an den aufwärts gerichteten Strömungen über dem Low Level Jet, welche den Energieeintrag in den Windpark begrenzen. Diese Ergebnisse widersprechen der Annahme, dass erhöhte atmosphärische Turbulenz den Energiezufluss in Windparks verstärkt. Folglich ist es erforderlich, atmosphärische Baroklinität in Windpark Anlagen-Design-Tools zu berücksichtigen.

Im **zweiten Teil** dieser Dissertation untersuchen wir wie Windschatten hinter Windparks weiter stromabwärts gelegene Windparks beeinflussen und vergleichen die Rückbildung der Windschatten hinter Windparks in einer neutralen Grenzschicht mit den Berechnungen aus Ingenieurmodellen. Ein besseres physikalisches Verständnis über die Rückbildung von Windschatten ist insbesondere notwendig, da Windparks sich gegenseitig beeinträchtigen.

In **Kapitel 5** untersuchen wir die Berechnung der Rückbildung von Windschatten hinter Windparks in einer Auswahl an Ingenieurmodellen, wie dem Jensen-Modell, dem gekoppelten Windschatten Grenzschichtmodell (CWBL), dem Turbulenz optimierten Park-Modell (TurbOPark) und dem Windpark-Modell von Niayifar and Porté-Agel (Energies 9, 741 (2016)), im Vergleich zu LES. Alle genannten Modelle überschätzen die Rückbildung von Windschatten im Vergleich zu den Beobachtungen in LES. In dem Szenario, in welchem zwei Windparks mit jeweils 72 Windkraftanlagen simuliert werden, sind Windschatteneffekte hinter Windparks, welche mit dem TubOPark-Modell vorhergesagt werden, am nächsten an den LES-Ergebnissen. Die Ergebnisse zeigen, dass aktuelle Ingenieursmodelle weiterentwickelt werden müssen um für die Planung und das Design neuer Windparks in der Nähe existierender Windparks geeignet zu sein.

Um den Einfluss von Windschatten hinter Windparks auf stromabwärtsgelegene Windparks detaillierter zu untersuchen, variieren wir das Layout der Windparks und die Distanz zwischen ihnen in **Kapitel 6**. Der Windschatten des stromaufwärts gelegenen Windparks verringert die Stromerzeugung der ersten Reihe des stromabwärts gelegenen Windparks um bis zu 33%, wenn die Distanz zwischen den Parks 5 km beträgt, und bis zu 13% bei einer Distanz von 15 km zwischen den Parks. Die Stromerzeugung der Windkraftanlagen weiter stromabwärts in dem stromabwärts gelegenen Windpark ist näher an den Werten der entsprechenden Windkraftanlagen in dem stromaufwärts gelegenen Park. Grund hierfür ist der abwärts gerichtete Energiefluss, welcher über dem stromabwärtsgelegenem Windpark verstärkt ist. Aus dem gleichen Grund ist die Rückbildung des Windschattens hinter dem stromabwärtsgelegenen Windpark schneller. Diese Ergebnisse zeigen, dass die Interaktion zwischen großen Windparks die gesamte Strömung auch über die Windparkskala hinaus beeinflusst, was die Modellierung der Wechselwirkung von großen Windparks in Ingenieurmodellen erschwert. Zusätzlich hängt die Rückbildung der Windschatten von dem Layout des Windparks ab. Insbesondere wurden stärkere Windschatten hinter Windparks beobachtet, in denen die Windkraftanlagen horizontal gestaffelt sind, als hinter Windparks in denen die Windkraftanlagen anhand der Strömungsrichtung ausgerichtet sind. Während das kürzlich entwickelte TurbOPark-Modell Windschatten hinter Windparks mithilfe von Turbulenzeffekten bereits besser modelliert als ältere Ingenieursmodelle, sind noch viele Schritte notwendig um Windschatten hinter Windparks in Ingenieursmodellen zu simulieren.

Abschließend fassen wir die Schlussfolgerungen aus den Fragestellungen, welche in **Kapitel 1** gestellt wurden, in **Kapitel 7** zusammen und bieten Perspektiven für zukünftige Projekte.

In Kürze

In dieser Dissertation haben wir LES entwickelt und angewandt um die Interaktion von Windparks und atmosphärischen Strömungen zu untersuchen. Wir zeigen, dass die Stromerzeugung von Windparks stark von benachbarten Windparks und von verschiedenen Phänomen abhängt, die auf Mesoskalen enstehen. Beispiele solcher Phänomene sind dynamische Änderungen der Windrichtung und Baroklinität. Desweiteren zeigen wir, dass effizientere numerische Modelle, welche für das Design neuer Windparks genutzt werden, diese Effekte nicht erfassen. Daraus folgt, dass diese Windpark-Design Modelle weiterentwickelt werden müssen, um die Effekte von Stömungsphänomen, die auf Mesoskalen enstehen, und die Interaktion von Windparks zu berrücksichtigen.

Acknowledgements

During the time of my PhD, I got support from so many people to whom I would like to express my gratitude. I apologize in advance in case that I have forgotten anyone. First of all I want to thank my supervisors, Richard and Detlef.

Richard, thank you so much for all your help! You took so much time to support me where you could - in the beginning of my PhD the time was spent in endless discussions and meetings and towards the end of my PhD the time went mostly into the proof-reading of several versions of manuscripts. I am very thankful for all of that, especially that you never got tired of correcting my writing. It is impressive how you even find the smallest mistakes like missing accents or wrong page numbers in references. Also, I very much appreciate your positive mindset in all the times when I picked special setups for which our code would crash and during all the endless bug searches. At the same time you always made sure that I did not get lost in projects which were not feasible within in the four years time frame. Furthermore, I thank you for sending me to conferences, even in the first year when I did not had anything to present (especially since most of the conferences afterwards were fully online due to Covid). Additional to conferences, you planned many events to bring the PoF wind farm group together. Even during the Lock-down times you got creative and arranged social events like online games. Thank you!

Detlef, you create a great working environment for the Physics of Fluids group and take many actions to support the exchange and bonding within the group. Like all PhD students in our group, I always knew that you would support me in any kind of problem and I am very thankful for all of that. Also, it was always fun to film PhD movies with you, it is great that you keep up this tradition.

Next, I would like to express my gratitude to my committee members, *Roberto Verzicco*, *Stefan Luding*, *Jan-Willem van Wingerden* and *Joachim Peinke.* I very much appreciate the time you spent in reading and evaluating my thesis, and of course for preparing the defense. My highly learned opponents,

thank you very much!

The great working atmosphere and solidarity in PoF is highly impacted by Joanita, Gert-Wim, Dennis, Bas, Martin and Thomas. *Joanita*, thanks a lot for organizing all events, your quick responses and solutions to any kind of problems and your calmness. It was also very nice to share the house with you in Belgium! *Gert-Wim*, I always came quite early to the office to work efficiently before the others arrived and then I got trapped by you and the coffee machine. Just kidding, I really enjoyed our morning chats! *Dennis*, you always help out wherever you can and I am very thankful for that. *Bas* and *Martin* thanks for all kind of technical support and *Thomas*, thanks for not throwing me off the stand-up paddle in Belgium.

I definitely spent the most time of my PhD with the wind farmers. *Srinidhi*, I really learned a lot from you and am very thankful for all your help! It is crazy how much time you spent on our code and the projects in general, always staying highly motivated! Additional to all the discussions and collaborations, I also enjoyed the conferences and wind farm events with you. *Jessica*, additional to the working group we also shared the office in pre-Covid times. Sometimes, it was really hard to get some work done, but I enjoyed lots of our chats and our common suffering about the untouchable candy on Stevens desk. Of course there is lots more, the trips to Nantes and Cork, all the sports and dinners with the other girls and all the outings and movies we organized together. Additionally, I am sure that my English improved a lot by having a Canadian by my side and I am very thankful for all the proof-reading you did for me!

Luoqin, you always have a smile on your face and help where ever you can. Thanks for many tips and discussions. Unfortunately our joined ALM and ADM-R project did not end up anywhere, but I learned a lot discussing these things with you. Also, I want to thank you for sharing the Chinese culture with us and for inviting us to dinner. I am very happy for you that you are on track to become a Professor now and enjoy the time in China with Danqi and Peppa. *Ariane*, you joined our group for a short time during the Lock-down and it was very nice to learn about noise propagation from you. *Jens*, I am glad that Richard directly integrated you into the baroclinicity project that Srinidhi and I just started to work on when you joined our group. Although the project took much longer than expected due to the code changes and the endless testing, we finally managed to end the first part of it. You have so many great ideas and question every result that we obtain, such that it is just great to work with you. Also thanks for your help with the Dutch translations!

Davide, Yang, Lucas and *Siem*, it was very interesting to get to know a new wind farm group configuration when Srinidhi, Luoqin and Jessica left. I am very curious on the future projects of this group and hope you enjoy the time here as much as I did, or even more without any pandemic.

* * *

While us wind farmer consider our large-eddy simulations of wind farms to be on the micro-scale, most of the other PoFers would laugh about that. It was always a pleasure to learn about phenomena on "real" micro-scales from other PoFers, like droplets and bubbles. Additionally to discussing science, I highly enjoyed the time in our lunch breaks, especially with the *RUN* group, which was initially created to train to run in the Batavierenrace but was used for so many other things. *Myrthe*, you kind of forced me to start running and I am very happy that you did! Additionally, I am still very thankful for getting your spare key for the cases when my train was canceled and I stranded in Enschede. *Maaike*, same holds for you, thanks for always having a spare bed for me. But of course also thank you for everything else, all the chats, walks, runs and your crazy biking trips with lunch breaks on our balcony were so nice. *Carola*, thank you for asking me to play Biljana in her movie when I just started my PhD. Filming that movie with you and Jelle was a lot of fun and I got to know so many PoFers during the shootings. And I hope that I did not embarrass you too much when playing you in your movie. *Liz*, the dinner you made for us was awesome, and filming your movie was so much fun.

* * *

Robert and *Alex*, I hope we will continue having our little coffee breaks! It was always fun to hear a bit about your Rayleigh-Bénard projects and to chat about one or the other difficulties during our PhDs. And, Robert, please do not forget to continue the Feuerzangenbowle tradition, which Alex initiated and I planned to continue but never did due to Covid-times. It was also great fun to play soccer with you guys and the rest of pre-Covid PoF-United team - *Pieter, Jelle, Álvaro, Misha, Youssef, Srinath, Utkarsch, Yaxing, Steven, Charu, Farzan* and *Marvin*, thank you for letting me join the team besides my limited soccer skills. I always had a lot of fun playing with you. *Jelle*, thanks for one or the other lunch walk and for organizing the yearly trips to Oktoberfest :D *Yaxing* and *Steven*, thank you for sharing the office with me. It was always fun talking to you and I still inspire *Steven* for not touching the huge amount of candy on the desk for several month. I also want to thank my current office mates *Edgar*, *Morgan* and *Mees* for not abandoning me from the office although I was almost always working from home during the last part of my PhD. And *Edgar*, I hope your "nose" operation in Mexico went well.

* * *

To my colleagues as a teaching assistant of the *Physics of Fluids* class, *Ricardo* and *Job*, I enjoyed preparing and discussing new problems with you for the working classes and assignments. It was fun to learn and relearn so many things during that time. I also had the pleasure to (co-)supervise students during their bachelor projects. *Tjeerd* and *Floris*, thanks for being my first students and for all the discussions we had. *Luuk*, you really did a great job in leading our participation in the Batavierenrace and I hope you will find some nice replacements for Maaike and me as co-organizers. *Sander*, it was a pleasure to run and cycle next to you during the last Bata and I hope your foot won't fall asleep next time. *Peter,* I will always remember how you walked around with a plate of cheese at our birthday party to get in contact with our German friends. Keep up being so open-minded and positive. *Pim W.*, I enjoyed filming Jessicas, Carolas and Maaikes movies with you - especially in Jessicas movie your acting was excellent. *Pierre*, I am still impressed how long you survived in the Netherlands despite the unbearable quality of food! Was always fun to chat with you. *Dennis B.*, I guess you won't read this but I still hope we will go diving together some day.

There are still many PoFers who I would like to thank for many nice chats during coffee or lunch breaks, PoF group outings or conferences, *CS, Rodrigo, Chris, Farzan, Vatsal, Ambre, Diana, Martin, Vanshu, Minkush, Jochem, Álvaro, Sarah, Udo, Yogesh, Pim, Bernardo, Duco, Mathieu, Michiel, Pablo, Guilia, Walter* and many others, thanks a lot!

* * *

Ich möchte auch meinen Freunden außerhalb von Enschede danken. *Daniela*, danke, dass du seit dem Kindergarten immer an meiner Seite bist und ich immer auf dich zählen kann. Ich rechne es dir auch hoch an, dass du mich auch hochschwanger noch als Trauzeugin begleitet hast! *Anna*, seit der 5. Klasse werden wir verwechselt und denken täglich um 11:11Uhr aneinander. Vielleicht finden wir auch irgendwann nochmal heraus, wie es damit angefangen hat. Danke, für eine so wundervolle Freundschaft! Als nächstes möchte ich den Geophysiker/innen danken - *Laura, Nele, Judith, Nico, Phlippy, Lukas, Veit, Matthias L.* und viele mehr - ihr habt mich durchs Studium begleitet und unsere Urlaube sind einfach jedes mal grandios! Auf viele weitere Fischtennisrunden! *Matthias H.*, mein *Berater*, wie meine Eltern dich seit dem Moment nennen, in dem sie eingesehen haben, dass wir nicht zusammen sind. Vielen Dank für all die unterhaltsamen Spaziergänge und legendären Parties - ganz besonders für das Silvester 2012/13, wo du mir sehr proaktiv nahegelegt hast, den Lukas doch mal genauer anzusehen. *Chrissie, Flo* und *Lars*, wir haben schon viele schöne Reisen zusammen erlebt und ich hoffe, dass wir das noch ganz oft wiederholen! Auch die *Larsi-Harsi & Co* Abende mit euch, *Miri, Janni, Lena, Bronsi* und *Klara* oder auch alles andere was wir so unternehmen ist immer wieder schön und ich freue mich auf viele weitere gemeinsame Zeiten - nobody works here! *Rieke*, immer wenn ich Pink oder die Toten Hosen höre, denke ich an dich. Eigentlich auch bei jeder Kirche oder jedem Pferd, dass ich sehe. Danke für deine gute Laune und tolle Freundschaft! Ich möchte auch meinen *Sauerländer Mädels* danken, *Jenny, Caro, Vera, Marie, Carina* und *Julia* mit *Benjamin* und *Basti*, es wird wieder Zeit für mehr Spielabende und Tage am Hennesee. Auch *Lukas Stammtisch* ist mir mittlerweile and Herz gewachsen - *Berit, Malte, Philip, Alina, Lukjan, Hermann, Tobias, Christian, Gerrit, Jojo, Matze, Jogi* und *Christoph* danke für viele schöne Tage und Abende. *Julia* und *Christian*, danke, dass ihr uns eure wunderschöne Wohnung überlassen habt - euer Haus finden wir auch sehr schön und übernehmen es sehr gerne. Nein, im Ernst, danke für die tolle Freundschaft.

Deweiteren danke ich dem *TC Manta*, insbesondere natürlich meinen Vorstandskollegen *Andreas, Simeon, Jan, Bernd, Holger* und *Michael*, aber auch *Michelle, Dagmar, Stephan, Pia, Fynn, Hannah, Maxim, Marius, Annika* und vielen anderen. Es ist immer wieder schön mit euch abzutauchen und auch außerhalb des Wassers haben wir viele schöne Momente miteinander erlebt. Auch die *Marathonis* dürfen nicht fehlen - ich bin zwar erst seit Kurzem dabei, danke aber ganz besonders *Verena, Harmke, Anne* und *Sandra*, dass ihr mich jeden Mittwoch und Samstag zum Laufen motiviert.

Last but not least danke ich den wichtigsten Menschen in meinem Leben - meiner Familie.

Pauline, Marlies, Jürgen und *Robin*, danke, dass ihr mich so warmherzig in eure Familie aufgenommen habt. Vor 10 Jahren hatte ich schon meine wunderbare Familie und dann hat mir Lukas euch nochmal dazu geschenkt. Ich bin sehr glücklich, euch in meinem Leben zu haben.

Opa Günter, Oma Rosemarie und *Oma Gisela*, danke, dass ihr immer an mich glaubt und danke, für alle schönen Augenblicke und Gespräche.

Lisa, ich hoffe mittlerweile bist du auch froh, dass Mama und Papa deinen Wunsch, mich als Baby zu verkaufen, ignoriert haben. Wir hatten eine wundervolle Kindheit zusammen und ich liebe es, deinen beiden Kindern, *Josefine* und *Leonard* beim Aufwachsen zuzusehen. Danke, dass du all diese Momente mit mir teilst. *Kevin*, auch du hast meine Familie vor ca. 10 Jahren erweitert und ich freue mich, dich als Schwager zu haben.

Mama und *Papa*, ihr tut so unendlich viel für mich und ich weiß, dass ihr immer hinter mir steht, egal ob ihr meiner Meinung seid oder nicht. Ich kenne niemanden, der so selbstlos, liebevoll und großzügig seinen Kindern gegenüber ist wie ihr und ich bin extrem dankbar für alles was ihr für mich tut. Bitte vergesst nie, auch an euch selbst zu denken!

Lukas, ich kann garnicht in Worten ausdrücken, wie wichtig du mir bist und wie dankbar ich dir für alles bin was du für mich und für uns tust. Egal wo wir sind, mit dir an der Seite fühle ich mich immer zuhause (solange es genug Essen gibt ;-)). Danke, für deine Liebe, deine Ehrlichkeit, dein Vertrauen, deine Offenheit, den Rückhalt den du mir gibst und so vieles mehr! Du zeigst mir, was im Leben wichtig ist und sorgst dafür, dass ich mich nicht überarbeite. Ich freue mich sehr auf unsere gemeinsame Zukunft.